This is to certify that the

dissertation entitled

A High Performance Ion Beam Instrument for the Investigation of Ion/Molecule Reaction Energetics

presented by

Paul Jude O'Connor

has been accepted towards fulfillment
of the requirements for

Ph.D. degree in Analytical Chemistry

John Allison
Major professor

Date 11-8-91

A HIGH PERFORMANCE ION BEAM INSTRUMENT FOR THE INVESTIGATION OF ION/MOLECULE REACTION ENERGETICS

by

Paul Jude O'Connor

A DISSERTATION

Submitted to
Michigan State University
in partial fulfillment of the requirements
for the degree of

DOCTOR OF PHILOSOPHY

Department of Chemistry

1991

ABSTRACT

A HIGH PERFORMANCE ION BEAM INSTRUMENT
FOR THE INVESTIGATION OF
ION/MOLECULE REACTION ENERGETICS

By

Paul Jude O'Connor

Gas-phase ion/molecule investigations provide a means of probing the most fundamental of chemical interactions in the absence of solvent or bulk matrix effects. The experimental approach used in the study of ion/molecule systems is dependent on the information desired. One type of experiment involves focusing a mass selected beam of monoenergetic ions into a collision zone which contains neutral target atoms or molecules. These so-called ion beam methods may be used to probe the intimate mechanistic and energetic details of ion/neutral interactions.

This dissertation describes the design and performance characterization of an apparatus designed to provide well-defined ion/molecule interactions with respect to the internal and translational energy of the reactants. The kinetic energy of the primary ion beam can be varied so that the energy dependent behavior (reactivity) of ion/molecule reactions, including endothermic processes, may be studied. Ions may be generated using conventional electron ionization (EI) or a high pressure drift tube (HPDT) source. The HPDT source assists in controlling the internal energy of the primary ions. The primary ion beam is mass (species) selected with a reverse geometry (BE)

double-foc

ions are st

decelerati

frequency

cell where

from the re

is followed

under aut

system.

Each p

studied a

using be

performa

sections f

double-focusing mass spectrometer. After mass analysis, the primary ions are strongly decelerated using a novel ion optical lens system. The deceleration lens focuses the energy-retarded beam into a radio frequency (rf) ocotopole ion beam guide which passes through a collision cell where ion/neutral interactions occur. Ionic species are extracted from the reaction zone and transferred to a quadrupole mass filter which is followed by a high efficiency detector. Experiments may be performed under automated control with a PC-based data acquisition/control system.

Each principle ion-optical component of the ion beam instrument was studied and designed using computer modeling and then characterized using beam visualization techniques. The overall operational performance was determined by measuring energy-dependent cross-sections for both endothermic and exothermic ion/neutral reactions.

In d

My

Sus

Erin

In dedication to

My parents, for their past encouragement and support

Susan, whose present love sustains me

Erin and Alan, who have become my future

ACKNOWLEDGMENTS

The focus of this dissertation project was the design, construction and characterization of a complex instrument. Yet, in all of my passion for the machine and for the new information it will yield, the most significant and, indeed, the most satisfying aspects of my graduate experience were not the hardware, but rather the relationships that were built during my years at MSU. I hold deep sentiment and gratitude towards my closest comrades Mark Sabo and Jeff Gilbert. Together, we battled the demons of experimental science and the wiles of the omnipresent Firey Dragon who inhabited our corner of the world. I have a rich heritage in remembering Karen, DK, DB, LT, Rich, Spike, Harry (Hairy?), Zippe Burritos and countless scores of cockroaches who made my life oh-so-interesting and enjoyable.

This project would not have been successful without the superior machining/instrument-making skills of Russ Geyer, Deak Watters and Dick Menke who tolerated my endless and unreasonable requests. I am indebted to the electronics expertise of Mike Davenport who always went above and beyond the call of duty in helping to keep the CH5 alive and kicking. Marty Rabb designed a good portion of the computer interface and tutored me in rf and digital electronics by answering nearly all of my stupid questions without making me feel stupid. I am also grateful to Scooter who proficiently wrote the computer control software and also to Tony (LT) Romero and Kurt Kneen who assisted in acquiring much of the early characterization data.

I would

optimism

Finally, I

eloquently

in addition

I would like to thank my co-advisor, George Leroi, for his youthful optimism and for his guidance and support even in the final hour. Finally, I am grateful to my major professor, John Allison, who so eloquently conveyed the precepts of chemistry and the scientific method, in addition to volumes on psychology and human behavior.

Table of Contents

Table

E.I. Ion
H.I. Ion

LIST OF TABLES

Figure

LIST OF FIGURES

Figure

Figure

3.17. Cro
ion

3.18. SIN
abe
ass

3.19. Exp
bea

3.20. Rel
eV.

3.21. Rel
eV

3.22. Th
dis

3.23. D
di

4.1. Io

4.2. Io

4.3. C

4.4. C

4.5. C

4.6. I

4.7.

4.8.

4.9.

4.10.

4.11.

4.12.

4.13.

Figure

Chapter 1

Introduction

I. Mass Spectrometry, The Universe, and Me

There is, perhaps, no other discipline of scientific inquiry that has a scope of application as broad as that of mass spectrometry.

As a qualitative and quantitative analytical technique, mass spectrometry embraces many diverse fields of science. Mass spectrometry is routinely used for structure elucidation and quantitative analysis of organic and inorganic compounds. Due to its extremely low limits of detection, mass spectrometry is uniquely applicable to biochemical problems such as natural products analysis and peptide sequencing where the analyte of interest may be exist in sub-picogram quantities.

Mass spectrometers are also employed in nuclear and atomic physics research. They are used as isotope separators and analyzers in high-energy particle accelerators. Mass spectrometry is also used as a diagnostic and research tool in the medical and forensic sciences. Techniques have been developed to analyze human urine for specific metabolites which are present in certain disease states, or to check for steroid abuse in athletes. Mass spectrometers have also been employed in hospital surgical rooms to provide real-time breath and blood analysis.

Mass s
extraterr
analysis
very valu
deposits.
structure
spectrom
miniatur
balloons
atmosph
on unma
to Mars
atmosph
associate

Mass
investiga
becomes
molecul
depicted

This
species
is accu
which
fundam
bulk m

Mass spectrometry has been implemented in both subterranean and extraterrestrial scientific endeavors. In addition to providing elemental analysis and carbon dating, mass spectrometric techniques have proven very valuable to geological science for the analysis of oil and shale deposits. This has provided a great deal of information on geological structures and petroleum migration. On the other hand, mass spectrometry has played a key role in astronomical science. Special miniaturized mass spectrometers have been launched in high-altitude balloons to study the composition and chemistry of the earth's upper atmosphere. They have also been used in exploratory space probes and on unmanned missions to celestial bodies. The recent Mariner mission to Mars relied heavily on mass spectrometry to study the surface and atmosphere of the planet and also to quantite chemical compounds associated with biological activity.

Mass spectrometric methods are also implemented for chemical investigations of a more fundamental nature. With mass spectrometry, it becomes possible to study the interactions of individual ions and molecules. For example, the elementary bimolecular reaction is often depicted as

$$A + B \rightarrow C + D \qquad (1.1)$$

This equation represents isolated species A encountering isolated species B, resulting in the formation of products C and D. This scenario is accurate only for appropriately low-pressure gas-phase conditions in which only single-collision processes occur. Under these conditions, fundamental interactions may be studied in the absence of solvent or bulk matrix effects. Such experimental environments may be afforded by

a carefully designed mass spectrometer system.

If the conditions of an elementary interaction are carefully controlled, and if the products can be appropriately characterized, a significant amount of chemical information may be obtained. This dissertation details the design, construction and implementation of a new tandem mass spectrometer designed for such investigations.

The MSU ion beam instrument, described here, enables the study of gas-phase ion/neutral chemistry under carefully controlled conditions. The design of the instrument allows for interactions that are well-defined with respect to the internal and translational energy of the colliding pair. Ion/molecule reactions and collision induced dissociation (CID) cross-sections may be studied as a function of ion internal and kinetic energy. This allows for the accurate determination of the energy required to "turn on" endothermic processes. This information may then be the related to bond dissociation energies and ionic heats of formation.

Current theoretical and experimental efforts in our laboratory have focused on the reactions of transition metal-containing ions with neutral organic molecules. Theoretical work has involved *ab initio* calculations at the electron correlation level for transition-metal ions bonded to small organic ligands [1]. This has given insight into the nature of the metal ligand bond as well as the geometry of the ion. Another area of theoretical study concerns the early dynamic events occurring in ion/molecule interactions [2]. Models have been developed to describe the forces that a neutral molecule experiences in the presence of a positively charged particle prior to collision. The electrostatic forces due to charged-induced polarizability and other interactions influence the trajectory of the ion as it approaches an organic neutral. This may lead

to favor

interacti

These ca

transitio

Exper

spectrom

informati

these in

undertak

This inv

spectrom

subseque

fluoresce

This em

spectrosc

The

informat

investiga

compreh

transitio

in the fie

This c

chemistr

in the st

respect

descripti

Succeedi

to favored ion/neutral orientations and preferred sites of orbital interaction (chemistry), and influence the final product distributions. These calculations continue to provide insight into the chemistry of transition-metal ions.

Experimental efforts have centered on ion cyclotron resonance mass spectrometry (ICR). A great deal of descriptive and mechanistic information on transition-metal ion chemistry has been obtained from these investigations [3]. Another experimental effort has been undertaken in this lab to investigate the structure of isolated ions [4]. This involves trapping the ions emitted from a quadrupole mass spectrometer in a low-temperature noble gas matrix. The ions are subsequently subjected to spectroscopic analysis such laser-induced fluorescence (LIF) and/or Fourier transform infrared spectroscopy (FTIR). This emerging technique appears promising for providing direct spectroscopic analysis of transition metal-containing ions.

The MSU ion beam instrument will provide complimentary information to the above mentioned theoretical and experimental investigations of transition-metal ion chemistry. It is anticipated that the comprehensive and multi-disciplinary approach to investigating transition-metal ion chemistry will usher in a new era of understanding in the field.

This chapter first introduces the significance of transition-metal ion chemistry in Section II. The major experimental techniques implemented in the study of gas-phase ion chemistry are discussed in Section III with respect to this research project. This section also gives a general description of the design and features of the MSU ion beam instrument. Succeeding chapters of this dissertation are devoted to the detailed

descripti
componer
of its perf

II. The S

There
catalytic
economic
and alka
low-pres
possible
compoun
of alkene
use of o
hydroge
activity
Organom
catalytic

Why
catalytic
processes
of transi
interme
orbitals
species.
highly re

description and the underlying principles of each of the major components comprising the ion beam instrument and the demonstration of its performance.

II. The Significance of Transition-Metal Ion Chemistry

There are numerous chemical reactions that are enhanced by the catalytic action of transition-metal compounds. Some of the more economically important reactions involve the activation of simple alkenes and alkanes to induce oxidation, reduction, and polymerization. The low-pressure and low-temperature polymerization of olefins is made possible only through the implementation of organo-aluminum/titanium compounds known as Ziegler-Natta catalysts [5]. The specific oxidation of alkenes to form aldehydes and ketones can be controlled through the use of organometallic catalysts [6]. The energy requirements for the hydrogention of alkenes can also be reduced through the catalytic activity of transition-metals in various degrees of oxidation [7]. Organometallics have been proposed as intermediates in a wide variety of catalytic processes [8].

Why do transition-metal species, in particular, exhibit such powerful catalytic activity? The specific role of the transitionmetals in catalytic processes is not fully understood. There are, however, unique properties of transition-metals that may contribute to the ability to act as catalytic intermediates. Transition metals have a high density of low-lying atomic orbitals that provide favorable bonding opportunities with organic species. This propensity towards bonding may enable the stabilization of highly reactive intermediates involved in specific reaction pathways.

An example of transition-metal catalytic activity may be found in the water gas shift reaction [9]. This particular reaction has gained considerable attention in the search for alternative energy sources since the species involved in the reaction are derived from bituminous coal. When coal is heated to moderately high temperatures, an equilibrium mixture of H_2O, CO, H_2 , and CO_2 is produced. The actual process involves the evolution of water and carbon monoxide which is converted to molecular hydrogen and carbon dioxide as shown below.

$$H_2O + CO \rightarrow H_2 + CO_2 \qquad (1.2)$$

There are several compounds with transition-metal centers (M= Fe, Ru, and Rh) which significantly shift the equilibrium to the product side. The forward reaction may be facilitated through a transition metal-carbon monoxide (M-CO) intermediate. Other reactions in which metal centers behave as catalysts have similar implications in which various metal-ligand (M-L) species may be the requisite intermediates.

A great deal of progress in understanding the role of transition metals in catalysis has been gained through the study of the gas-phase chemistry of transition metal-containing *ions* with organic molecules. Under appropriately low pressure conditions, unique species may be generated and studied using a variety of mass spectrometric techniques. In the gas phase, bare metal ions , M^+ (M= Fe, Ni, Co, etc.), are easily formed. In the gas phase it is also possible to generate species that would be impossible to form under condensed-phase conditions due to high reactivity or instability. For example, ligated metal ions with varying degrees of coordinative unsaturation such as M^+-CO_n , M^+-CO_{n-1} , M^+-CO_{n-2} , etc. (M= Fe, Ni, Co, etc.) are easily generated as gas-phase

ions.

The r
neutral
decade
primarily
metal io
effects o
trends h
gas-pha
reactivit
Thus, th
phase n
processe

Altho
reactivit
unansw
are they
characte
ion reac

The
to probe
informa
formatic
energy
will ena
process
electron

ions.

The reactivity of many such transition metal-containing ions with neutral organic molecules has been studied extensively in the past decade [3]. Although most of the work in the field to date has been primarily descriptive in nature, the mechanisms of many transitions-metal ion/organic molecule reactions have been elucidated. Also, the effects of various ligands on metal ion reactivity and periodic reactivity trends have also been investigated. The information obtained from many gas-phase transition-metal ion studies has been correlated with the reactivity of transition-metal compounds in condensed phases [10]. Thus, the behavior of transition-metal ion systems observed in the gas phase may have direct application to understanding bulk catalytic processes.

Although much has been learned regarding the structure and reactivity of transition metal-containing ions, many questions remain unanswered. For example, what is the nature of various M^+-L bonds: are they primarily electrostatic interactions or are they of covalent character? What orbitals and electronic states are important in metal ion reactivity? How strong are the various M^+-L bonds?

The MSU ion beam instrument is a valuable tool which can be applied to probe many of these unanswered questions. Valuable thermochemical information such as bond dissociation energies and ionic heats of formation for M^+-L species may be obtained by studying translational-energy dependent ion/neutral interactions. The ion beam instrument will enable the investigation of periodic reactivity trends for endothermic processes. These studies may add insight into the transition-metal electronic configurations and orbitals involved in many M^+-L bonds. In

the MSU ion beam instrument, metal ions may be selectively prepared in the ground electronic state and/or in well-defined state distributions. This allows the state-specific reactivity of transition-metal ions to be investigated.

Thus, the MSU ion beam instrument will play a role advancing the current level of understanding of transition-metal ion chemistry. It is anticipated that a sound relationship between transition-metal ion structure and reactivity will be developed. This will provide an unprecedented level of predictive ability with respect to intelligent catalyst design.

III. Experimental Techniques for Gas-Phase Ion/Molecule Investigations

A. Overview

In the gas phase, the most fundamental of chemical interactions can be studied. The use of *ionic* species in the gas phase affords certain experimental advantages over systems of purely neutral atoms and molecules. The inherent electrical properties of ions allows for their facile manipulation and detection through the use of applied electric and magnetic fields. A variety of mass spectrometric techniques have been applied to study ion/molecule reactions. The particular experimental approach used in the investigation of ion/molecule systems is dependent on the information desired. This chapter section will cover the application of conventional mass spectrometers used in the investigation of transition-metal ion chemistry. When equipped with variable energy electron or photon ionization sources, conventional mass spectrometers

can pro

concern

specializ

study i

cyclotro

beam m

merits a

relevanc

B. C

Altho

three b

spectro

1.1. Th

system.

usually

system

atoms o

of samp

with hig

thus for

directed

physical

charge (

the mos

field per

can provide some limited thermochemical and mechanistic information concerning transition-metal ions. In addition, some of the more specialized mass spectrometric techniques that are presently available to study ion/molecule reactions will also be presented, such as ion cyclotron resonance mass spectrometry, SWARM techniques, and ion beam methods. The basic operating principles, along with the relative merits and shortcomings of each technique, will be reviewed with relevance to the study of transition-metal ion chemistry.

B. Conventional Mass Spectrometric Threshold Methods

Although there is no universal mass spectrometer design, there are three basic components that are common to most conventional mass spectrometers. A block diagram for a typical system is shown in Figure 1.1. The four basic components of a mass spectrometer, the sample inlet system, the ion source, the mass analyzer and the ion detector, are usually housed in a vacuum chamber which is connected to a pumping system to provide a low pressure ($<10^{-5}$ torr) environment. Neutral atoms or molecules are introduced into the ion source through some type of sample inlet system. The gas-phase neutrals in the source interact with high energy electrons or photons and become ionized. The ions thus formed in the source are extracted with electrostatic optics and directed into the analyzer region of the instrument. There are many physical devices which can separate ions on the basis of their mass-to-charge (m/z) ratio and satisfy the requirements of the analyzer. One of the most common methods involves injecting the ions into a magnetic field perpendicular to the principal direction of ion motion. The force

Figure 1.1. Conventional mass spectrometer Block diagram.

exerted on the ions by the magnetic field will result in curved ion trajectories. The ions will be dispersed on the basis of their momentum in the magnetic analyzer. A description of this type of ion analyzer may be found in Chapter 2 of this dissertation. Another common ion analyzer is the quadrupole mass filter. The device consist of four parallel electrodes to which radio frequency (rf) and direct current (DC) potentials are applied. Ions traveling through the device experience complex trajectories. The proper combination of rf and DC potentials may be applied to enable the device to operate as a mass filter. A brief description of this type of mass analyzer may also be found in Chapter 2 of this dissertation. The ion detector may be a simple device such as a Faraday cup to measure ion current, or it may be some sort of particle (electron) multiplier to amplify small ion currents.

A block diagram of a typical electron ionization (EI) source is found in Figure 1.2. A detailed description of the principles of EI source operation is given in Chapter 2 of this dissertation. Basically, electrons are emitted from the resistively heated filament located outside the ion source. An electric field, created by the potential difference between the filament and the ion source, accelerates the electrons through the source and towards an electron collector. If an electron with sufficient energy interacts with a neutral atom or molecule, the neutral species becomes excited and emits an electron to form a positively charged molecular ion. Polyatomic molecular ions may be formed with significant excess internal energy. This results in rapid unimolecular decomposition of the parent ion to produce fragment ions. The ion population thus formed in the source is extracted by an electrostatic lens system and transfered to the analyzer and detector regions of the mass spectrometer.

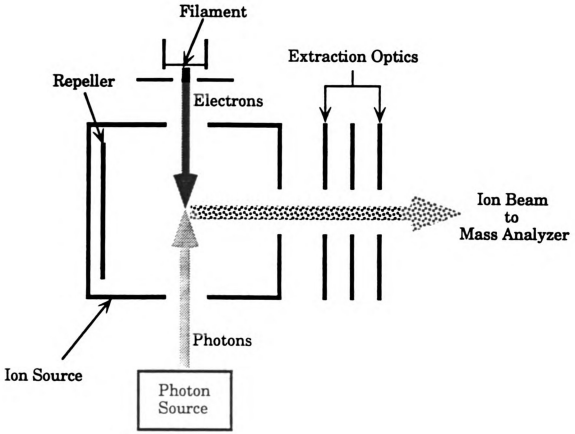

Figure 1.2. Mass spectrometer ion source.

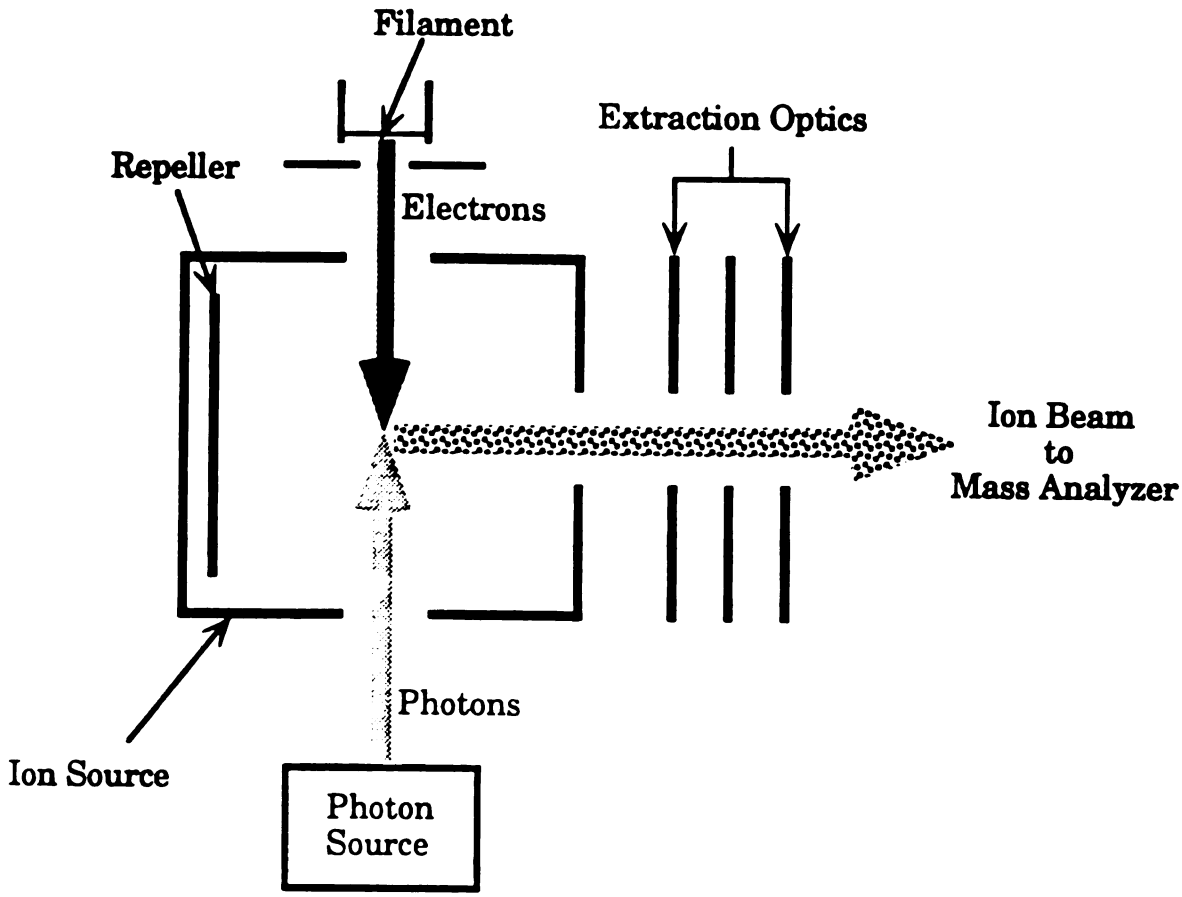

Figure 1.2. Mass spectrometer ion source.

The nom
potentia
kinetic e
molecul
obtaine
producti
of comp
energy r
below:

The
energy.

If th
heat of
followin

or

Even
the eff
fragmer
each fr
clastog
1.3 [11]

The nominal kinetic energy of the ionizing electrons is determined by the potential difference between the filament and the source. The electron kinetic energy may be varied while monitoring the relative production of molecular and fragment ions. Useful thermodynamic information may be obtained by monitoring effects of electron kinetic energy on ion production for a given compound. For example, the ionization energy (IE) of compound, A, may be measured determining the minimum electron energy required to detect the formation of the ion, A^+. This is expressed below:

$$A + e^- \rightarrow A^+ + 2\,e^- \qquad (1.3)$$

The the enthalpy change for this process is equal to the ionization energy.

$$IE(A) = \Delta H_{rxn}. \qquad (1.4)$$

If the heat of formation of the neutral compound is known, then the heat of formation (ΔH_f) of the ionic species may be determined from the following relationship.

$$IE(A) = \Delta H_{rxn} = \Delta H_f(A^+) - \Delta H_f(A) \qquad (1.5)$$

or

$$\Delta H_f(A^+) = IE(A) + \Delta H_f(A) \qquad (1.6)$$

Even more information may be derived experimentally by monitoring the effects of ionizing energy on the production of molecular and fragment ions. A plot of the relative abundance of the molecular ion and each fragment ion as a function of electron energy is known as a clastogram. A clastogram for chromium hexacarbonyl is shown in Figure 1.3 [11]. The minimum electron energy required to form the parent ion is

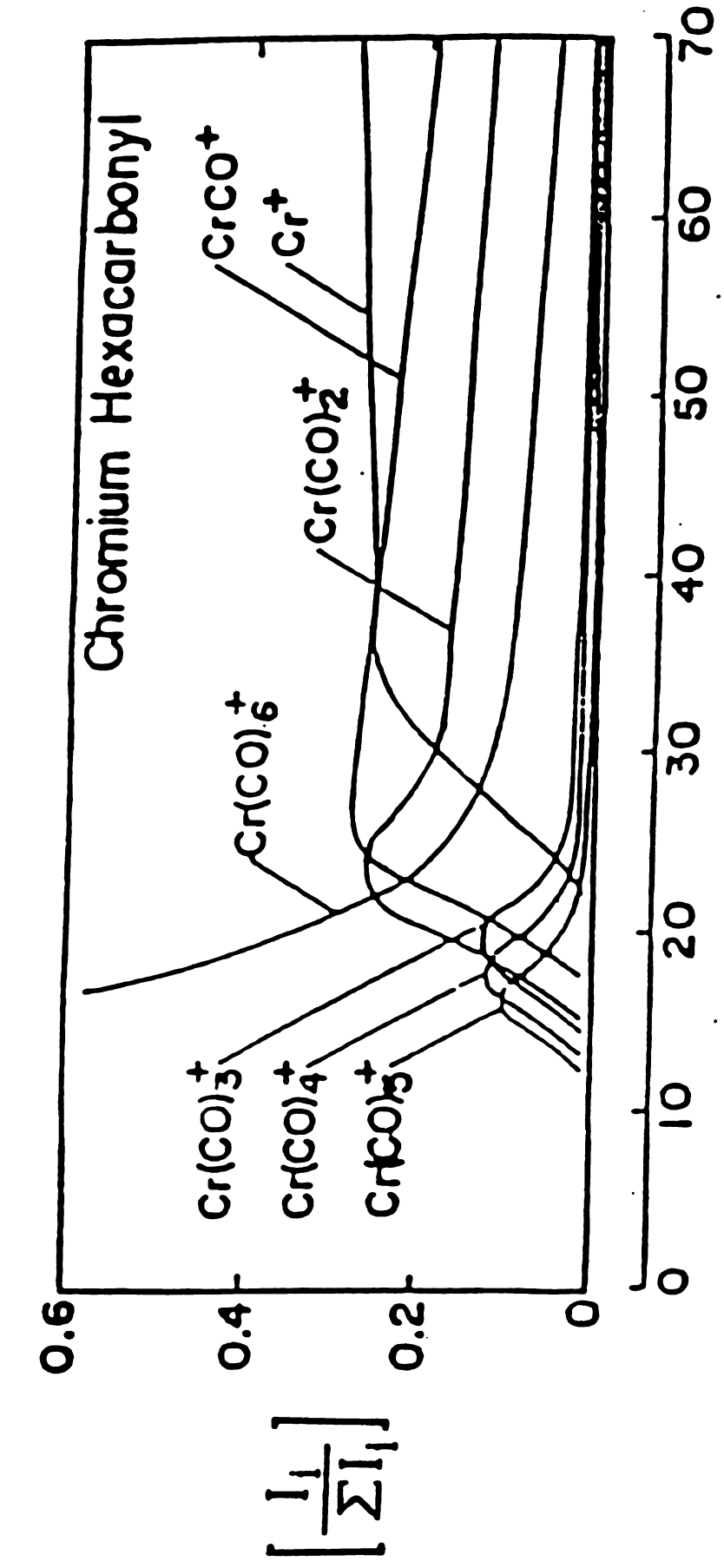

Figure 1.3. Clastogram for Chromium Hexacarbonyl.

taken as the ionization energy of the molecule. This can be related to the heat of formation (ΔH_f) of the ionic species if the gas-phase heat of formation of the neutral precursor is available. From the plot shown in Figure 1.3, the electron energies required to form various ions in the series shown below can be determined.

$$Cr(CO)_6 + e^- \rightarrow Cr(CO)_5^+, Cr(CO)_4^+, Cr(CO)_3^+, ..., Cr^+ \quad (1.7)$$

The minimum electron energy which results in the formation of a particular fragment is taken as the appearance energy (AE) of that species. For example, the authors determined the appearance energy of Cr^+ from $Cr(CO)_6$ to be 17.7 ±0.3 eV [11]. The balanced chemical equation for this process is shown below.

$$Cr(CO)_6 + e^- \rightarrow Cr^+ + 6CO + 2e^- \quad (1.8)$$

This information may then be related to the heat of formation of the bare metal ion, Cr^+. If the heats of formation for the neutral precursor and neutral products are known the ionic heat of formation may be derived as follows.

$$AE(Cr^+, Cr(CO)6) = \Delta H_{rxn}(1.8) \quad (1.9)$$

$$\Delta H_{rxn}(1.9) = \Delta H_f(Cr^+) + 6\,\Delta H_f(CO) - \Delta H_f(Cr(CO)_6) \quad (1.10)$$

combining equations (1.9) and (1.10)

$$\Delta H_f(Cr^+) = AE(Cr^+, Cr(CO)_6) - 6\Delta H_f(CO) + \Delta H_f(Cr(CO)_6) \quad (1.11)$$

Although the energy-dependent behavior of ionization processes can yield important thermochemical information, there are significant limitations. The difficulty in obtaining accurate thermodynamic information from experiments such as these arise from two major

sources
error a
electron
in the v
ignores
(contac
the pen
Spatial
beam s
additio
a Maxw
for a fil

The
efforts
Experi
ion sou
retardi
method
ion pro
12). V
vanishi
slope n
method

The
with e
radiati
have b

sources, experimental and phenomenological. Experimental sources of error are dominated by the uncertainty in the kinetic energy of the electrons. The nominal kinetic energy is usually taken as the difference in the voltages applied to the filament and the source which, of course, ignores potential variations caused by the junction of dissimilar metals (contact potentials). The electron energy is also strongly influenced by the penetration of ion repeller and extraction fields inside the source. Spatial variation of potentials inside the source and the effect of electron beam space-charge also contribute to electron energy uncertainty. In addition the electrons are emitted from a high temperature filament with a Maxwellian energy distribution. This is approximately 0.5 eV (FWHM) for a filament temperature of 1500 °C [12].

There have been numerous experimental and data manipulation efforts to circumvent the problems related to electron energy spread. Experimental improvements include the implementation of sophisticated ion sources that employ electron monochromators [13] and electron retarding-field devices [14]. An excellent discussion of the various methods of extracting threshold energies from electron energy-dependent ion production curves is found in a monogragh by Westmore (reference 12). Various data manipulation techniques are discussed such as the vanishing current method, the linear extrapolation method, the critical slope method, the semilogarithmic plot method, in addition to derivative methods.

The great uncertainty in energy of the ionizing medium associated with electron ionization sources lead, in part, to the development of *radiation* sources for ionization. Photoionization mass spectrometers [15] have been constructed in which photons are used as the ionizing

medium
few mil
monoch
studies
intense
large va
selectio
by anal
radiatio
studies
been d
experim
two sep

In ac
thermo
there a
associa

For
compou

The
assume
transla
(primar
any tra
sophist

medium. The energy resolution of the photons is often on the order of a few milli-electronvolts. However, it is very difficult to produce monochromatic radiation in the energy range necessary for ionization studies (5-20 eV). Pseudo-continuum radiation sources may employ intense hydrogen or rare gas discharges. These are optically coupled to large vacuum UV monochromators to provide high resolution wavelength selection on the order of 1 Å or less. Internal calibration is accomplished by analyzing noble gas emission lines. More recently, tunable laser radiation in the vacuum UV range has been used in photoionization studies [16]. Also, extremely sophisticated experimental techniques have been developed to induce multi-photon ionization [17]. These experiments require very intense laser sources and may even incorporate two separate laser sources (two-color ionization)

In addition to the experimental uncertainties encountered in obtaining thermodynamic information from variable energy ionization sources, there are severe, and often restricting, *phenomenological* uncertainties associated with such threshold methods.

For example Equation (1.3) gives the electron ionization process for a compound A.

$$A + e^- \rightarrow A^+ + 2\,e^- \qquad (1.3)$$

The expression for the heat of formation of A^+ (Equation (1.5)) assumes that all of the reaction products possess no excess internal or translational energy. It implies that the kinetic energy of the ionizing (primary) electron is completely utilized by the neutral molecule. Also, any translational energy of the ejected electron is neglected. Some sophisticated experimental methods have been devised to measure the

kinetic

ionizin

techniq

electro

uncerta

Ano

thresh

fragmer

Cr(CO)

discuss

In a

found i

(Equati

excess

ground

ligands

configu

lies ap

Cr(CO

electro

The io

Cr(CO

form

appea

with t

kinetic energy of the ejected electron when photons are used as the ionizing medium. These photoionization-photoelectron spectroscopy techniques explicitly account for the translational energy of ejected electrons and provide highly accurate ionization energies.with uncertainties of less than 0.002 eV.

Another more severe phenomenological problem arises when threshold methods are used to determine the thermodynamics of fragmentation processes. The production of the bare metal ion, Cr^+, from $Cr(CO)_6$ as shown in Equation (1.8) will serve as an example for this discussion.

$$Cr(CO)_6 + e^- \rightarrow Cr^+ + 6CO + 2e^- \qquad (1.8)$$

In addition to not explicitly accounting for any excess kinetic energy found in the products, the expression for the heat of formation of Cr^+ (Equation (1.10)) assumes that all of the reaction products possess no excess *internal* energy. Also, the assumption that Cr^+ is produced in its ground state may not be accurate. When bonded to the 6 carbonyl ligands, the Cr metal center of the neutral precursor has an electron configuration associated with a low-spin singlet excited state. This state lies approximately 3.7 eV above the ground state for free Cr. When $Cr(CO)_6$ undergoes electron ionization to form free Cr^+, a high-energy electron configuration similar to that of the neutral Cr may be retained. The ionization processes may be viewed as removing the six ligands from $Cr(CO)_6$ to leave the free metal center and then removing an electron to form Cr^+ in a highly excited state. In fact, information from careful appearance potential measurements of Cr^+ from $Cr(CO)_6$ have correlated with the formation of excited state Cr^+ d^5 ($^2I_{(1\ 1/2)}$) [13].

The

depend

is supp

found

ionized

thresh

such

reactivi

B. I

If a

magne

is beca

expres

The

In this

magne

determ

rotatio

The

the io

typical

can th

The state of a metal ion formed by electron ionization is therefore dependent on the state of the metal center in the neutral precursor. This is supported by other studies in which the heat of formation of Fe^+ was found to range form 14.7 to 16.1 eV depending on the neutral being ionized [18]. Thus, the thermodynamic information from source threshold methods is often inaccurate. This limits the applicability of such thermochemical information to understanding ground state reactivity of transition-metals in condensed phase catalytic processes.

B. Ion Cyclotron Resonance Mass Spectrometry

If an ion with charge q is moving with a velocity **v** in a uniform magnetic field having intensity **B** the ion will follow a curved path. This is because of the force exerted on the ion by the magnetic field as expressed below:

$$F = q\mathbf{v} \times \mathbf{B} \qquad (1.11)$$

The force constrains the ion to a circular path as shown in Figure 1.4. In this figure, the ion velocity is restricted to the x-y plane and the magnetic field is perpendicular to x-y plane. The ion mass and velocity determine the radius of the curved trajectory, but the *frequency*, f, of rotation is dependent on the mass, m, as expressed below.

$$f = qB/2\pi m \qquad (1.12)$$

The angular frequency, $\omega = 2\pi f$, is known as the cyclotron frequency of the ion and is usually on the order of several hundred kilohertz for typical magnetic field strengths (~1 tesla). The ion mass/charge value can thus be related to the frequency of ion orbit. These principles have

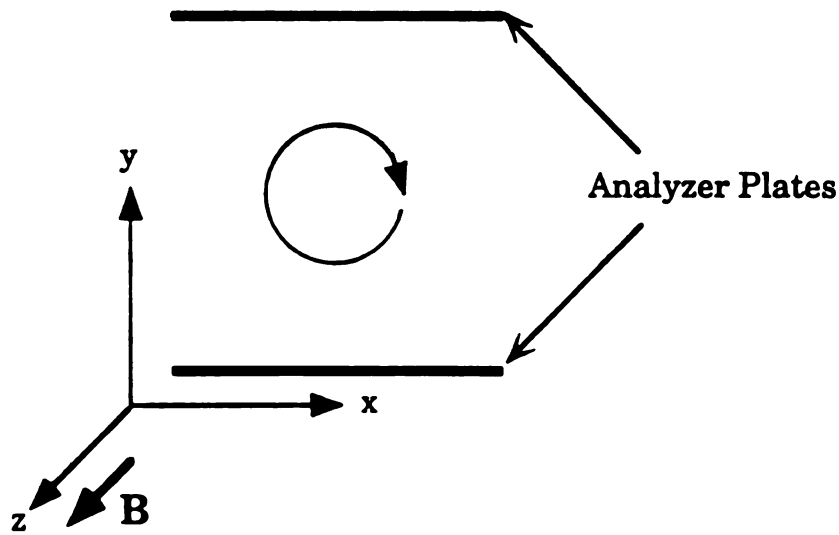

Figure 1.4. Ion cyclotron motion.

been
spectro
Ion
more s
of the
frequer
will ab
power
related
detecti
plates.
cyclotr
the IC
packe
packet
signal
values
conver
mass,
know
Alt
than j
a mag
and lo
neutr
subse
study

been applied to develop ion cyclotron resonance (ICR) mass spectrometers[19].

Ion manipulation and detection can be accomplished by using one or more sets of analyzer plates as shown in Figure 1.4. The periodic motion of the ions may be detected by applying a signal at the ion cyclotron frequency to the analyzer plates. Ions orbiting at the applied frequency will absorb power and experience an increased trajectory radius. This power absorption can be sensed with the electrical circuitry and be related to the ion population in the ICR. Another powerful method of ion detection involves briefly applying a complex waveform to the analyzer plates. This small "chirp" signal usually contains all of the possible ion cyclotron frequencies (within a given mass range). Ions present inside the ICR cell will absorb the power and begin to move in coherent ion "packets" on the basis of their m/q value. The motion of these ion packets will in turn induce a signal on the analyzer plates. This complex signal will contain frequencies associated with all of the different ion m/q values present in the cell. A Fourier transformation may be applied to convert the complex signal information to the frequency, and hence mass, domain. This technique of ion manipulation and detection is known as Fourier transform ICR or simply FTMS [20].

Although actual ICR and FTMS instruments are much more complex than just described, one significant feature is that ions can be trapped in a magnetic field for a substantial period of time (in the millisecond range and longer). Trapped ions may be allowed to interact with a low-pressure neutral gas and the ionic products of such an interaction may be subsequently analyzed. This makes ICR instruments very useful for the study of ion/molecule reactions.

Alth

ICR ins

ions w

hexaca

below v

If an or

electro

Thu

chrom

suffici

will ev

and c

popul

from

speci

stora

relat

ion p

gas p

mos

ion/

obse

ther

for t

Although other techniques such as laser ionization exist [21], most ICR instruments utilize high energy electrons (~70eV) to form primary ions within the analyzer cell. For example, if neutral chromium hexacarbonyl is subjected to electron ionization, ions in the series shown below will be formed in the ICR cell.

$$Cr(CO)_6 \; EI \rightarrow Cr(CO)_5^+, Cr(CO)_4^+, Cr(CO)_3^+, ..., Cr^+ \qquad (1.13)$$

If an organic gas such as propane is present, it too will be ionized by the electrons and produce ions such as those shown below

$$C_3H_8 \; (EI) \rightarrow C_3H_8^+, C_3H_6^+, C_2H_4^+, \; \text{etc.} \qquad (1.14)$$

Thus, the primary ions in the ICR cell will consist of a mixture of chromium carbonyls and hydrocarbon fragments. If the pressure is sufficiently high and the residence time is sufficiently long, these ions will eventually interact with other neutral molecules such as the propane and chromium hexacarbonyl present in the ICR cell. The resulting ion population in the ICR cell from both the primary ions and those resulting from ion/molecule reactions, can be very difficult to interpret. Therefore, special techniques such as double resonance [22] and selective ion storage have been developed to provide clear precursor ion/product ion relationships. By monitoring the intensity of precursor ion and product ion populations as a function of time, while carefully controlling reactant gas pressure, kinetic studies may be performed. It has been shown that most reaction rates occur within an order of magnitude of the ion/neutral collision frequency. This implies that most product ions observed in ICR investigations proceed through exothermic (or thermoneutral) channels and that no significant enthalpy barriers exist for the forward reaction.

A la
contain
technic
branch
Studies
ions wi
groups
periodi
metal a
Mos
be desc
the act
metal
informa
(BDEs)
examp
dehydr
exother
produc
The
system
CH_3
The

A large body of information on the reactivity of transition metal-containing ions with organic neutrals has been generated using ICR techniques[23]. Most of the information concerns the product ion branching ratios resulting from exothermic ion/molecule reactions. Studies have been performed to determine the relative reactivity of metal ions with respect to the organic reactant chain length [24] and functional groups [25]. Also, studies directed towards understanding metal ion periodic reactivity trends [26], and the the effects of ligands bound to metal anions have been conducted [27].

Most of the chemical interpretations from ICR investigations tends to be descriptive in nature. However, a great deal of information regarding the actual mechanisms of activation of organic species by transition-metal ions has been obtained. In addition, some thermochemical information such as metal ion-ligand (M-L) bond dissociation energies (BDEs) for ionic species has been inferred from metal ion reactivity. For example, the bare nickel ion has been found to induce dehydrohalogenation in i-propylchloride to form $Ni(HCl)^+$ as an exothermic process. Since the most thermodynamically favorable neutral product is propene, the reaction can be written as

$$Ni^+ + CH_3(CHCl)CH_3 \rightarrow Ni(HCl)^+ + CH_3CHCH_2 \quad (1.15)$$

$$\Delta H_{rxn(15)} \leq 0$$

The dehydrohalogenation process for the neutral i-propylchloride system shown below is an endothermic process.

$$CH_3(CHCl)CH_3 \rightarrow HCl + CH_2(CH)CH_3 \quad \Delta H_{rxn} = +0.83 \text{ eV} \quad (1.16)$$

The thermodynamics of reactions 1.15 and 1.16 suggest that the Ni^+-

HCl bon

Liga

transit

recent

of nick

observ

Fro

greater

Alth

get acc

ICR te

ion ch

energ

meas

the in

ther

repr

I

NiC

NiC

the

and

rea

abs

che

HCl bond bond dissociation energy is ≥0.83 eV.

Ligand displacement reactions can also be used to bracket BDEs in transition-metal ion systems. An example of this may be found in a recent article by Stepnowski and Allison [28]. In a study of the reactions of nickel-containing ions with neutral PF_3 the following reaction was observed.

$$NiCO^+ + PF_3 \rightarrow NiPF_3^+ + CO \quad \Delta H_{rxn} \leq 0 \qquad (1.17)$$

From this reaction it can be concluded that the Ni^+-PF_3 BDE is greater than the Ni^+-CO BDE.

Although *relative* BDEs can be determined, it is, however, difficult to get accurate and *absolute* thermochemical information by implementing ICR techniques. In addition, for most investigations of transition-metal ion chemistry using ICR, the most common method of ionization is high energy (~70 eV) EI. As discussed in the section on source threshold measurements, this method of preparation results in great uncertainty in the internal energy of the reactant ions. Thus, many of the reactions and thermochemical implications derived from ICR work may not be representative of ground state chemistry.

In the example of a ligand displacement reaction (equation 1.17),.the $NiCO^+$ reactant ion was prepared by electron ionization of $Ni(CO)_4$. Is the $NiCO^+$ fragment ion in the ground electronic and vibrational state? Or is the $NiCO^+$ ion population in the ICR cell a distribution of ground state and excited state ions? Is the observed chemistry due to ground state reactivity or is it exclusive to $NiCO^+$ in an excited state? What is the absolute Ni^+-PF_3 bond dissociation energy? This illustrates just one chemical system for which many questions remain unanswered by the

limitati

C. S

Low

investi

ions a

helium

flowing

reactar

drift tu

The

severa

genera

high e

state

the fl

proce

after

trace

throu

that

selec

of io

vers

regi

inte

limitations of typical ICR methodology.

C. Swarm Methods

Low energy interactions between ions and neutral species can also be investigated using so-called 'swarm' techniques. In these techniques, ions are injected into a flowing stream of an inert buffer gas such as helium or argon in a drift tube. A reactant gas is also introduced into the flowing stream. The 'swarm' of ions may interact with the neutral reactants to form new ionic products. A general schematic diagram of a drift tube instrument is found in Figure 1.5.

The ion source shown at the left side of Figure 1.5 may be one of several designs. In the flowing afterglow (FA) technique, ions are generated in the source region by a high energy electrical discharge or high energy electrons which initially form a large population of excited state He atoms and ions [29]. The highly-excited plasma traveling with the flowing buffer gas generates photons through a number of relaxation processes and creates a bright glowing region - hence the term flowing afterglow. If another species such as molecular nitrogen is present in trace quantities, ionic species such as N_2^+ and N^+ may be formed through Penning ionization and charge transfer precesses. It is obvious that the flowing afterglow source gives very little control over the selection of primary ions injected into the drift tube. This limits the type of ionic systems that may be studied with FA sources. Another, more versatile, ion source employs a standard EI or chemical ionization (CI) region preceding a quadrupole mass filter. In this manner the ions of interest may be injected into the flowing stream of buffer gas as a mass-

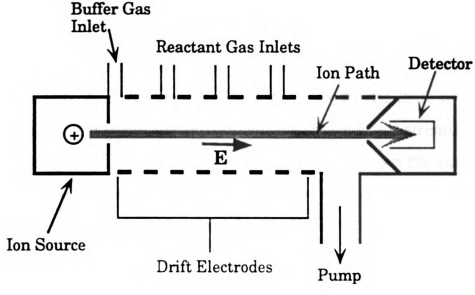

Figure 1.5. Flow tube schematic diagram.

selected ion beam. This is commonly referred to as Selected-Ion Flow Tube (SIFT) methodology [30].

The source region of the instrument is followed by the drift region. The buffer gas is introduced at one end of the flow tube and pumped away at the other end. Very high gas flow rates are required to maintain typical operating pressures of ~0.5 torr. These high gas loads also demand a very rigorous pumping system. The drift region of the instrument is usually lined with a series of ring electrodes. By applying an appropriate bias to the drift electrodes, a linear longitudinal electric field is created inside the flow tube. The ions traverse the flow tube by a combination of the bulk motion of the flowing buffer gas and the force exerted by the electric field. By controlling both the buffer gas flow rate and the electric field strength, the residence time of the ions in the drift tube may be varied. Reactant gases are introduced into the flowing stream through a number of inlet ports, located at various distances from the source end of the flow tube. The ion/neutral interaction time may also be varied by selecting different ports for introducing the neutral reactant gas. After traveling the length of the drift region, primary and product ions are extracted into the detector region through a differentially pumped housing.

The ion detector may be a simple (non-selective) device such as an electron multiplier which only provides total ion flux information. Other detection systems employ quadrupole mass filters or even tandem mass spectrometers [31]. This type of detection allows the ion population at the end of the flow tube to be well characterized.

Since the pressure in the flow tube is quite high, the primary ions experience thousands of collisions prior to encountering any neutral

reacta
highly
groun
kineti
systen
flowin
cover
systen
under
the ra
measu
ion/n
such
may b
Alt
conce
restri
swarm
distril
orders
quite
swarm
proce
transi
ion cl
activi

reactant molecules. This results in the collisional relaxation of any highly excited electronic states present. Thus, swarm methods allow ground state ion/molecule processes to be studied. The actual ion kinetic energy is a complex function of the physical temperature of the system, the strength of the applied drift field and the linear velocity of the flowing stream of buffer gas. The ion/molecule interaction energies can cover a range from approximately 0.03 to 3 eV in the best swarm systems. By observing the relative primary and product ion abundances under carefully controlled conditions (i.e. well defined interaction times), the rate constants for various ion/molecule processes may be accurately measured. By conducting reaction rate experiments as a function of the ion/neutral interaction energy, important thermodynamic parameters such as ionic heats of formation, reaction entropies and proton affinities may be quantitated [32].

Although swarm methods can provide a great deal of information concerning fundamental ion/molecule processes, there are some restrictions and limitations. The ion/neutral interactions observed using swarm methods are characterized by broad (Maxwellian) energy distributions. And although an interaction energy range of nearly two-orders of magnitude is often available, the high energy limit of a few eV is quite restricting. This upper energy limit precludes the application of swarm methods to the study of highly endothermic ion/molecule processes which may be important in understanding the chemistry of transition-metal ions. Also, at high pressures, collisional stabilization ion clustering processes, instead of reactive processes, may dominate ion activity for some sytems.

D. Ion Beam Methods

1. Overview

The traditional approach to studying ion/molecule interactions has involved measuring reaction rates and product branching ratios by implementing ICR and SWARM techniques. Ion beam methods differ from ICR and SWARM techniques in that they can be used to probe the intimate dynamic and energetic details of ion/molecule interactions. It is of great importance to understand the exact series of microscopic events that occur when an ion encounters a neutral molecule and the atoms involved are transformed into new chemical entities. The goal of modern research in ion/molecule reaction dynamics is to fully understand these elementary reactive encounters in the evolution of products from reactants. Ion beam methods enable the study of elementary processes by providing exceedingly well-characterized ion/molecule interactions and close observation of the results of the interactions. The information obtained from ion beam methods can be closely tied to theory and can, in fact, provide a measure of the accuracy of potential energy (PE) surface calculations.

Ion beam techniques may be subdivided into two related, yet distinctly different, categories: (a) Crossed Beam and (b) Single Beam. The particular information desired from a chemical system dictates which approach is most appropriate. Crossed beam systems are used to investigate reaction dynamics whereas single beam instruments are more suitable for acquiring accurate thermochemical information.

2. Crossed Beam Methods

Consider the hypothetical ion/molecule reaction of a mono-atomic ion/diatomic neutral system as shown below.

$$A^+ + BC \rightarrow AB^+ + C$$

There may be numerous questions concerning the reaction dynamics and energetics of this system. Is the process exothermic or endothermic? Are there specific orientations of BC with respect to A^+ that are required to allow products to be formed? Is the product AB^+ formed in excited electronic, vibrational and/or rotational states? How does the reaction cross-section vary as a function of interaction energy? What is the lifetime of the three body collision complex?

Unfortunately, it is currently impossible to view the motion of submicroscopic atomic particles directly. However, evidence of the intimate atomic interactions may be obtained by analyzing the trajectories of the particles before and after the reactive encounter. The initial velocity and direction of the interacting species may be controlled by using a crossed beam apparatus. A block diagram of this type of instrument is shown in Figure 1.6. Ions are formed in the source region and the ionic species of interest is selected by the first mass analyzer. Ideally, the ion source could generate ions in specific internal energy states or at least well-characterized internal energy state distributions. Electrostatic optics are used to establish the translational energy of the ions emerging from the mass selection device. This mass-resolved primary ion beam should be nearly monoenergetic and highly collimated. These conditions ensure well defined velocity vectors for the primary ions in the laboratory frame of reference.

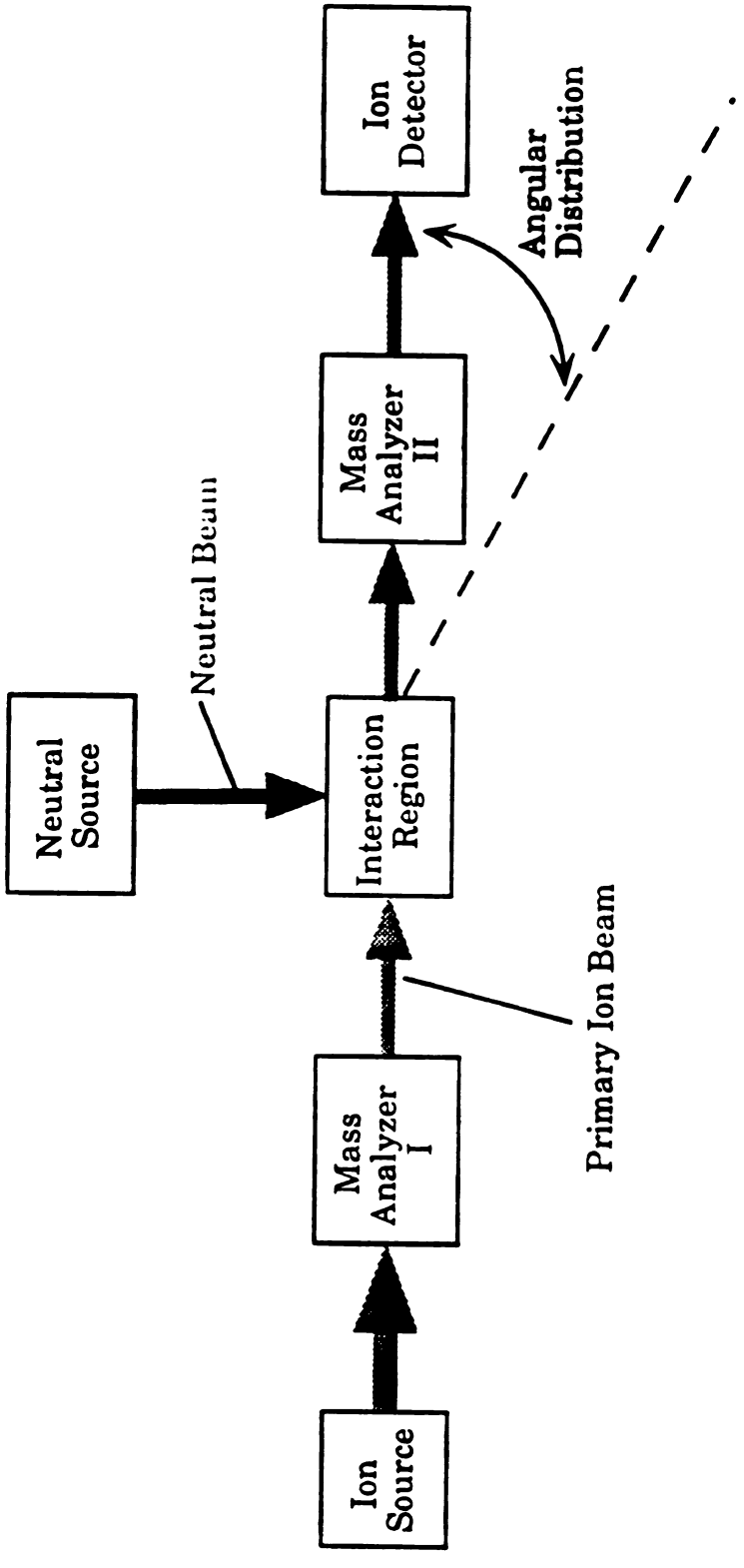

Figure 1.6. Block diagram of a crossed beam instrument.

The n
nozzle
apertu
supers
that is
of the
masse
molecu
extren
supers
The
in the
and th
highly
prima
analyz
rotata
and pr
In
ion flu
differe
specie
to pro
mass
yield
ion/n
instru

The neutral reactant beam is usually generated using a supersonic nozzle and skimmer in combination with a series of collimating apertures. If a molecule of interest is 'seeded' in a buffer gas, the supersonic expansion process also produces a neutral molecular beam that is vibrationally and rotationally cooled. The kinetic energy (velocity) of the neutral can also be varied by changing the relative pressures and masses of the molecular and buffer gases. In addition, exotic neutral molecular radicals or mono-atomic species such as O, H, or N which are extremely unstable may be produced with sufficient intensity using supersonic beam sources.

The neutral beam is oriented perpendicular to the primary ion beam in the laboratory frame. The characteristics of the primary ion source and the neutral beam source result in well-defined scattering centers and highly characterized ion/neutral interaction energies. The flux of the primary and product ions are measured with a second mass analyzer/detector combination. This system is usually mounted on a rotatable mount to provide angular (directional) resolution of the reactant and product ions.

In a complete collision analysis, the scattered primary and product ion flux is measured as function of angle about the collision center. This differential is supplemented with kinetic energy analysis of the ionic species. Kinematic treatment of the energy/flux/direction data is applied to produce Cartesian velocity-space contour diagrams in the center-of-mass frame of the collision pair. This information can be interpreted to yield the mechanistic details and energy transfer processes involved in ion/neutral interactions [33]. Although most crossed ion beam instruments analyze only the ionic products of the ion/neutral

interaction, an ideal instrument would also be capable of ascertaining the identity and internal/translational energy of the neutral products generated.

The earliest crossed beam instrument designed to provide both angular and translational energy resolution for ionic reactions was developed by Herman and Wolfgang in 1969 [34]. Their apparatus had an ion kinetic energy distribution of ~0.5 eV and could produce beams with ion translational energies as low as 3 eV. A more sophisticated crossed beam instrument was developed by Futrell and coworkers in 1975 [35] which incorporated high angular resolution over an arc of 110° in the laboratory frame. Improved ion optics in this instrument allow very low energy (~0.5 eV) ion beams to be generated. Mahan and coworkers also constructed a crossed beam instrument to study low energy (<5 eV) ion/neutral processes [36]. More recently, Futrell and coworkers developed a new supersonic beam mass spectrometer for the study of collision-induced dissociation of ions in the energy range of <1 to 3000 eV [37]. This instrument has exceptional ion kinetic energy dynamic range, but the novel hemispherical energy analyzer incorporated in the instrument suffers from poor energy resolution and transmission at energies below 50 eV.

These and other crossed beam instruments have provided detailed studies on the dynamics of ion/neutral processes. Because the instruments are designed to extract so much information (mass, angular, and energy distributions), the overall sensitivity of the instruments is often quite low. In addition, poor, and often biased, collection efficiencies of highly scattered primary and product ions preclude the use of crossed beam instruments to obtain quantitative integrated (total) reaction cross-

sectio

Sir
accur
accor
produ
neces
neutr
throu
gas d
condi
then
ion fl
Th
sourc
beam
distri
intera
This
exper
therm
intera
eV la
meas
Be

sections as a function of ion kinetic energy.

3. Single Beam Methods

Single beam instruments have been designed to provide more accurate total reaction cross-sections measurements. This is often accomplished in these instruments by limiting angular resolution and product kinetic energy information. Since directional information is not necessary for total cross-section measurements, a highly-characterized neutral beam is not required. Instead, the primary ion beam is directed through a region of the instrument which contains a neutral gas. The gas density is kept sufficiently low ($<10^{-3}$ torr) to ensure single collision conditions. The unreacted primary ions and ionic reaction products are then extracted into a second mass analyzer/detector for mass-dependent ion flux measurements.

The velocity and angular distribution of neutrals from molecular beam sources is very small. In contrast, the neutral collision gas in a single beam experiments is characterized by an isotropic Maxwellian velocity distribution. This condition results in a distribution of ion/neutral interaction energies even if the primary ion beam is truly monoenergetic. This presents a limit to the absolute energy resolution for single beam experiments. However, the relative contribution of the neutral gas thermal energy spread to the overall uncertainty of the ion/neutral interaction energy becomes critical only at very low collision energies (<2 eV lab). In addition, if the temperature of the collision gas is accurately measured, the cross-section data can be corrected for this effect.

Because the kinetic energy of the primary ion beam is variable, single

beam instruments can provide excellent total reaction cross-section measurements as a function of ion/neutral interaction energy. Threshold experiments may be performed to determine the minimum kinetic energy required to overcome energy barriers encountered in endothermic ion/neutral reaction channels. This allows important thermodynamic information such as bond dissociation energies and ionic heats of formation to be derived from single beam studies.

One of the first single beam instruments designed to study low energy ion/neutral processes was developed by Futrell and coworkers in 1965 [38]. This tandem instrument was comprised of two sector-type mass spectrometers linked together. Both mass spectrometers consisited of an electric sector followed by a magnetic sector (EB configuration). A complex ion optical system was used to establish the kinetic energy of the ions exiting the the first mass analyzer. The ions were then focused into a small collision cell containing the static neutral reactant. Primary and product ions scattered in the forward direction in the laboratory frame were then analyzed by a second high resolution EB mass spectrometer. This instrument was able to generate mass-selected beams of primary ions having very low (<0.5 eV) kinetic energies.

Another single beam instrument based on tandem quadrupole mass spectrometers was constructed by Beauchamp's group at the California Institute of Technology in 1977 [39]. This instrument was later modified by Armentrout so that a magnetic sector, instead of a quadrupole, was utilized as the first mass analyzer [40]. Ions exiting the mass analyzer region are focused and decelerated to the desired kinetic energy with a complex deceleration unit before injection into the collision cell containing the neutral gas. A grid and lens combination serves to extract

the primary and product ions into the quadrupole mass analyzer. The instrument was designed primarily to measure onset energies for endothermic ion/neutral processes. This requires very high sensitivity since the rate of product ion formation approaches zero at the reaction threshold energy. To achieve high signal-to-noise ratios for low intesity ion fluxes, a modulated detection system was employed. The primary ion beam was pulsed into the reaction chamber and only those ions events occuring at the modulation frequency were detected with a phase-sensitive amplifier system. Numerous investigations on the reactivity of transition-metal ions with small organic neutrals were performed on this instrument [41]. These experiments yielded the first direct measurements of BDEs for various transition-metal ions bonded to organic ligands. Comprehensive studies have resulted in the correlation of thermochemical properties with reactivity trends in transition metal systems [42].

In the single beam instruments described thus far, the collision cell is usually constructed as a small metal box or tube with a path length of a few centimeters. The cell usually has very small apertures on each end to define the electric field inside the box and to provide minimal gas conductance to the main vacuum chamber. An appropriate DC bias is applied to the collision cell to establish the kinetic energy of the primary ions while they travel through the cell. The beam of primary ions is usually highly collimated about the central (ion-optical) axis of the collision cell. When the primary ions collide with neutral species, they may be scattered at high angles relative to their initial trajectories in the laboratory frame. Other reactive ion/molecule processes may result in the production of product ions which have trajectories that are non-

coline
intera
symm
encou
able t
the se
of ur
instru
On
effects
some
accom
theory
lon be
the c
energy
guide
featu
trapp
millis
Wher
proce
prim
mass
prim
octo
sign

colinear with the ion-optical axis of the collision cell. At very low interaction energies, long-lived ion/neutral complexes may result in a symmetric or isotropic distribution of products from the reactive encounter. Only those ions which have very low-angle trajectories will be able to exit the collision cell through the small aperture and proceed to the second mass analyzer and detector. There is, therefore, a high level of uncertainty in the total collection efficiency in single beam instruments of this type.

One way to eliminate measured ion flux bias from such dynamic effects and to improve total ion collection efficiency is to incorporate some type of ion trapping field within the collision region. This may be accomplished by using dynamic-field ion beam guides. Details on the theory and operation of rf-only ion beam guides are covered in Chapter 4. Ion beam guide methods were pioneered by Teloy and Gerlich in 1974 in the construction of a tandem mass spectrometer used to study low energy ion/molecule reactions [43]. In addition to using an ion beam guide, this single beam instrument incorporated several new innovative features. First, the ionization source employed a radio-frquency (rf) trapping field that allowed long ion storage periods on the order of a few milliseconds. Conventional EI sources have ion residence times of ~1μs. When operated under high-pressure conditions, multiple-collision processes resulted in electronically cooled primary ions. Second, the primary mass analyzer implemented a unique two-stage quadrupole mass filter that allowed both ion mass and velocity selection. The primary ion beam exiting the mass/energy filter was then focused into an octopole ion beam guide. This beam guide was perhaps the most significant feature of the instrument. It was constructed from eight

parallel rods arranged in an octogonal array. An rf-only signal is applied the octopole rods to create a radial trapping field within the interior volume of the beam guide. The rf field does not influence the longitudinal velocity of the ions traveling in the guide. But an inward restoring force continually directs the ions toward the central axis of the device. The beam guide is followed by a magnetic sector mass analyzer with a highly-efficient detector.

The ion beam guide passes through a collision cell into which a low pressure gas is introduced. When ion/neutral interactions occur that produce highly scattered ions, they are effectively contained within the ion beam guide. The motion of a scattered ion traveling through the octopole may viewed as a series of specular reflections off the potential walls created by the rf field. The use of dynamic trapping field ion beam guides allows very accurate total reaction cross-sections to be measured.

This guided beam technology was implemented in an ion beam instrument constructed at the University of California at Berkeley where Gerlich did post-graduate work with Anderson in the laboratory of Y.T. Lee [44]. They constructed a single beam instrument that utilized a photoionization source to prepare primary ions in specific vibrational states. Since the ionization process was so specific, no mass spectrometer was needed to produce the primary ion beam. Reactant ions where formed directly in a dodecapole beam guide. The primary ions were transferred to a collision region and finally to a quadrupole mass analyzer using a series of five separate rf octopole ion beam guides. This instrument was used to study the effects of translational and vibrational excitation on ion/molecule reactions. Anderson subsequently constructed a similar instrument at (SUNY at Stoney Brook) for the study

of sm

Be

devic

incor

cons

instr

using

sourc

magn

decel

guide

varia

collis

quad

and

infor

react

inves

forma

the s

It

cited

expa

resol

a sta

densi

(deter

of small metal-cluster ions using guided ion beam technology.

Because of the significant advantages prodided by an active trapping device in the collision region of single beam instruments, Armentrout incorporated an octopole beam guide in the design of an instrument constructed at Berkeley in 1983 [45]. A full description of this instrument can be found in reference 46. The ions may be generated using EI, surface ionization (SI) or a high pressure drift tube (HPDT) source. The primary ion beam is mass-selected using a low resolution magnetic sector mass spectrometer. An exponential lens is used to decelerate the ion beam before it is injected into an octopole ion beam guide which passes through a collision gas cell. The primary ion beam is variable in energy over the range of ~1 to 750 eV. After traversing the collision region, product and primary ions are analyzed with a quadrupole mass analyzer followed by a Daly-type detector. Armentrout and coworkers have utilized this instrument to generate a large body of information on the kinetic energy dependence of transition-metal ion reactions with small organic and inorganic neutrals [47]. These investigations have yielded very accurate BDEs and ionic heats of formation. By carefully controlling the initial ion formation processes in the source, state-specific reactivity studies have also been performed.

It is of interest to note that two of the guided ion beam instruments cited above [44,46] contained design provisions to utilize a supersonic expansion neutral beam source. This would achieve a greater level of resolution of the ion/neutral interaction energy over that obtainable from a static neutral gas in the collision region. However, because the number density in a neutral beam is quite low and the interaction volume (determined by the ion and neutral beam physical cross-sections) is very

small, no success from crossed-beams in guided ion beam instruments been reported to date.

The MSU ion beam instrument is of single beam design and incorporates an octopole ion beam guide and a static gas ion/neutral interaction region. This provides a high level of efficiency for the collection of scattered ions. A schematic diagram of the MSU apparatus is shown in Figure 1.7. A general description of the instrument may be found in the first section of Chapter 2. Details of the vacuum system, the primary ion sources, and the primary ion analyzer are provided in succeeding sections of Chapter 2. In addition, the theory and operation of the octopole ion beam guide, the quadrupole mass analyzer and the detector system are also covered in Chapter 2. Chapter 3 is devoted entirely to the theory and design of the ion deceleration optics. Operational/control concepts of the MSU ion beam instrument and demonstration of the instrument performance for exothermic and endothermic chemical processes are given in Chapter 4.

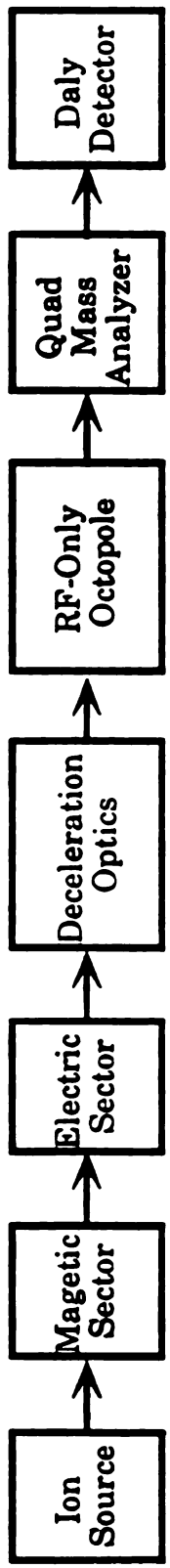

Figure 1.7. MSU ion beam instrument block diagram.

1. Mavri
2482.

2. Hank
3624

3. Allisc

4. Sabo

5. Ziegl

6. Agui

7. Wilk
139.

8. Koch
Pres

9. Ung

10. Rad

11. Win

12. Wes
by

13. Not

14. Fox
Inst

15. Dar

16. Rett
198
198

17. Bers

LIST OF REFERENCES
Chapter 1

1. Mavridis, A.; Harrison, J.F.; Allison. *J. Am. Chem. Soc.* **1989**, *111*, 2482.

2. Hankinson, D.J.; Miller, C.B.; Allison, J. *J. Phys.. Chem.* **1989**, *93*, 3624.

3. Allison, J., *Prog. Inorg. Chem.* **1986**, *34*, 627.

4. Sabo, M.S., Ph.D. Disseration, Michigan State University, 1991.

5. Ziegler, K. *Adv. Organometal. Chem.* **1968**, *6*, 1.

6. Aguilo, A. *Adv. Organometal. Chem.* **1967**, *5*, 321.

7. Wilkinson, G. *Proc. R.A. Welch Found. Conf. Chem. Res.* **1966**, *9*, 139.

8. Kochi, J.K. "Organometallic Mechanisms and Catalysis", Academic Press, New York, **1978**.

9. Ungerman, C. *J. Am. Chem. Soc.* **1979**, *101*, 5922.

10. Radecki, B.D.; Allison, J *J. Am. Chem. Soc.* **1984**, *106*, 946.

11. Winters, R.E.; Kiser, R.W. Inorg. Chem. **1965**, *4*, 157.

12. Westmore, J.B. in "Mass Spectrometry of Metal Compounds", edited by Charalambous, J., Butterworth & Co., London, **1975**, p.61.

13. Nottingham, W.B. *Phys. Rev.* **1939**, *55*, 203.

14. Fox, R.E.; Hickman, W.M.; Grove, D.J.; Kjeldaas, T; *Rev. Sci. Instrum.* **1955**, *26*, 1101.

15. Darland, E.J.; Ph.D. Dissertation, Michigan State University, **1978**.

16. Rettner, C.; Marinero, E.; Zare, R. Kung, A. in "Excimer Lasers-1983", edited by Rhodes, C., American Istitute of Physics, New York, **1983**, p.345.

17. Berstein R.B. *J. Phys.. Chem.* **1982**, *86*, 1178.

18. Allis

19. Beat
196

20. Wilk

21. Jac

22. McI
471

23. Cod

24. Tsa

25. Cas
Soc

26. Bab

27. McF

28. Step

29. Feh
Phy

30. Ada
21,

31. Lan
198

32. Gra

33. Wo

34. Her
Ins

35. Ves
Ins

36. Har
375

37. Shu
J.H.

38. Futr

18. Allison, J., Ph.D. Disseratation, University of Delaware, **1977.**

19. Beauchamp, J.; Anders, L.; Baldeschewieler, *J. Am. Chem. Soc.* **1967**, *89*, 4569.

20. Wilkins, C.L.; Gross, J.L.; *Anal. Chem.* **1981**, *53*, 1661A.

21. Jacobson, D.B.; Freiser, B.S.; *J. Am. Chem. Soc.* **1983**, *105*, 5197.

22. McIver, R.; Dunbar, R. *Int. J. Mass Spectrom. and Ion Phys.* **71**, *7*, 471.

23. Cody, R.; Burnier, R.; Freiser, B *Anal. Chem.* **1982**, *54*, 96.

24. Tsarbopolous, A.; Allison, J *J. Am. Chem. Soc.* **1985**, *107*, 5085.

25. Cassady, C.J.; Freiser, B.S.; McElvany, S.W.; Allison, J *J. Am. Chem. Soc.* **1984**, *106*, 6125.

26. Babinec, S.J.; Allison, J. *J. Am. Chem. Soc.* **1984**, *106*, 7718.

27. McElvany, S.W.; Allison, J *Organometallics* **1986**, *5*,416.

28. Stepnowski, R.; Allison, J. *J. Am. Chem. Soc.* **1989**, *111*, 449.

29. Fehensenfield, F.C.; Ferguson, E.E.; Schmeltekopf, A.L. *J. Chem. Phys.* **1966**, *44*, 3022.

30. Adams, N.G.; Smith, D. *Int. J. Mass Spectrom. and Ion Phys.* **1976**, *21*, 349.

31. Lane K.R.; Lee, R.E.; Sallans, l.; Squires, R.R.; *J. Am. Chem. Soc.* **1984**, *106*, 5767.

32. Graul, S.T.; Squires, R.R. *J. Am. Chem. Soc.* **1990**, *112*, 2517.

33. Wolfgang, R.; Cross, R.J. Jr. *J. Phys.. Chem.* **1969**, *73*, 743.

34. Herman, J.D.; Kerstetter, J.D.; Rose, T.L.; Wolfgang R. *Rev. Sci. Instrum.* **1969**, *40*, 538.

35. Vestal, M.L.; Blakley, C.R.; Ryan, P.W.; Futrell, J.H. *Rev. Sci. Instrum.* **1976**, *47*, 15.

36. Hansen, S.G.; Farrar, J.M., Mahan, B.H. *J. Chem. Phys.* **1980**, *73*, 3750.

37. Shukla, A.K.; Anderson, S.G.; Howard, S.L.,Sohlberg, K.W.; Futrell, J.H. *Int. J. Mass Spectrom. and Ion Process.* **1988**, *86*, 61.

38. Futrell, J.H.; Miller, C.D. *Rev. Sci. Instrum.* **1966**, *37*, 1521.

39. Armentu
66, 216

40. Arment

41. Arment
76, 24

42. Halle,
963.

43. Teloy,

44. Ander
75, 21

45. Ervin,
87, 3

46. Ervin,

47. Arme

39. Armentrout, P.B.; Halle, L.F.; Beauchamp, J.L. *J. Chem. Phys.* **1977**, *66*, 2162.

40. Armentrout, P.B.; Beauchamp, J.L. *J. Chem. Phys.* **1981**, *74*, 2819.

41. Armentrout, P.B.; Halle, L.F.; Beauchamp, J.L. *J. Chem. Phys.* **1982**, *76*, 2449.

42. Halle, L.F.; Armentrout, P.B.; Beauchamp *Organometallics* **1982**, *1*, *963*.

43. Teloy, E.; Gerlich, D. *Chem. Phys.* **1974**, *4*, 417.

44. Anderson, S.; Houle, F.; Gerlich, D.; Lee, Y. *J. Chem. Phys.* **1981**, *75*, 2153

45. Ervin, K.; Loh, S. ; Aristov,N.; Armentrout, P. *J. Phys Chem*, **1983**, *87*, 3593.

46. Ervin, K.M. ; Armentrout, P.B. *J. Chem. Phys.***1985**, *83*, 166.

47. Armentrout, P.B.; Beauchamp, J.L.; *Acc. Chem. Res.* **1989**, *22*, 315.

I. Overview

As discu
operational
to perform
include the
characterize
energy. Ide
state-specifi
primary a
transmitte
should prov
minimal ma

A block
1.7. In this
component
addition, a
will be provi

A schem
The primary
focusing m

Chapter 2

Ion Beam Instrument Design and Construction

I. Overview

As discussed in Chapter 1, there are very specific design and operational criteria that are required in an ion beam instrument intended to perform accurate thermochemical measurements. These criteria include the ability to generate primary ion beams which are well characterized/controlled with respect to translational as well as internal energy. Ideally, the experimental apparatus would be able to monitor state-specific or state-characterized ion/molecule interactions. Scattered primary and secondary ions must be efficiently contained and transmitted to the secondary mass analyzer. The detection system should provide high (unit) detection efficiency of ionic species and exhibit minimal mass-dependent discrimination.

A block diagram of the MSU ion beam instrument is found in Figure 1.7. In this chapter, the design and operational principles of each major component comprising the ion beam instrument will be detailed. In addition, a description of the the vacuum chambers and pumping system will be provided.

A schematic representation of the instrument is shown in Figure 2.1. The primary ion generation system consists of a MAT CH5-DF double-focusing mass spectrometer of reverse (BE) geometry. Ions may be

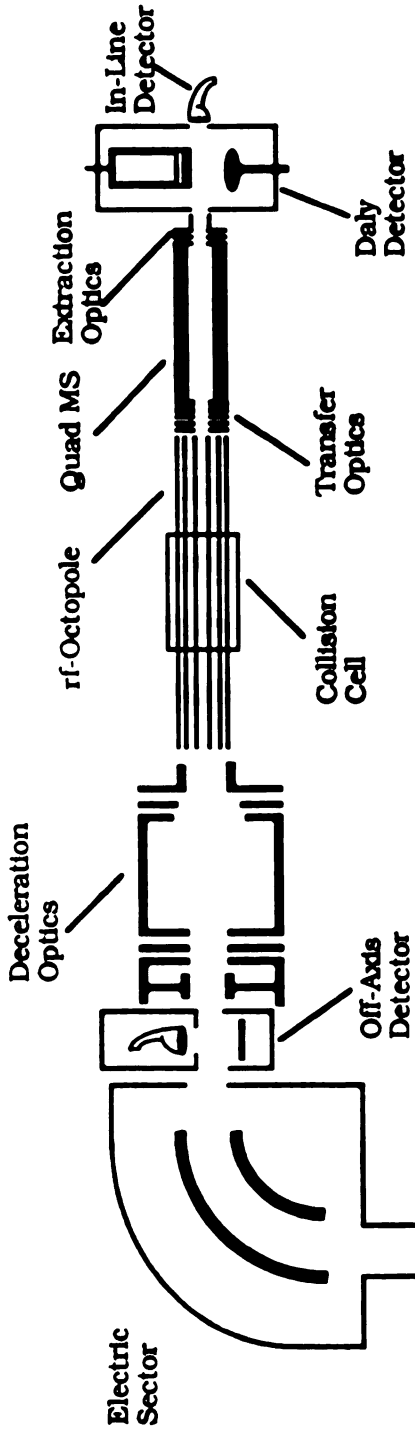

Figure 2.1. Ion Beam Instrument Schematic Diagram.

produced
(EI), chem
and fast
followed b
allows op
complete

A nov
primary i
regime of
Chapter
rigorous
decelerat

The c
gas collis
passes th
at a num
transfer
focuses
analyzer
second se
Two type
dynode e
measuren
used to q

To app
consider t
the ion b

produced by a variety of ionization schemes including electron ionization (EI), chemical ionization (CI), High Pressure Drift Tube (HPDT) processes, and fast atom bombardment (FAB). The primary mass analyzer is followed by an intermediate continuous dynode, off-axis detector. This allows operation of the primary mass spectrometer independent of the complete ion beam optical system.

A novel two-stage deceleration system provides attenuation of the primary ion energy from a high nominal initial value to the low energy regime of interest prior to injection into the collision (interaction) region. Chapter 3 is devoted entirely to the this lens system. It includes a rigorous theoretical treatment that promotes an understanding of ion deceleration optics.

The collision region is comprised of an ion beam guide and a static-gas collision cell. A radio-frequency (rf-only) octopole ion beam guide passes through a chamber which contains the neutral collision partner at a number density sufficient for single-collision conditions. A set of transfer optics extracts ionic species from the collision region and focuses them into a quadrupole mass filter. This secondary mass analyzer is used to discriminate product ions from primary ions. A second set of optics is used to transfer ions into the final detector region. Two types of charged particle detectors are employed. A continuous dynode electron multiplier is positioned along the ion optical axis for measurement of high current ion beams. A sensitive Daly [1] detector is used to quantitate low intensity ion beams.

To appreciate the complexity of the ion optical system, it is useful to consider the kinetic energy of an ion as it traverses the various regions of the ion beam instrument. A diagram of the ion kinetic energy as a

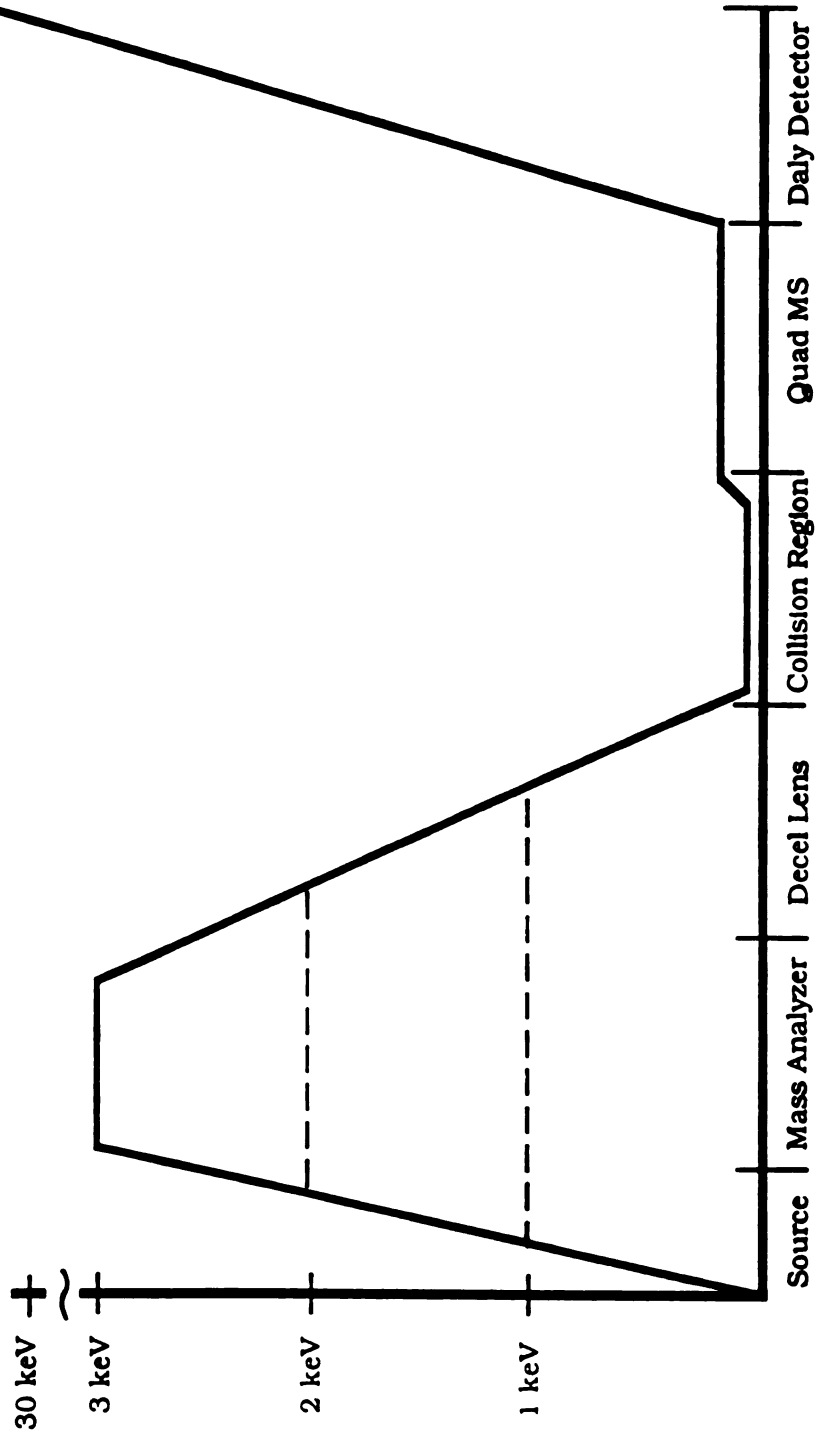

Figure 2.2. Ion Beam Instrument Kinetic Energy Diagram.

function c
EI source
distributi
K]. The
analysis
decelerat
energy m
laborator
kinetic er
is emplo
30,000 e
The p
of this p
throughc
meters.
accompli
system.
designed
modelin
was imp
instrume

II. Vacu

The v
out of w
made wi

function of position in the instrument is plotted in Figure 2.2. When the EI source is used, for example, ions are initially formed with a thermal distribution of kinetics energies dictated by the source temperature (~300 K). The nascent ions are strongly accelerated to the nominal mass analysis energy of 1000, 2000, or 3000 eV. The high energy beam is decelerated and introduced into the collision region. The final interaction energy may range from near thermal (<1 eV) to several hundred eV in the laboratory frame. Mass analysis in the quadrupole analyzer occurs at kinetic energies ranging from <10eV to ~100 eV. When the Daly detector is employed, ions are accelerated after mass filtering to an additional 30,000 eV.

The performance of the ion beam instrument and the ultimate success of this project was dependent on the ability to transfer ions efficiently throughout a wide energy range and an optical path that approaches 4 meters. It must be emphasized that this could not have been accomplished without the development of a high performance ion optical system. Therefore, each component constructed for the instrument was designed using a sound understanding of ion optics based on theoretical modeling. The PC-based ion trajectory simulation program SIMION [2] was implemented in the design of each component in the ion beam instrument.

II. Vacuum Chambers and Pumping Systems

The vacuum chambers associated with the CH5-DF are constructed out of welded stainless steel. Flange seals are simple compression type made with tin/silver or gold wire gaskets. The entire vacuum housing

may be h
heaters.
spectrom
diffusion
CFM). C
following
electric s
(150 l/s)
mechani
diffusion
(polyphe
be isola
different
loads a
sufficien
Pressur
with Per

The
housed
CH5-DF
sector-li
spectro
detector
electric
assemb
valve w
remainc

may be baked out with the use of externally applied surface-plate heaters. Three separate pumping regions are maintained on the mass spectrometer. The ion source region utilizes an Edwards EO4 (600 l/s) diffusion pump backed by an Edwards E2M8 two stage rotary pump (5.8 CFM). Conductance into the flight tube is limited by an aperture following the ion source slit. The magnetic sector flight tube and the electric sector chamber are each separately pumped by an Edwards EM2 (150 l/s) and diffusion pump. These share a common Alcatel 5 CFM mechanical pump. To maintain clean high vacuum conditions, the diffusion pumps are cold trapped at -60 °C and Santovac 5 (polyphenlylether) is used in all three pumps. Each pumping stack may be isolated from the vacuum chamber by a butterfly valve. This differential pumping scheme allows the source to accommodate high gas loads as encountered when using CI and FAB while maintaining sufficiently low pressures (~10^{-6} torr) in the mass analysis regions. Pressures may be monitored in the source chamber and flight regions with Penning gauges.

The deceleration lens, octopole, quadrupole and detector system are housed in two rectangular vacuum chambers. Connection between the CH5-DF and the beam line chambers is accomplished by using a large sector-linking bellows assembly salvaged from a DuPont CEC-110 mass spectrometer. An adapter flange couples the bellows to the original detector region of the CH5-DF immediately following the exit slit after the electric sector. The off-axis detector is situated near the bellows assembly. The bellows is terminated by an Airco 2" ID pneumatic gate valve which allows isolation of the primary mass spectrometer from the remainder of the beam instrument.

The tw
wide, and
aluminum
rectangul
length of
mounted
are made
access to
vacuum
requirem
developm
accompli

The fi
the decel
is also s
detector
pumpin
conduct

The
(800 l/s
pump (
prevent
employs
Cemco
cold tra
closed-
system

The two beam chambers are each approximately 56 cm long by 30 cm wide, and 30 cm in height. They are constructed from 1.6 cm thick aluminum plate stock with inert-gas welds on the internal seams. A rectangular aluminum ion optical rail is suspended through the entire length of the beam chambers. The ion optical components are easily mounted and are interchangable on the rail system. The chamber tops are made of 1.27 cm thick tempered-glass providing complete visual access to the chamber interior. Although the large dimensions of the vacuum chambers are non-ideal from a vacuum system (pumping requirement) standpoint, the environment is well suited to instrument development. All seals in the beam chamber tops and side flanges are accomplished using elastomer o-rings.

The first chamber is divided into two separate pumping regions: (a) the deceleration region and (b) the octopole region. The second chamber is also separately pumped and houses the quadrupole mass filter and detector system. Pressure transmittance is limited between the three pumping regions by ion optical apertures, which provide the only conductance paths between regions.

The deceleration region is pumped by a Varian M4 diffusion pump (800 l/s) and is backed by a Sargent Welch Duoseal R-1376 mechanical pump (10.6 CFM). A Bendix water-cooled chevron baffle is employed to prevent backstreaming of pump fluid. The octopole/collision cell region employs a Varian VHS-6 diffusion pump (2400 l/s) that is backed by a Cemco Hyvac 45 mechanical pump (18 CFM). A high speed Varian 362-6 cold trap (2000 l/s) tops the diffusion pump and is cooled to -60 C by a closed-cycle refrigerator. The quadrupole/detector chamber pumping system consists of a Varian VHS-6 Diffusion pump which is backed by a

11.6 CF
all three
diffusion
The b
Airco pn
system p
the temp
foreline
pump fa
cooling v
valves ar
The p
using Ba
base pr
pressure
the octo
lower in
pressur
usually
even un
Howe
high vac
because
To mini
such as
rapidly h
from 30

11.6 CFM Trivac mechanical pump. Due to the large reservoir volumes, all three beam chamber pumps are filled with silicone based (DC 705) diffusion pump fluid.

The beam chamber pumps are connected to the chamber housing via Airco pneumatically-operated gate valves. A relay-logic safety interlock system provides fail-safe operation [3]. The interlock system monitors the temperature of each diffusion pump and the foreline pressure. If the foreline pressure exceeds a preset limit because of a leak or mechanical pump failure, or if the diffusion pump temperature goes too high from a cooling water failure, the diffusion pump power is turned off and the gate valves are automatically closed.

The pressure in the individual pumping regions may be monitored using Bayard-Alpert ionization gauges. The vacuum system achieves a base pressure in the chambers of ~2 X 10^{-7} torr. With a high gas pressure in the collision cell of ~1 X 10^{-4} torr, the high pumping speed in the octopole chamber maintains a pressure ~1-2 orders of magnitude lower in the chamber immediately outside the collision cell. The pressures in the deceleration and quadrupole/detector regions are usually 3-4 orders of magnitude lower than the collision cell pressure, even under high gas loads.

However, because the aluminum chambers have not had any special high vacuum pre-treatment, pumpdown time may be excessively long because of outgassing of adsorbed water after exposure to atmosphere. To minimize this effect, venting is normally performed with a dry gas such as nitrogen. In addition, radiant heaters have been installed to rapidly heat the interior walls of the chamber. The heaters are fabricated from 300 watt quartz security lamps and may be procured from the local

K-Mart™ s

III. Ion Ge

There a
DF mass
combinati
home-bui
EI/FI/FD
ionizatior
processes
sources c
which wil

A. Int

Electr
and the
systems.
covered
transitior
process
energy a
internal
operating
threshol
ability to

K-Mart™ store for about $10.00 each.

III. Ion Generation

There are currently three ion sources in our laboratory for the CH5-DF mass spectrometer. These include an Intensitron EI-only source, a combination EI/Field Ionization(FI)/Field Desorption(FD) unit, and a home-built high pressure drift tube (HPDT) source. The combination EI/FI/FD source may also be used for fast atom bombardment (FAB) ionization. Ion formation through conventional chemical ionization processes may be performed using the HPDT source. The ionization sources of primary interest to this work are the EI and HPDT sources which will be covered in this section.

A. Intensitron Electron Ionization Source

Electron impact ionization has been practiced since the early 1900s and the phenomenon is well understood at least for simple chemical systems. An excellent review of the fundamentals of EI has been recently covered by Märk [4]. As discussed in Chapter 1, the generation of transition metal ions by EI has found widespread utility. The ionization process may lead to the production of ions possessing excess internal energy and hence a wide electronic state distribution. However, excess internal energy and excited state populations may be minimized by operating the ionization source with electron kinetic energies near the threshold required for production of the species of interest. Thus the ability to finely control the electron kinetic energy is a key feature of a

versatile i

The M

Figure 2.

by the pu

end. The

exit the

pusher a

ionizatio

in the vi

ionizatio

product

kinetic e

verified

the rf-on

Ions

The acc

beam al

the slit

the acce

panel of

the resis

potentia

imperfec

The e

the elect

volts.

current

versatile ion source used to studied ion thermochemistry.

The MAT Intensitron source is shown schematically in the top panel of Figure 2.3. It consists of an ionization box or housing which is bounded by the pusher on the back end and the extraction plates on the ion exit end. The split extraction plates form a narrow slit through which ions exit the ionization box. Potentials applied to the ionization housing, pusher and extraction plates determine the electric field in the region of ionization. The source design provides a very homogeneous electric field in the vicinity of electron/neutral interactions. A voltage diagram of the ionization region is found in the center panel of Figure 2.3. According to product literature, the source is designed to produce ions with an initial kinetic energy spread of ~0.3 eV. This kinetic energy spread has been verified experimentally using retarding potential field measurements with the rf-only octopole.

Ions are accelerated out of the source through a series of electrodes. The acceleration lens design allows for independent focusing of the ion beam along the length of the source slit (z-direction) and transverse to the slit (r-direction). The potentials applied to the various electrodes in the acceleration system are shown in the voltage diagram in the bottom panel of Figure 2.3. The source control unit (CH5 Module BHD) houses the resistive divider network that supplies the accelerating and focusing potentials. Most of the electrodes are split to provide compensation for imperfections or asymmetry in the electrode alignment.

The emission control unit (CH5 Module BER) houses the circuitry for the electron filament. The nominal electron accelerating potential is 70 volts. Emission currents are regulated by monitoring the electron current incident on the collector. Feedback electronics control the

Figure

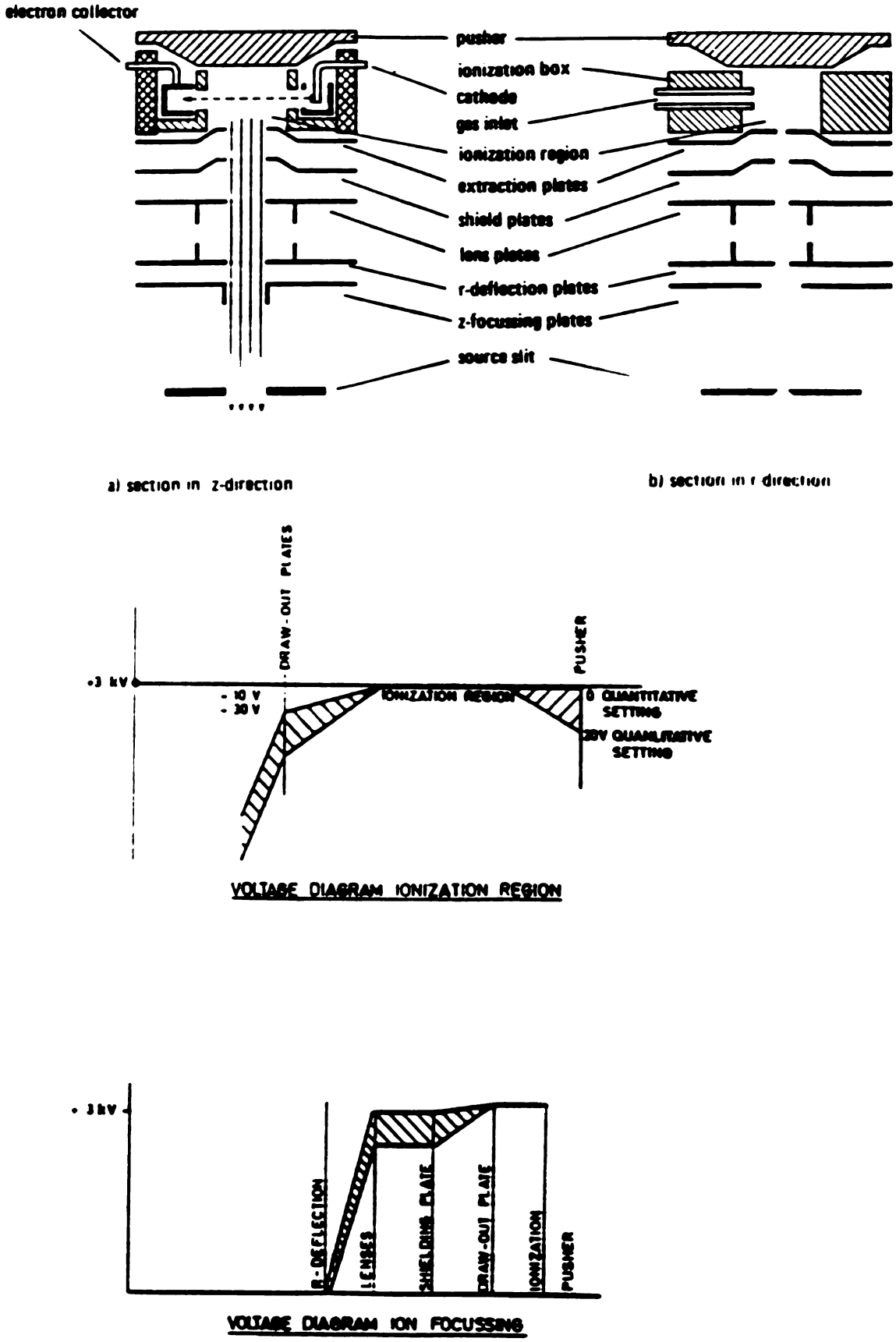

Figure 2.3. Intensitron Electron Ionization Source Schematic Diagram.

current thi
current, w
electronics
other than
energy to
a precisio
the emiss
burnout c

B. Hig

Mole
excess ir
The frag
states w
the sour
state lif
order of
is often
of speci
the tru
relative
metal i
availabl

For
0.25 ar
and Ar

current through the filament to maintain the desired electron emission current, which is continuously variable from <1 μA up to 1 mA. The electronics unit also has provisions for operating at an electron energy other than 70 eV. An appearance potential (AP) mode allows the electron energy to be finely adjusted between 4.5 and 29.5 eV through the use of a precision potentiometer. When the source is in the AP mode, however, the emission current is fixed at a level of 15 μA to prevent space-charge burnout of the filament, which is prevalent at low electron energies.

B. High Pressure Drift Tube Ion Source

Molecular cations created via EI mechanisms often have appreciable excess internal energy which may result in unimolecular decomposition. The fragment ions may exist in excited vibrational and/or electronic states which may be sufficiently long lived ($\geq 10^{-6}$ s) to be extracted from the source region before relaxation to the ground state. In fact, excited state lifetimes of bare transition metal ions are calculated to be on the order of seconds due to parity-forbidden relaxation schemes [5]. Hence it is often difficult to assess or control the electronic and vibrational states of species formed via EI. This introduces a great deal of uncertainty in the true ion/molecule interaction energy and precludes assignment of relative state reactivity. This is particularly a problem with transition metal ions since there is a high density of low-lying electronic states available for population.

For example, the first (^{4}F) and second (^{4}D) excited states of Fe^+ lie 0.25 and 0.98 eV above the ground state (^{6}D), respectively [6]. Elkind and Armentrout [7] have studied the state-specific reaction of Fe^+ with

H_2 to form

orders of n

generated

translation

high-lying

One me

the excited

drift tube.

uniform lo

buffer/reag

technique

[8] to form

Futrell and

ground sta

An ioni

tube (HPD

beam inst

Figure 2.4

The HPDT

1 cm inte

area of ~

perpendi

accommo

housing

plates wi

accommo

The ion

H_2 to form FeH^+ and found that the first excited state was over two orders of magnitude more reactive than the ground state. When Fe^+ is generated by EI it exhibits some reactivity towards H_2 at low translational energies. This has been attributed to the population of high-lying (>1 eV) electronic states corresponding to ~44% of the ions.

One method employed to quench excited states involves interacting the excited ions with a thermal population of inert buffer gas inside a drift tube. A drift tube is a cylindrically symmetric chamber which has a uniform longitudinal electric field. The chamber is usually filled with a buffer/reagent gas to a pressure ranging from 0.01 to 1.00 torr. This technique has been successfully exploited by Armentrout [6] and Bowers [8] to form transition metal ions with minimal excited state populations. Futrell and coworkers have also used high pressure sources to generate ground state noble-gas ions [9].

An ionization source that incorporates an integral high pressure drift tube (HPDT) region has been designed and constructed for the MSU ion beam instrument. A cross-sectional view of the HPDT source is shown in Figure 2.4. It is similar to the designs of Butrill [10] and Munson [11]. The HPDT source is comprised of an aluminum ionization housing with a 1 cm internal diameter. A circular electron entrance aperture with an area of ~0.1 mm^2 permits the entrance of an ionizing electron beam perpendicular to the direction of ion motion. The ionization housing accommodates the standard CH5 filament assembly. The ionization housing is followed by a series (1-5) of 0.25 inch thick aluminum drift plates with a 1 cm diameter cylindrical bore. The terminal drift plate accommodates a 0.005 inch thick stainless steel (SS) circular aperture. The ion exit plate can be easily interchanged with others that have

Figure

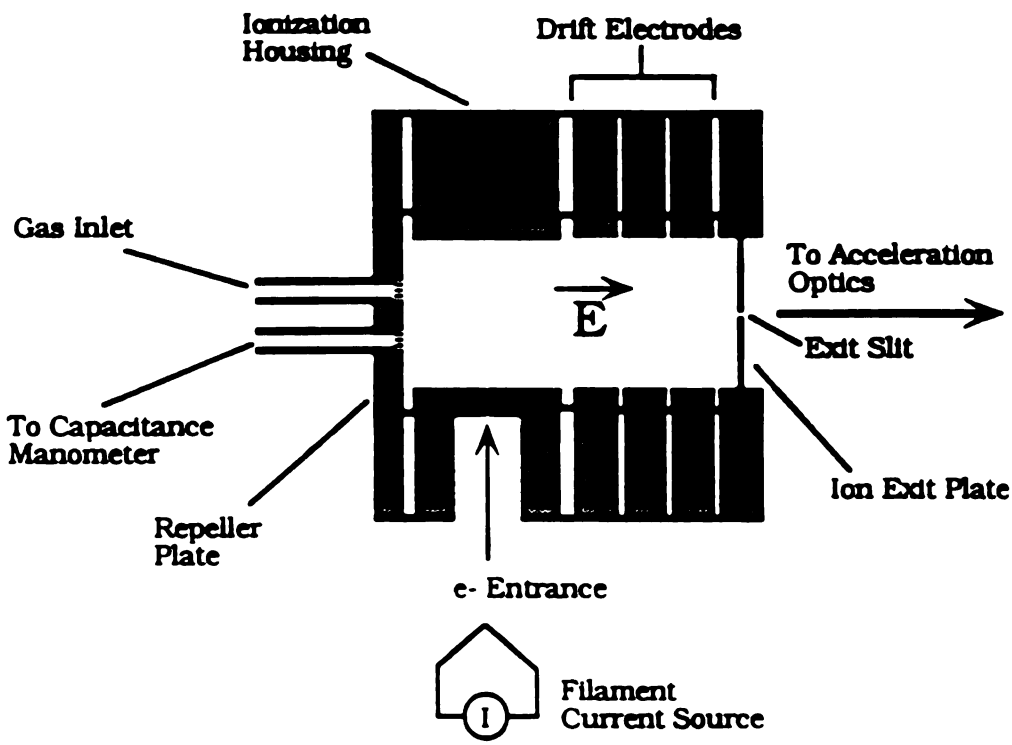

Figure 2.4. High Pressure Drift Tube Source schematic diagram.

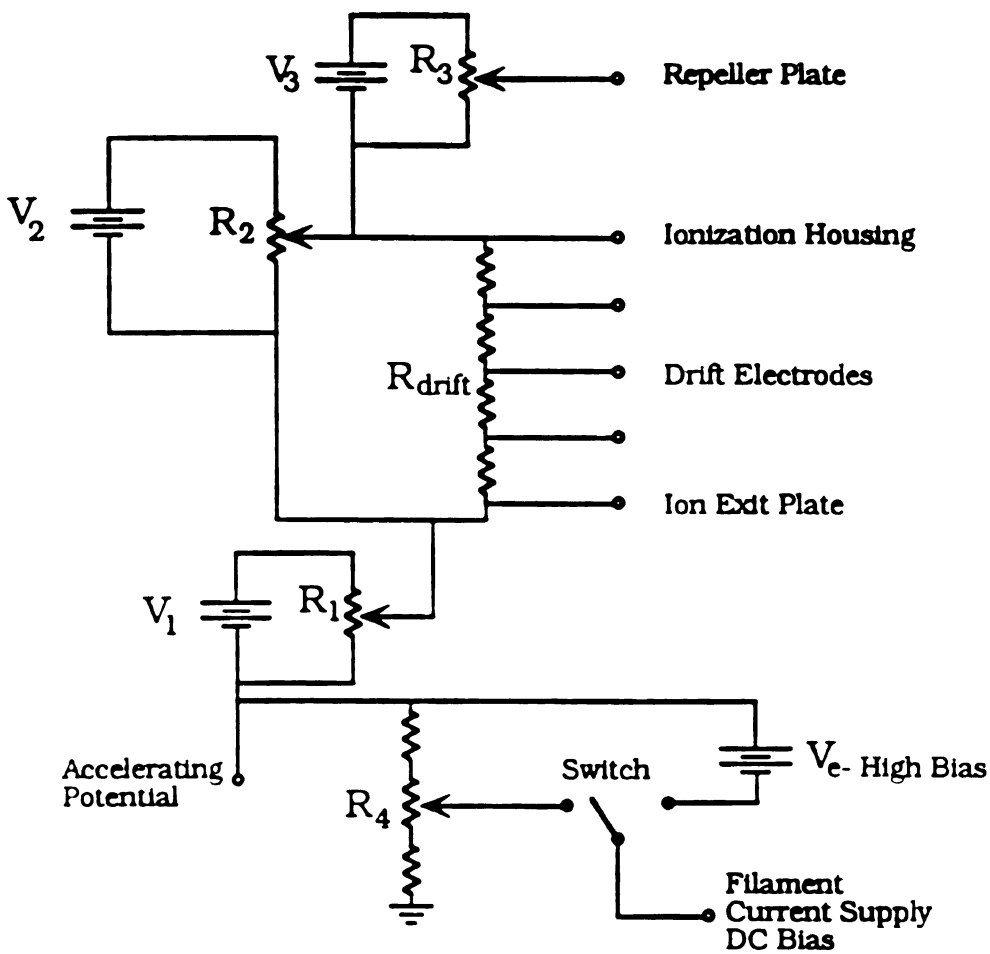

Figure 2.5. High Pressure Drift Tube Source circuit diagram.

various ex
center-lin
plate. An
opening t
thickness
rear plate
clamped t
hole cerar
the stand
exiting th
lens syste

Care h
source.
port in t
construc
manomet
0.001",
maintain
source va
tube con
collisions

The s
HPDT so
One mod
the ioniz
better pe
also allo

various exit apertures with either circular or rectangular dimensions. A center-line gas inlet is provided in the 0.0625" thick SS rear repeller plate. An optically flat SS screen has been spot-welded over the gas inlet opening to maintain a uniform electric field. Teflon gaskets of 1 mm thickness provide electrical insulation and a gas tight seal between the rear plate, ionization housing, drift rings and ion exit plate. The unit is clamped together with four SS threaded rods that run through single-hole ceramic rods for electrical isolation. The entire HPDT unit replaces the standard ionization housing on the Intensitron EI source. Ions exiting the HPDT source are accelerated and focused by the EI source lens system.

Care has been taken to minimize the conductance out of the HPDT source. Pressure inside the source may be measured via a second gas port in the rear repeller plate. Alternatively, a special drift ring was constructed with an 1/8" ID conduit to connect to a capacitance manometer. With an ion exit slit having a height of 4 mm and a width of 0.001", a pressure differential of ~4 orders of magnitude may be maintained between the interior of the drift tube and the surrounding source vacuum manifold. This is sufficient to provide high pressure drift tube conditions of >0.1 torr while minimizing ion losses due to scattering collisions outside of the drift tube.

The standard EI electronics have been modified for operation of the HPDT source. The circuit diagram for the source is shown in Figure 2.5. One modification has been implemented to increase the kinetic energy of the ionizing electrons entering the drift tube to >200 eV. This enables better penetration of the electron beam into the high pressure gas and also allows for higher emission currents since the space-charge limit

increase
the elec
housing
potentia
current
two cur

The
variabl
In this
divider
The va
the fila
nomina
variabl
housir
magni
energy

The
electro
referer
changi
from 7
emissi
advant

The
circuit
curren

increases with electron energy. The electron kinetic energy is dictated by the electric potential difference between the filament and the ionization housing. The filament is normally biased relative to the accelerating potential. Thus, by simply lowering the bias voltage of the filament current power supply the electron energy may be increased. There are two currently available circuit schemes that accomplish this.

The first scheme involves a voltage divider circuit that allows a variable potential to be used as the filament current power supply bias. In this mode the accelerating potential is connected to a three-resistor divider network. The center resistor, R_4, is a precision variable resistor. The value of the resistors are selected such that the reference potential to the filament supply is approximately 100 to 200 volts lower than the nominal accelerating potential. The normal 70 eV electron energy is then variable between 170 and 270 eV. In drift tube operation the ionization housing is biased higher than the accelerating potential by the magnitude of the applied drift voltage. Thus to calculate the electron energy in this mode, the drift potential must be taken into account.

The second mode of high electron energy operation provides a fixed electron energy of ~270 eV. This is accomplished not by changing the reference potential to the filament electronics, but rather by internally changing the voltage offset to the filament. The normal offset is changed from 70 volts to 270 volts through a voltage regulator circuit inside of the emission control unit. This mode of high energy operation has the advantage of utilizing the emission control circuits.

The electron emission may also be regulated by the conventional EI circuits if a few wiring changes are employed. Normally, the electron current on the collector is used as the feedback for filament current

control.
current t
filament
that norr

A uni
creating
The total
be varied
series (1
evenly a
network
resistors
adjusted
potentio
source a
consistir
used to
potentia
kinetic e
adjustin
condition
under HI

Succe
generati
volume c
describe
shows a

control. Since the HPDT source does not utilize a collector, the electron current to the ionization housing may by monitored and used as the filament current feedback. This is accomplished by connecting the lead that normally goes to the collector directly to the ionization housing.

A uniform potential gradient is maintained in the drift region by creating a uniform voltage drop between each of the drift ring electrodes. The total drift field voltage is determined by the potential V_2, which may be varied by a precision potentiometer R_2. A pair of 67 volt batteries in series (134 V) supplies the voltage source for V_2. The drift field voltage is evenly applied to each of the drift electrodes via an integral divider network formed by linking the electrodes with 1 MΩ high-precision resistors. The potential of the rear repeller plate may be independently adjusted using the voltage source V_3 (normally 9 volts) and the potentiometer R_3. The ion exit plate is usually biased at the nominal source accelerating potential. However, an additional circuit feature consisting of the voltage source V_1 and the potentiometer R_1 may be used to trim the ion exit plate potential relative to the accelerating potential. This is useful when ions exiting the source have a slight kinetic energy component along the axis of ion beam propagation. By adjusting the potential to the ion exit plate, the standard operating conditions of the accelerating lenses and mass analyzer may be utilized under HPDT source operation.

Successful operation of the high pressure source implicates the generation of a highly uniform electric field throughout the internal volume of the source. The ion optical properties of the drift tube source described here have been thoroughly modeled using SIMION. Figure 2.6 shows a cross-sectional view of the source. In this model a total drift


Drift Electrodes

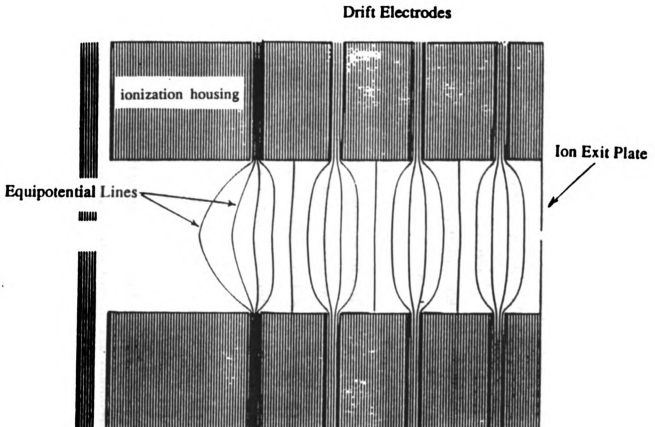

Figure 2.6. SIMION model of High Pressure Drift Tube Source.

potential
5 volt incr
is present
The th
treatment
state cha
In additi
source c
Of partic
ions. T
accelera
portion
monoat
also inc
energy
effectiv
Mason

Wh
the te
pressu
tempe
energy
tempe
vibra

potential of 100 V was applied and the equipotential lines are plotted for 5 volt increments. It can be observed that a highly parallel electric field is present for greater than 70% of the internal diameter.

The theory of ion motion in a drift tube has received extensive treatment in the literature [12,13]. The salient points relavent to the state characterization of transition metal ions are found in reference 14. In addition to the thermalization of excited electronic states, the HPDT source can be applied to vary the internal energy of polyatomic species. Of particular interest is the excitation of vibrational modes in molecular ions. The kinetic energy gained by ions under high-electric field acceleration is attenuated by collisions with the neutral buffer gas. A portion of the kinetic energy is converted into translational energy of the monoatomic neutral collision partner. The internal energy of the ion is also increased as a consequence of collisions. The steady-state kinetic energy of the ions in a high pressure drift field is often viewed as an effective translational temperature, T_{eff}. This has been quantitated by Mason [11] as a function of the drift velocity, V_{drift}, as expressed below

$$T_{eff} = T + M(V_{drift})^2/3k_b$$

Where is k_b the Boltzmann constant, and the parameters T and M are the temperature and mass of the buffer gas respectively. Under high pressure and drift field conditions (>100 volts/cm-torr) the effective ion temperature can achieve several thousand kelvins. The effective internal energy of the ions can also be on the order of the effective translational temperature. Thus, molecular ions can be made to populate elevated vibrational levels and possibly higher electronic states. By varying the

field stre
Excess vi
internal
energy in
by imple
The p
from che
to gene
collision
investig
field cor
the wor
Howeve
typicall
produc
the ver
conduc

IV. Pri

The
spectr
sector
and fo
focusi
In
magne

field strength, the extent of ion vibrational energy can be controlled. Excess vibrational energy can, of course, lead to ion fragmentation when internal energies exceed bond dissociation values. Thus, the effects of energy in vibrational as well as translational modes may be investigated by implementation of the HPDT source.

The properties of the HPDT source allow for the production of ions from chemical ionization processes. In addition, the source may be used to generate species that arise from endothermic processes such as collision induced dissociation. This source has been characterized by investigating high pressure (>0.1 torr) methane under high and low drift field conditions. The ion populations observed agree quantitatively with the work on methane chemical ionization by Munson and Field [15]. However, one drawback of the HPDT source is that the ion output is typically one or more orders of magnitude lower than ion currents produced by the high efficiency Intensitron EI source. This is because of the very small ion exit slits employed in the source to minimize gas conductance.

IV. Primary Mass Analyzer

The primary mass analyzer is a MAT CH5-DF double focusing mass spectrometer of reverse (BE) geometry. It consists of a 90° magnetic sector followed by a 90° electric sector. The principals of ion dispersion and focusing in sector fields as well as the important concept of double focusing will be briefly discussed.

In Chapter 1, the force experienced by an ion moving in a uniform magnetic field was described. The trajectory of an ion with mass M and

charge q moving with velocity v perpendicular to a magnetic field, B, will have a radius r_B given by

$$r_B = Mv/qB$$

Thus ions will be dispersed in a magnetic field as a function of their mass and velocity. Magnetic sectors may be used as ion momentum filters. In addition to dispersion, a uniform magnetic field also provides focusing of ion trajectories. A trajectory diagram for a 60° magnetic sector is shown in the top panel of Figure 2.7. Consider a beam of ions originating at the same point source and having identical velocities but having different initial directions to form a distribution of initial trajectory angles (divergent beam). If the ions are directed into a magnetic sector of the the proper geometry, the magnetic field will provide refocusing of the ion beam at a distant point in space. This type of focusing is referred to as angular or direction focusing.

In a uniform electric field, E, an ion will have a trajectory of radius r_E, given by

$$r_E = 2KE/qE$$

Where KE is the kinetic energy and q is the charge on the ion. Thus an electric field will provide radial dispersion of ions on the basis of kinetic energy. In addition, directional focusing of angularly diverging ions may also be obtained in a field created by concentric parallel plates similar to the phenomenon in a magnetic field.

Under perfect magnetic focusing conditions, the dispersion in the ion beam at the angular focal point in a magnetic sector system will be

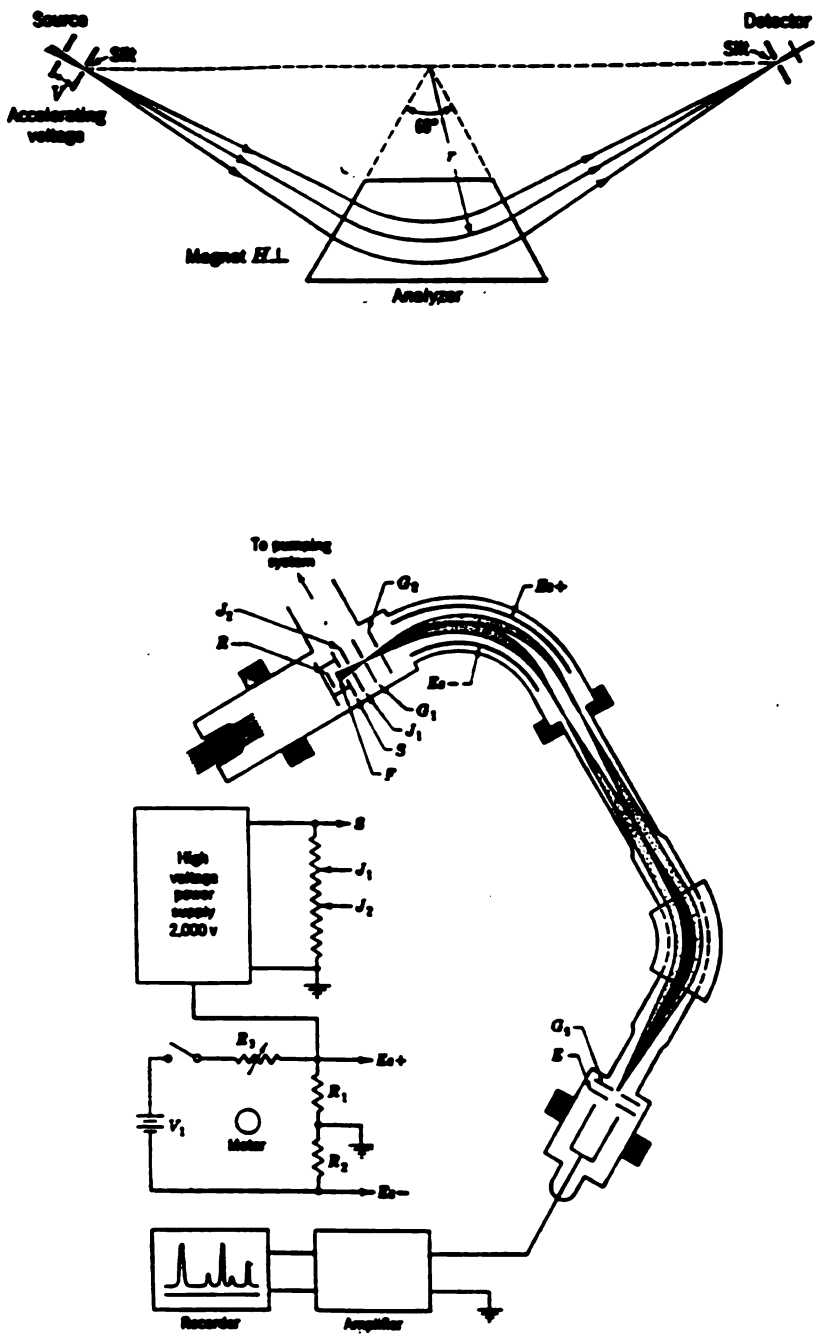

Figure 2.7. Neir Double Focusing Mass Spectrometer.

limited only by the monochromaticity of ion kinetic energy. In the early 1930s, Dempster recognized that the resolution of a magnetic mass analyzer could be improved by using an electric sector to provide kinetic energy filtering of the ion beam preceding the momentum analyzer. However, this type of tandem sector arrangement was not considered true double focusing. On the other hand, if a magnetic sector is combined with an electric sector such that the dispersion due to velocity in the magnetic sector focus is equal and opposite to the velocity dispersion in the electric sector, perfect double focusing may be achieved. In this configuration a sizable ion kinetic energy spread may not preclude high-resolution operation.

Neir has described a forward geometry (EB) mass spectrometer configuration that also provides double focusing [16]. The schematic diagram of a Neir double focusing instrument is shown in the lower portion of Figure 2.7. In this design, the intermediate slit between the two sectors is quite wide. The electric sector effectively energy-disperses divergent ions of different energies into a plane of energy-resolved beams at the entrance to the magnetic sector. In this way, the ions are presented to the magnetic sector at the proper spatial positions to be momentum-focused to a single point in space after traversing the magnetic sector. This geometry tolerates an appreciable ion kinetic energy distribution while maintaining high mass resolution.

Thus the CH5-DF mass spectrometer of BE design is capable of transmitting ion populations with a kinetic energy spread on the order 1% or more of the nominal accelerating energy. The energy acceptance for our instrument as a function of accelerating potential has been characterized and may be found Appendix A.

The instrument has a mass range of up to m/z 3,600 when operated at an acceleration potential 1000 V. The magnetic field strength is measured using a Hall effect probe. The field strength is displayed in Hall m/z units normalized for operating at a 3000 V accelerating potential. The relationship between Hall values and ion m/z values for operation at 1000, 2000, and 3000 volt accelerating potentials is documneted in Appendix B.

The mass resolution is dependent on the source (object) and detector (image) slit dimensions. The nominal resolution is ~250 with both slits wide open. The maximum attainable resolution is ~20,000 according to the instrument specifications, but has a practical limit of <3,000. For ion/molecule investigations in the beam instrument, the slits are usually maintained at full width to provide maximum ion current.

V. Intermediate Off-Axis Detector

In the CH5-DF stock configuration, an in-line Faraday cup and secondary electron multiplier were located immediately following the electric sector exit (image) slit in a small vacuum housing. The detector housing has been replaced with a flexible bellows assembly which provides a vacuum interface to the beam chambers. (The bellows assembly was originally used as the electric/magnetic sector union in a DuPont CEC-110 mass spectrometer.) An off-axis detector was designed and implemented in the transfer region. This provides for detection of ions, immediately after the electric sector, independent of the terminal detector system.

A schematic diagram of the interface bellows and off-axis detector

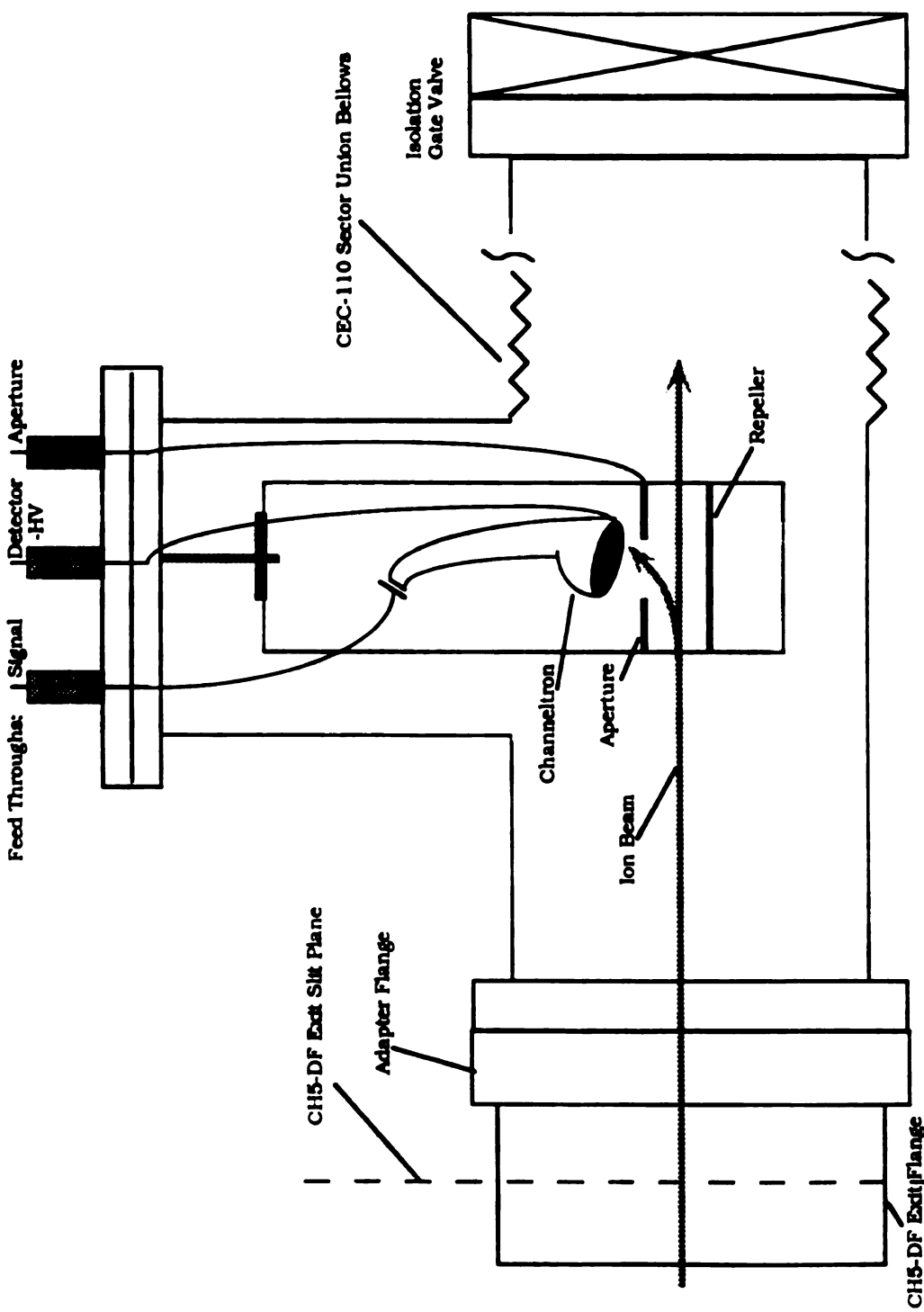

Figure 2.8. Intermediate Off-Axis Detector

system is shown in Figure 2.8. The bellows assembly was modified by welding a 2.5 " ID tube perpendicular to the central axis. A continuous dynode detector and beam deflection system was mounted onto the flange capping the tube. The detector was constructed from components of a Galileo 4770 series Channeltron detector. The inlet horn of the detector is positioned at an angle of approximately 70° with respect to the ion beam optical axis. An integral pair of deflection electrodes with a spacing of 1.3 cm is centered on the ion optical axis. The upper deflection electrode has a 1 cm diameter aperture through which ions pass to reach the input of the electron multiplier. A high transmission SS grid has been spot welded over the aperture to minimize penetration of the detector dynode bias potential. Additional shielding of the dynode has been achieved by a connecting a SS plate to the aperture electrode. This shield runs parallel along the length of detector.

If no potentials are applied to the detector system, the ion beam exiting the CH5-DF continues on to the ion beam optical system uninterrupted. Potentials applied to the aperture and repeller are dictated by the ion beam energy. For a nominal ion energy of 3000 eV, the repeller is normally held at ground potential. The detector is normally biased at around -2900 volts and the aperture is set at ~-2800 volts. The potential applied to the aperture may be varied through the use of a voltage divider circuit that is powered from the detector bias voltage supply.

The detector current generated by the off-axis detector is approximately two orders of magnitude lower than that recorded at the terminal in-line detector for the same ion beam current. There are two main factors that contribute to the relatively low sensitivity. First, the

4770 Channeltron used in the off-axis system was salvaged from another mass spectrometer. It had been removed from service since its useful current-gain lifetime had been expended. Second, the terminal in-line detector is a 4800 series high gain model from Galileo which has an inherent gain two orders of magnitude greater than the 4770 series detector.

One problem encountered in operating the off-axis detector involves charge build up on insulating surfaces inside the interface vacuum housing when the highest energy ion beams were in use (3000 eV). During detector power-up, the deflection optics direct the primary ion beam onto surfaces which are non-conducting. The primary ion beam may also strike (conducting) surfaces from which charged species are sputtered onto non-conducting surfaces. As a result, when the off-axis detector is turned off and the ion beam proceeds into the beam chamber, it travels through a region which contains residual charge (stray fields). This causes the ion beam to be deflected in a nonsymmetric manner. This beam distortion phenomenon was observed with the use of a Channel Electron Multiplier Array (CEMA) detector, which provides a visual representation of the ion beam profile. Under surface charge conditions the normally rectangular beam profile would become highly asymmetric and take on the appearance of a Normal Smiley Face (NSF). In fact, under certain conditions the author has observed the beam profile to strangely resemble various celebrities such as Vanilla Ice, Milli Vanilli, and, of course, Elvis (from an era prior to his final pathetic and obese state). When beam distortion occurred, it would gradually diminish over the course of several hours as the static charge dissipated. However, be must be noted that beam distortion was prevalent only when

the ion energy was >>1000 eV.

VI. Deceleration Lens

The deceleration lens utilized in the beam instrument is fully described and characterized in Chapter 3. A complete analysis of ion deceleration optics from both a theoretical and a practical approach is included. The ion deceleration lens employed in the MSU ion beam instrument presents an ion beam with minimal angular divergence (<5°) to the octopole beam guide. Ions may be decelerated from the initial accelerating energy to to <1 eV with excellent transmission efficiency.

VII. Octopole Ion Beam Guide and Collision Cell

The energy/mass selected ion beam is directed into a reaction zone containing a neutral reagent gas. Depending on the reaction dynamics and the interaction energy, secondary ions can be widely scattered about the collision center in the laboratory frame. Quantitative threshold measurements require product ions from the ion/neutral interaction to be efficiently collected for subsquent mass analysis. The MSU ion beam instrument employs an ion beam guide that provides dynamic ion trapping in the ion/neutral interaction region.

There are several stringent requirements for an ion beam guide suitable for use in an instrument intended for thermochemical measurements. It must provide highly efficient trapping of ions scattered off-axis in the laboratory frame. Ions of different mass-to-charge ratios should be transmitted with equally high efficiency (i.e. no mass

discrimination effects). This is especially important for reactive collision processes where the charged species may instantaneously have a very large positive or negative change in mass. Quantitative measurements require that the ion population in the collision region be effectively transferred into the second mass analysis region. The ion beam guide must thus possess strong focusing properties. Finally, and perhaps most importantly, the dynamic trapping process associated with the ion beam guide must not greatly perturb the initial ion kinetic energy distribution so that the ion/neutral interaction energy may be known with a high degree of certainty.

The octopole ion beam guide first employed for ion/molecule reaction containment by Teloy and Gerlich [17] fulfills the above operational criteria. The ion optical principles that govern dynamic trapping in an octopole will be briefly discussed. A detailed description covering the design and construction as well as the the electronics associated with our octopole device will be presented.

A. Multipole Trapping Theory

An exhaustive theoretical perspective of oscillatory electric field multipole devices has recently appeared in the literature as a series of articles by Szabo [18-21]. A comparative study on use of quadrupole, hexapole, and octopole ion traps concluded that the higher order multipole devices are far better suited for rf-only ion beam guides.

An octopole ion beam guide consists of eight parallel cylindrical rods equally spaced in an octagonal array. Circular rods may be used to approximate an ideal eight-fold hyperbolic potential surface. Radio

frequency (rf) potentials, 180° out of phase, are applied to adjacent rods. The inhomogeneous electric field creates an effective trapping potential in the interior tubular volume of the array. However, there is no net force exerted on an ion in the longitudinal direction inside of an rf multipole device.

This concept of dynamic trapping may be demonstrated by the SIMION model of an octopole cross-section shown in Figure 2.9. The top panel shows the potential surface created by eight circular rods at a point in time such that the potential between adjacent rods is very small. The lower panel shows the same system at a phase in which the potential between adjacent rods is much greater. In times of high potential difference, the octopole electric field creates a radial force towards the center of the array for regions of the surface of higher potential, such as indicated by the arrow. As the phase changes, alternate regions of the internal volume will exhibit centrally restoring forces. If the angular frequency of operation exceeds the transverse velocity of ions travelling longitudinally through the device, there will be a net radial force directed towards the central axis of the array. For example, a hydrogen ion with a transverse velocity component of 1 eV will require an operating frequency of >2 MHz.

A modified program for ion optical simulation using time-varying potentials was developed with SIMION to calculate ion trajectories in rf multipole devices. Figure 2.10 shows a cross-sectional model of an octopole trapping device. The system is modeled at a 300 V_{p-p} potential operating at an angular frequency of 1 MHz. Trajectories are calculated for a m/z 100 ion with an initial transverse kinetic energy of 0.026 eV starting at an initial position, r, of 0.30 of the distance from the center of

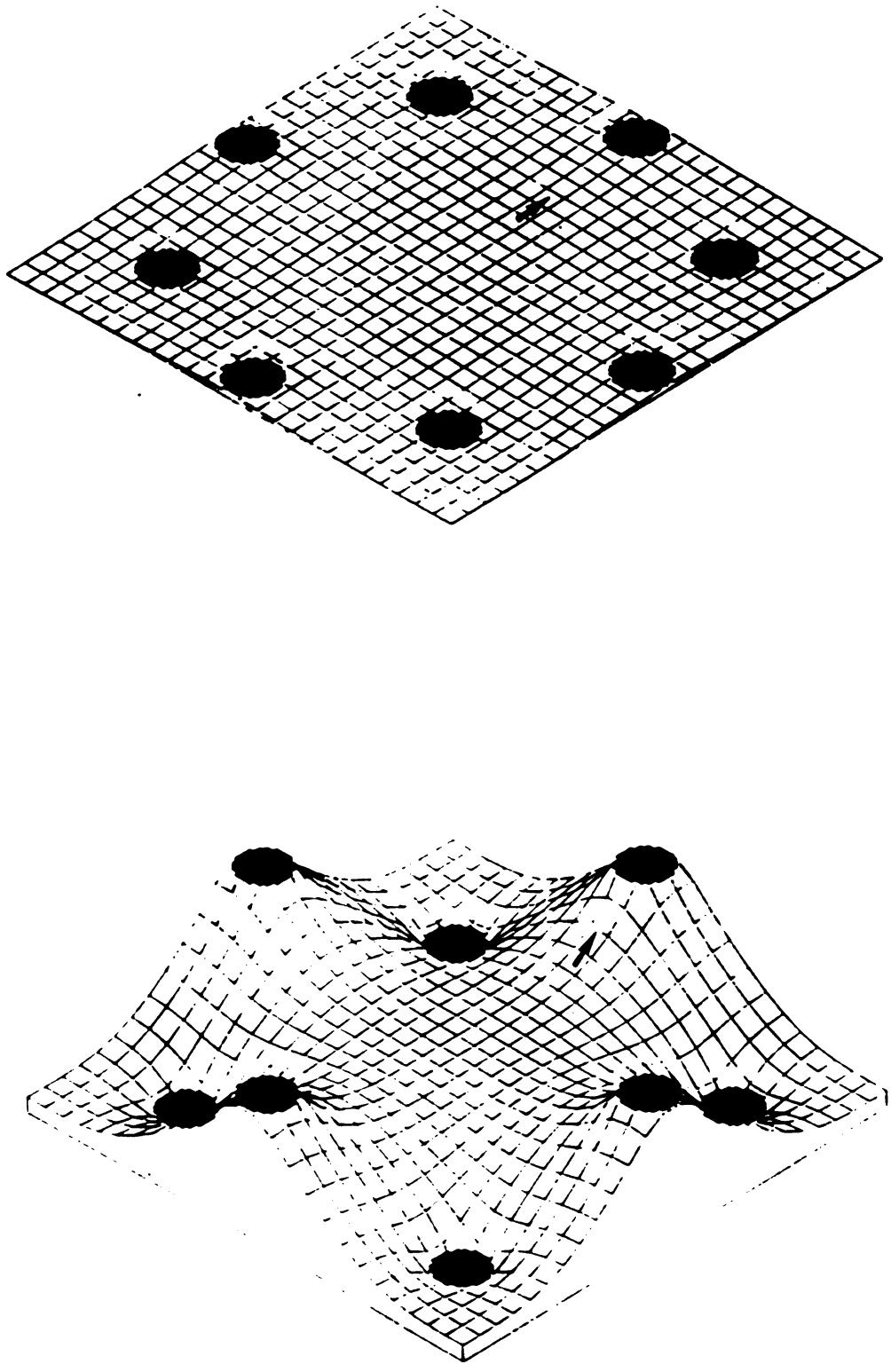

Figure 2.9. SIMION model of octopole potential surface.

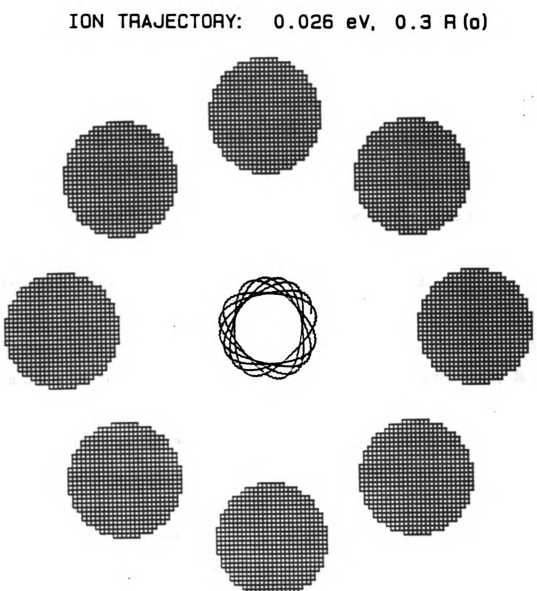

Figure 2.10. SIMION model of trajectories in rf octopole.

the array to the rods.

The effective radial potential well for a multipole trap is dependent on the multiplicity of poles and the physical dimensions of the device. The potential restoring force, U_{eff}, may be expressed a function of the radial distance from the center of the array as shown below [22].

$$U_{eff} = \left[\frac{n^2 q^2 V_o^2}{4m\omega^2 r_o^2}\right]\left[\frac{r}{r_o}\right]^{2n-2}$$

The number of poles is 2n; q and m are the charge and mass of the ion, respectively; r_o is the inner radius of the array. The rf potential applied to the rods is $V_o\cos^2(\omega t)$. Thus it can be seen that the relative potential is proportional to the number of poles minus 2.

From the above expression, the relative trapping potential was calculated for a series of multipole devices. The plot of trapping potential as a function of relative radial distance is shown in Figure 2.11. It can be seen that the devices with higher orders of poles exhibit radial potentials that better approximate square-well potentials. Thus, an octopole provides a more ideal trapping environment compared to lower order multipoles.

Another point of octopole superiority concerns the transverse ion energy. The longitudinal kinetic energy is not affected inside the ion beam guide. However, ions inside the rf field will possess a time-dependent transverse energy component as they oscillate through the beam guide. This transverse energy must be considered in the total kinetic energy of ion/molecule reactions. The transverse motion is mainly influenced by three initial factors as an ion enters the trapping

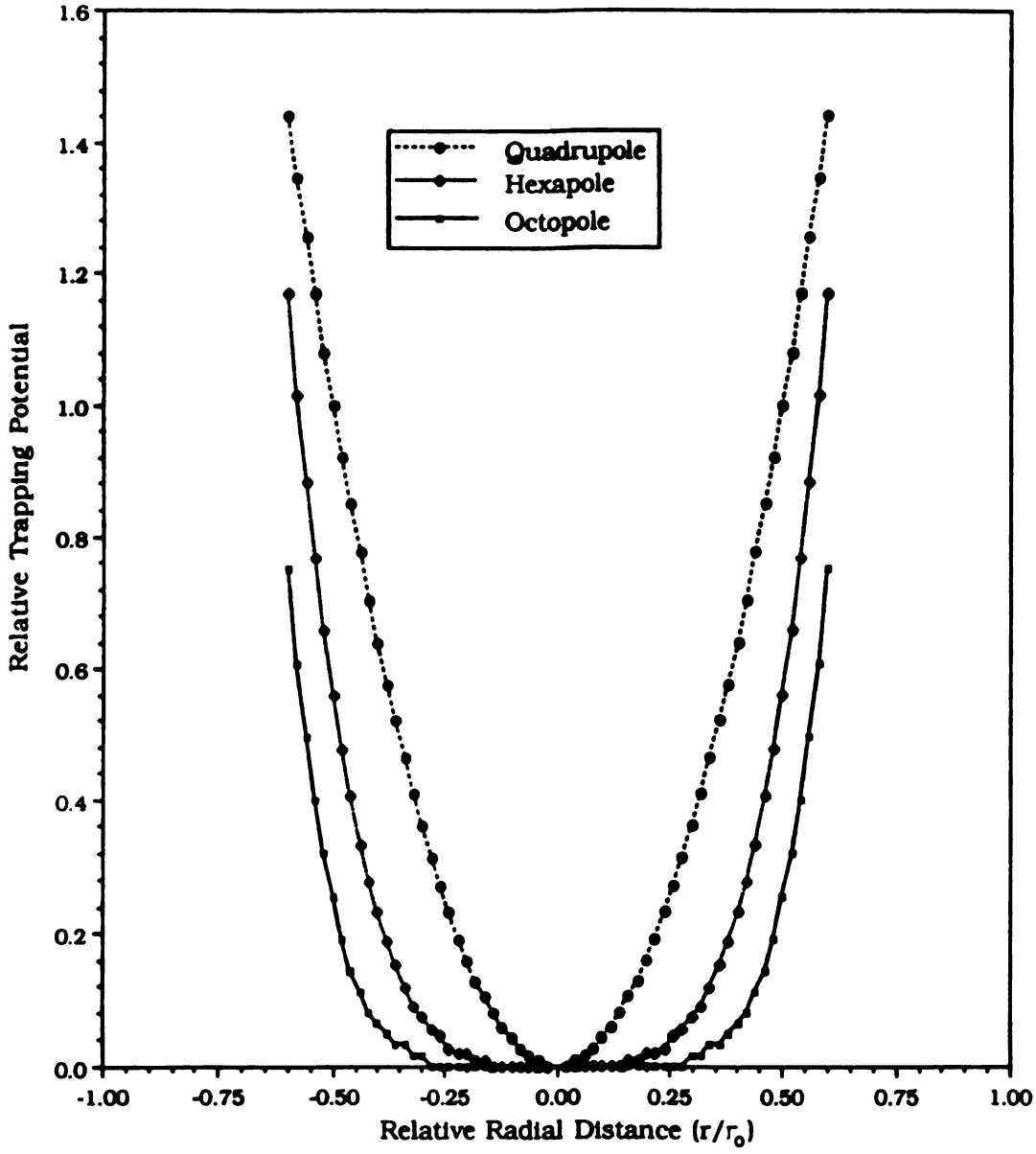

Figure 2.11. Theoretical rf multipole trapping potential.

field: (a) off-axis spatial orientation, (b) phase of the rf-field and (c) the initial transverse velocity component.

The various factors that influence transverse kinetic energy for both quadrupole and octopole beam guides were studied. SIMION models with time-varying potentials were used to determine the relative effects of rf phase, initial position, and initial angle of entry. An ion was subjected to oscillatory forces for a typical residence time of 20 ms and the transverse kinetic energy was then plotted as a function of time. One such result is shown if Figure 2.12. In this model, an ion with an m/z value of 100 and nearly thermal initial kinetic energy (0.02 eV) was started at a position of 0.2 r_0. Both the quadrupole and the octopole were operated at an rf amplitude of 300 volts and a frequency of 1 MHz. It can be seen that the energy of the ion in the quadrupole varies greatly as a function of time and the value may exceed 1.5 eV at times. The time-weighted average of the transverse energy in the quadrupole is 0.530 eV. In contrast, the transverse energy of the ion in the octopole did not exceed 0.1 eV. The time-weighted average kinetic energy of the ion in the octopole is 0.022 eV, which is very near the initial value. Numerous trajectory calculations have suggested that the transverse kinetic energy perturbation by an octopole electric field is usually minimal when the ion enters the octopole at a radial position of $\leq 0.2\ r_0$.

From the above result, it may be concluded that quadrupole beam guides would introduce a high level of uncertainty in an ion/neutral interaction energy. In addition, the initial rf phase relative to the point of ion injection has an extreme effect on the transverse kinetic energy in quadrupole devices, but is of little importance in octopole systems.

Another important point involves the mass range over which stability

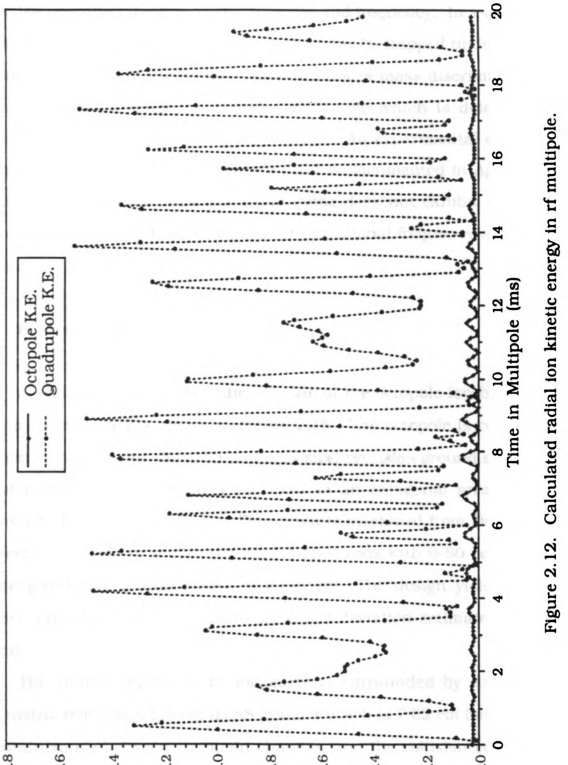

Figure 2.12. Calculated radial ion kinetic energy in rf multipole.

(trapping) is achieved in an rf multipole. The ion stability is determined by the operational values of the potential and frequency. In a quadrupole device there is a narrow mass range that may be trapped under constant voltage/frequency conditions. This introduces mass discrimination for transmission through an rf-only quadrupole which is deleterious to quantitative cross-section measurements. An experimental example of mass-dependent transmission in a quad is documented in Appendix C. In contrast, the octopole ion beam guide does not exhibit significant mass-dependent behavior over a wide operational frequency and voltage range.

B. Construction

A scaled sideview schematic diagram of the octopole ion beam guide and collision cell is shown in Figure 2.13. The octopole is constructed from eight 3.18 mm diameter stainless steel precision ground shafts from Small Parts Inc. The rods are fixed in an octagonal array with an inscribed radius of 8.73 mm. Four mounts machined from DuPont SP-1 Vespel are used to secure the back-tapped rods with 0-80 screws. The ion guide has a total length of 33.6 cm. The design yielded a very mechanically-sound array with a parallel deviation estimated at <0.03 mm.

The central region of the ion guide is surrounded by collision cell constructed from a 5.1 cm ID SS cylinder which is 7.62 cm long. To limit conductance between the main chamber and the collision cell interior, each end of the collision cell is terminated by an extension tube with an ID of 2.22 cm and a length of 6.35 cm. The diameter is slightly larger

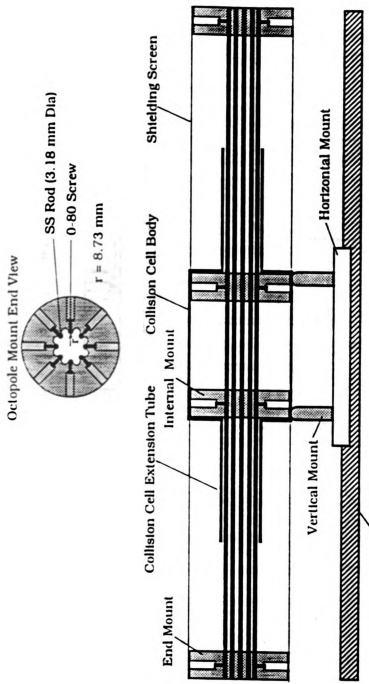

Figure 2.13. Octopole side view schematic diagram.

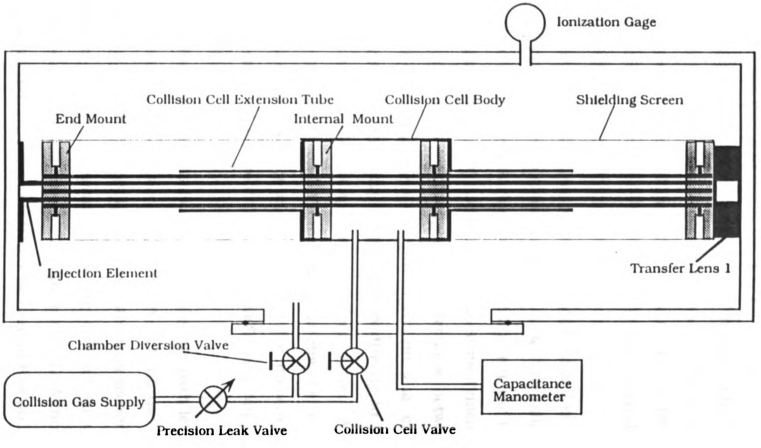

Figure 2.14. Octopole top view schematic diagram.

than the OD of the octopole rod array. A high transmission grid surrounds the length of the octopole to provide electrical shielding. This prevents penetration of stray fields and maintains a high degree of radial symmetry throughout the length of the device. The octopole assembly is constructed on a single 4" long horizontal mount for the ion optical rail. It is electrically insulated from the rail by two vertical rods fabricated from SP-1 Vespel.

A schematic diagram of the vacuum chamber containing the octopole/collision cell is shown in Figure 2.14. The collision cell has two 1/4" Cajon Ultratorr fittings positioned at the center of the cell to provide reagent gas introduction and cell pressure measurement. Teflon tubing provides electrically-insulating gas transfer lines between the collision cell and the Cajon gas feedthroughs on the chamber flange. Reagent/collision gas may be introduced directly to the collision cell through a Granville-Phillips precision leak valve. Alternatively, the collision gas may be diverted into the main chamber to make corrective background cross-section measurements. The pressure in the center of the collision cell is monitored by an MKS Baratron 310 capacitance manometer.

The inability to precisely define the effective path length and the gas density inside the collision cell may, in fact, be the most significant contribution to the uncertainty of absolute cross section measurements. Absolute pressure measurements are difficult to make with high precision and accuracy in the 0.1 mtorr region. Although hot cathode ion gauges (Bayard-Alpert type) may be used in this pressure range, they suffer from gas dependent response because the technique relies upon a secondary property of the gas such as ionization. The species dependent

response is because electron ionization cross sections, and hence the detector response, varies greatly from species to species.

Thus, it is advantageous to use a pressure measurement technique that utilizes a primary effect of gas density and temperature, such as force. Absolute pressure measurements are obtainable using a capacitance manometer. The mechanism of operation measures the force exerted by a gas which is independent of the nature of the gas. However, the uncertainty in of pressure measurement at 0.1 mtorr or lower may be more than ±25% even with the best capacitance manometer currently available. Also, the measured pressure must be corrected for thermal transpiration effects [23].

In addition to gas number density, the effective path length must also be precisely known for absolute cross section determinations. The collision cell ends present a relatively high conductance path to the surrounding vacuum manifold The effective length of the gas cloud at the measured pressure inside the collision cell is thus somewhat less than the physical length of the collision cell. Approximations for the pressure profile through the length of the cell can be applied to give an approximate effective collision cell length. One model results in a trapezoidal pressure profile through the length of the collision cell [24]. The effective length of our collision cell can be calculated from the cell body and extension tube dimensions. We can assume that pressure inside the 7.62 cm long collision cell body is constant. If the pressure decreases linearly from the end of the cell body along the extension tubes then the effective length of the extension tube is one-half of the physical length (6.35 cm). Thus, the overall effective length of the collision cell may be approximated as sum of the cell body length plus the effective

extension tube lengths which results in a value of 13.97 cm.

C. Octopole Electronics

The octopole ion beam guide must be operated at a frequency of 1 to 10 MHz with potentials in the 200 to 2000 V_{p-p} range in order to provide efficient trapping and strong focusing. A brute-force method to supply these power levels would be to simply connect the device to an extremely high power rf generator. Unfortunately, such a generator costs in excess of $20,000 and presents a very inefficient and unsophisticated approach to the operational requirements.

A more appealing solution applied here involves the use of rf transformers and tuned oscillator circuits. Figure 2.15 shows the fundamental circuitry associated with the transformers and oscillating circuits pertinent to this project. An effective method of stepping up ac potentials in the rf range is through the use of an air gap transformer. As shown in the top portion of Figure 2.15, a magnetic field is produced by applying an ac current to a primary inductor. If a secondary inductor is aligned properly in close proximity, the magnetic field from the primary coil will induce a current in the secondary coil. A voltage gain may be produced by having a greater number of turns in the secondary coil than in the primary coil.

A highly efficient means of producing high power ac oscillations at a fixed frequency is by employing a tuned inductor/capacitor circuit. An inductor (L) coupled in series to a capacitor (C) is called an LC tank circuit as shown in Figure 2.15. Under the proper resonance frequency conditions, power is alternately stored in the capacitor and in the

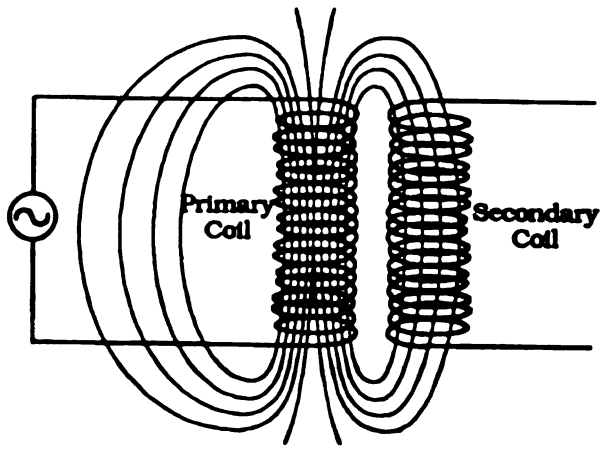

Transformer

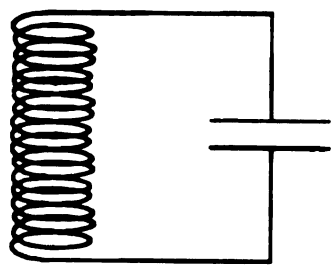

LC Tank

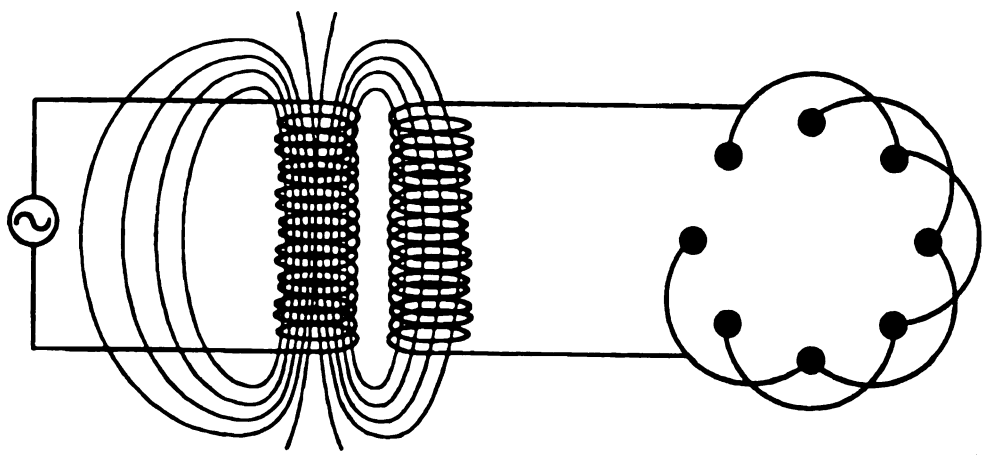

Octopole rf circuit

Figure 2.15. Radio Frequency Oscillator Circuits.

magnetic field of the inductor. An LC circuit has a resonance frequency of oscillation that is dictated by the value of the inductance, L, and the capacitance, C. The resonance frequency in cylces/second, f, is given as

$$f = \frac{1}{2\pi\sqrt{LC}}$$

If no resistive losses were present the capacitor could charge and discharge itself indefinitely without additional power input. Thus, an ac potential could be maintained across the capacitor plates. Practical LC circuits have a finite resistance that is mostly dominated by the length of wire used in the inductor. The resistance of the inductor is inversely related to a value referred to as the quality or Q of the inductor. The resistance of the inductror and attached circuitry determines the amount of power required to maintain oscillations of a given amplitude. In addition, internal circuit resistance determines the frequency range over which resonance occurs. Hence, for high amplitude oscillations at a very specific frequency, a high quality inductor should be used.

The LC circuit used to generate the octopole rf potentials is shown in simplified form in Figure 2.15. The inherent rod-to-rod capacitance is used as the capacitor in the LC tank. The capacitance of the octopole assembly has a measured value of ~50 picofarads.

A detailed schematic of the entire octopole electronics is shown in Figure 2.16. It consists of a frequency synthesizer, an rf power amplifier, a power meter, a tuning circuit and the transformer/LC tank circuit. A modified Extrel Model E High-Q head comprises the transformer portion of the circuit. The primary coil is shown as L_1 and the secondary coil,

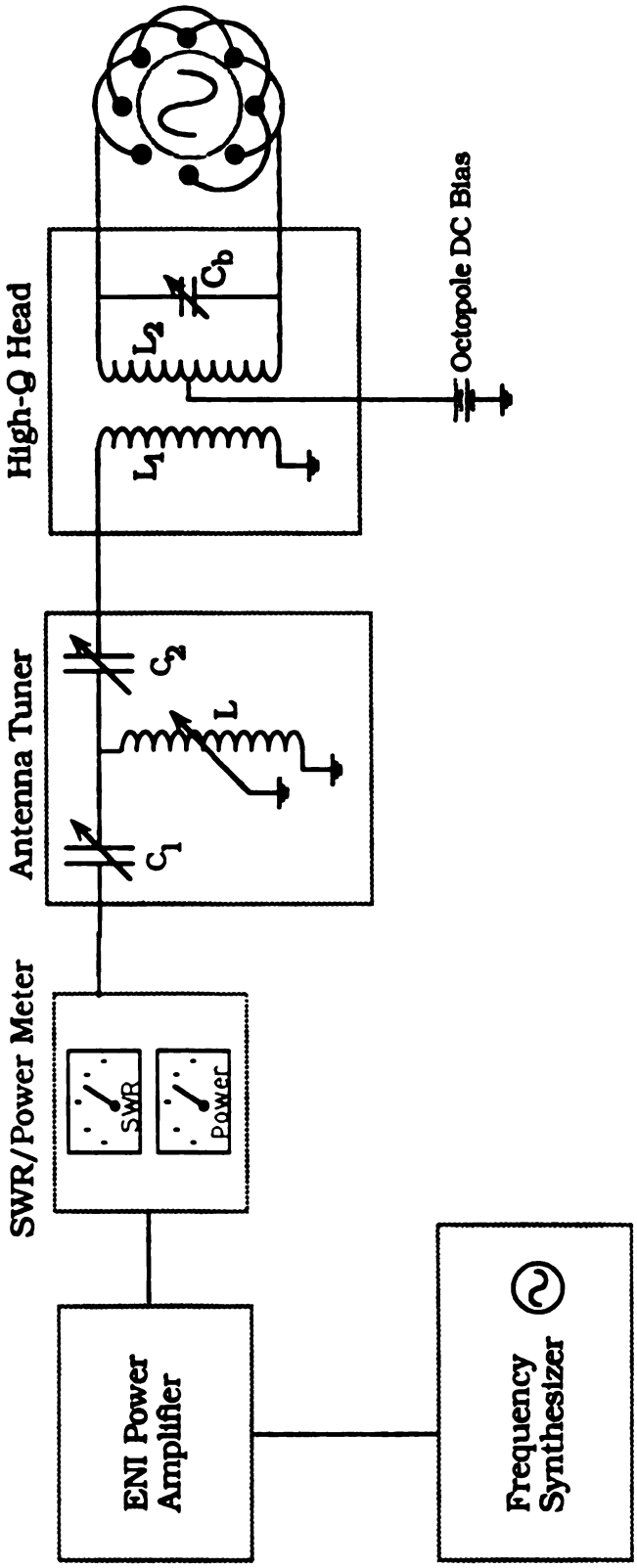

Figure 2.16. Octopole electronics schematic diagram.

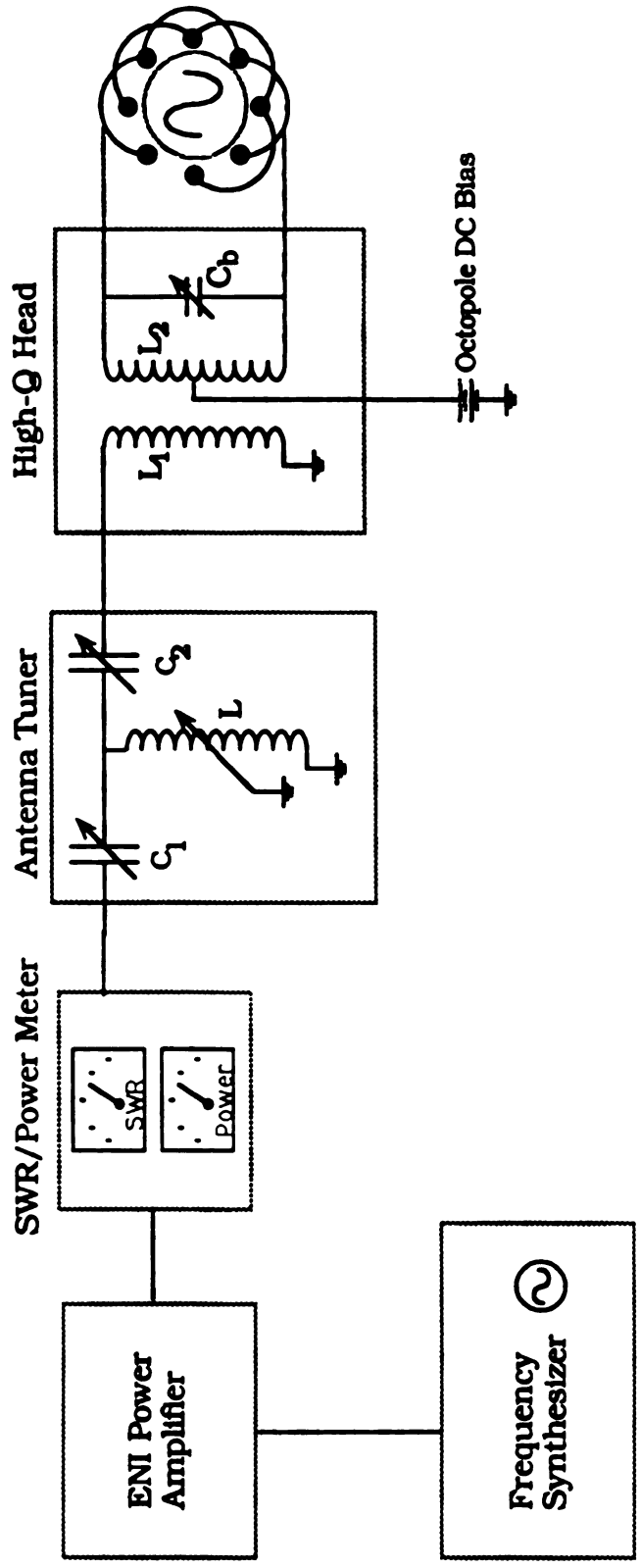

Figure 2.16. Octopole electronics schematic diagram.

L_2, is part of the LC tank circuit. A balance capacitor, C_b, is used to trim capacitance from one half of the octopole rods to the other in order to maintain a symmetric push-pull (balanced) waveform on the rods. A DC bias may be applied to the octopole through a center tap on the secondary coil. The resonant frequency of the LC (octopole) system is ~2.5 MHz.

A high precision (sub-ppm) Schomandl ND 30M-B frequency synthesizer is used to produce the primary signal. The synthesizer was salvaged from a Bruker NMR and has a continuously variable frequency range from 0.1 Hz to 30 MHz. The output amplitude is adjustable from ~ 0.1 to 1.0 volts at 50 ohms. The signal is fed into a ENI Model A-150 power amplifier. Broadband amplification of up to 150 watts into 50 ohms (85 V_{rms}) may be achieved in the 0.3 to 35 MHz range.

Since tuned LC circuits oscillate over a specific frequency range, the tank circuit power absorption is frequency dependent. If rf power is not absorbed by the circuit it is reflected back to the signal source. Reflected power represents wasted energy that must be absorbed by the amplifier and should be minimized for efficient operation. In addition, most of the line circuitry between the secondary inductor and the amplifier exhibit frequency-dependent impedance and, hence, transmission. General discussions on rf circuitry and transmission concepts may be found in any edition of the American Radio Relay League (ARRL) handbook.

To maximize forward power and minimize reflected power, a radio antenna tuner is inserted in the transmission line between the power meter and the primary coil. The Heathkit Model HFT-9A antenna tuner consists of a variable capacitor, C_1, a variable inductor, L, and a second variable capacitor, C_2, in series. By carefully adjusting the values of the

capacitors and inductor, a 50 ohm impedance match between the amplifier and the high Q head may be made. This results in maximum power transfer and minimized reflected losses.

A relationship exists between forward and reflected power that is quantitated as the standing wave ratio or SWR. In a perfect reactance match the SWR approaches a value of unity. The Heathkit Model HM-9 QRP Wattmeter measures and displays the forward power and the SWR directly. The SWR may be monitored while adjustments are made in the tuner circuitry until the lowest SWR value is achieved. In addition, the source frequency may be adjusted until maximum power absorption is attained. The antenna tuner and source frequency adjustments may be made in an iterative manner until the best settings are reached.

The tuned circuit described above has achieved phenomenal efficiency. At a frequency of ~2.5 MHz, the system can produce potentials of 1000 V_{p-p} between adjacent octopole rods while consuming < 1 watt of rf power. For conditions when the SWR approaches unity, an empirical relationship has been established between the forward output voltage displayed on the amplifier and the octopole peak-to-peak voltage as shown below.

$$V_{p-p}\,(\text{octopole}) = \sim 200\, V_{rms}(\text{amplifier})$$

The octopole has been successfully operated at potentials as high as 5000 V_{p-p} without dielectric breakdown or electrical discharge in the vacuum chamber. The octopole system has proven to be very stable over time and effective at providing high ion trapping/transmission efficiency.

VIII. Transfer Optics and Secondary Mass Analyzer

Ions are extracted from the exit aperture of the octopole beam guide and transferred to an Extrel quadrupole mass filter for subsequent mass analysis. The principles of quadrupole mass filters have been well documented in the literature [25]. The Extrel operator's manual provides an excellent resource for the practical aspects of the theory, electronics, and operation of quadrupole mass spectrometers.

The transfer optics must be able to effectively focus ions of a wide energy range into the quadrupole. Depending on the ion interaction energy in the octopole and the final ion analysis energy in the quad, the optics may have to perform both acceleration and deceleration in the same experiment.

Figure 2.17 shows the geometry of the transfer lens system, which is similar to the optical arrangement of the Extrel Model 041-1 Axial Molecular Beam Ionizer. The lens stack consists of 5 independently controlled electrodes which are isolated by sapphire bearings. The internal apertures are all 13 mm. The optimal electrode potentials are determined by the energy range encountered in the octopole/collision region and the final analysis energy desired in the quadrupole. Extensive SIMION modeling has shown that this lens configuration can provide excellent transmission over a broad energy range.

The voltages for the transfer optics are generated by a single high voltage power supply and a resistive divider network with eight outputs at two different voltage ranges. For an initial nominal ion energy of 1000 eV and a quad analysis energy of 50 eV, typical operating potentials are 520, 920, 1026, 907, and 975 volts for electrodes 1 through 5,

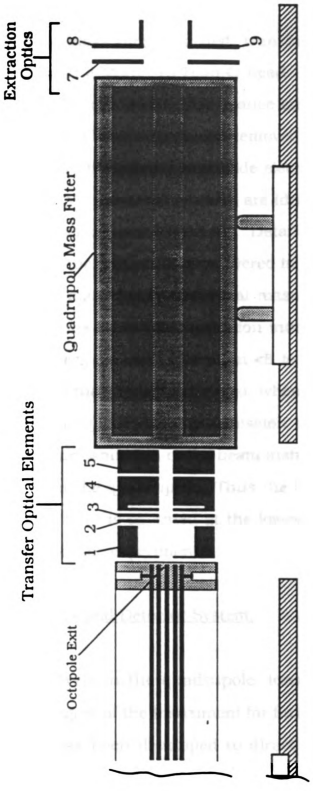

Figure 2.17. Octopole/Quadrupole Transfer and Quadrupole Extraction Optics.

respectively. Ion transmission through the transfer optics is nearly 100%.

The quadrupole mass filter is a high transmission Extrel #4-324-9 model combined with a Model 15 High-Q head. The unit has an upper m/z limit of ~350. To increase the acceptance area of the mass filter, the ELFS leaky dielectric element has been removed. The standard high Q head circuitry has been modified to provide electric isolation at DC-bias potentials up to 5 kV. The modifications are identical to those found in the Special HV Head offered by Extrel. Details of the operation and computer control of the mass filter are covered in Chapter 4.

The quadrupole mass filter is an ideal mass analyzer for ion beam work since it performs mass discrimination independent of ion energy. Typical analysis energies may range from <5 to >100 eV depending on the requirements of the experiment. Also, when it is operated in a low resolution mode, the quadrupole transmission efficiency can be >80%. In fact, the overall transmission of the beam instrument is limited by the resolution setting of the quadrupole. Thus the highest ion currents are obtained when the filter is operated at the lowest resolution compatible with the chemistry of the experiment.

IX. Extraction Optics and Detector System.

After mass analysis in the quadrupole, ions are transferred to the terminal detector region of the instrument for flux measurement. A set of extraction optics has been developed to direct a focused ion beam to either of the two detectors. The focusing system is a modified einzel lens design as shown in Figure 2.17. The first element of the lens is the exit

aperture of the quadrupole housing. The center element (7) is a circular plate electrode. A split tube electrode (8,9) with an extension tube comprises the final element of the einzel lens. The electrodes are separated by 4mm ceramic insulators. Potentials for the extraction optics are obtained from the same power supply/divider network as used for the octopole transfer optics.

The extraction optics and the detector system are shown in Figure 2.18. When the Daly detector is in operation, the split tube lens may be asymmetrically biased so that the ion beam is directed toward the center of the conversion dynode. This allows high efficiency at any ion energy or conversion dynode potential. For an ion energy of 1000 eV and a quad DC bias potential of 950 volts, the extraction elements 7, 8, and 9 are nominally set at 0, 750 and 700 volts, respectively, when the conversion dynode is biased at -30,000 volts.

Ions may be detected by either a continuous dynode electron multiplier or a Daly detector. A Galileo 4800 series Channeltron detector and a shielding enclosure are mounted on the ion optical rail. The input horn of the detector is coaxial with the ion optical axis. The detector is normally operated in an analog current mode for measurement of relatively high ion currents. When coupled to a electrometer/picoameter, the Channeltron can quantitate ion currents that are less than 10^{-17} to more than 10^{-10} amps in the analog mode. This corresponds to count rates of ~100 ions/second to 10^9 ions/second. The electron multiplier also has the capabilities of fast response time for high ion currents. This feature facilitates beam instrument diagnostics and rapid scanning for tuning of the quadrupole mass filter.

For quantitating very low ion currents such as are encountered in

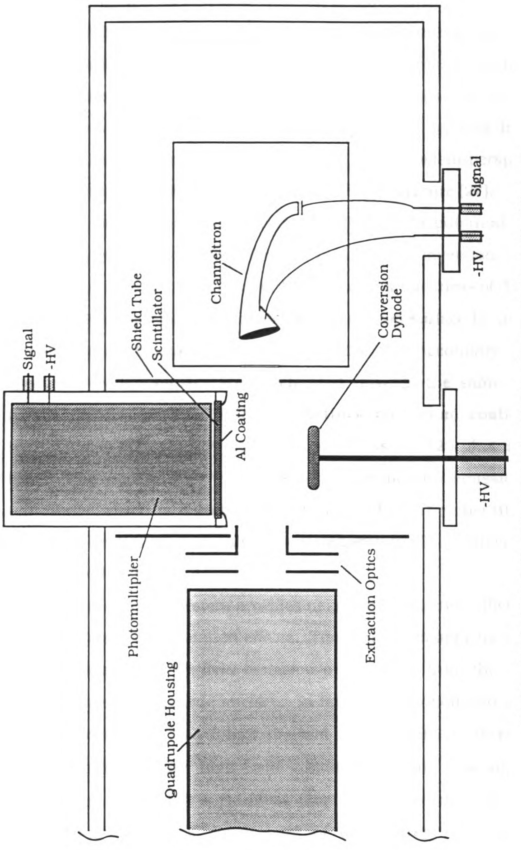

Figure 2.18. Extraction Optics and Detector System Schematic Diagram.

threshold measurements, ion counting techniques must be employed. The Channeltron may be configured for pulse counting, but it suffers from poor initial conversion efficiency and serious mass discrimination. Therefore we have developed a highly efficient Daly detector as shown in Figure 2.18. The concepts and operation of this detector have been described and characterized elsewhere [26]. An excellent perspective on the measurement of low ion fluxes is found the literature [27].

In this design, ions are accelerated through a potential of up to 30,000 V by the conversion dynode bias. The conversion dynode is constructed from a 1.25" diameter SS disk with a thickness of 0.25". The dynode has been polished optically flat on the top surface by using 3 μm grit on an electrochemical electrode polisher. Secondary electrons sputtered by ion impact are accelerated through the same field to a plastic scintillator disk with a 3 Å thick aluminum coating. The scintillator is optically coupled to a Hamamatsu R-425 photomultiplier tube. The high energy electrons stimulate photon emission in the scintillator which is detected by the phototube. The operation of the computer-controlled electronics associated with the Daly detector system are covered in Chapter 4.

The Daly detector system provides nearly unit detection efficiency with minimal mass discrimination effects. The dark count appears to be most strongly dominated by field emission of electrons from the negatively biased conversion dynode surface. In fact, a highly polished aluminum conversion dynode was found to yield dark counts in excess of 10^4 counts/second under high field conditions. This was significantly reduced by employing a stainless steel conversion dynode. The raw undiscriminated dark count rate of our system is typically <20

counts/second under a standard conversion dynode potential of -30,000 volts and a photomultiplier bias around 1000 volts. The background may be reduced to fewer than 5 counts/second by utilizing the discrimination circuitry.

LIST OF REFERENCES
Chapter 2

1. Daly, N. R.; *Rev. Sci. Instrum.* **1960**, *31*, 264.

2. Dahl,D.A.;Delmore, J.E. ,*SIMION PC/PS2 Version 4.0*, EGG-CS-7233 Rev.2, April **1988**.

3. Darland, E.J.; Ph.D. Dissertation, Michigan State University, 1978.

4. "Electron Impact Ionization", T.D. Mark in "Gaseous Ion Chemistry and Mass Spectrometry" ed. J. Futrell , John Wiley and Sons, New York, **1986.**

5. Garstang,R.H.; *Mon. Nat. R. Astron. Soc.* **1962,***124*, 321.

6. Corliss, C.; Sugar,J. *J. Chem Phys. Ref Data*, **1982,***11*, 135.

7. Elkind,J. ; Armentrout, P. *J Chem Phys.*, **1986,***90*, 5736.

8. Van Koppen, P.; Kemper, P.; Illies, A.; Bowers,M. , *Int. J. Mass Spectrom. and Ion Proc.*, **1983**, *74*, 263.

9. Birkinsaw, K; Shukla, A. ;Howard, S. ;Biggerstaff, J. ;Futrell, J. *Int. J. Mass Spectrom. and Ion Proc.*, **1988,***84* , 283.

10. Price, P.; Swofford, H.; Butrill, S. *Anal Chem*, **1977**, *49*, 1497.

11. Blom, K.; B. Munson *J. Am. Chem. Soc.*, **1983**, *105*, 3793.

12. McDaniel, E.W., "Collision Phenomena in Ionized Gases", Wiley, New York, Ch. 9, **1967.**

13. H.E. Riveracome and E.A. Mason, Anal Chem.,1975, 47, 970.

14. Elkind,J. L.; Armentrout, P.B. *Int. J. Mass Spectrom. and Ion Processes.* **1988**, *83*, 259.

15. Munson, M.; Field, F. *J. Am. Chem. Soc* **1966**, *88* , 2621.

16. Johnson, E.G.; Neir,A.O. *Phys. Rev.* **1953**, *91*, 10

17. Teloy, E.; Gerlich, D. *Chem. Phys.* **1974**, *4*, 417.

18. Szabo, I. *Int. J. Mass Spectrom. and Ion Proc.*, **1986**, *73*, 197.

19. Hagg, C.; I. Szabo, *Int. J. Mass Spectrom. and Ion Proc.*, **1986**, *73*, 237

20. Hagg, C.; I. Szabo, *Int. J. Mass Spectrom. and Ion Proc.*, **1986**, *73*, 277

21. Hagg, C.; I. Szabo,*Int. J. Mass Spectrom. and Ion Proc.*, **1986**, *73*, 295

22. Landau L.; Lifschitz, E. "Mechanics", Permagon Press, Oxford p. 93 **1960**

23. Loriot, G.; Moran, T.; *Rev. Sci. Instrum.*, **1975**, *46*, 140.

24. Amdur,I.; Jordan, J.: *Adv. Chem. Phys.* **1966**, *10*, 29.

26. Dawson, P. *Mass Spec. Rev.*, **1986**, *5*, 1

27. Romero, L. A.; Masters Thesis, Michigans State University, **1989**.

28. Wetner, H. *Int J Mass Spectrom and Ion Physics*, **1972**, *8*, 459.

Chapter 3

Understanding Ion Deceleration Optics

I. Overview

One of the most critical components of the MSU ion beam instrument is the ion deceleration lens. The traditional approach for obtaining highly-collimated low energy (<200 eV) beams from high energy (1-10 keV) sector mass spectrometers involves the use of a complex exponential deceleration lens assembly. Through ion optical modeling of the exponential lens and other less-complex lens designs, the fundamental features that contribute to deceleration lens performance were investigated. From this evaluation, a simple high-performance lens was designed, constructed and characterized. The novel lens described here decelerates a 3 keV ion beam down to the 3-200 eV range while providing low angular divergence, excellent focusing and excellent transmission.

II. Introduction

There are various applications in mass spectrometry in which it is necessary to decelerate ions having an initial translational energy of 1 to 10 kiloelectron volts, to a final translational energy of 1-200 electron volts in the laboratory frame-of-reference. Ion deceleration is accomplished by passing the high energy ions through an energy-

retarding field. Historically, the ion optical device selected to create the decelerating field has depended on the specific requirements of the experiment. The deceleration lens may often prove to be the the most critical ion optical component in determining the overall performance of an instrument that bridges the gap between high translational energy (keV) and low translational energy (eV) domains.

Recently there has been a great deal of effort directed towards developing versatile mass spectrometric instrumentation that combines both sector and quadrupole or quistor mass analyzers [1-4]. In some so-called "hybrid" instrument configurations the first mass spectrometer consists of a magnetic sector (B) or a combination of magnetic and electric (E) analyzers preceding a radio frequency-only quadrupole collision cell (q) in tandem with a quadrupole mass analyzer (Q). Other hybrid configurations incorporate sector mass spectrometers followed by various combinations of quistor ion traps and quadrupole mass analyzers. In a hybrid mass spectrometer of BEqQ geometry, for example, ions are extracted from the source and accelerated through a nominal potential of 1 to 10 kV. If low energy (1-200 eV) ion/neutral collisions are desired in the rf-only quadrupole, ions exiting the electric sector must be decelerated and focused into the first quadrupole. The ion optical device required for this task may consist of as few as two or three electrodes that establish the energy retarding field and provide focusing. The angular and energy acceptance of rf-only quadrupoles and quistor devices is often quite broad [5]. Therefore the decelerated beam of ions may have a half-angle of divergence as great as 25° and may exhibit a broad kinetic energy distribution (>5 eV FWHM). This is sufficient to provide reasonable transmission through the collision region

for typical analytical applications where the kinetic energy of the ion need not be accurately known.

There is a significant field of gaseous ion chemistry that is interfaced with surface science and materials research. This has lead to the development of numerous experimental procedures to study low energy ion/surface interactions. These include surface induced dissociation (SID) [6], "soft landing" of polyatomic ions for surface modification [7], atomic ion implantation studies [8,9] and ion/surface scattering investigations [10]. In many of these applications, ion production occurs in an electron ionization source and the ion of interest is selected by accelerating the ions to high translational energy and dispersing them in a magnetic field or other mass separation device such as a Wein filter. The mass selected ion beam exiting the mass selection device must be decelerated to the desired energy and directed toward the surface. Here, the ion beam is typically tightly focused to a small region of the surface. This type of spatial focusing can often be accomplished with a deceleration assembly consisting of a small number of ion optical elements.

Another developing area of mass spectrometric instrumentation requiring strong ion deceleration optics is high-pressure external-source Fourier transform mass spectrometry [11]. In this technique, the high-pressure ion formation region is remotely located from the the low-pressure, high magnetic field region where mass analysis is performed. Ions are extracted from the source and accelerated to high kinetic energy (~2 keV) for transport through several stages of differential pumping. High ion kinetic energy also facilitates penetration into the solenoid magnetic field without significant scattering losses (magnetic mirror

effect). Prior to injection into the analysis cell, the ions must be attenuated in energy to approximately 2 eV or less to be compatible with the applied trapping fields. The ion deceleration optics for such an instrument have been constructed with as few as two elements.

Another recent application of ion deceleration is found in the work of Kemper and Bowers [12] in which a high pressure drift tube is coupled to a reverse geometry (BE) mass spectrometer. Ions are initially accelerated to 5 keV and then mass analyzed. The high energy ion beam emerging from the electric sector is decelerated in two stages by an assembly of five cylindrical elements. Final ion translational energies between 0.5 and 10 eV were obtained with this deceleration lens design.

In contrast, for hybrid ion-beam instruments designed to accurately probe the energetics and dynamics of ion/molecule interactions there are greater demands on the deceleration system. The deceleration lens must manipulate a high energy ion beam from a sector mass analyzer and (ideally) produce a highly collimated, monoenergetic beam of ions having low translational energy. Several types of deceleration systems have beam designed to create highly-collimated ion beams. Armentrout and Beauchamp [13] developed a hybrid mass spectrometer of BQ geometry which utilized a complex lens assembly known as a "Menzier Deceleration Unit". Recently, Futrell and coworkers developed a hybrid tandem supersonic beam mass spectrometer for the study of CID processes in the energy range of <1 to 3000 eV [14]. Their ion deceleration system followed a magnetic sector and implemented a total of six separate stages of deceleration. Each stage consisted of a two-element cylindrical (tube) lens.

However, the traditional design for such high performance

deceleration system involves creating an exponentially-decaying retarding potential field. This system is considered to be the "state-of-the-art" in deceleration lens design but its implementation normally requires a complex lens assembly, often incorporating 40 or more electrodes [15].

In determining the deceleration optics for the MSU ion beam instrument, the following question was addressed: can a high performance deceleration lens suitable for ion beam applications be designed without implementing a complex exponential retardation field? The design approach was to first evaluate the performance of a state-of-the-art exponential lens system using the ion optical simulation program SIMION PC/PS2 [16]. A simple two-electrode deceleration lens design was also modeled to investigate ion deceleration from a fundamental perspective. From these studies, a high performance deceleration lens incorporating as few as two active elements was proposed (an active element is defined here as an ion-optical electrode to which some nonzero potential is applied). This versatile design has been constructed and its ion transmission and angular divergence characteristics determined.

III. Deceleration Lens Criteria

The MSU hybrid ion beam instrument of BEoQ geometry (o = rf-only octopole collision cell) has been constructed to study ion/molecule reactions and collision induced dissociation cross-sections as a function of translational energy. Since the ultimate goal of this project is to obtain accurate thermodynamic values for the onset of endothermic processes (e.g. ionic heats of formation), the instrument design emphasis is on

establishing a well-defined interaction energy between the ion and the neutral collision partner. To attain this goal, the deceleration system must satisfy the following criteria:

1. Decelerate a 1000, 2000, or 3000 eV beam to <2-200 eV
2. Provide good focusing (final beam diameter <4.25 mm)
3. Convert the beam symmetry from planer to cylindrical
4. Produce a highly-collimated beam (divergence half-angle <5°)
5. Maintain high ion transmission
6. Produce minimal kinetic energy perturbation (KE spread <0.5 eV)
7. Mechanical simplicity for precise alignment (minimize aberrations)

A block diagram of the MSU ion beam instrument is shown in Figure 3.1a. As discussed in preceding chapters, the primary ion beam is generated using a Varian MAT CH5-DF reverse geometry double focusing mass spectrometer which utilizes a 90° magnetic sector followed by a 90° electric sector. The nominal accelerating potential of the instrument is selectable at 1000, 2000 and 3000 volts with an upper mass limit of 1,200 daltons at the full accelerating potential. Ions exiting the final focusing slit after the electric sector travel through a 50 cm field-free region containing an off-axis detector, and then enter the deceleration assembly. After deceleration to the desired kinetic energy, ions are introduced into an rf-only octopole ion beam guide which passes through a collision cell containing the neutral target gas. The octopole and collision cell are DC-biased and referenced to the source accelerating potential to establish the ion kinetic energy in the collision region. Unreacted primary ions and ionic reaction products are extracted into a

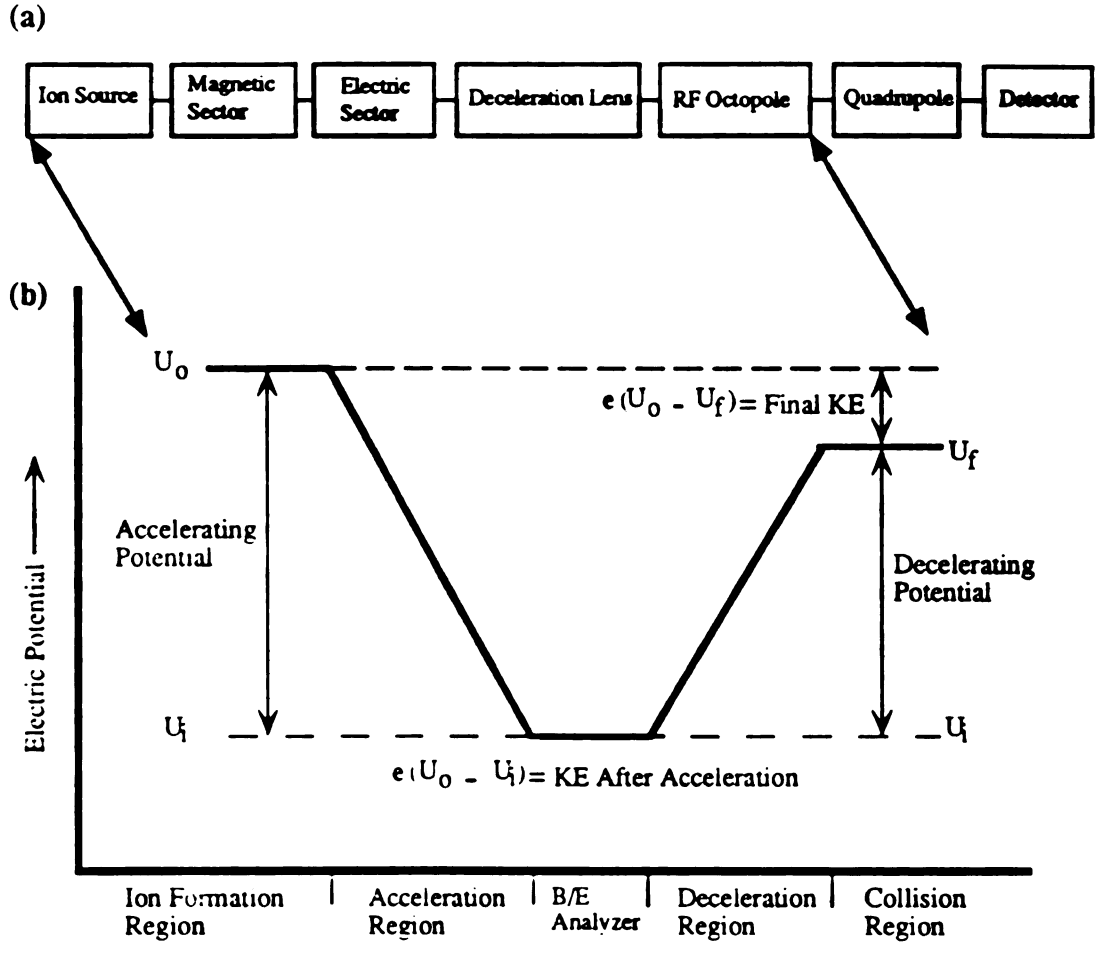

Figure 3.1. MSU Ion Beam Instrument Block Diagram and Electric Potential Diagram.

quadrupole mass filter and the intensity measured with a Daly-type scintillation detector operated in the pulse counting mode.

The ion acceleration/deceleration sequence for our instrument is graphically presented in Figure 3.1b. In this diagram, the ion source is positively biased at the accelerating potential, U_o, with respect to instrument ground, U_i. Ignoring the initial thermal energy spread of the gas being ionized and spatially-varying ion source potentials (ΔU_o), ions are formed initially at rest (E_o = zero) in space at the potential U_o and are then accelerated through the potential given by $U_o - U_i$ as shown in the figure. The kinetic energy, E_i, gained from the accelerating field by ions carrying a single charge is simply $e(U_o - U_i)$, where e is the elementary unit of charge. After mass analysis in the B/E region, the ions are decelerated to the appropriate energy by the decelerating potential, U_f, which is applied to electrodes in the deceleration region relative to U_i. The final ion kinetic energy after deceleration, E_f, may be taken nominally as the difference in electric potential between the ionization region and the deceleration region, $E_f = e(U_o - U_f)$.

In order to properly design the ion optics for a deceleration system for this instrument, the dimensions and angular divergence of the ion beam emerging from the CH5-DF was measured. This was done for 1000, 2000 and 3000 volt nominal accelerating potentials. A Galileo 3040 channel electron multiplier array (CEMA) equipped with a P20 phosphor screen deposited on a fiber optic bundle was placed in the path of ions exiting the electric sector. Ions incident on the detector produce an image on the phosphor screen which may be observed through the fiber optic .

The experiment required the removal of the stock CH5-DF detector housing and installation of a suitable vacuum enclosure to house the

CEMA. A discarded detector housing from a CEC-110 mass spectrometer with an ID of ~9 cm and a length of ~15cm and an ample number of high voltage feed-throughs was attached to the electric sector with an adapter flange. The experimental configuration is shown in Figure 3.2. Since the CEMA entrance plate is biased at a high negative potential (-1400 V), a high transparency stainless steel grid was placed a few millimeters in front of the CEMA and held at ground potential to maintain a field-free ion flight path prior to detection. The beam exiting the electric sector was visualized at two different distances (9 and 20 cm) from the the exit slit. Beam images were recorded on slide film using a 35 mm camera. After development of the slide film, the beam images were projected onto a large section of paper, traced and measured. For all three source accelerating potentials, the beam cross-section immediately after the exit slit of the electric sector has an approximate height of 4 mm and a width of 0.75 mm with the source and exit slits fully open. For the 3000 eV ion beam, the half-angle of divergence in the plane perpendicular to the length of the slit is ~0.25°. The 1000 and 2000 eV beams possessed slightly higher angular divergence in this plane. There was no measurable angular divergence in the plane parallel to the slit length for all three ion beam energies. Thus, the ion beam exiting the electric sector can be described, to the first approximation, as paraxial .

After traversing the 72 cm field-free region between the electric sector slit and the entrance to the deceleration region, the ion beam profile is approximately 4 mm high by 3 mm wide. The 3000 eV ions must be decelerated and injected into the rf-only octopole which has an inner radius, r_0, of 8.5 mm. The deceleration lens should be capable of

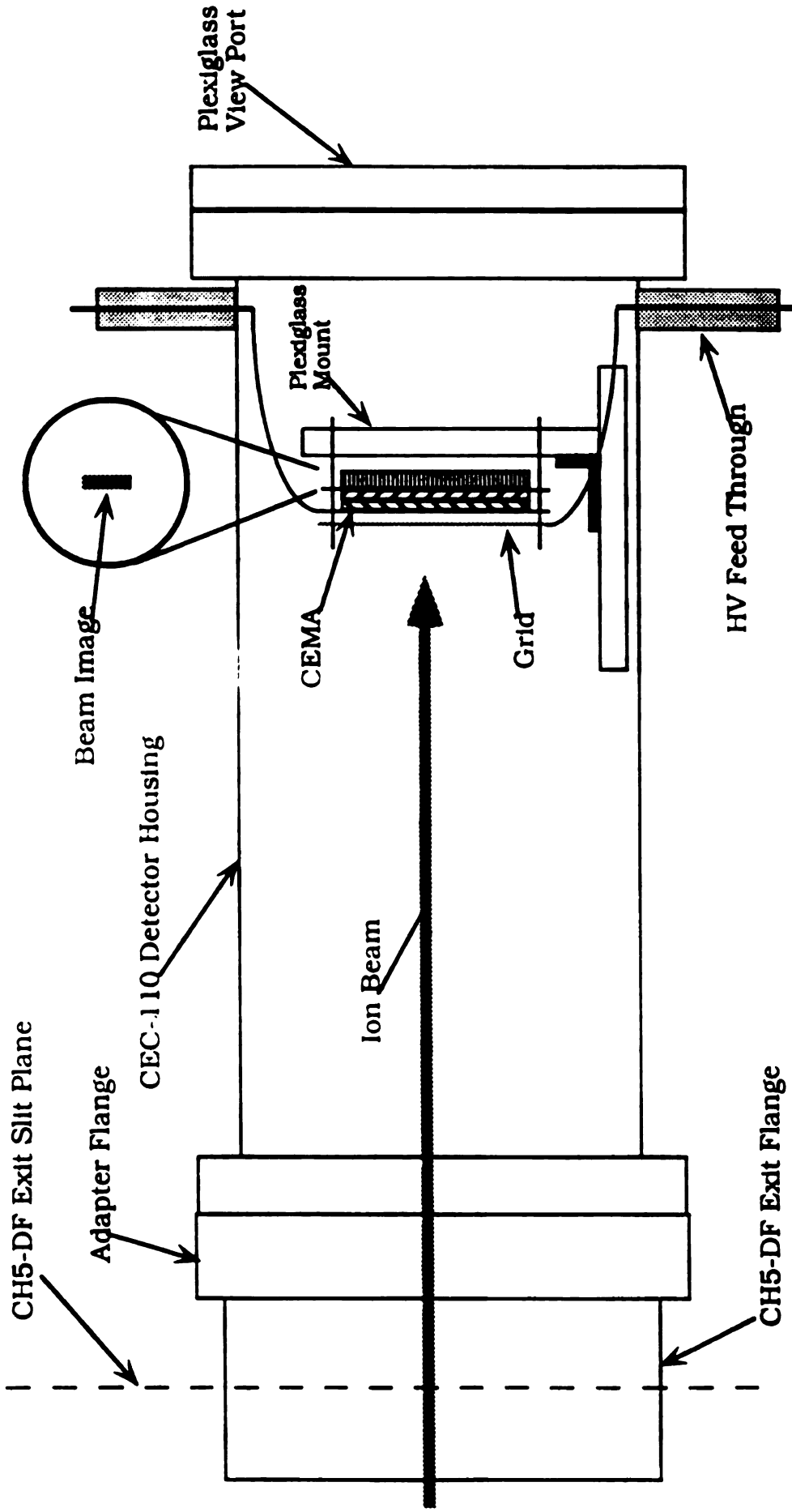

Figure 3.2. Experimental configuration for CH5-DF beam visualization.

producing an ion beam variable in energy from ~1 to 300 eV in the laboratory frame. In addition, it would be advantageous to convert the planar symmetric (rectangular profile) beam from the sector region to a beam having a circular cross-section to match the axially symmetric octopole/quadrupole regions of the instrument.

Although rf-only multipole beam guides have no longitudinal electric field components, the oscillatory radial trapping field can have a profound effect on the transverse ion motion. In order to provide accurately known ion kinetic energies in the octopole beam guide, the time-dependent component of kinetic energy transverse to the principal axis of motion must be minimized. Computer modeling of the ion-optical properties of rf-only multipoles performed in this laboratory (see Chapter 2), and also reported in a recent article by Davies and Wright [17], suggest that there are particular characteristics of an ion beam entering the multipole beam guide that preserve minimal transverse energy components as the ions travel through the oscillatory field. This requires that ions entering the rf-only device must have trajectories nearly parallel to the main axis of motion (highly collimated) and that the ion beam must have a small diameter (tightly focused). Our modeling suggests that an ion beam should have a cross-sectional radius of less than 0.25 r_0 (r_0= octopole inner radius) when entering an rf-only octopole field. For our system (r_0= 8.5 mm) this requires a decelerated beam diameter of ≤4.25 mm. A small initial beam at the entrance of the ion beam guide also insures the highest transmission of the primary ion beam through the device. More importantly for our application, a nearly paraxial beam (divergence half-angle <5°) entering the octopole minimizes ion losses during collision processes such as dissociation or ion/molecule reactions

that result in an instantaneous change in the mass of the charged species while in the oscillating field [18]. This eliminates the need to correct for dynamically-dependent transmission features of the octopole when measuring total reaction cross-sections.

Ideally, manipulation of the ion beam by the deceleration system should not perturb the kinetic energy distribution the ions found at formation. Much effort has been directed towards the development of ionization sources that provide beams with low energy spread. Conventional electron impact ionization sources produce beams with translational energy variations of <0.5 eV FWHM. A small ion kinetic energy spread after deceleration will provide well-defined ion/neutral interactions.

Also, having a minimum number of elements in the deceleration assembly is very advantageous. Aberrations or imperfections in the focal properties of the lens can arise from very slight imperfections in the construction and alignment of ion-optical components. Ellipsoidal aberrations, in particular, can be very pronounced in deceleration systems because of the strong retarding fields involved. In addition, when the deceleration occurs in a series of stages or involves several internal cross-over points, aberrations due to misalignment are compounded within the lens system. Therefore, it is best if a lens system can be devised that utilizes a minimum number of active elements.

IV. Ion Optical Modeling

The design process utilized the ion trajectory simulation program SIMION PC/PS2 to first model the typical high performance deceleration

lens systems of the exponential type currently in use for ion beam instruments. They were evaluated with respect to their basic ion-optical properties and suitability for our specific application. The next step was to gain a more fundamental understanding of ion deceleration by modeling a simple, two-electrode deceleration lens. The final design of our deceleration system evolved from this simple model.

A. The "Over-Focusing" Effect

The difficulties associated with producing a highly collimated low energy ion beam from a high energy beam have been discussed in an early monograph by Hasted [18]. When the kinetic energy of an ion beam is reduced to less than about 5% of its original value in a lens system, the resulting beam will be highly divergent. That is to say the lens exhibits an extremely short focal length.

An illustrative example of this effect is found in Figure 3.3. This figure shows the cylindrically symmetric SIMION model of a two-element tube-type deceleration lens with left electrode at ground potential (0 V) and the right electrode at 2990 V. Equipotential contour lines are plotted along with trajectories for a group of paraxial ions entering the lens with an initial kinetic energy of 3000 eV (principal ion motion is from left to right). The ions are decelerated by the retarding field to a final energy of 10 eV, a 99.7% decrease in energy.

As shown in Figure 3.3, The ions enter the lens gap with trajectories parallel to the central axis, but diverge wildly after traversing the decelerating field. The region of minimum beam diameter is not characterized by a global axis cross-over (global focal point). Rather, the

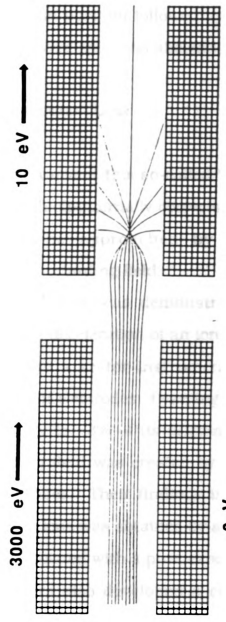

Figure 3.3. Overfocusing effect in two-element deceleration lens.

ion trajectories cross over the center axis over a fairly broad region and then diverge greatly. In fact, the outermost ions which entered the lens system closest to the electrode have a final divergence half-angle approaching 90° (i.e. final trajectories are perpendicular to the desired direction of motion)! This display of focal points which are strongly dependent on initial beam position followed by high angular divergence may be categorized as severe spherical aberration.

B. Exponential Deceleration Lens

One approach to circumvent this so-called "over-focusing effect" is to create a potential field which internally corrects for the short focal length. This correction may be approached by implementation of an exponentially-decreasing retarding field.

An early exponential lens was demonstrated by Gustafsson and Lindholm in 1958 for the deceleration of an ion beam of 2000 or 3000 eV in energy emerging from a sector instrument [19]. The lens design consisted of a series of slit electrodes of varying thickness designed to the attenuate the ion energy to ~3% of its original value. A semi-empirical exponentially-decreasing field was created by applying the appropriate potentials to the electrodes. Their findings indicated that much more efficient operation of the lens was obtained by significantly deviating from electrode potentials associated with a pure exponential field.

Futrell and coworkers also developed a crossed ion beam/neutral beam instrument that utilizes a high performance deceleration lens [15]. The lens was designed to produce a pure, axially-symmetric exponentially-decaying field. This sophisticated device required a stack of

more than 40 separate electrodes with 12.5 mm ID circular apertures. A complex resistor divider network was utilized to develop the necessary exponentially-decaying voltages on the electrodes. Futrell and coworkers reported excellent performance of the lens when decelerating a 0.5 mm diameter beam of 750 eV ions down to the 0.2 to 10 eV range. Transmission of very low energy ions in this system was reported to approach the theoretical space-charge limit. This particular design has gained considerable acceptance as the standard in attenuating the energy of ion beams by two or more orders of magnitude [20-22]. More recently, an exponential retarding field deceleration lens was used by Kofel and McMahon [11] to transfer an ion beam from an external high pressure source into a Fourier transform ion cyclotron resonance mass spectrometer.

B.1. Theory

For an axially symmetric exponentially-decaying decelerating field, if the major axis of motion is in the positive x direction, the electric potential, U, along the central axis, should be of the form

$$U(x) = -\alpha U_0 e^{-\beta x} \qquad (3.1)$$

In this expression, U_0 is the ion stopping potential of the ions entering the deceleration field (assuming $U_1 = 0$). The constants α and β may be empirical or derived from solutions that satisfy Laplace's equation. Equation 3.1 also represents one of the few potential distributions that is amenable to ion trajectory calculations by direct

integration using the paraxial ray expression. In order to calculate ion trajectories in fields that differ from theoretical exponential potential distributions, we have implemented the ion-optical simulation program SIMION PC/PS2. This modeling approach also allows the calculation of ion trajectories through lens systems with realistic electrode geometries.

To a first approximation the electric field between two parallel plates with circular apertures (a single lens gap) is linear. Therefore, creating a smooth exponential field requires a large assembly of electrodes with exponentially-decreasing voltages applied to successive elements.

B.2. Gustafsson and Lindholm Exponential Lens

A SIMION model of the semi-empirical exponential lens of Gustafsson and Lindholm is shown in Figure 3.4. The ten-element lens is designed to decelerate 2000 eV ions emerging from the exit slit of the sector instrument represented on the left-hand side of the figure. The ions are decelerated to a final energy of 30 eV as they enter the collision region represented on the right-hand side of the figure. The system is modeled with semi-empirical exponential electrode potentials as described in the reference. Potentials on the second and third electrodes are slightly lower than those required to form a pure exponentially-decaying field. This results in some focusing action in regions of the lens where the decelerating field is the strongest. As shown from the ion trajectories of Figure 3.4, the lens produces a smooth beam cross-over after traversing approximately one-third of the lens system. Ion angular divergence is also very low after the focal point. However, it can be seen that only those ions with initial trajectories which begin very near the central axis of the lens are successful at entering the collision region.

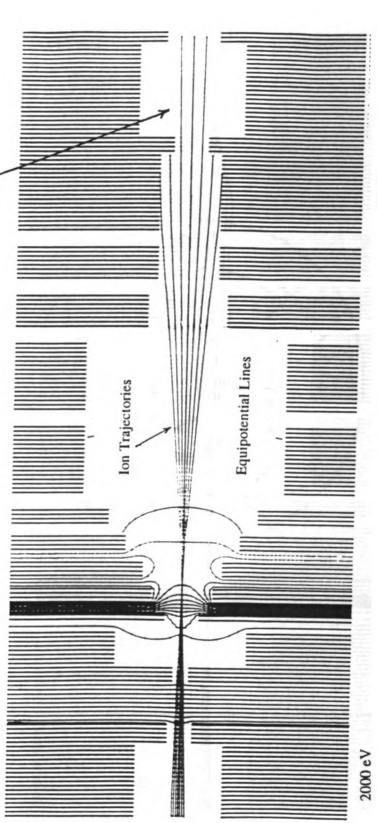

Figure 3.4. Simion model of Gustaffson semi-exponential deceleration lens with literature electrode potentials.

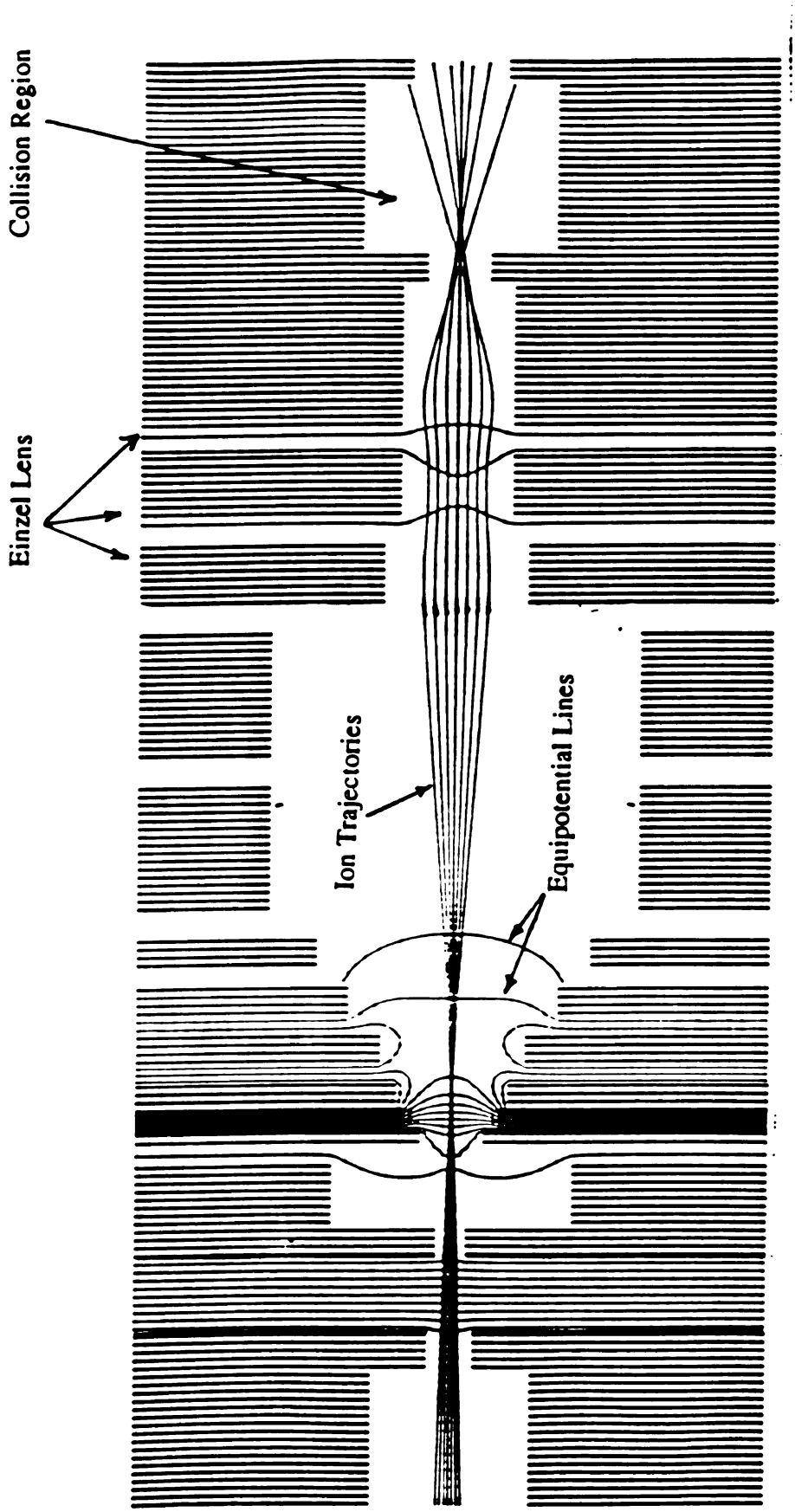

Figure 3.5. Simion model of Gustaffson semi-exponential deceleration lens with einzel focusing.

The lens of Figure 3.4 exhibits a transmission efficiency of ~50% for the trajectories modeled. Ideally, a lens system should provide 100% transmission. An attempt was made to improve the number of ions that can be decelerated and injected into the collision region by using the final three electrodes of the deceleration assembly as an einzel lens. Figure 3.5 shows the SIMION model of the Gustafsson and Lindholm deceleration lens with the additional einzel focusing near the exit of the assembly. The potential on the second-to-last electrode is higher than electrodes on either side of it, thereby forming a decelerate/accelerate einzel lens. The effect of this einzel focusing significantly enhances the transmission of decelerated ions into the collision region. This example also supports the conclusion of Gustaffson and Lindholm that the performance of an exponential ion deceleration lens may be improved by deviating from a pure exponentially-decaying field.

B.3. Futrell Exponential Deceleration Lens

The next modeling study explored an ion deceleration lens that employed a pure, axially symmetric exponentially-decaying field. This lens was implemented by Futrell and coworkers [15] to decelerate a beam of 750 eV ions to ~1.2 eV. The electrode assembly consists of 42 parallel plates with circular apertures equally spaced over a distance of 22 cm. Since the principal direction of motion is in the positive x-dimension, the electrode potentials were calculated from the following exponential-decay expression.

$$U(x) = U_0 - \alpha U_0 e^{-\beta x}$$

The constants α and β were calculated using the method described by Futrell et al. which allows the exponential field to have a fixed focal length for a given final energy. If the first focus is to occur at a specific position along the x coordinate, x', the constant β may be calculated from the relationship:

$$\beta = \frac{4\pi}{x' \sqrt{3}}$$

For our model, a focal plane is desired 1.63 cm beyond the last electrode of the deceleration lens. This provides a first focus at a position corresponding to the entrance of the collision region. Therefore, x' = 23.63 cm if the entrance electrode is considered to be the located at the origin (x=0) and β is calculated as $0.307/cm^{-1}$. The constant α is normally taken as unity.

The final expression for the axial electric potential, in units of volts, for the deceleration of 750 eV ions to 1.2 eV is given as

$$U(x,cm) = 750 - 750 \exp[-(0.307/cm^{-1})x]$$

From the above expression, the potential for each electrode was calculated. A plot of the electrode potential as a function of the x-axis displacement is found in Figure 3.6. The points on the graph correspond to the calculated electrode potentials. As can be seen from the curve, the electric potential asymptotically approaches, but does not attain, 750 eV.

Figure 3.7 shows the cylindrically symmetric SIMION model of the 42-element deceleration lens preceding a DC-biased collision region. The

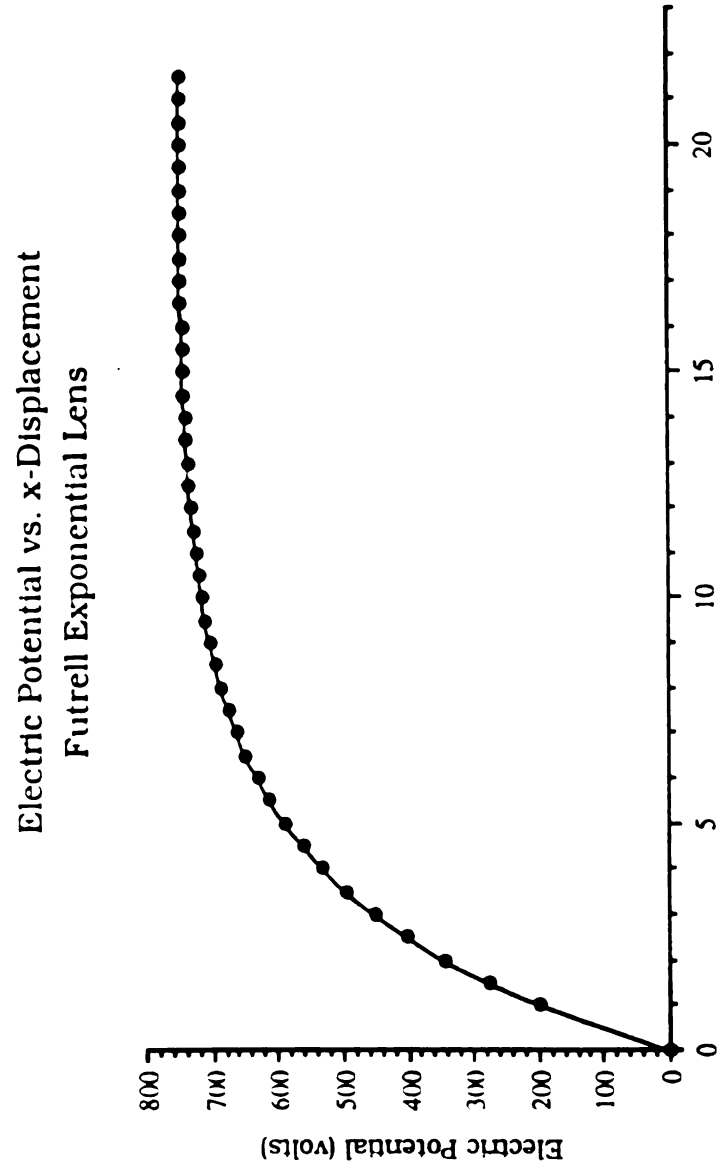

Figure 3.6. Exponential potential distribution

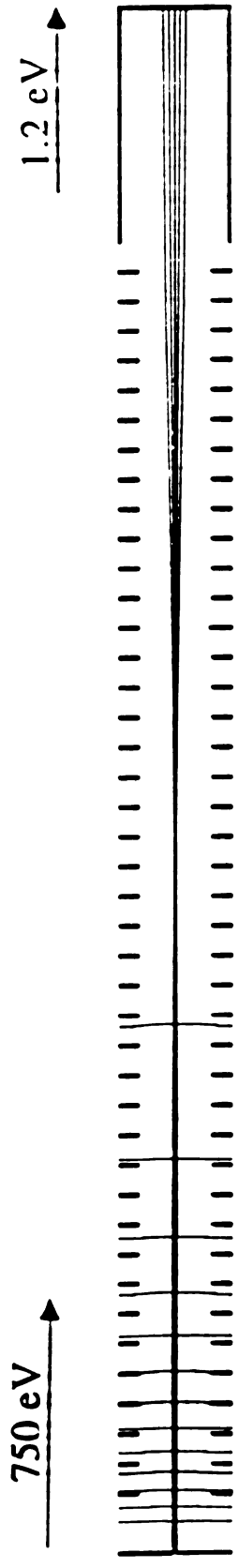

Figure 3.7. Simion model of Futrell 42 element exponential deceleration lens.

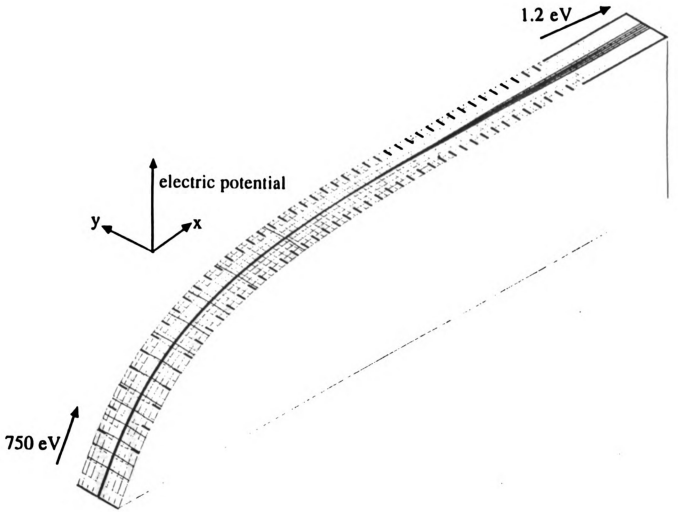

Figure 3.8. Potential surface of Futrell 42-element exponential deceleration lens.

model represents a stack of electrodes electrodes equally spaced over a distance of 22 cm along the x-dimension. Electrode aperture diameters correspond to 12.5 mm. The exponential lens is terminated with a collision region 37 mm long with an inner diameter of 17 mm. The collision cell potential is held common to the potential on the last element of the deceleration lens. Equipotential contour lines are plotted in 50 V increments. Trajectories are calculated for ions corresponding to a 0.5 mm diameter paraxial beam having an initial kinetic energy of 750 eV, as characterized in the article by Futrell et al [15].

A more conceptual presentation of the lens system is shown in Figure 3.8. In this SIMION model, the electrodes are plotted in the x- and the y-dimensions, and the electric potential is plotted in the z-(relief) dimension. This view clearly shows the exponentially-decaying profile of the decelerating field in the x-z plane.

As the ions travel (from left to right) through the lens system, a nominal beam cross-over occurs about midway through the deceleration assembly. After the focal point, the ions proceed towards the collision region with a divergence half-angle of approximately 1°. The final ion kinetic energy is 1.2 eV which represents a 99.8% reduction in translational energy.

These modeling studies of the Futrell lens demonstrate that, indeed, a low-energy highly-collimated ion beam may be generated with a pure exponentially-decaying deceleration field. But many questions regarding ion deceleration remain unanswered. What qualities of the exponential lens enable high performance? Also, are these properties unique to pure, axially symmetric exponentially-decaying fields?

B.4. 3000 eV to 30 eV Exponential Deceleration Lens

Since our interest is directed towards gaining a fundamental understanding of ion deceleration, further modeling studies were performed on exponential deceleration lenses. A primary exponential deceleration lens model was developed with respect to our particular application. This model was critically analyzed in order to uncover the underlying lens qualities that provide high performance operation.

A SIMION model of an exponential lens designed to decelerate an ion beam with an initial energy of 3000 eV to a final energy of 30 eV was developed. The cylindrically symmetric model consists of 40 individual electrodes, each with an aperture diameter corresponding to 16 mm and equally spaced over a distance of 20 cm. The deceleration lens is followed by a collision cell with an 8 mm diameter opening. The end of the collision cell and the deceleration entrance lens are terminated with a thin element simulating a grid. This was done to establish boundary conditions which reduce calculation time during potential array refinement, and to provide more uniform fields.

By following the method of discussed by Futrell et al, [15], the potentials for all electrodes in the deceleration lens were calculated from the equation given below with a=1 and b=0.363/cm-1 to theoretically yield a first focus at the entrance of the collision cell.

$$U(x,cm) = 2970 - 2970 \exp[-(0.363/cm^{-1})x]$$

The final ion stopping potential applied is 2970 V since the entrance

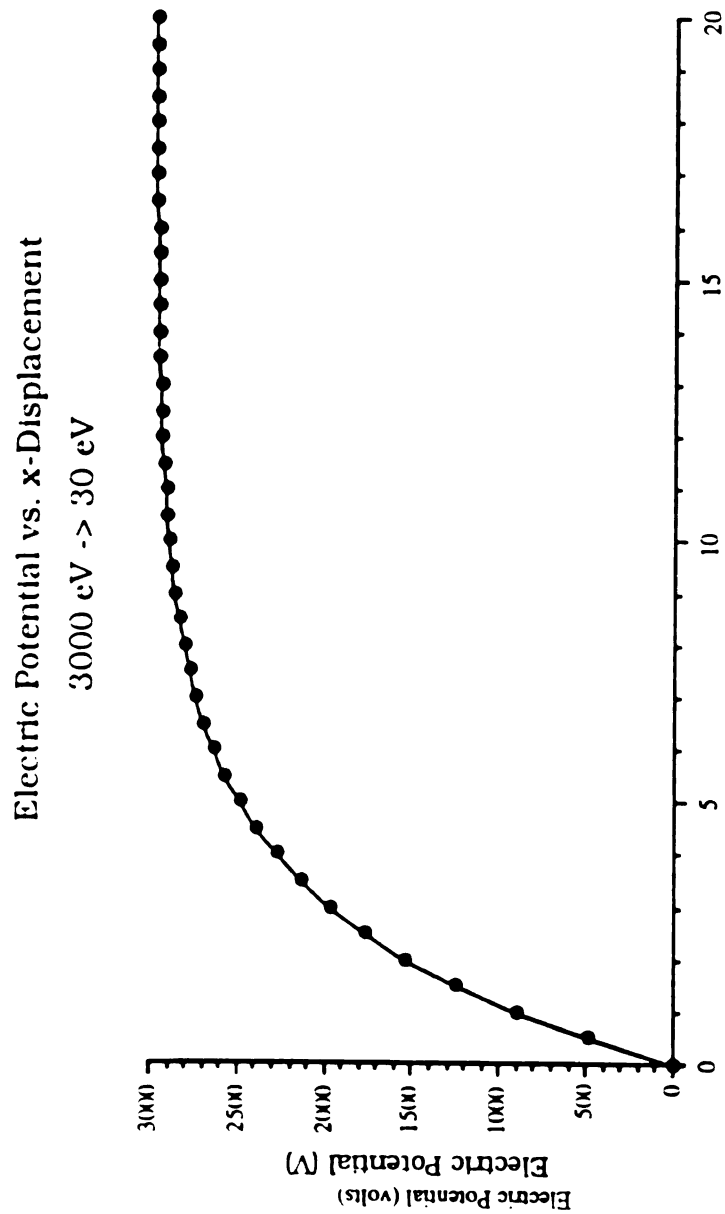

Figure 3.9. Exponential potential distribution.

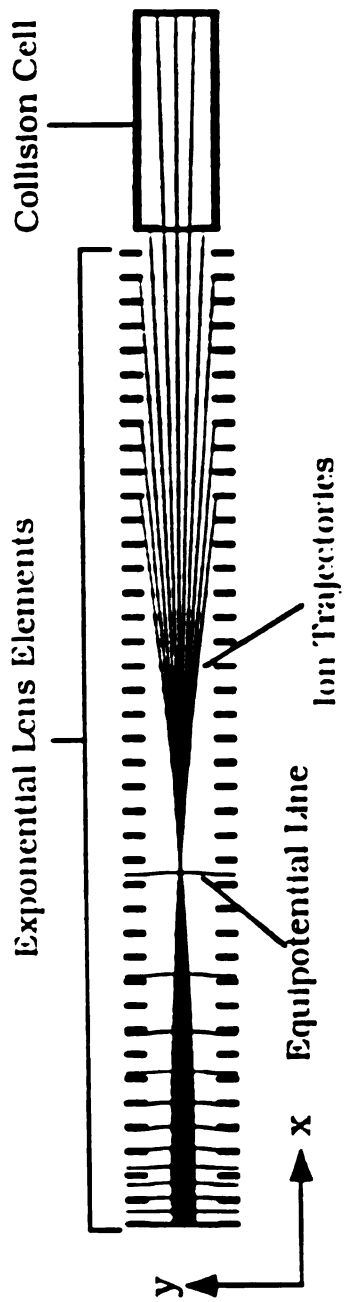

Figure 3.10. 40-element exponential deceleration lens.

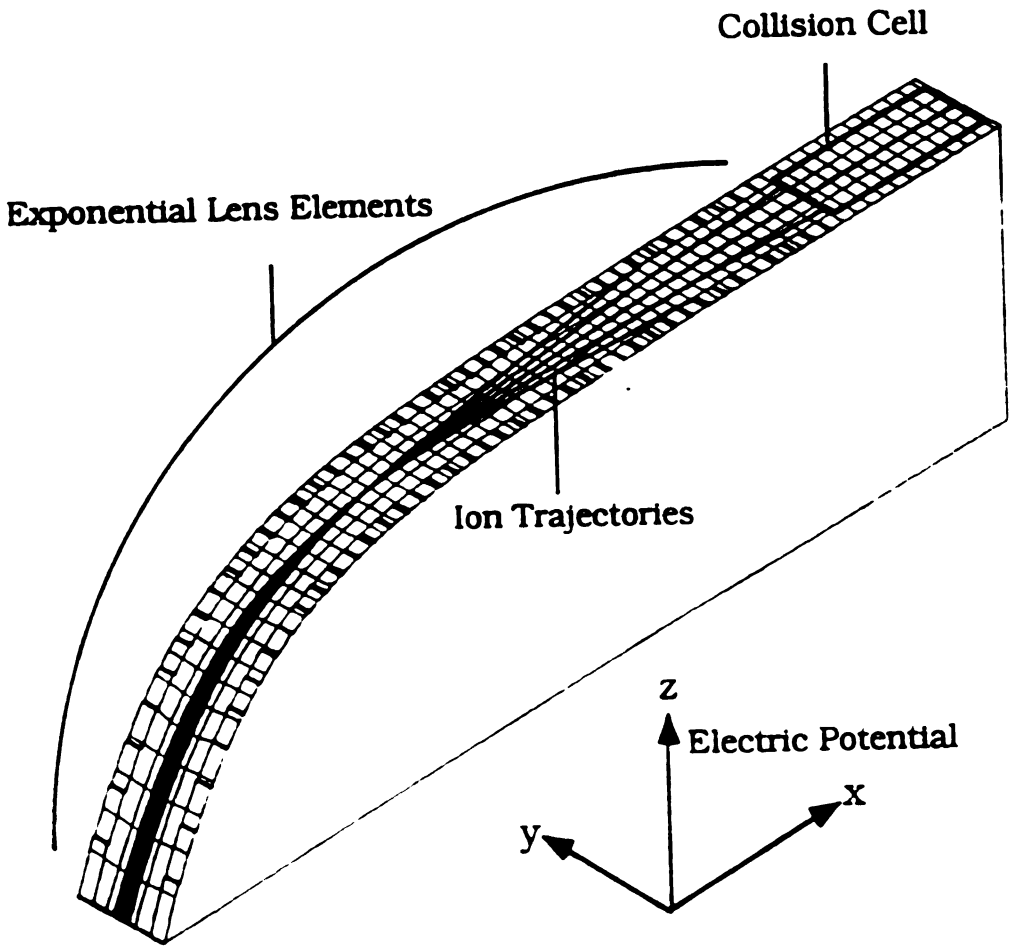

Figure 3.11. 40-element exponential deceleration lens potential surface.

aperture of the decelerating field is assigned a potential of zero volts. The electric potential of the exponential field asymptotically approaches 2970 volts. This electric potential distribution is plotted in Figure 3.9.

In the SIMION model found in Figure 3.10, the DC-bias of the collision cell is 2970 volts, which results in the ion beam being reduced in energy to a final value of 30 eV. Equipotential contour lines are shown for 250 volt increments. Figure 3.11 displays a three-dimensional view of the exponential model with the electric potential plotted in the z-(relief) dimension. In this view the smooth exponentially-decreasing field is clearly displayed.

Ions emerging from a plane source provide a useful test for determining the fundamental ion optical properties of the lens. Representative ion trajectories are plotted for an monochromatic ion beam having an initial energy of 3000 eV, a divergence half-angle of 0° (paraxial), and an initial cross-section of 5 mm and 4 mm in Figure 10 and Figure11, respectively. The exponential field produces a beam cross-over about one-third of the distance through the lens. After this cross-over the beam diverges with a half-angle of approximately 2°. Although the final angular divergence is quite low, because of the short focal length of the lens, only those ions with initial trajectories which begin very near the central axis enter the collision region.

Close examination of the equipotential contours in Figure 3.10 and of the potential surface in 3.11 reveal the electric field characteristics which result in the inherently short focal length. Near the central axis of the lens, the equipotential lines exhibit very little curvature in contrast to regions in space very near the lens electrodes. Under high magnification, the three-dimensional plot reveals a concave or trough-like topography of

the potential surface for the majority of the axial dimension of the lens. With the exception of the lens entrance region (first one or two electrodes), the potential surface concavity is most pronounced in regions of high potential gradient (dU/dx) along the longitudinal direction. This curvature is thus most distinct in the steepest regions of the retarding potential hill, which occurs within the first ten electrodes for this model. Also, the degree of curvature (dU/dy) increases as y approaches the edge of the electrode. This causes ions (with initial trajectories removed from the central axis) to be forced in the y-dimension to produce an early cross-over approximately midway through the lens at an energy of ~200 eV.

Since dU/dy increases with increasing y values, ions experience very little force in the y-direction if the initial beam diameter, D_b, is quite small relative to the lens aperture diameter, D_a. The relative ratio (D_a:D_b) for the model shown in Figure 3.10 is 7.2:1 . Successful trajectories (ions which pass through the 8 mm aperture and enter the collision cell) are found only for ions corresponding to a D_a:D_b ratio of 15:1 or greater. Other trajectory calculations show that the focal properties of the exponential lens are very sensitive to D_a:D_b. In fact, as this ratio is decreased, the nominal beam crossover point moves to lower x values and the angular divergence of the decelerated ion beam increases.

Ion transmission in the exponential lens may actually be improved by having a *non-paraxial* initial beam. Increasing the angular divergence of the incoming beam can compensate for the inherently short focal length. For the model shown, an ion beam with an initial divergence half-angle of 4-5° reduces the D_a:D_b ratio in which successful trajectories may be

found (increase in lens acceptance area).

The SIMION model reveals that reasonable transmission and low angular divergence may be obtained for a low energy ion beam when it is decelerated in an axially symmetric exponentially-decaying field under certain geometrical constraints which provides a D_a:D_b ratio of at least 15:1. In fact, further studies suggest that *the successful performance of the exponential lens design is more dependent on the D_a:D_b ratio than on the exponential nature of the decelerating field.* Therefore, the excellent operation of the lens design of Futrell et al. [15] may be attributed to the small initial beam diameter (0.5 mm) relative to the electrode aperture diameter (12.5 mm): here D_a:D_b has a value of 25:1. Since the initial beam diameter for our application is approximately 4 mm, an exponential deceleration lens would require a lens aperture diameter of at least 60 mm (D_a:D_b > 15:1) to maintain high transmission and low angular divergence. If a 60 mm diameter exponential lens precedes an ion-optical element with an entrance diameter of 17 mm, as in our instrument, the deceleration field would be dominated by the potential on the small diameter element penetrating into the region of large open area.

Also, an exponential lens has focal properties which are dependent on the final energy of the beam. The inflexibility of a purely exponential field would place limitations on the final beam characteristics when the experiment requires that ions be decelerated to a range of final energies.

C. Fundamental Studies:

1. A Simple, Two-Element Deceleration Lens

After modeling ion behavior in an exponential deceleration system, the ion optical properties of the other extreme approach, a simple two-

element deceleration lens, were investigated. Figure 3.12 shows the SIMION model for a lens consisting of two parallel plates with circular apertures having a diameter of 15 mm and a separation distance of 4 mm. The extreme boundaries of the potential array were set at the potential of the nearest element to minimize calculation time and provide a more accurate field, as in the exponential model.

Ion trajectories simulating the deceleration of a 3000 eV ion beam from a 5 mm diameter planar source having a 0° divergence half-angle are plotted in Figure 3.12 With a final kinetic energy of 10 eV the system yields an ion beam with a nominal divergence half-angle exceeding 25°. This lens may be characterized as having severe spherical aberrations.

The three-dimensional view of the simple lens potential surface shown in Figure 3.13 provides a powerful conceptual model for understanding the ion optical properties of this deceleration system. This model provides an enhanced view of the similar potential surface features discussed in the exponential lens section. As ions with initial trajectories non-coincident with the center axis approach the lens gap the convex nature of the surface (dU/dy) exerts an outward (radial) force in the y-dimension. This results in increasing divergence of the beam as it moves up the retarding hill in the first half of the lens assembly. The beam broadening from this effect is minimal due to the relatively high velocity of the ions in this region. Approximately half-way through the lens gap the potential surface attains a concave or trough-like structure. Thus ions in the outer part of the beam experience an inward force as they traverse this region of the lens.

Having been attenuated in energy by the retarding field, the ions move at relatively low velocity through the second half of lens, the exit channel.

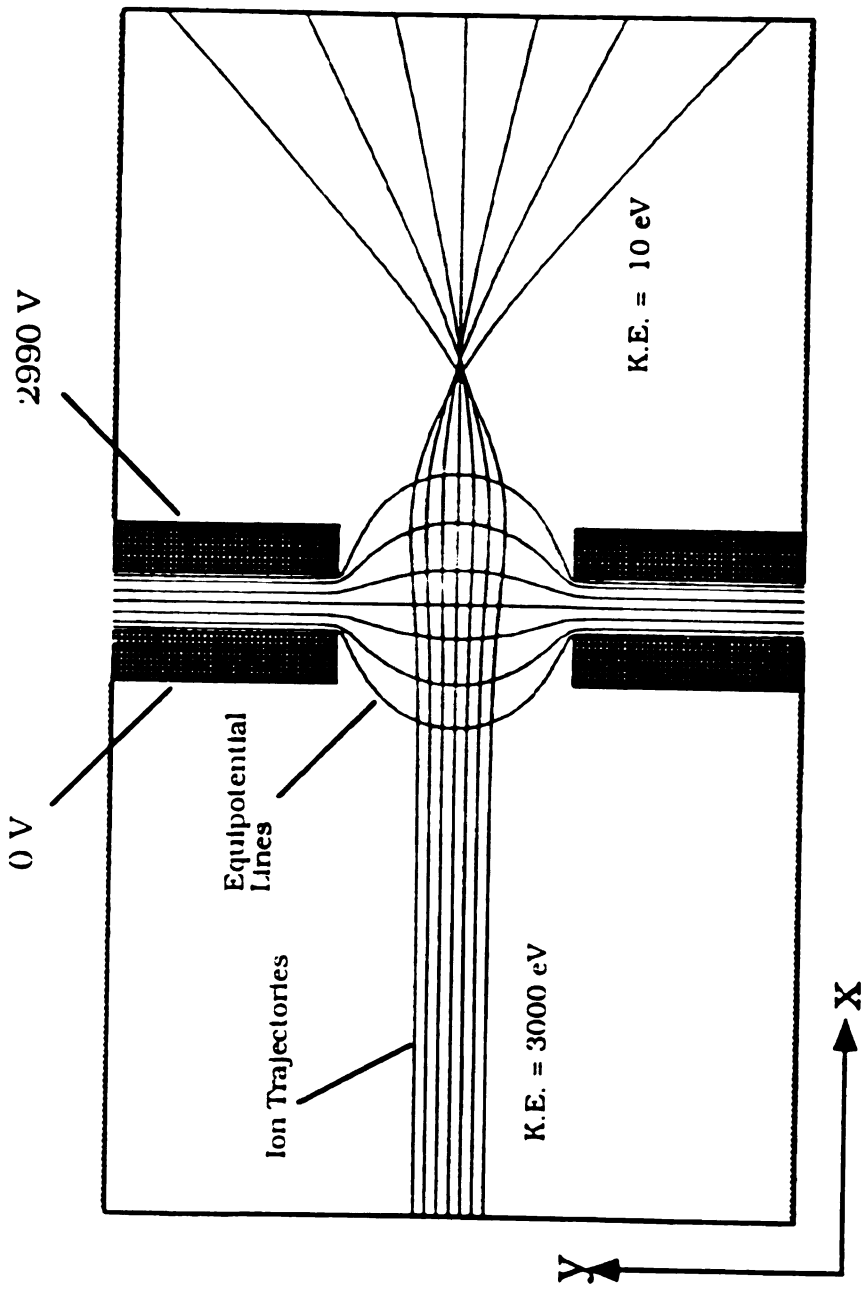

Figure 3.12. Simple two-element deceleration lens.

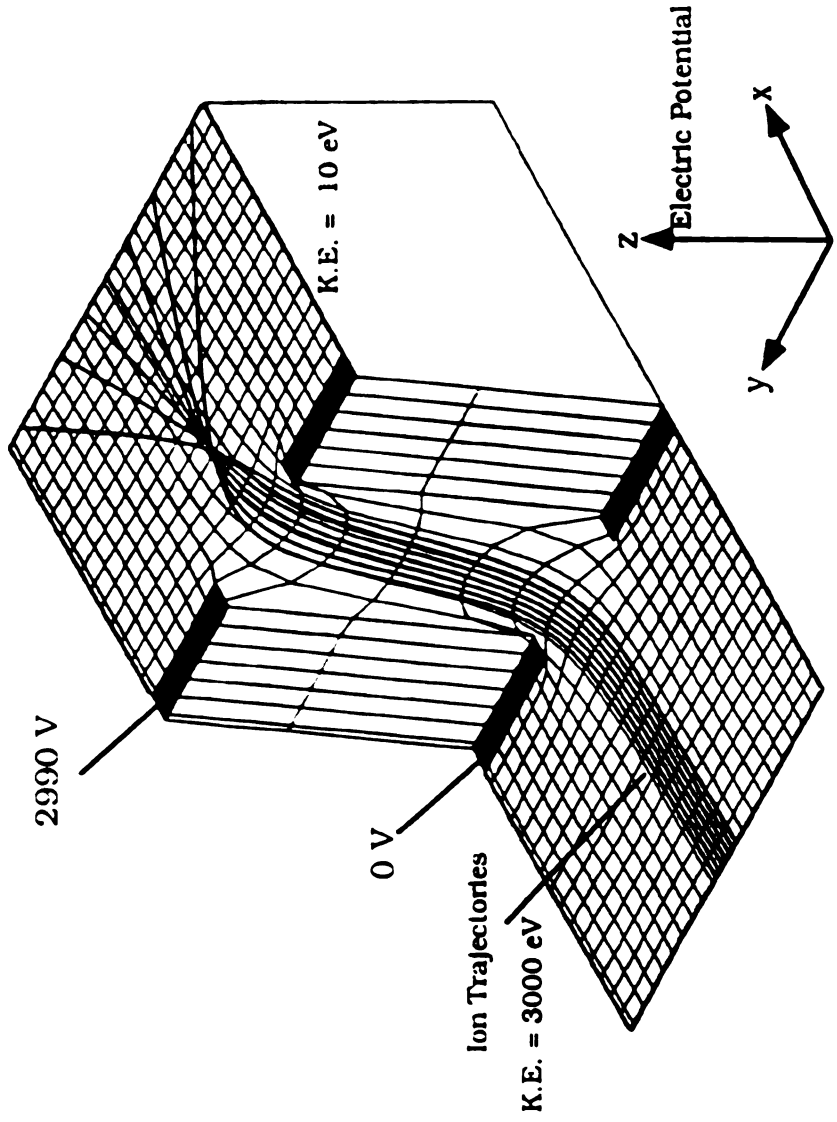

Figure 3.13. Potential surface for simple, two-element deceleration lens.

with reduced longitudinal velocity, the inward radial force dominates the forward momentum resulting in a sharp cross-over and a highly divergent ion beam after deceleration. This over-focusing effect, a severe spherical aberration, is an inherent property of both simple and complex deceleration systems and *is more pronounced as the ion beam diameter approaches the element aperture dimensions.*.

C.2 Einzel Focusing Followed by Deceleration

From SIMION modeling of the exponential and two-element deceleration systems it was noted for both cases that angular divergence is minimized when trajectories are restrained to regions near the central axis of the electrode assembly. This may be accomplished by having a relatively high D_a:D_b ratio as in the exponential design of Futrell and coworkers. Alternatively, we have proposed the use of an einzel focusing lens preceding the decelerating field of a simple decelerating lens of moderate aperture diameter. The einzel lens is used to focus ions prior to the deceleration stage, effectively decreasing the diameter of the ion beam at the deceleration stage of the lens.

A SIMION model for a simple deceleration lens which included a 15 mm ID einzel focusing stage preceding the deceleration stage was developed. In this system, the decelerating field is established by applying the desired decelerating potential to a single tube-type injection electrode terminated with a circular plate. The 15 mm ID injection electrode is adjacent to two other entrance electrodes of slightly larger diameter which are normally held at ground potential. The injection element is used to decelerate and, for our experiment, transfer the ions

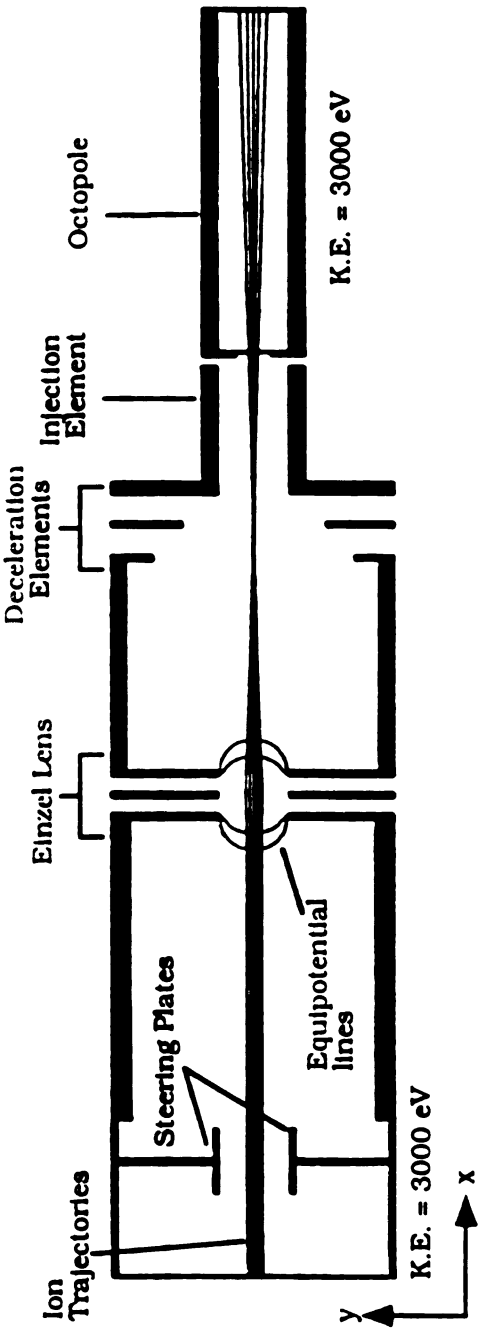

Figure 3.14. Simion model of three stage deceleration lens with only einzel focusing stage in operation.

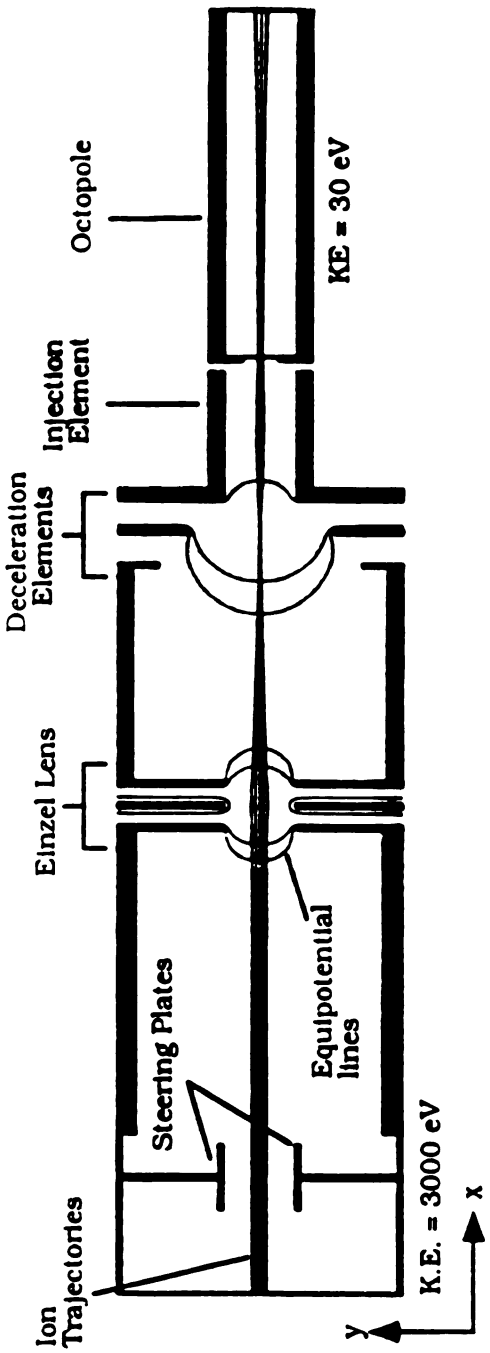

Figure 3.15. Simion model of three stage deceleration lens with deceleration stage and einzel focusing stage in operation.

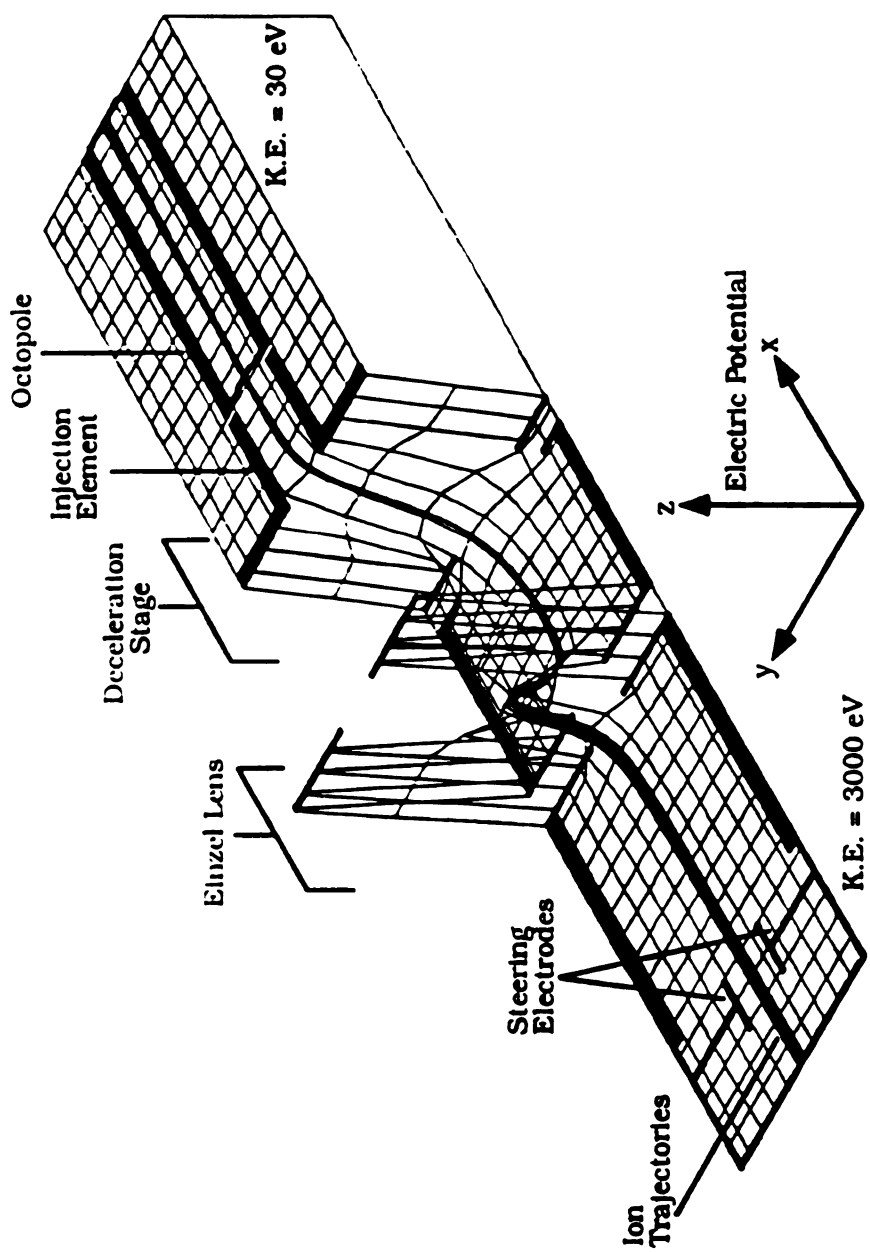

Figure 3.16. Potential surface of three-stage deceleration lens with einzel focusing stage and deceleration stage in operation.

into the octopole collision region which has an entrance aperture of 8 mm. For the modelling with DC potentials only, the octopole region is biased with same potential as the injection electrode of the deceleration stage. The full design also includes horizontal and vertical deflection fields for alignment of the high energy ion beam with the einzel focusing and deceleration stages.

Figure 3.14 shows the SIMION model of the system with only the einzel focusing stage in operation. The horizontal aligning plates, as well as the deceleration injection and octopole collision region electrodes, are held at ground potential. The einzel lens is operated in the decelerate-accelerate mode with a center element potential of 4300 V. The trajectories plotted in Figure 3.14 were calculated for 3000 eV ions characteristic of our sector instrument (4 mm diameter, divergence half-angle < 0.25^{o}) which results in a nominal beam cross-over midway through the decelerating stage. The einzel focusing causes the 4 mm initial beam diameter to be reduced to less than 1 mm near the beam cross-over. This maintains a *very small beam profile as ions traverse the most critical high-field region of the retarding stage.*

The combination of einzel lens focusing preceding a simple deceleration stage is modeled in Figure 3.15. The simulated trajectories for 3000 eV ions characteristic of our sector instrument, decelerated to final energy of 30 eV, are plotted. The only active electrodes in the assembly are the center element of the einzel lens (4300 V), the final injection element of the deceleration lens (2970 V), and the octopole collision region (2970 V). The potential surface view of this model, displayed in Figure 3.16, reveals the saddle-type topology of the einzel lens which focuses the high energy ion beam into the deceleration zone.

As clearly shown in Figures 3.15 and 3.16, the focusing stage reduces radial excursions of the ions as they pass through the convex surface of the exit channel. This enables ions to avoid regions of the deceleration potential surface having high radial fields (dU/dy). Thus, the ion trajectories favor the formation of a highly collimated, low energy beam. The ion beam, having a kinetic energy of 30 eV, exhibits a divergence half-angle of less than 3° at the entrance to the octopole beam guide region. In this system, low angular divergence is achieved with only 2 active elements in the lens assembly.

More than 20 different deceleration systems which involved the principle of einzel focusing preceding a deceleration stage were studied. Several different deceleration stage variations were modeled. Some lenses implemented a simple two-element deceleration gap. Some models involved creating a linear deceleration field with a series of 3 to 10 electrodes. Other models also included some focusing electrodes within the deceleration stage. This is similar to the "zoom" type deceleration lens utilized by Cooks and coworkers [2]. However, for most models studied, the general lens performance was determined primarily by the relative ion beam diameter through the critical regions of the deceleration field. Thus, we decided to implement a simple deceleration lens in which the deceleration field is produced by a single lens gap.

V. Construction

The final SIMION model was translated into a working drawing for construction. For versatility and ease of mechanical alignment, the lens components were designed around a universal horizontal mount that

affixes to an ion optical rail as detailed in a previous chapter. The rail is housed in a differentially-pumped vacuum chamber that connects to the sector instrument with a 2.88 inch ID flexible bellows. A pneumatic gate valve is used to isolate this beam chamber, which is located 72 cm from the exit slit of the CH5-DF.

A cross-sectional schematic drawing of the axially symmetric lens assembly is shown in Figure 3.17. The design incorporates an einzel focusing stage followed by the deceleration stage integrated on a single 100 mm aluminum mount for permanent mechanical alignment. In addition, a separate 50 mm mount containing a set of horizontal and vertical deflection plates was made to align the incoming ion beam with the focusing and deceleration stages.

As in the final SIMION model, the einzel lens has an aperture diameter of 15 mm and a spacing of 4 mm between elements. All plate elements in the assembly are constructed from 0.8 mm thick stainless steel sheet. The deceleration stage consists of a series of one or two plates with increasingly smaller apertures separated by 5 mm ceramic spacers followed by a tube-type injection element which was machined from a single rod of stainless steel. The 15 mm inner diameter injection element is 28 mm long and protrudes through a wall in the vacuum chamber that separates the deceleration and octopole collision regions. This injection electrode geometry provides a minimal conductance path between the differentially-pumped chambers.

In addition, a 53 mm i.d. stainless steel tube with a wall thickness of 1.6 mm and a length of 42 mm is situated between the einzel lens stage and the deceleration stage. The tube is in held in physical and electrical contact with last element of the einzel lens and the first element of the

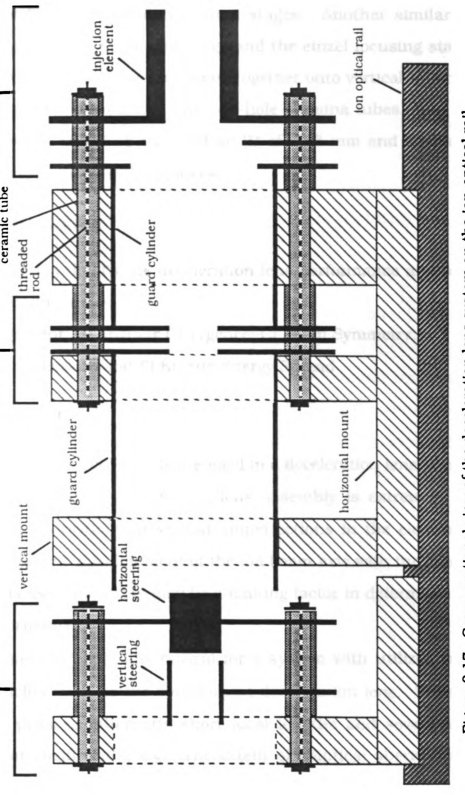

Figure 3.17. Cross-sectional view of the deceleration lens system on the ion-optical rail.

deceleration lens. This tube is used to guard against stray potentials as well as to maintain cylindrically symmetric fields in the regions between the einzel focusing and deceleration stages. Another similar tube is placed between the alignment stage and the einzel focusing stage. The entire electrode assembly is clamped together onto vertical mounts using 2-56 threaded rod insulated with one-hole alumina tubes. The alumina tubes have an OD of ~5 mm and an ID of ~2.5 mm and were obtained from Scientific Instrument Services.

VI. Characterization

This section details the deceleration lens performance and operation in the following areas:

A) Alignment; B) Angular Divergence; C) Beam Symmetry;

D) Transmission; and E) Kinetic Energy Spread

A. Alignment

When strong electric fields are used in a deceleration lens, mechanical alignment of the beam with the lens assembly is extremely crucial. Ellipsoidal aberrations arise from imperfections in the electrodes and from mechanical misalignment of the ion beam axis with the central axis of the lens assembly. This may be a limiting factor in determining overall lens performance.

Alignment is especially critical for a system with utilizes very high electric fields such as the two-element deceleration lens. These lenses typically possess inherently short focal lengths and severe spherical aberration coefficients, C_S. The extent of elliptical aberration due to

improper alignment of the beam and apertures has been quantitated by the relationship [23] expressed below.

$$C_e = C_s\left(\frac{\Delta e}{f}\right)^2$$

In this expression, C_e is the ellipsoidal aberration coefficient, f is the focal length, and Δe is the off-center displacement or mis-alignment. From the equation, it can be seen that when Δe is nonzero, a short focal length (as is the case for most deceleration lenses) highly exaggerates aberrations due to alignment imperfections.

We have performed ion optical modeling studies to determine the effect of mechanical imperfections and beam misalignment on decelerated beam properties such as angular divergence and focal position. Figure 3.18 shows an example deceleration lens model for decelerating 3000 eV ions to 10 eV prior to injection into a collision region. The nearly paraxial ion beam enters the lens assembly from the left-hand side of the figure. In this model, there is a slight misalignment of the guard cylinder with the ion-optical axis of the system. This causes asymmetry in a critical region of the decelerating field. The trajectories shown exhibit a focal position that is skewed with respect to the central axis of the system. These and other results suggest that the central axis of the incoming beam must be within $\leq$1 mm of the center of the deceleration assembly to minimize ellipsoidal aberrations.

Alignment of the deceleration assembly with the sector instrument to extremely close tolerances was facilitated by constructing a set of decelerations lens electrodes with 0.5 mm apertures. A He-Ne laser was

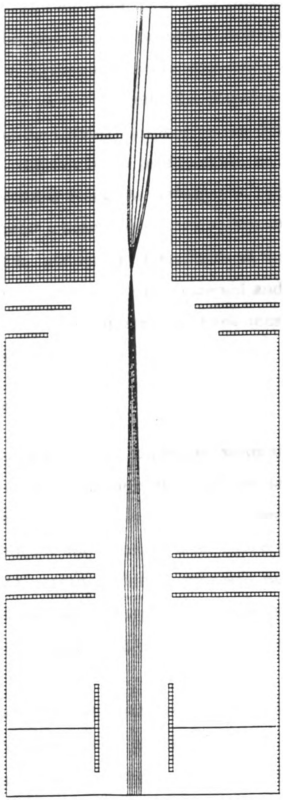

Figure 3.18. Simion model of deceleration lens exhibiting severe aberrations resulting from mechanical imperfections in the electrode assembly.

used to create an optical axis between the collision region and the exit slit of the CH5-DF. The ion optical rail was then adjusted to set the deceleration assembly co-axial with the optical axis of the laser.

During operation, further alignments were made with the horizontal and vertical deflection plates preceding the entrance of the deceleration system. By placing the CEMA/phosphor screen detector directly after the injection lens, the ion beam profile could be visualized. Exact alignment of the incoming beam was performed by applying a potential to the einzel lens to create a beam cross-over approximately 1 cm in front of the detector. In this manner the aberrations of the beam exiting the einzel lens could be visualized. The horizontal and vertical deflection plate potentials were then adjusted until the most symmetric beam profile was obtained.

B. Angular Divergence

The angular divergence of the ion beam exiting the deceleration lens was determined by measurement of the ion beam profile as depicted in Figure 3.19. The CEMA/phosphor screen combination for beam visualization includes a fine stainless steel screen positioned 2 mm in front of the CEMA entrance plate. This was normally held at the potential of the deceleration lens injection element, thereby shielding the beam from the high negative potential applied to the CEMA entrance plate (-1400 V).

The detector was first positioned on the ion optical rail immediately after the injection element of the deceleration lens. A video camera was used to record the ion beam profile of Ar^+, formed by EI in the source of

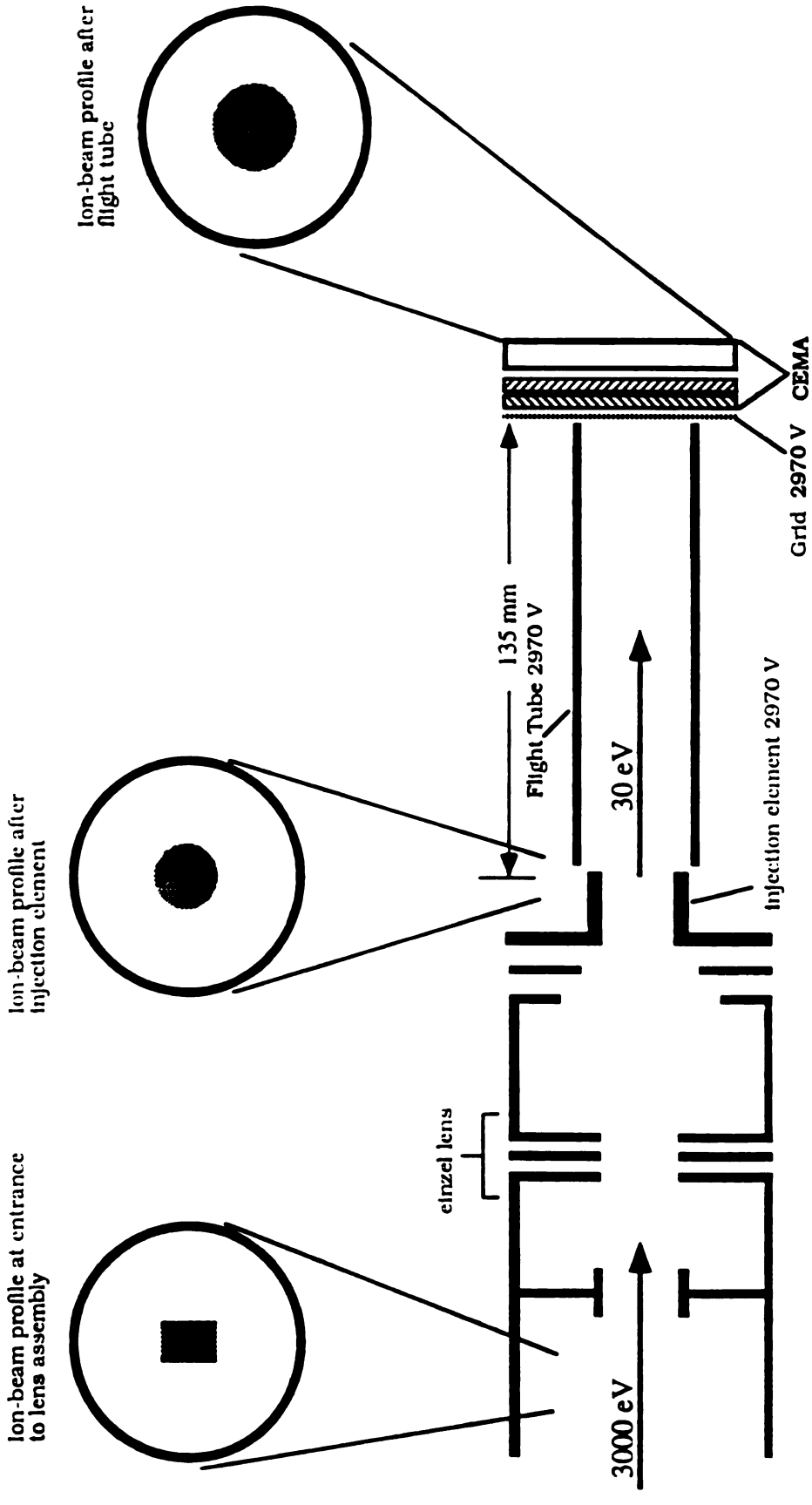

Figure 3.19. Experimental configuration for measuring the decelerated beam angular divergence.

the CH5-DF, as a function of both the final ion energy and the central einzel element potential. A second set of beam profiles were recorded by placing the CEMA at the end of a 135 mm long flight tube which was held at the potential of the injection element.

A resistive divider network originating from the source accelerating potential was used to supply the voltage to the injection element of the deceleration lens. The nominal final ion energy was taken as the difference between the potential applied to the source ionization housing and the potential applied to the injection element of the deceleration lens as measured with a floating digital voltmeter. This method of ion energy determination includes several sources of uncertainty in the true electric potentials such as surface charging, space charging and contact potentials from the junction of dissimilar metals. Most significantly, the potential applied to the source ionization housing may not accurately reflect the electric potential in space where ionization occurs. Because of the ion source extraction field, the electric potential at which the ions are formed may be as much as several volts lower than the potential applied to the source. Thus, the nominal final ion energy represents an *upper limit* of the true kinetic energy. Further discussion of ion beam energy considerations follows. A recent article provides a quantitative study on the effect of source operating parameters reflected in ion translational energy measurements [24].

As predicted by the SIMION model, the optimal potential applied to the einzel lens for minimum angular divergence was dependent on the final ion energy selected. It was found, however, that a static einzel lens potential of 5 kV provided excellent focusing for final ion energies in the 10-140 eV range. With an initial beam energy of 3000 V the decelerated

beam divergence half-angle was less than 5° in this energy range. This suggests that the beam energy may be selected with control of only the potential applied to the injection element of the deceleration lens. When the einzel lens potential was optimized for various final energies, the decelerated beam divergence half-angle was less than 2° for ion energies between 30 and 300 eV, and less than 5° for ion energies between below 30 eV.

It was observed that the vertical and horizontal position of the decelerated beam varied with the potential applied to the deceleration injection element. For example, as the final ion energy was scanned from 100 to 30 eV, the beam image on the CEMA would exhibit a lateral shift in position of ~2 mm. This type of behavior has been modeled with SIMION as shown in Figure 3.18. The extent of this energy-dependent displacement was dependent on the potentials applied to the horizontal and vertical steering electrodes. This beam displacement is indicative of mechanical imperfections and beam misalignment. In fact, the extent of image displacement, Δy, as a function of relative lens potential, ΔV, is directly proportional the relative beam misalignment, Δe, as found in the expression below [23]

$$\Delta y \alpha \Delta e(\Delta V/V)$$

C. Beam Symmetry

One significant aspect of the deceleration lens performance is the conversion of the beam from the rectangular slit profile to a circular cross-section as displayed in Figure 3.19. Due to the circular apertures, the high electric field in the deceleration zone is cylindrically symmetric.

This forces the rectangular beam into an axially symmetric potential well, thereby converting the beam to the desired circular cross-section. This effect, to the best of our knowledge, has not been previously discussed in the literature. Beam symmetry conversions such as this normally require the implementation of complex ion-optical components such as DC quadrupole lenses.

The ability to change the ion beam profile from rectangular to circular with just the plate-type electrodes further reduces the complexity of our deceleration assembly in comparison to previous lens designs. The deceleration lens employed by Cooks and coworkers [2] consisted of a two-stage dual "zoom" deceleration lens system for energy retardation with an intermediate DC quadrupole singlet lens for beam shaping. Armentrout and coworkers also employ DC quadrupole lens pairs for ion beam shaping prior to injection into an exponential lens assembly [21,22].

D. Transmission

Ideally, one would like to obtain absolute values of ion transmission through the deceleration lens. In concept, the measurement is easily performed by placing a Faraday plate in front of and immediately following the lens to record ion current. However there are numerous experimental difficulties in such a procedure. Measurement of high energy (keV range) beams with faraday plates is often complicated by ion/surface interactions, which result in ion or electron sputtering. The detection efficiency of faraday plates is also dependent on the geometry and materials of construction. Also, a means of moving the faraday plate

into and out of the beam path while maintaining vacuum is required. Furthermore it is difficult to measure ion beam intensities below 10^{-12} amps with conventional faraday plate/electrometer systems. Ion beam currents from our sector instruments are typically less than 10^{-13} amps.

Therefore, transmission measurements of the ion beam through our deceleration lens were performed using a single, continuous dynode electron multiplier placed immediately after the final injection element. Two high transmission stainless steel grids were situated in front of the detector. The grid nearest the deceleration lens was held at the injection lens potential and the second grid was held at ground. This minimizes penetration of the detector potential (-2900 V) into the deceleration region.

The intensity of a 3000 eV Ar^+ beam entering the deceleration lens was measured by setting the einzel lens and injection lens at ground potential and trimming the horizontal and vertical fields for maximum signal. Potentials were then applied to the einzel lens and deceleration lens injection electrode while again adjusting the horizontal and vertical deflection elements to achieve the maximum signal.

When the einzel lens potential is optimized for a final nominal beam energy of ~5 eV, approximately 90% transmission of the incoming beam is achieved. Figure 3.20 shows the relative ion intensity (a value of 1.0 equals the decelerated signal maximum) plotted as a function of the nominal final beam energy. This was obtained by scanning the potential of the injection element of the deceleration lens while the potential applied to the einzel lens was held constant at 4860 V. This results in a sharp local intensity maximum centered around 5 eV and approximately 50% attenuation of the beam for final energies up to ~130 eV. The

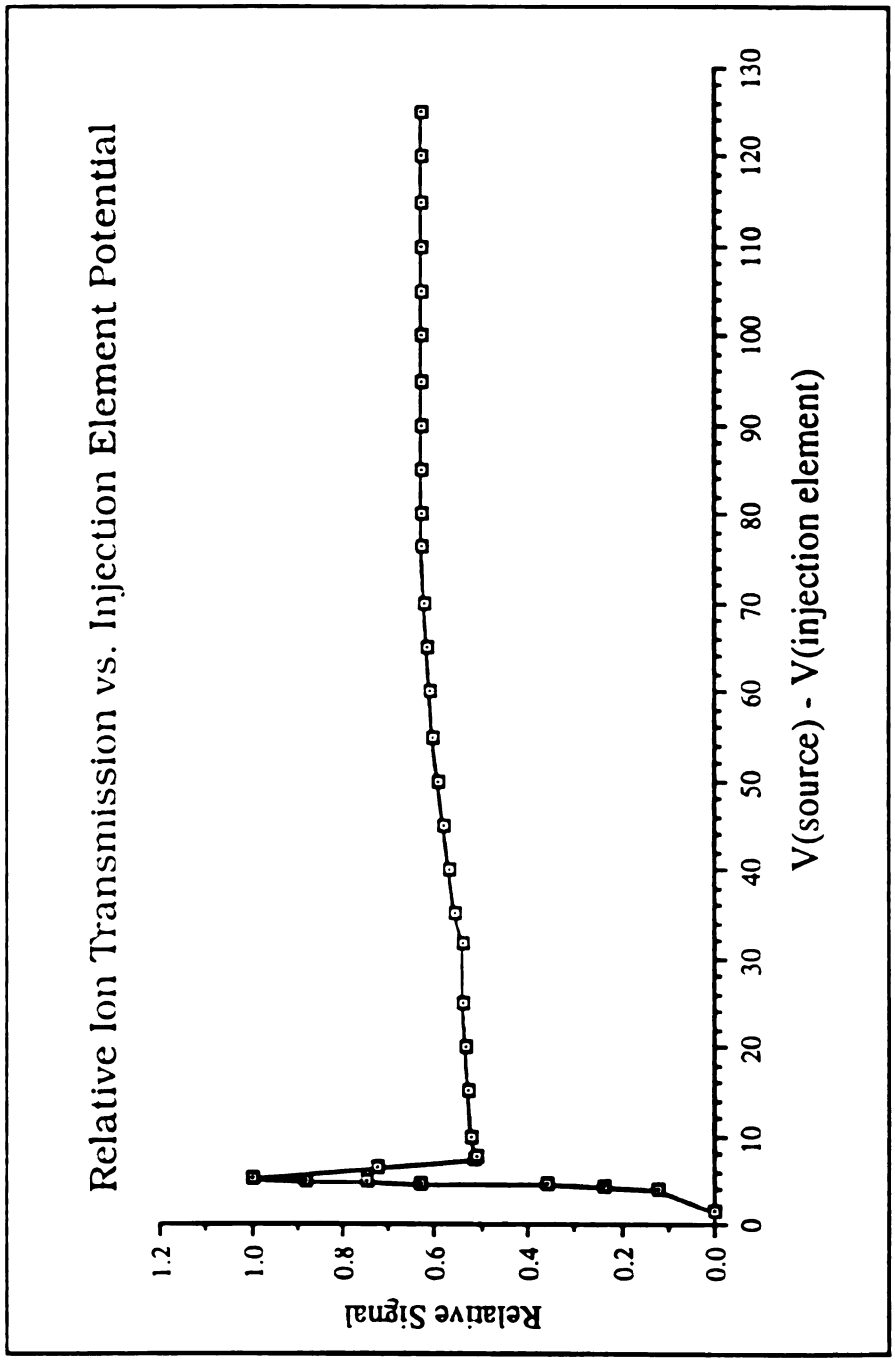

Figure 3.20. Relative ion transmission with einzel focusing optimized at 5 eV.

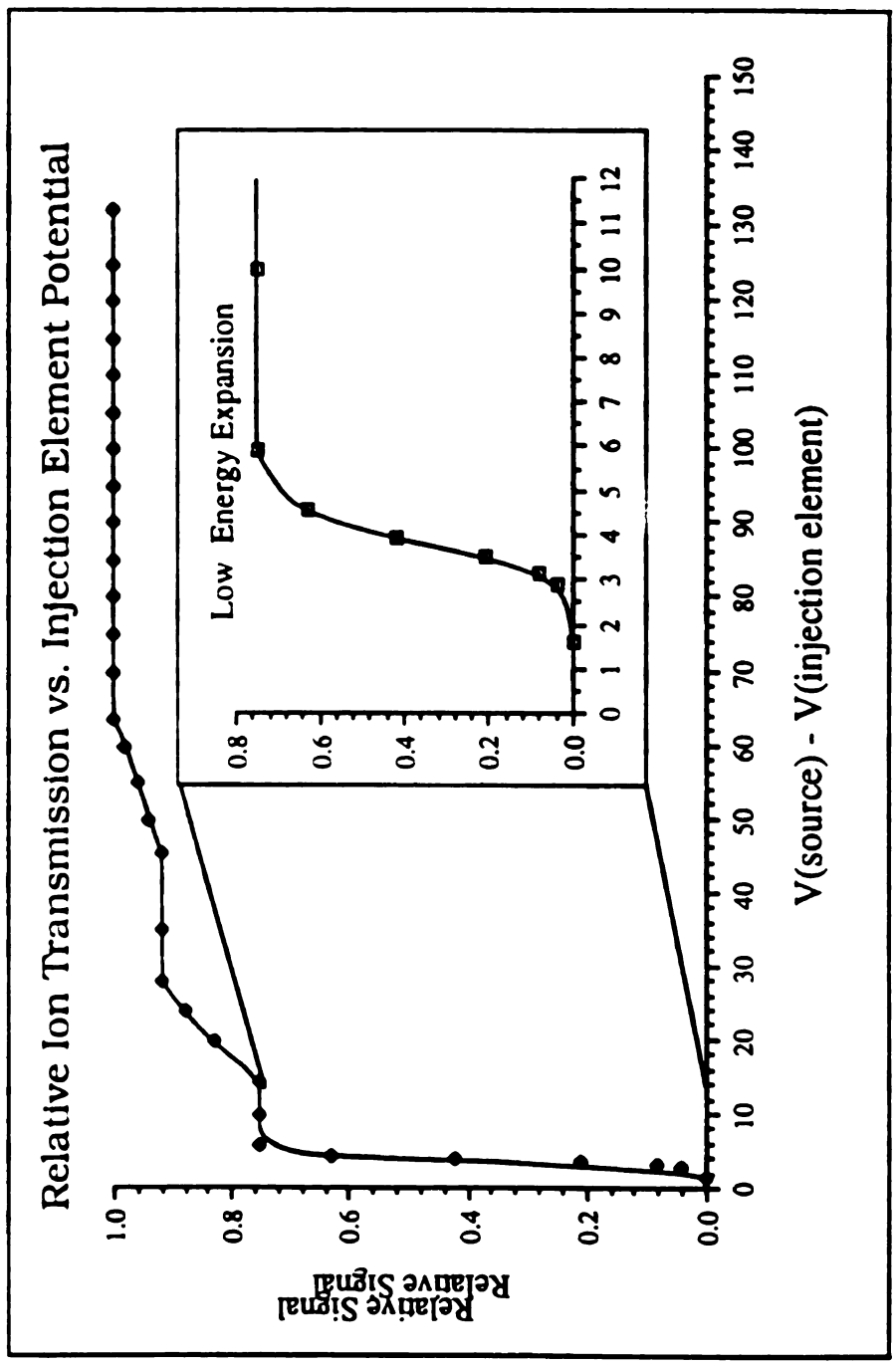

Figure 3.21. Relative ion transmission with einzel focusing optimized at 30 eV.

energy-dependent transmission is due to the change in focal length of the decelerating portion of the lens as a function of final beam energy.

If the einzel lens potential is optimized for an energy of ~30 eV, then a fairly flat transmission profile, approaching 80 % transmission for the energy range <5-130 eV, is obtained as shown in Figure 3.21. This demonstrates that reasonable transmission over a broad energy range may be attained by varying the potential of a single electrode in the lens assembly. In actual practice, when low collision energies (<10 eV) are desired, it is more effective to inject ions into the rf-only octopole with somewaht higher energy (>50 eV) and perform the final deceleration using the DC-bias of the ion beam guide. This is due to the rf fringing fields that can easily deflect low energy ions at the entrance to the octopole, resulting in lowered overall transmission. It is also advantageous to form very low energy beams (< 1eV) *within* the radial trapping field of ion beam guide. This allows effective ion currents that exceed the densities imposed by space-charge limitations.

For each final beam energy there exists an optimum einzel lens focal length that yields maximum transmission. Since the einzel lens power supply is programmable, it could be adapted to computer-controlled operation. Scanning the einzel lens potential in conjunction with the decelerating potential would provide the highest ion transmission as a function of beam energy.

E. Kinetic Energy Spread

Ideally, an ion beam instrument designed to investigate the translational energy dependence of ion/neutral interactions would

posses a monochromatic primary beam source variable in energy, but having no inherent kinetic energy spread. This reduces uncertainty in the ion/neutral interaction energy. Typical electron impact ionization sources for double focusing instruments are reported to produce ion beams with energy spreads of <0.5 eV (FWHM)[25]. At best, all of the ion-optical components of the primary ion source/mass analyzer and of the deceleration assembly, in particular, should not greatly contribute to the ion energy spread. However, if the kinetic energy spread of the ion beam can be accurately characterized, this information may be used for data deconvolution.

There are numerous approaches found in the literature for determining the spread of ion kinetic energy. The simplest experimental approach involves the use of a series of three (or more) parallel grids placed in the ion beam path normal to the principal axis of motion and preceding a detector[26]. This configuration is shown in Figure 3.22a. With grid 1 at ground potential (U_i), a retarding potential applied to grid 2 (U_f) establishes a linear energy-retarding field between the grids 1 and 2. The transmitted ion beam is measured by the detector. Grid 3 serves to shield the deceleration field from the detector bias. When the retarding potential is swept through the highest electric potential at which ions were formed (U_o max), the ion transmission vanishes. The fall-off profile of the ion current versus applied retarding potential plot should reveal the variation in the ion beam energy distributed around the mean potential at which the ions were formed. The most significant origin of kinetic spread in EI sources is the spatial variation of the source potential (ΔU_o) within the ionizing electron beam dimensions from the ion extraction field. For such an achromatic ion source, the mean potential

at which ion formation occurs can be considered to be U_o. This is the potential at which the mean ion kinetic energy equals zero.

Other methods of ion energy analysis require a higher level of instrumental sophistication. These include the use of hemispherical energy analyzers[27], tandem parallel-plate electric sectors[28], or deceleration within a dynamic-field trapping device such as rf-only multipoles [29]. We attempted to measure the KE spread of a high energy ion beam exiting the electric sector of the CH5-DF using the three-grid retarding potential analyzer situated immediately after the injection electrode of the deceleration lens as shown in Figure 3.22a. A (3000 eV) Ar^+ beam, formed by EI with the stock MAT CH5 Intensitron ion source, was directed onto the analyzer after traversing the field-free region between the exit slit and detector. All of the electrodes in the deceleration assembly were held at ground potential. The potential on grid 2 was scanned up to and beyond the source accelerating voltage while the transmitted ion intensity was measured to produce the stopping potential curve shown in Figure 3.22b. Here, the potential difference [V(source) - V(retarding grid)] is defined as V_{stop}. The ion transmission begins to decline at a V_{stop} value of ~30 V and makes a nearly linear drop in intensity between V_{stop} values of to 20 V and 5V, respectively. The ion current reaches a minimum level at a V_{stop} value of ~3.5 V. This implies that highest electric potential at which ions were formed and transmitted through the analyzer is approximately 3.5 V below the applied source potential for the source parameters used in the experiment.

It is also of interest to note that the minimum signal found in the retarding potential experiment was higher than the base noise level of the

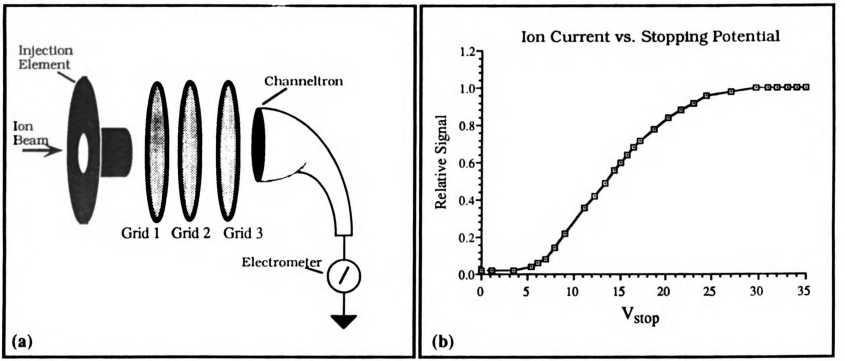

Figure 3.22. Three grid energy analyzer and apparent ion kinetic energy distribution.

detector/electrometer combination. The minimum signal always approached a level approximately two orders of magnitude lower than the signal associated with the maximum beam current. The minimum signal level was found to persist even when the potential applied to grid 2 exceeded the source accelerating potential by >66 V. It also scaled linearly with ion current exiting the source as measured by varying the electron emission level of the source filament. When the grid 2 voltage exceeded the source accelerating potential, biasing grid 3 at potentials between -5000 V and +5000 V had no appreciable effect on this minimum signal level. We therefore concluded that this signal was due to neutral particles or x-rays striking the electron multiplier. This may be expected since the detector is co-linear with the ion-optical axis of the instrument and fast secondary neutral particles may be sputtered at the exit slit (a limiting aperture) with low-angle trajectories.

The data in Figure 3.22b also suggest a very broad kinetic energy distribution in the ion beam of approximately 25 eV. This energy range is significantly higher than the specifications of the Intensitron EI source (FWHM < 0.3 eV) and much higher than typical ion energy spreads reported for other double-focusing instruments when using an EI source.

A large number of similar retarding potential experiments were performed using a variety of retarding field analyzer configurations (see Appendix D). The grid number, grid type (thickness, pore size and percent open area), grid spacing, and detector type (single continuous dynode and CEMA) were varied as well as the orientation of the analyzer relative to the optical axis of the beam. Both the energy-zero and the kinetic energy spread obtained in these experiments were strongly dependent on the configuration of the retarding field analyzer. The use

of different EI sources and accelerating potentials (1000, 2000 and 3000 V) did not yield the expected energy spread result (FWHM <0.3 eV) with any energy analyzer configuration. For most cases, the apparent ion energy range corresponded to approximately 1% of the accelerating potential. This was quite disturbing since ion kinetic energy spreads in the range of those measured (~25 eV for a 3 keV beam) would preclude the use of the EI source/CH5-DF as the primary ion source in a high performance ion beam instrument due to unacceptable energy resolution.

Retarding potential energy analysis using parallel grids suffers from severe experimental uncertainties and difficulties in proper implementation. The majority of these may be explained by considering the actual requirements of the retarding field. First, the electric field established by the grids must be perfectly perpendicular to the principal component of ion velocity to ensure an accurate measurement of the energy-zero (U_o). If perfect alignment is not achieved, then only a fractional component of the applied stopping potential is effective towards attenuating the forward motion of the ion beam. Second, the retarding field between the grids should be spatially uniform to minimize ion losses from divergence. This requires that all of the grids used be perfectly flat, which is difficult to achieve considering the mechanical stability typical of grids having a thickness of ~0.1 mm. Field uniformity is also compromised in a grid-type energy analyzer since the grids do not truly establish a unipotential boundary due to the penetration of electric potentials into the deceleration zone from nearby sources, such as the high potential applied to the detector. Most, however, is the fact that grids can be considered to be a series of apertures of square or circular

cross-section uniformly distributed in a plane. Therefore, two grids in parallel represent, ion-optically, a large array of misaligned lenses. When used to provide a deceleration field, the very non-ideal lens system yields poor transmission and thus a very distorted profile of the ion kinetic energy distribution.

The retarding potential analysis method which employed parallel grids was henceforth abandoned as a means of obtaining accurate ion energy spreads. A more accurate method of energy analysis involves the implementation of a hemispherical energy analyzer, tandem parallel-plate electric sectors, or deceleration within a dynamic-field trapping device such as a rf-only multipoles. We have used the octopole ion beam guide of our instrument to measure the ion kinetic energy spread of ions exiting the deceleration assembly. When the final ion energy retardation is performed inside the rf-only octopole, ion losses normally associated with space-charging and high angular divergence are eliminated. In this experimental configuration, the octopole beam guide is aligned co-axially to and directly following the injection element of the deceleration stage, as shown schematically in Figure 3.23a. An off-axis Daly-type detector employing a conversion dynode biased at -30 kV is used to detect ions exiting the rf-only octopole. The retarding potential (U_f) was applied as a DC-bias to the octopole radio frequency signal using a computer-controlled power supply referenced to and floating at the source accelerating potential.

The retarding potential profile of a decelerated $NiPF_3^+$ ion beam from the CH5-DF is shown in Figure 3.23b. The ions were formed with the Intensitron EI source, at an nominal source accelerating potential of 1000 V, mass analyzed and decelerated to approximately 200 eV before

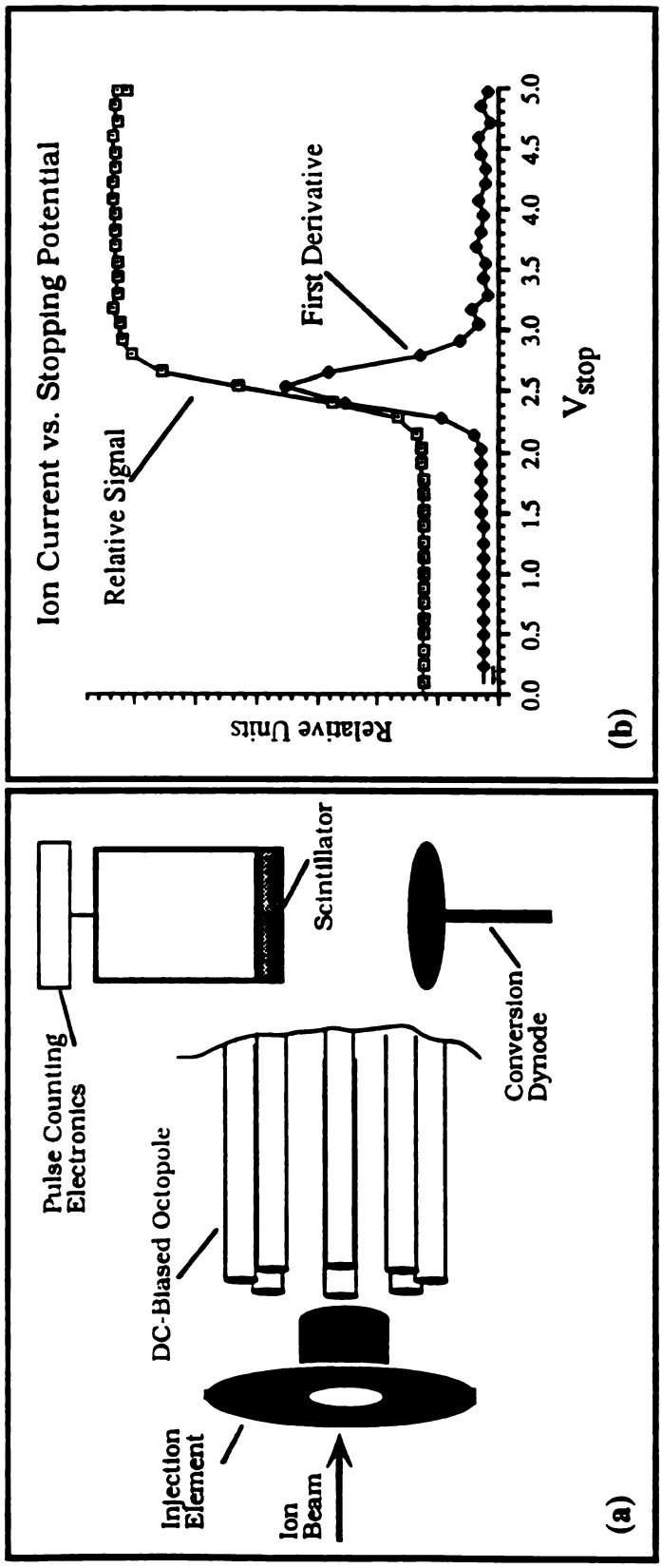

Figure 3.23. DC-biased RF octopole and apparent ion kinetic energy distribution.

injection into the rf-only octopole. The ion intensity is plotted as a function of the difference in electric potential between the ion source and the octopole DC-bias. This quantity, (V_{source} - $V_{octopole}$), is defined as V_{stop}. As this potential difference decreases below V_{stop} = 2.75 volts the level signal exhibits a rapid decrease in intensity. The ion current vanishes at an approximate V_{stop} value of 2.15 volts. Also given in Figure 3.23b is the first derivative of ion current with respect to octopole DC-bias. The mean potential of ion formation, the source potential (U_0), is found at the maximum of the first derivative curve which appears at V_{stop} = 2.54 volts. The mean potential of ion formation is thus 2.54 volts below the potential applied to the ion source housing. The ion kinetic energy spread appears as a distribution around this potential. On the plot shown, the ion energy spread is ~0.3 eV FWHM, which agrees quite favorably with the design specifications of the Varian MAT Intensitron EI source of 0.3 eV FWHM (as reported in the product literature). Similar stopping potentials are obtained for much lower octopole injection energies. These data indicate that the simple ion deceleration lens design allows significant ion energy attenuation without adding any additional ion kinetic energy spread to that found in the nascent ion beam.

VII. Conclusion

Through ion optical modeling of the complex exponential and simple two-electrode deceleration lenses, the fundamental features that govern lens performance have been elucidated. When creating an energy retarding field with electrodes having circular apertures, the electric field

exhibits steep gradients perpendicular to the central axis. These transverse gradients lead to the over-focusing of ions (high angular divergence) at the exit of the deceleration region. This effect is most pronounced for ion beams with initial diameters that approach the electrode aperture diameters. It is suggested that the ratio of the initial beam diameter to the electrode aperture diameter (D_a:D_b) is the most significant criterion in determining the performance of ion deceleration lenses, and not the complexity of the retarding field. In order to avoid excessive force on the ions perpendicular to the main direction of motion it is necessary to constrain the ion beam near the central axis of the lens assembly. This may be accomplished by using very large electrode apertures relative to the initial beam diameter as in the conventional exponential decelerating lenses.

We have proposed the use of a simple two- or three-electrode assembly with moderate aperture diameters to establish the retarding field. Ions are constrained near the central axis through the critical portion of the decelerating field by a an einzel lens that precedes the deceleration stage. This new deceleration system is able to decelerate a 3000 eV ion beam down to <3-200 eV while maintaining low angular divergence, minimal kinetic energy perturbation, and good transmission. In addition, the lens converts the high energy ion beam with a rectangular profile (plane symmetry) to a low energy ion beam with a circular profile (axial symmetry). The combination of these features makes the deceleration lens described suitable for implementation in an ion beam instrument designed to probe the energetic and dynamic details of ion/neutral interactions. Thus, it has been demonstrated that a simple deceleration lens does not compromise high performance versus

a complex deceleration lens when the fundamental ion-optical aspects of ion deceleration are well understood.

LIST OF REFERENCES
Chapter 3

1. Glish, G.L.; McLuckey, S.A. *Anal. Instrum.* **1986**,*15*, 1.

2. Schoen, A.E.; Amy, J.W.; Ciupek, J.D.; Cooks, R.G; Dobberstein, P.; Jung, G.*Int. J. Mass Spectrom. and Ion Proc.* **1985**, *65*, 125.

3. Harrison, A.G.; Meecer, R.S.; Reiner, E.J.; Young, A.B.; Boyd, R.K.; March, R.E.; Porter,C.J. *Int. J. Mass Spectrom. and Ion Proc.* **1986**, *74* , 13.

4. Suter, M.J.-F.; Gfeller, H.; Schlunegger, U.P. *Rapid Commun. Mass Spectrom.* **1989**, *3*, 89.

5. Dawson, P.H. *Mass Spectrom. Rev.* **1986**,*5*, 1.

6. Laue, H-J; Amy, J.W.; Winger, B.; Cooks, R.G. *Proceedings of the 36th Conference on Mass Spectrometry and Allied Topics* **1988**, p 958.

7. Franchetti, V.; Solka, B.H.; Baitinger, W.E.; Amy, J.W.; Cooks, R.G. *Int. J. Mass Spectrom. and Ion Phys.* **1977**, *23*, 29.

8. Pohlit, H.M.; Erwin, W.R.; Reynolds, F.L.; Lemmon, R.M.; Calvin, M. *Rev. Sci. Instrum.* **1970**, *41*, 1012.

9. Youchision, D.L.; Nahemow, M.D. *Rev. Sci. Instrum.*. **1990**, *61*, 2184.

10. Liebl, H.; Bohdansky, J.; Roth, J.; Dose, V. *Rev. Sci. Instrum.* **1987**, *58*, 1830.

11. Kofel, P.; McMahon,T.B. *Int. J. Mass Spectrom. and Ion Proc.* **1990**,*98*, 1.

12. Kemper, P.R.; Bowers, M.T. *J. Am. Soc. Mass Specrtrom.* **1990**,*1*, 197

13. Armentrout, P.B.; Beauchamp, J.L. *J. Chem. Phys.* **1981**, *74*, 2819.

14. Shukla, A.; Anderson S.; Howard, S.L.; Sohlberg, K.W., Futrell, J.H. *Int. J. Mass Spectrom. and Ion Phys.* **1988**, *86*, 61.

15. Vestal, M.L.; Blakley, C.R.; Ryan, P.W.; Futrell, J.H. *Rev. Sci. Instrum.* **1976**, *47*, 15.

16. D.A. Dahl; J.E. Delmore *SIMION PC/PS2 Version 4.0*, EGG-CS-7233 Rev.2, April 1988.

17. Davies, S.C.; Wright, B. *Rapid Commun. Mass Spectrom.*, **1990**, *4*, 186.

18. Hasted, J B. In *Atomic and Molecular Processes* ; Vol. 13; D.R. Bates, Ed.; Academic Press: New York, **1962**; p 696-720.

19. Hasted, J B. In *Atomic and Molecular Processes* ; Vol. 13; D.R. Bates, Ed.; Academic Press: New York, **1962**; p p 705.

20. Hansen, S.G.; Farrar, J.M.; Mahan, B.H. *J. Chem. Phys.* **1980**, *73*, 3750.

21. Ervin, K.; Armentrout, P.B. *J. Chem. Phys.* **1985**,*83*, 166.

22. Loh, S.K; Hales, D.A.; Pan , L.; Armentrout, P.B. *J. Chem. Phys.* **1989**, *90*, 5466.

23. Brewer, G.R.; Wilson, R.G. *Ion Beams*, John Wiley and Sons **1973**

24. Quian, K.; Shukla, A.; Futrell, J. *Anal. Chem.* **1990**, *62*, 1547.

25. Beynon,J.H.; Baitinger, W.E.; Amy, J.W.; Komatsu,I. *Int. J. Mass Spectrom. and Ion Phys.* **1969**, *3*, 47.

26. Hodges, R.V.; Armentrout, P.B.; Beauchamp, J.L. *Int. J. Mass Spectrom. and Ion Phys.* **1979**, *29*, 375.

27. Siegal, M.W.; Vasile, M.J. *Rev. Sci. Instrum.* **1981**, *52*,1803.

28. Gentry, W.R.; McClure, D.J.; Douglas, C.H. *Rev. Sci. Instrum.* **1975**,*46*, 367.

29. Teloy, E.; Gerlich, D. *Chem. Phys.* **1974**, *4*, 417.

Chapter 4

Ion Beam Instrument Computer Controlled Operation and Reaction Cross-Section Measurements

---

I. Introduction to Reaction Cross-Sections

The purpose of the ion beam instrument is to measure the energy dependence of ion/neutral reactions. The most important energy contribution for reactions and that which can be carefully controlled in the beam apparatus is the kinetic energy of the reactant ions. Because of the conservation of momentum, the energy which is utilized by the colliding pair for chemical transformation is not the motion in the laboratory frame, but the relative kinetic energy in the center-of-mass (CM) reference frame. If the motion of the neutral gas is neglected, the kinetic energy in the CM frame (KE_{cm}) may be calculated from the relative masses of the collision partners as shown below.

$$KE_{cm} = KE_{lab}\,(m/(m + M))$$

Here KE_{lab} is the nominal kinetic energy in the laboratory frame, m is the mass of the stationary neutral, and M is the mass of the reactant ion.

The reaction cross-section refers to the extent to which a particular process occurs as a result of a collision. This is a quantitative measure

of the probability that a collision will lead to specified products. The total reaction cross-section, σ, can be viewed in terms of attenuation of the primary ion beam, I_o, as it travels a distance, l, through a static collision gas with a number density, n. This relationship is given in an integrated Beer's law form below.

$$I_R = I_o \exp(-\sigma n l)$$

The term I_R is the intensity of the primary ion beam transmitted through the collision cell length. The initial primary ion intensity can be considered to be equal to the sum of the transmitted intensity and the product ion intensity, I_P, as shown below.

$$I_o = I_R + \Sigma I_P$$

Thus cross-section measurements only require the determination of the transmitted primary and product ions, the effective length of the interaction region, and the density of the collision gas. The number density can be derived from the gas temperature and pressure.

If cross-section measurements are performed at different nominal kinetic energies, the energy-dependent behavior of a reaction system may by studied. The details of data interpretation, including deconvolution and determination of threshold energy as well as extraction of thermodynamic information has been documented elsewhere in the literature [1,2].

This chapter describes the measurements of reaction cross-sections on the MSU ion beam instrument utilizing computer-controlled data

acquisition. Two chemical systems are studied to characterize the instrument. The first system involves the *endothermic* collision-induced dissociation (CID) of Mn_2^+ with argon as shown below in reaction 4.1.

$$Mn_2^+ + Ar \rightarrow Mn^+ + Mn + Ar \qquad (4.1)$$

The second system presented here is the *exothermic* reaction of argon ion with molecular deuterium to form ArD^+ as shown in reaction 4.2.

$$Ar^+ + D_2 \rightarrow ArD^+ + D \qquad (4.2)$$

II. Instrument Control

Energy-dependent collision cross-sections are measured by introducing a neutral reactant gas into the collision cell. The pressure is maintained at 0.1 mtorr or less in order to minimize the probability that an ion experiences more than one collision while traveling the length of the collision cell. The nominal interaction energy is established by the DC potential between the ionization source and the octopole/collision cell. The ion current is measured at the detector for the primary ion and each product ion of interest. The interaction energy, quadrupole mass filter setting and detector signal are all controlled/monitored by a computer system as shown in Figure 4.1. The system is comprised of a 12 MHz 80286 PC running MS DOS. Two IBM DACA interface boards are controlled using custom programs developed in the ASYST 2.0 platform.

The timing sequence for a typical experiment is shown in Figure 4.2. The octopole/collision cell potential is stepped through the desired range

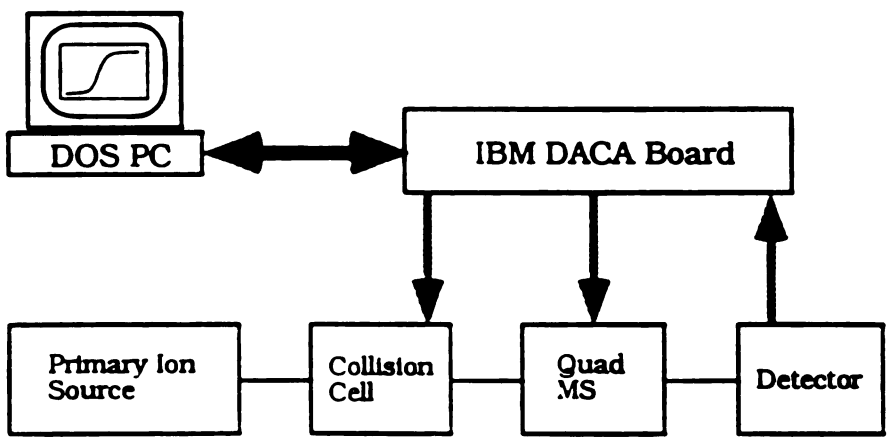

Figure 4.1. Ion Beam Instrument Control Schematic Diagram.

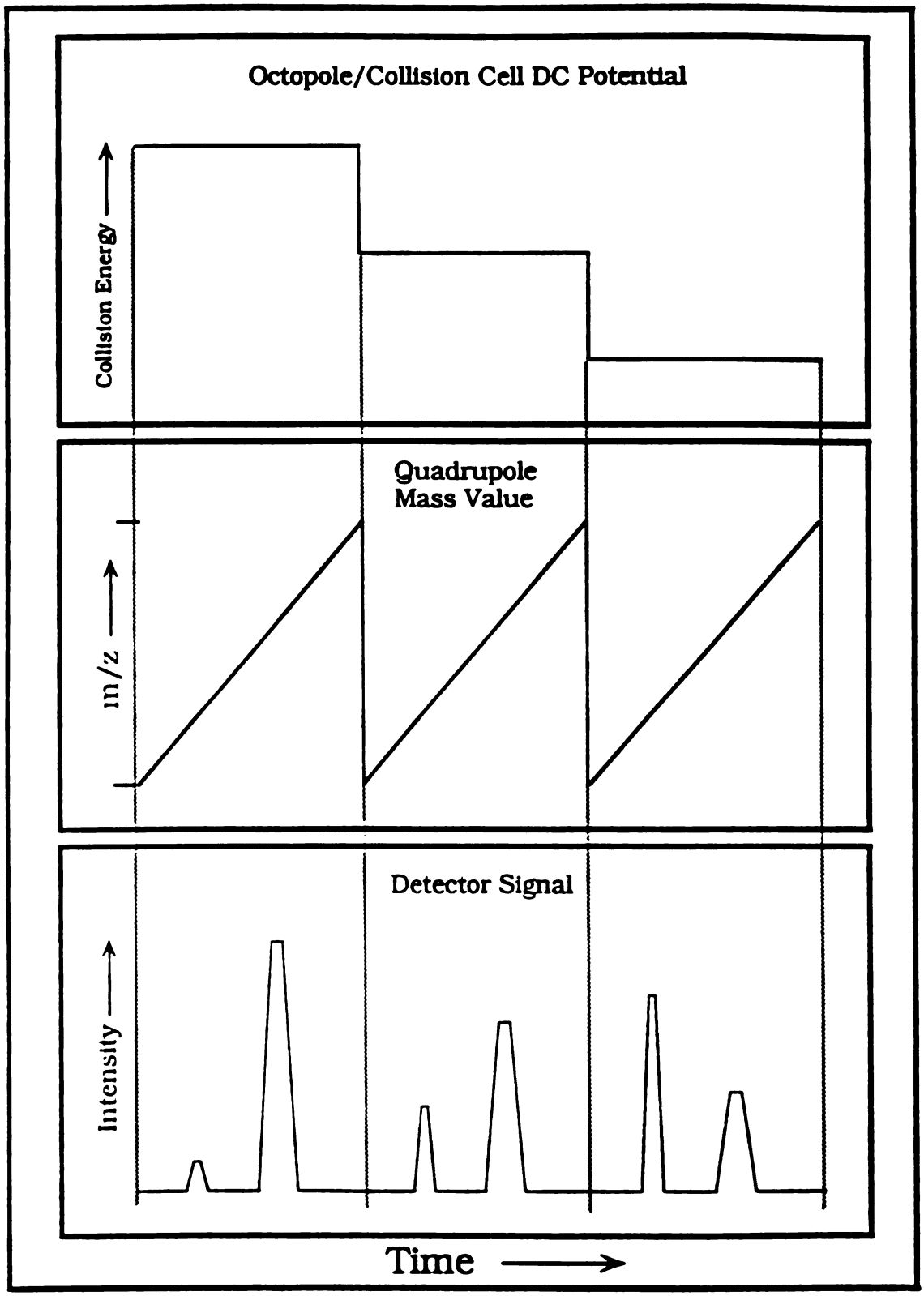

Figure 4.2. Ion Beam Experimental Sequence Diagram.

of interaction energies. At each energy setting, the quadrupole may be scanned over the mass range of interest while the detector signal is monitored. An alternative, and more efficient method involves stepping the quadrupole filter to the primary and product ion m/z values instead of scanning over a wide mass range. In this mode, the optimum mass values should be determined by scanning the quad over the primary and product mass profiles in a preliminary experiment.

The interface control scheme for biasing the octopole collision cell is shown in Figure 4.3. A zero to -500 V floating power supply is used to generate the offset potential. The supply is referenced to the ion source accelerating potential to compensate for any drift in the source electronics. A +5V power supply is connected in series to the accelerating potential. This five volt over-potential ensures that ions with energies greater than the accelerating potential will be covered in a stopping potential analysis. It also allows the DC supply to be operated in a linear region of output.

The DC power supply may be programmed using a 0-5 volt driver. The driver potential is generated using a 12 bit DAC. Since the power supply is floating at the source potential of 1000 to 3000 volts, it cannot be directly connected to the computer interface. A circuit was designed to eletrically isolate the DACA interface from the floating DAC and power supply utilizing high voltage opto-isolators.

The 12 bit DAC allows the octopole supply to produce a voltage controllable in 4095 increments. To provide a highly accurate and precise value of the interaction energy, the output of the octopole power supply was measured as a function of the digital number sent to the DAC from the computer. The voltage calibration curve is shown in Figure 4.4.

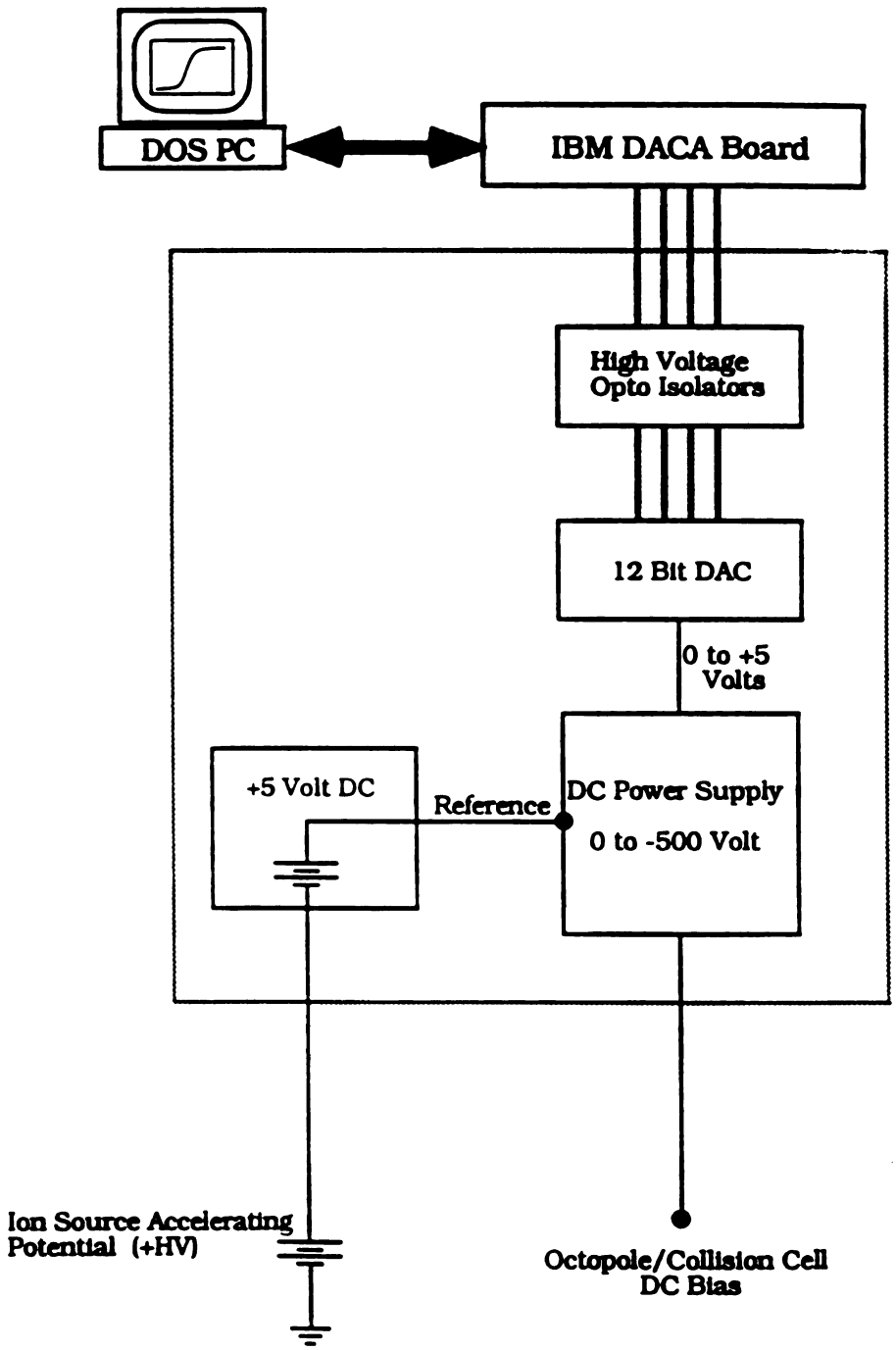

Figure 4.3. Octopole/Collision Cell DC Bias Schematic Diagram.

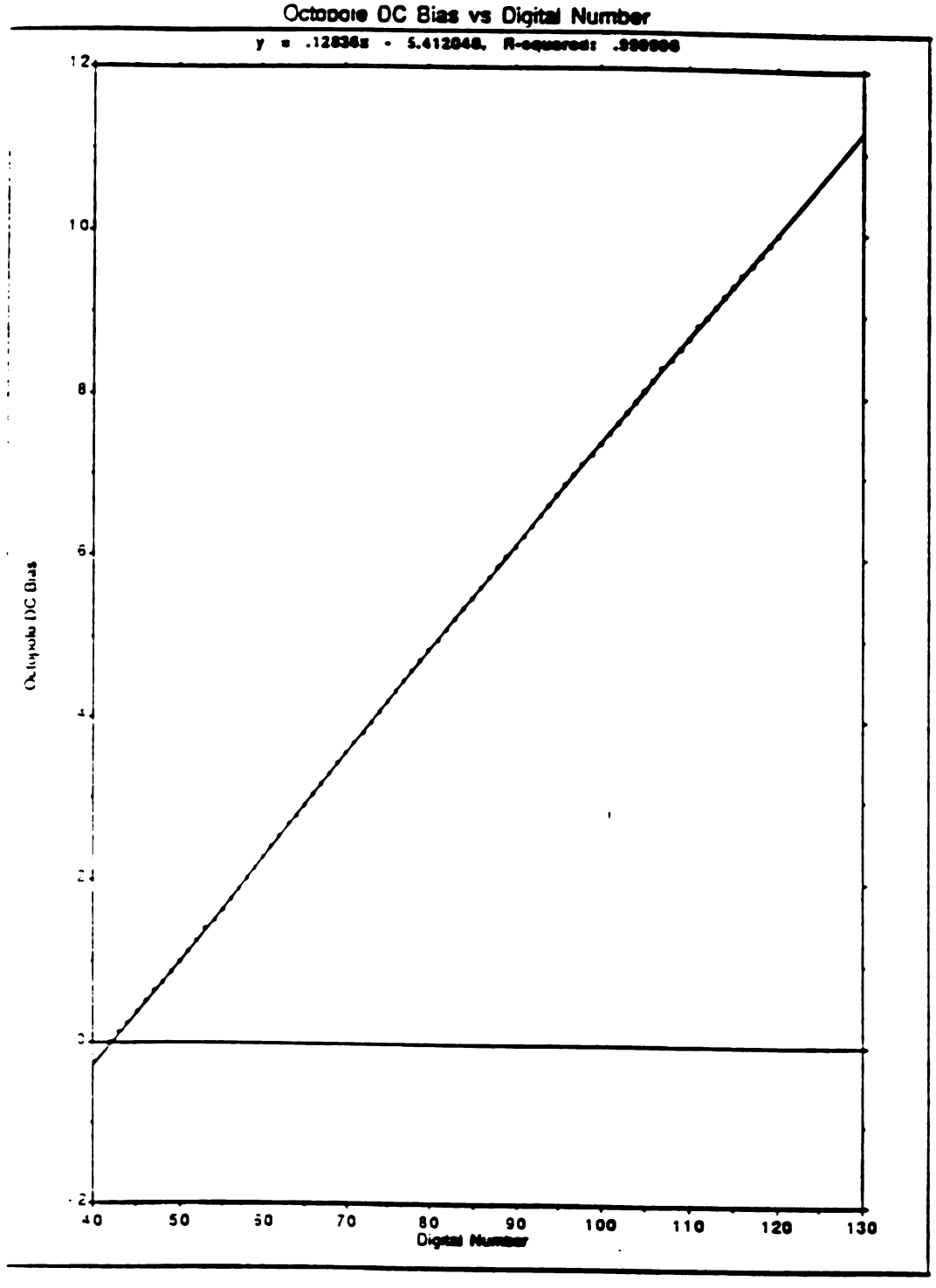

Figure 4.4. Calibration of digital interface for octopole DC bias supply.

The regression equation fit to the line is displayed at the top of the plot has a high degree of linearity (R=0.999998). This equation is thus used in data analysis to determine the relative ion energy in the collision cell which may be incremented in units of 0.128 volts. This limits the uncertainty in the relative interaction energy to ~±0.064 eV in the laboratory frame.

The interface electronics associated with the quadrupole mass filter is shown in Figure 4.5. The m/z stability (pass) value is determined by the amplitude of the rf and DC potentials generated on the rods. The rf potential is generated by a high power rf amplifier and the DC voltages are obtained by rectification circuitry in the High-Q Head. There is a linear relationship between the rf/DC amplitude and the magnitude of the m/z value which is stable in the filter. The quadrupole control electronics and rf amplifier are driven by a 0-10V DC signal. Thus a simple linear relationship exists between the drive voltage and the mass axis. An analog output on one of the DACA boards is dedicated to the quad driver. It allows the m/z value to be set to ~±0.1 unit.

In addition, a DC offset may be independently applied to the quadrupole as shown in Figure 4.5. The difference between the quad DC bias and the ionization source accelerating potential establishes the nominal ion kinetic energy through the quadrupole mass filter.

A conceptual diagram of ion signal generation and measurement with the Daly detector is depicted in Figure 4.6. The PMT produces a temporally narrow (<50 ns) negative pulse generated by a single ion event. The pulse is amplified by an MIT F-100T amplifier with an integral discriminator circuit. A narrow TTL level output pulse is generated by the preamplifier for each input signal that exceeds a certain threshold.

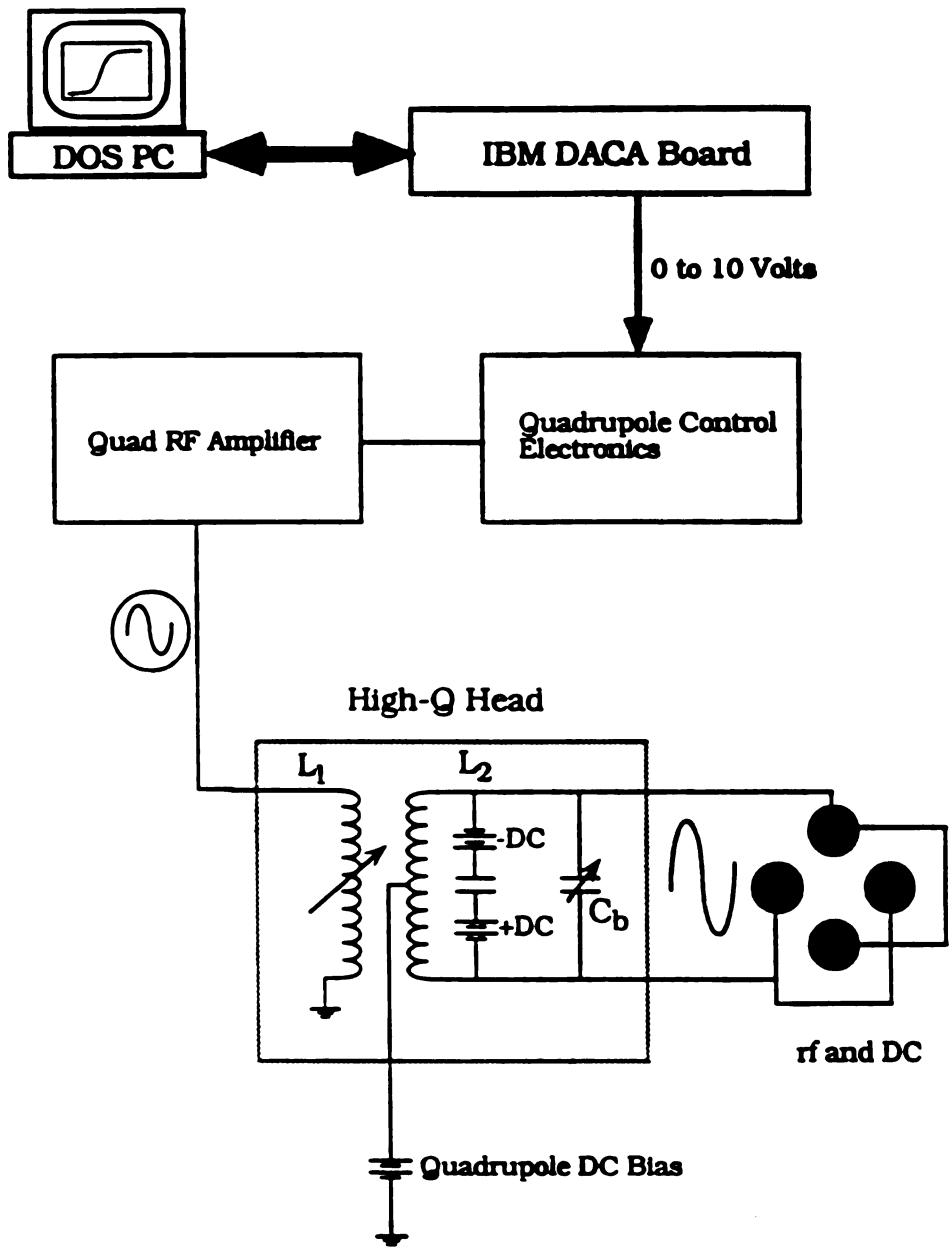

Figure 4.5. Quadrupole Electronics Schematic Diagram.

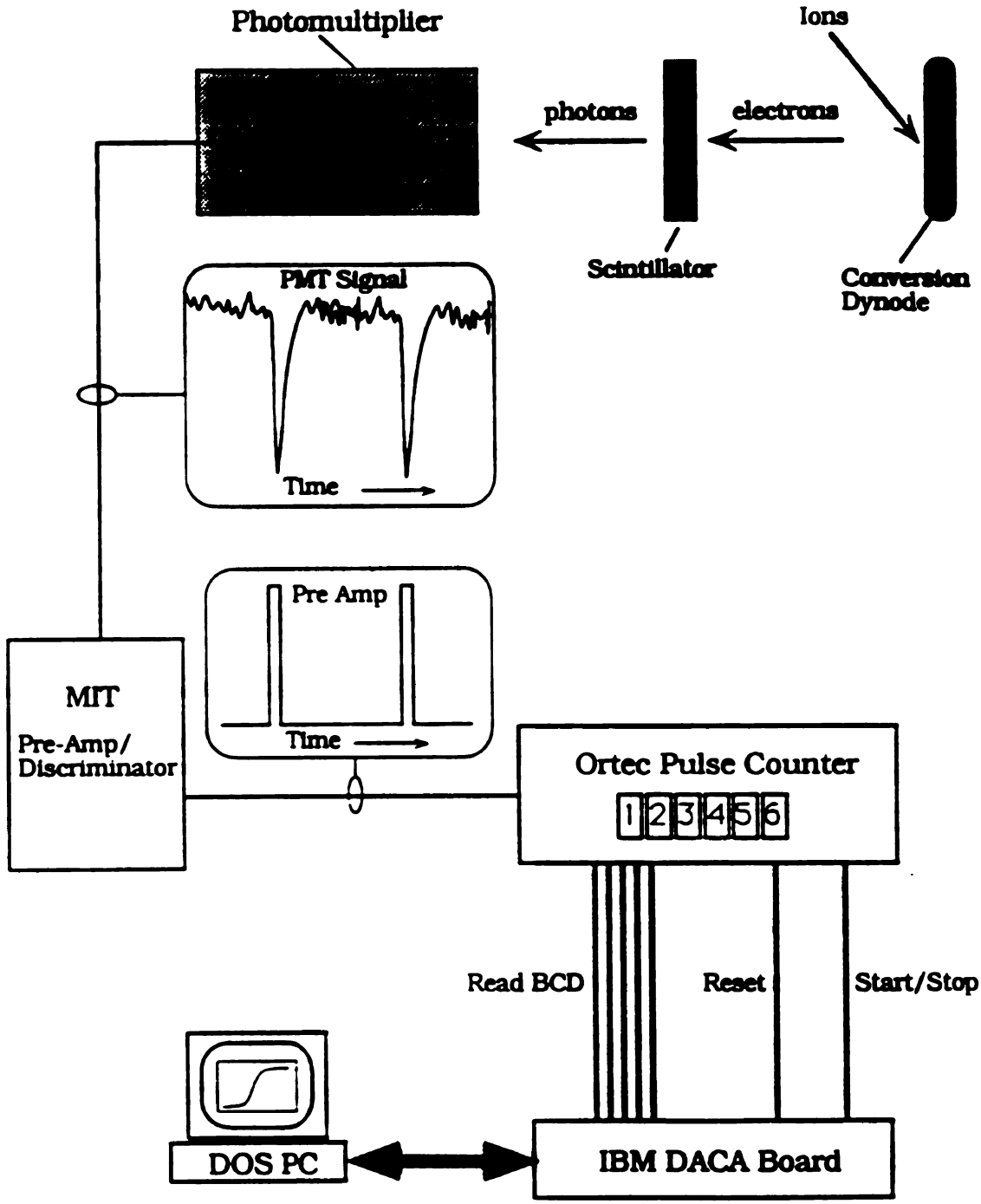

Figure 4.6. Detector Electronics Schematic Diagram.

By judicious setting of the threshold level, signals originating from spurious events may be discriminated from signals related to ion events.

Pulses from the preamplifier are detected by a six digit ORTEC 775 pulse counter. The counter has been modified in-house for digital interfacing. This is accomplished by parallel readout of the binary coded decimal (BCD) value in each of the six LED displays. The start count and stop count states are also controlled by computer digital output signals. The counter control software has been rigorously tested and includes software corrections to establish exact counting time intervals.

The overall bandwidth of the Daly detector system electronics exceeds 1 MHz. This system provides the requisite sensitivity and broad dynamic range for the measurement of small ion/molecule reaction cross-sections encountered in threshold measurements.

II. Reaction Cross-Section Measurements

A. Collision Induced Dissociation of Mn_2^+

The collision induced dissociation (CID) of singly charged manganese dimer ion was studied in the ion beam instrument using Ar as a collision gas. This is shown in reaction 4.1. All of the operating parameters used in the CID experiment are documented in Appendix E. The reactant Mn_2^+ primary ions were formed by electron ionization of $Mn_2(CO)_{10}$. Solid $Mn_2(CO)_{10}$ was introduced to the source through the direct probe inlet. Since the vapor pressure of the compound is quite low at room temperature, the butterfly valve was used to throttle the source diffusion pump until reasonably high primary ion currents (~10^6 counts/second) could be attained. A range of ionizing electron energies were used to

generate Mn_2^+. However, excess internal energy in the primary ion results in slow metastable decomposition of the dimer ion at energies much greater than the appearance energy. Therefore, the results presented here utilized 18.13 eV electrons, which minimized excessive internal energy effects. The electron accelerating voltage circuitry was calibrated by measuring the ionization potential of N_2 as a standard. The threshold plot for nitrogen ionization is shown in Appendix E.

As discussed in Chapter 3, because of a variety of effects in the ion source, the nominal ion energy may differ significantly from the source accelerating potential. The true ion energy is determined by performing a stopping potential experiment. This is done by monitoring the primary ion current while sweeping the octopole DC bias through the accelerating potential. A plot of the Mn_2^+ (m/z 110) ion count rate versus the octopole DC bias relative to the ion source potential is shown in Figure 4.7. The ion current exhibits a very rapid rise to the maximum value of approximately 5.4×10^5 counts/second after the threshold near 1 volt. The first derivative plot may be used to determine the energy zero and the inherent kinetic energy profile in the primary ion beam. From the first derivative plot, an energy spread of about 0.3 eV (FWHM) is measured. This value is in agreement with EI source specifications. For an approximately Gaussian energy distribution, the apex of the first derivative plot may be used to determine the average ion energy or potential of energy zero. Since the energy spread is narrow relative to the octopole voltage step size, it is more accurate to use the extrapolated potential required to stop 50% of the ion population. This value is 1.488 volts as shown Figure 4.7. The energy zero potential is implemented in the data analysis to correct the nominal octopole DC bias potential.

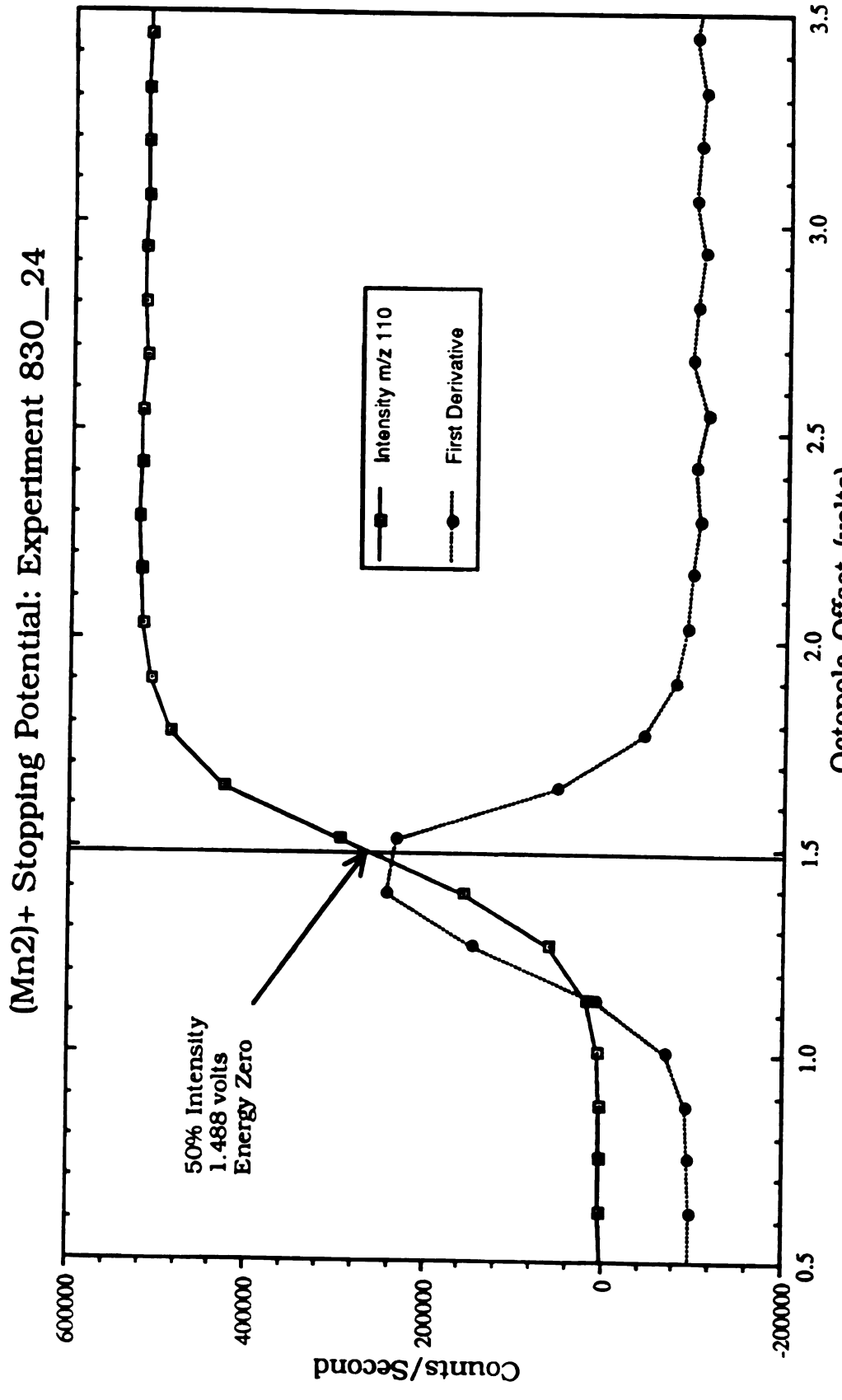

Figure 4.7. (Mn2)+ stopping potential.

The effect of various instrumental parameters (such as source potentials, deceleration (injection) energy, and octpopole operational values) on ion stopping potentials were studied using Ar^+ as a model ion. This stopping potential data is compiled in Appendix F.

The collision cell was filled with high purity argon to a typical pressure of ~0.1 mtorr. Interfering reactions of Mn_2^+ with background water were observed at low interaction energies when technical grade Ar was employed. Cross-section data exhibiting this low energy interference feature is detailed in Appendix G. These interferences were not present when either a gas scrubber or high purity argon were used.

Since the product and primary ions differ significantly in mass, the quadrupole could be operated at a very low resolution setting. This enabled nearly 100% transmission of mass selected ions. The quadrupole was stepped between m/z 110 and m/z 55 to monitor Mn_2^+ and Mn^+, respectively. The product ion transmission was highly dependent on the quadrupole DC bias as shown in Figure 4.8. This results presumably because the product ion varies greatly in kinetic energy with respect to the primary ion. The data suggest that the Mn^+ species is formed with very little forward momentum in the laboratory frame. Therefore, the quadrupole DC bias was set at a potential lower than the minimum octopole DC bias to maintain complete product ion transmission.

Primary and product ion intensities were measured for incident ion translational energies ranging from zero to 20 eV in the laboratory frame. Raw ion counts were background corrected by subtracting the average dark count rate from the ion intensities. Dark count measurements were

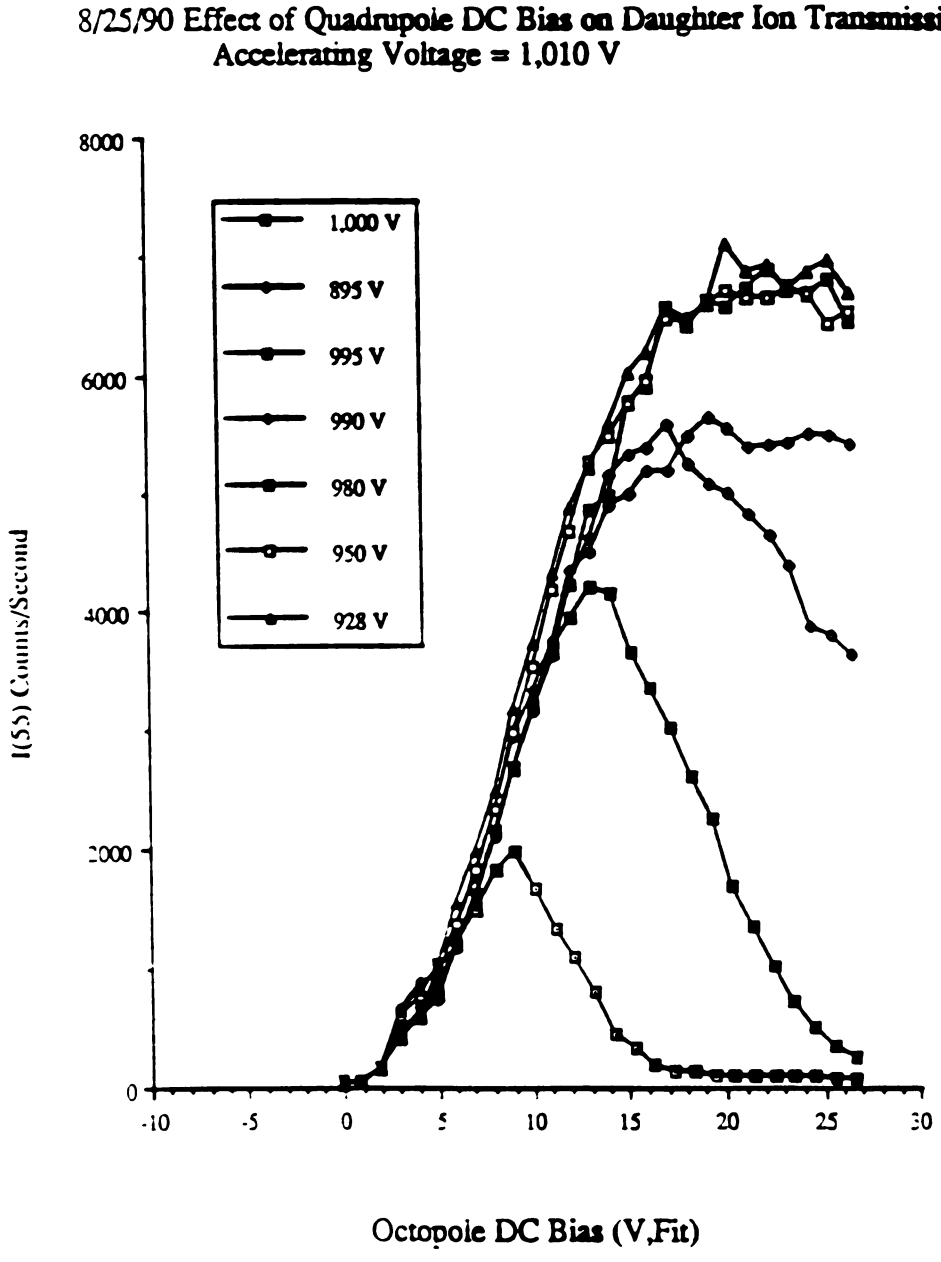

Figure 4.8. Effect of quadrupole mass filter DC bias for Mn_2^+ CID.

performed for each experiment at all collision energies by tuning the qudrupole mass filter to an m/z value where no ion transmission is obtained. The laboratory frame ion energy was converted to CM collision energy. Reaction cross-sections were calculated from the equation shown below.

$$\sigma = \frac{-\ln\left(\frac{I_{Mn_2^+}}{I_{Mn^+} + I_{Mn_2^+}}\right)}{nl}$$

Diffusion of the collision gas cloud into the vacuum chamber results in an uncertainty in the length of the interaction region. Therefore, relative cross-sections (σ/σ_{max}) were calculated as opposed to absolute cross-sections.

Figure 4.9 shows a plot of the relative Mn_2^+ CID cross-section as a function of the CM collision energy. Because of the background subtraction, some relative cross-section values are less than zero at energies below the CID threshold. In these cases, negative cross-section values have been truncated at zero. The data points for the two runs plotted exhibit a high degree of precision considering the complexity of the experiment. The run-to-run cross-section variation is usually around 3%.

The threshold region of the reaction cross-section is shown in an expanded plot in the top panel of Figure 4.10. The energy accuracy of our cross-section data may be determined by comparison with a previous study on Mn_2^+ by Armentrout (PBA) and coworkers [3]. The lower panel of Figure 4.10 shows the PBA absolute cross-section data for Mn_2^+

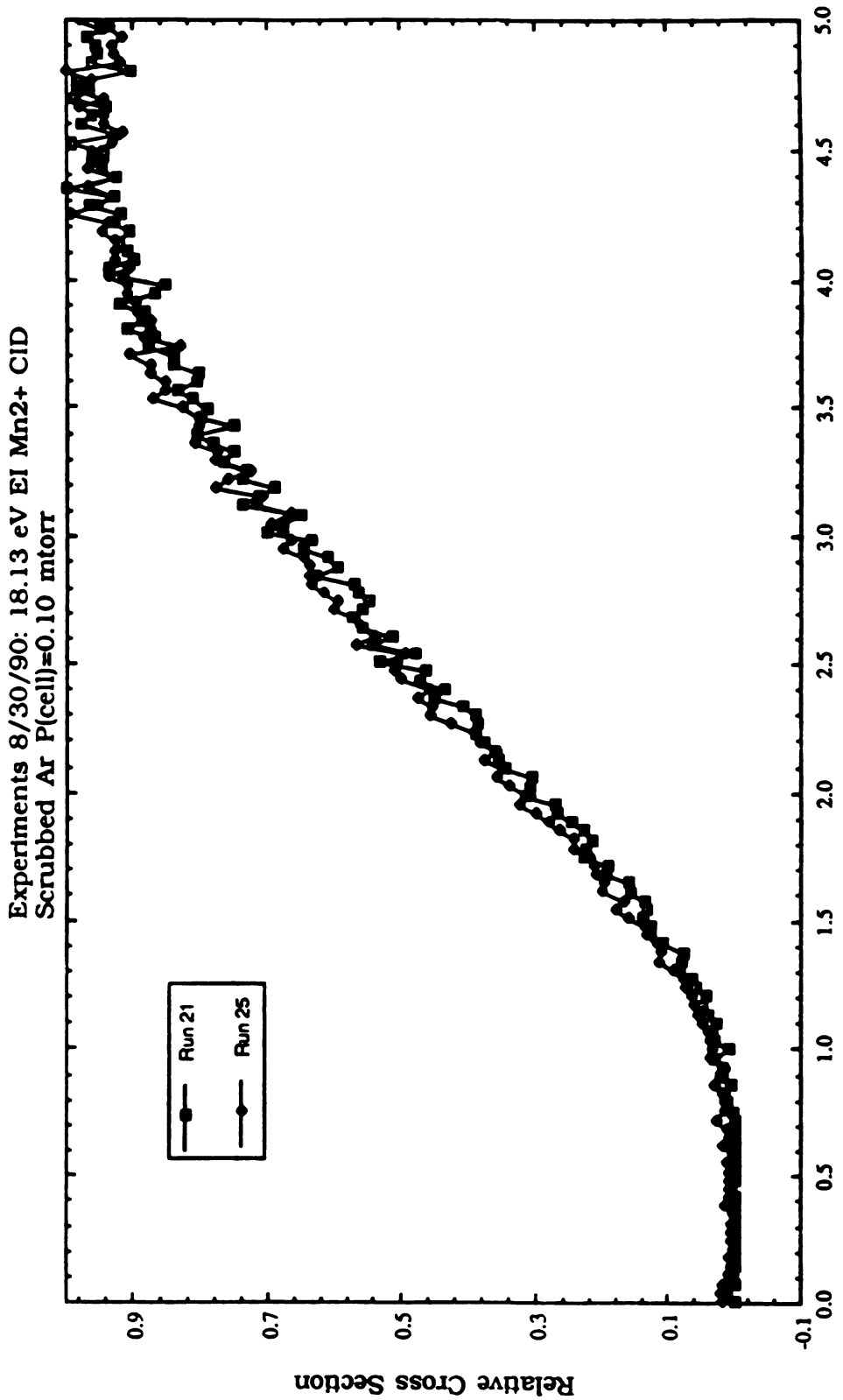

Figure 4.9. Energy-dependent (Mn2)+ CID Cross-Section.

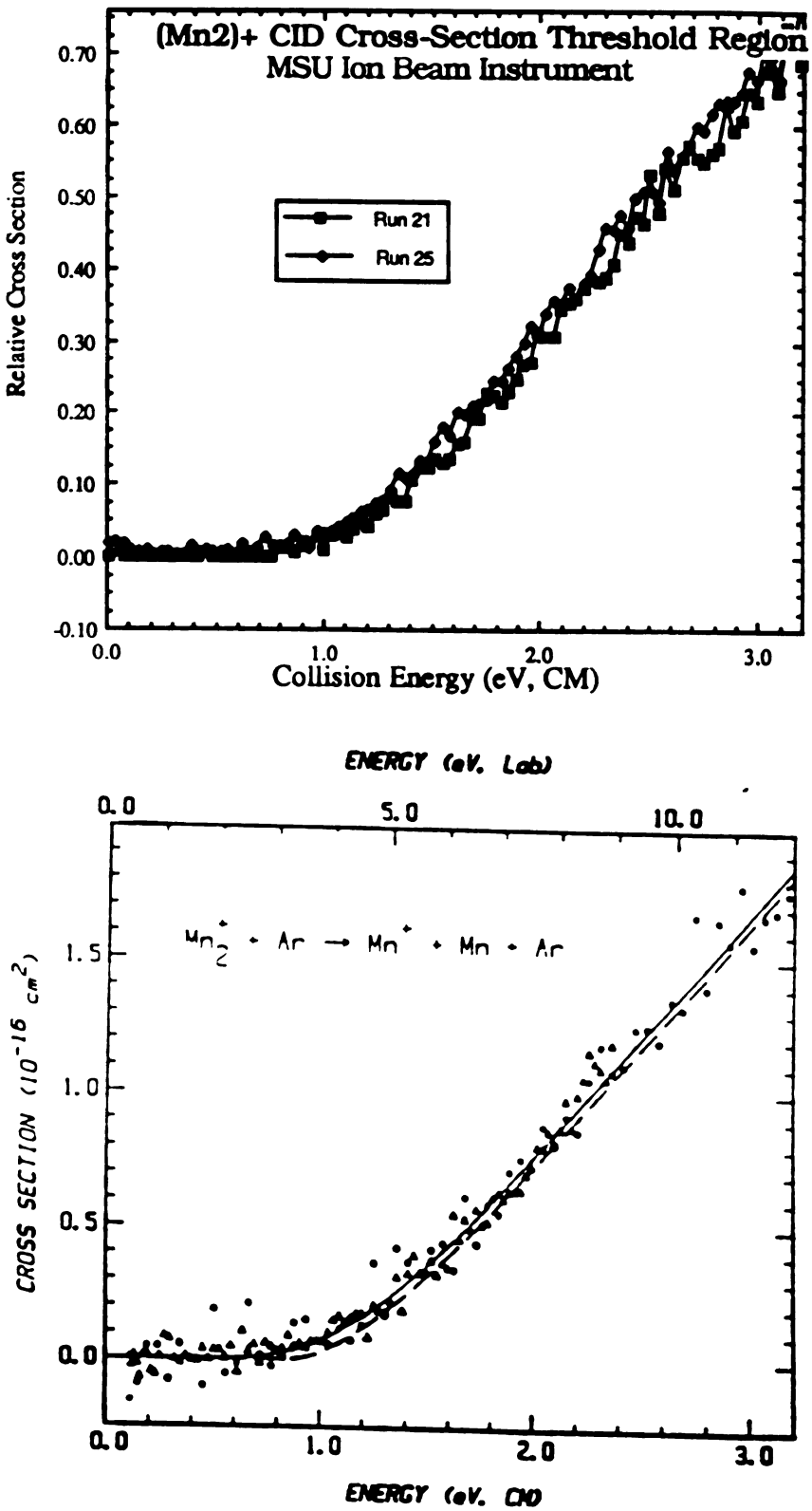

Figure 4.10. Comparison of Mn_2^+ CID threshold region.

formed by ~18 eV electron ionization. It can be seen that our data is in quantitative agreement with the PBA energy axis. Through sophisticated curve-fitting and deconvolution techniques, the PBA data yield a translational energy threshold of 0.85 eV for the Mn_2^+ dissociation process. From error analysis and internal energy considerations, the Mn_2^+ bond dissociation energy, $D°(Mn_2^+)$, was determined by PBA as 0.85 ± 0.2 eV.

The Mn_2^+ CID study demonstrates that the MSU ion beam instrument can be used to obtain reproducible, energy-accurate realative cross-section measurements for endothermic processes.

B. Exothermic Reaction of Ar^+ with D_2

The reaction of singly charged argon ions with molecular hydrogen and deuterium has received extensive treatment in the literature [1]. Reaction 4.2, shown below, is exothermic by 1.50 eV for ground state reactants and products.

$$Ar^+ + D_2 \rightarrow ArD^+ + D \qquad \Delta H = -1.50 \pm 0.03 \text{ eV} \quad (4.2)$$

This presents an excellent candidate system to study exothermic ion/molecule reactions in the ion beam apparatus.

The complete operational parameters utilized in this experiment are documented in Appendix H. The primary ion beam was generated by 70 eV electron ionization of argon at a source pressure of around 5×10^{-6} torr. Primary ion currents on the order order of 2×10^6 ions/second could be easily produced. Stopping potential analysis were performed

using the octopole DC bias to determine the energy axis zero and the initial ion kinetic spread. A typical stopping potential curve is shown in Figure 4.11. In this experiment the collision cell was at base pressure and the quadrupole mass filter was operated in the rf-only mode at an amplitude corresponding to m/z 20. From the first derivative plot of the stopping curve it can be seen that the initial ion kinetic energy spread is <0.4 eV (FWHM).

For reaction studies, the collision cell was filled with technical grade deuterium to a pressure of approximately 0.1 mtorr as measured with a capacitance manometer. The chamber background pressure could be maintained at ~1 x 10^{-6} torr as measured by a Bayard-Alpert ionization gauge. Reactions were monitored from zero to 20 eV in the lab frame, which corresponds to center-of-mass collision energies up to 1.8 eV. The quadrupole mass filter was operated at the lowest resolution capable of separating the primary and product ions. Since the mass difference is only 2 amu, the resolution setting limited the total ion transmission through the quad to <50%.

Exothermic ion/molecule reactions exhibit maximum cross-sections at the lowest translational energies. In addition, the negative enthalpy change may be manifested in the production of translationally hot reaction products. Both of these factors contribute to primary and product ions highly scattered about the collision center. This presents a high degree of difficulty for monitoring low energy interactions in a longitudinal ion beam instrument. Thus, by monitoring the transmitted primary and product ion flux, the performance of the ion beam instrument can be rigorously examined.

Figure 4.12 shows the results of a set of experiments in which the

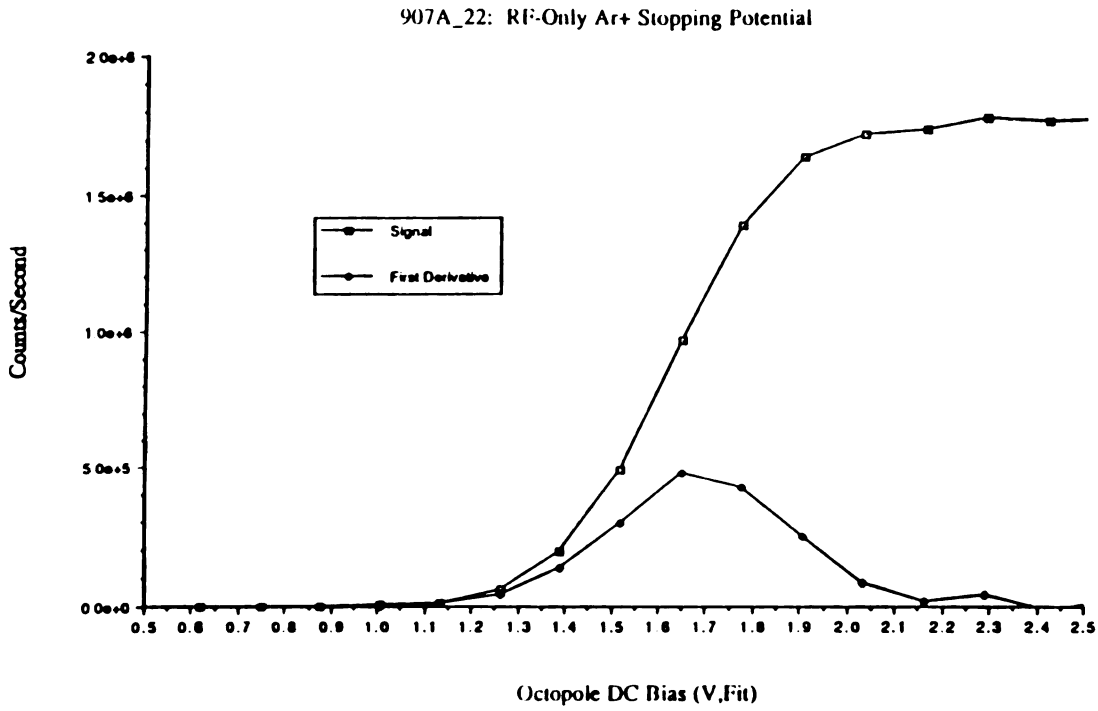

Figure 4.11. Ar^+ stopping potential.

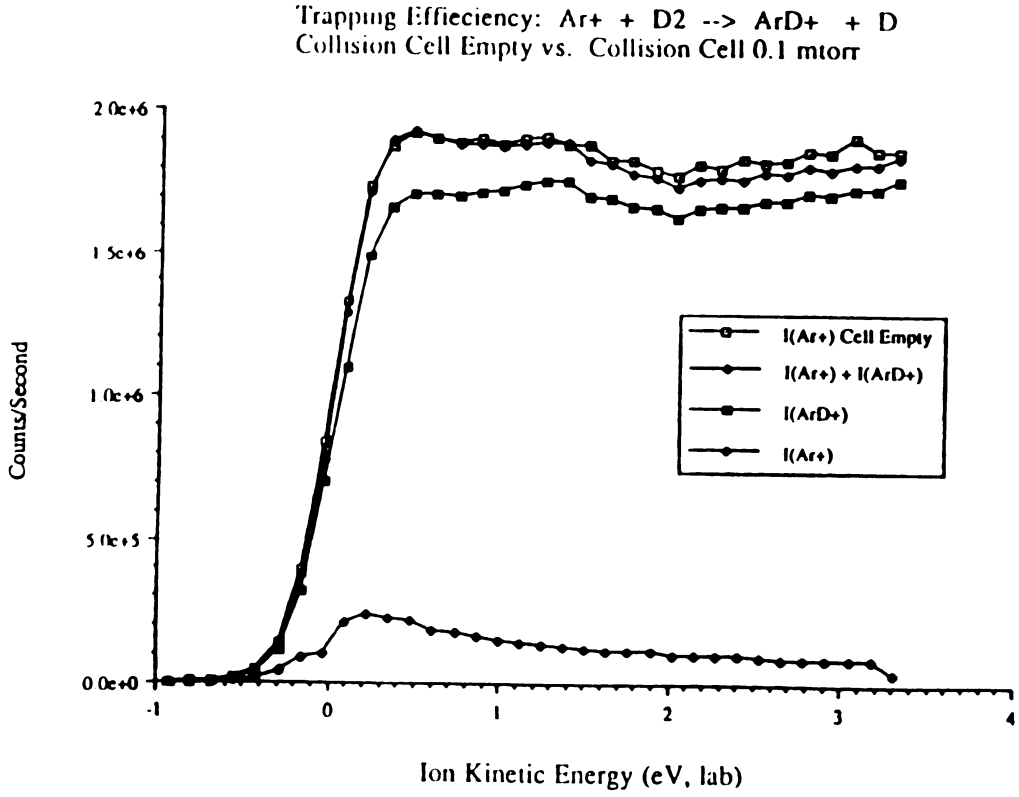

Figure 4.12. Ar^+/D_2 trapping efficiency.

instrument trapping/transmission efficiency is measured. The argon primary ion current was monitored at a function of kinetic energy with the collision cell empty. The collision cell was filled with D_2 to a pressure of 0.10 mtorr. The transmitted primary ion, Ar^+, and product ion, ArD^+, currents were then measured. As shown in Figure 4.12, the sum of the transmitted primary and product ion current compares quite well to the intensity of the primary ion beam measured in the absence of collision gas. These data verify that the dynamic trapping process in the octopole is effective collecting highly scattered primary and secondary ions even at very low interaction energies. In addition, the quadrupole mass filter exhibits very little mass dependent transmission over this particular energy and mass range.

Data were collected for the argon/deuterium reaction and converted to CM collision energies as described previously. The energy dependent relative cross-section is plotted in Figure 4.13 as an average of four separate experiments. The data exhibit a reaction maximum at the lowest energies and an exponential decay towards higher interaction energies. This is consistent with Longevin-Gioumousis-Stevenson (LGS) rate theories based on ion/neutral captures driven by ion/dipole and ion-induced/dipole attractive forces [4].

The greatest uncertainty in obtaining absolute values of the reaction cross-section comes from the inability to precisely measure the effective length of the interaction region and the absolute number density of the collision gas. To determine the effective cell length, the reaction data are plotted as a product of the cross-section and the path length (σl) as a function of the collision energy. The effective path length may be derived by comparison with accepted absolute cross-section values found in

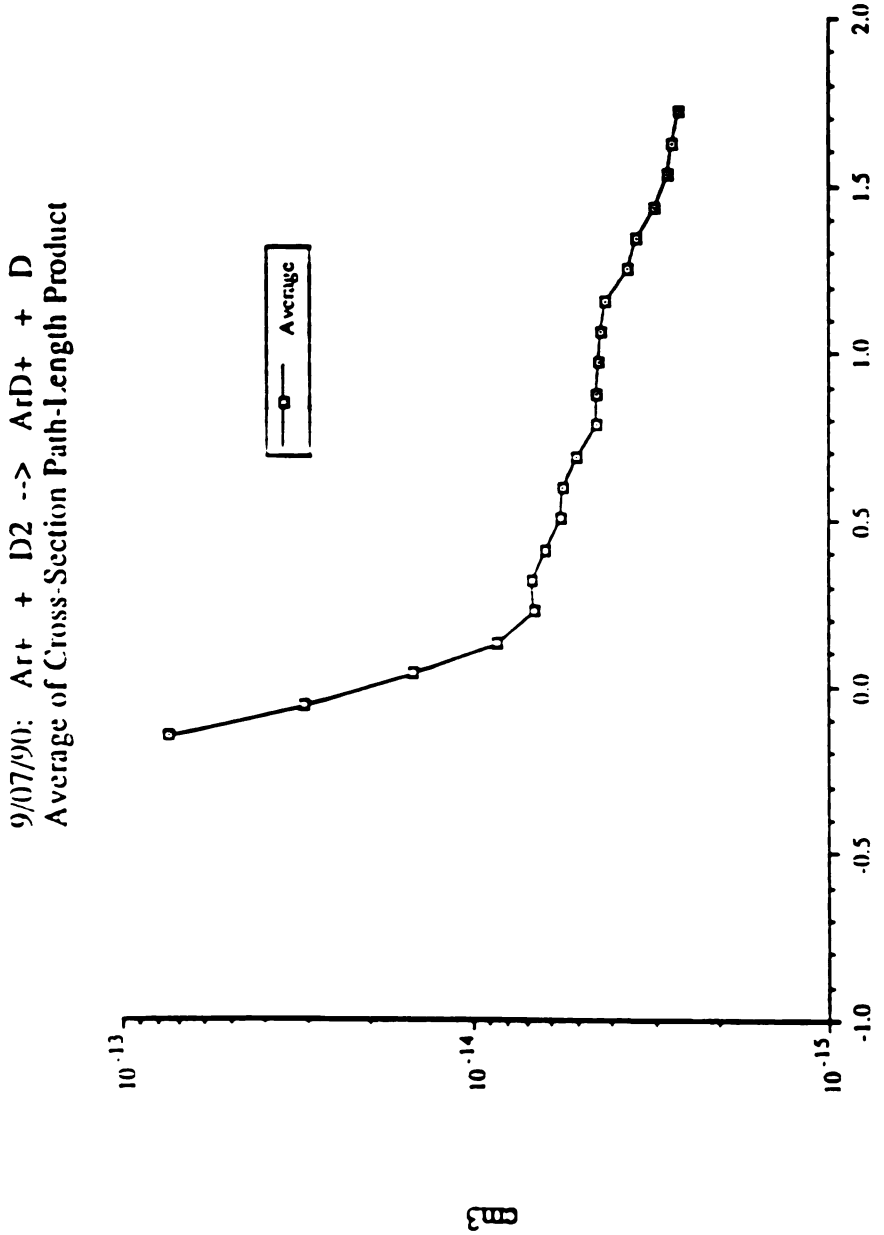

Figure 4.13. Ar^+/D_2 energy-dependent cross-section path-length product.

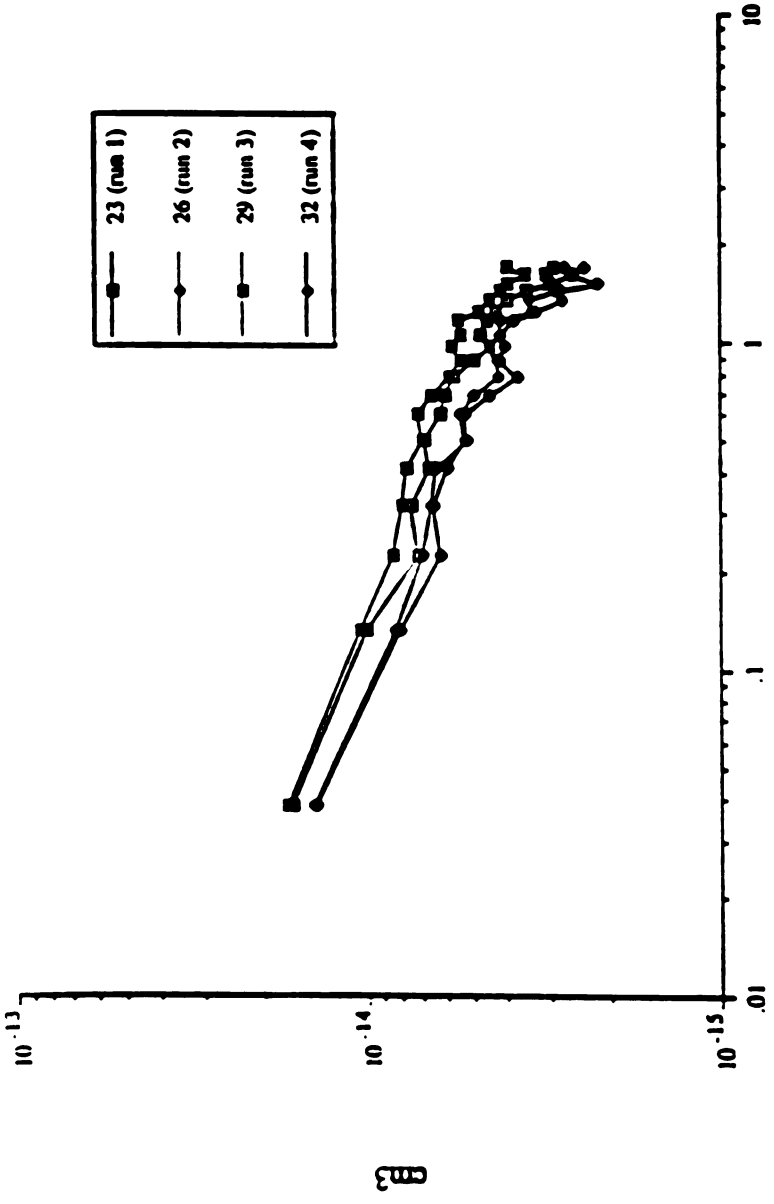

Figure 4.14. Ar^+/D_2 energy-dependent cross-section path-length product.

reference 3. The energy average effective path length is calculated at approximately 6 ±5 cm. The high level of imprecision may explained by examining the data from the four individual runs plotted in Figure 4.14. The curves for the individual runs have similar shape and run, approximately parallel, but are of slightly different magnitude.

The extent to which the curves are off-set may be explained in terms of the limited precision and accuracy of the gas number density value. It is very difficult to measure absolute pressures in the 10^{-4} torr range, as required in a beam experiment. This pressure is slightly outside the range where a capacitance manometer can make accurate and precise measurements. In addition, the capacitance manometer used in the ion beam instrument is, like many of the ion beam components, salvaged from the REsource For Unwanted Scientific Equipment (REFUSE). Therefore, a better method for pressure measurement and control should be implemented to obtain absolute cross-section measurements.

The argon/deuterium reaction demonstrated the high trapping/transmission efficiency for exothermic ion/molecule reactions attainable with the MSU ion beam instrument. Because of imprecise determinations of the neutral gas pressure, high precision absolute cross-section values were not obtained. However, it must be emphasized that the inability to obtain absolute cross-section values does not preclude the measurement of accurate endothermic reaction threshold energies.

An effective instrument for the energy-dependent mesurement of both endothermic and exothermic relative reaction cross-sections has been constructed and demonstrated. The instrument should now be employed in the energy-dependent study of new ion/molucule reactions.

LIST OF REFERENCES
Chapter 4

1. Ervin, K.; Armentrout, P.B. *J. Chem. Phys.* **1985**,*83*, 166.

2. Armentrout, P.B.; Beauchamp, J.L. *J. Chem. Phys.*, **1981**, *74*, 2819.

3. Ervin, K.; Loh, S. ; Aristov,N.; Armentrout, P. *J. Phys Chem*, **1983**, *87*, 3593.

4. Gioumousis, G.; Stevenson, D.*J. Chem. Phys.*, **1958**, *29*, 294.

Appendix A

Measurements of the CH5-DF Analyzer Energy Acceptance

The range of ion kinetic energies from an ion source that can be accepted and effectively transmitted by an analyzer is known as the energy acceptance. The energy acceptance for the CH5-DF was measured by using the using the Combination EI/FD/FI ion source operated in the EI mode. Ar^+ was used as the test ion. Since the EI source produces a narrow kinetic energy distribution ion beam, the ion source accelerating potential was varied to present a range of ion kinetic energies to the BE analyzer while the transmitted ion intensity was recorded.

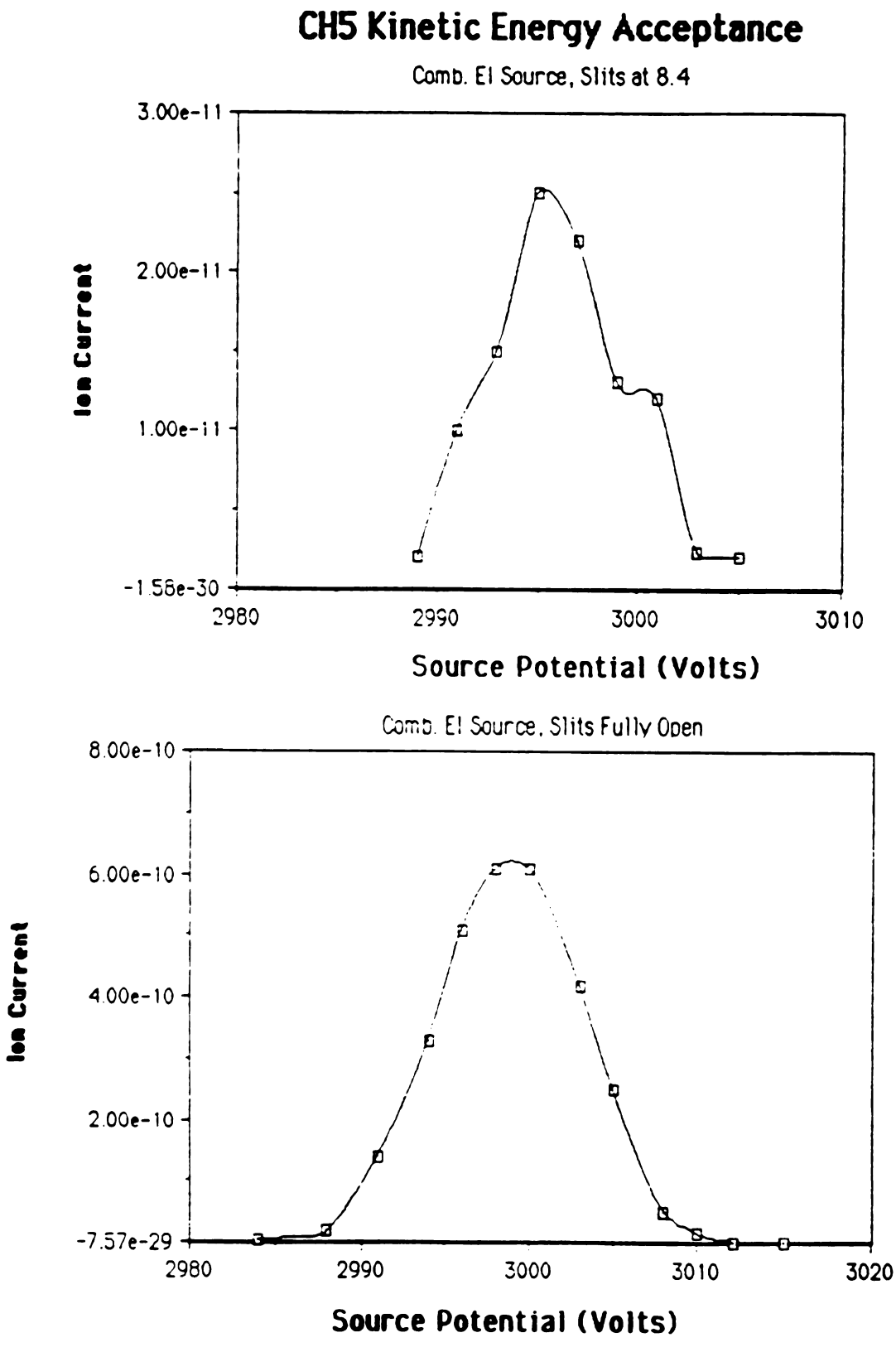

Figure A.1. Ion kinetic energy acceptance at 3000 V acceleration

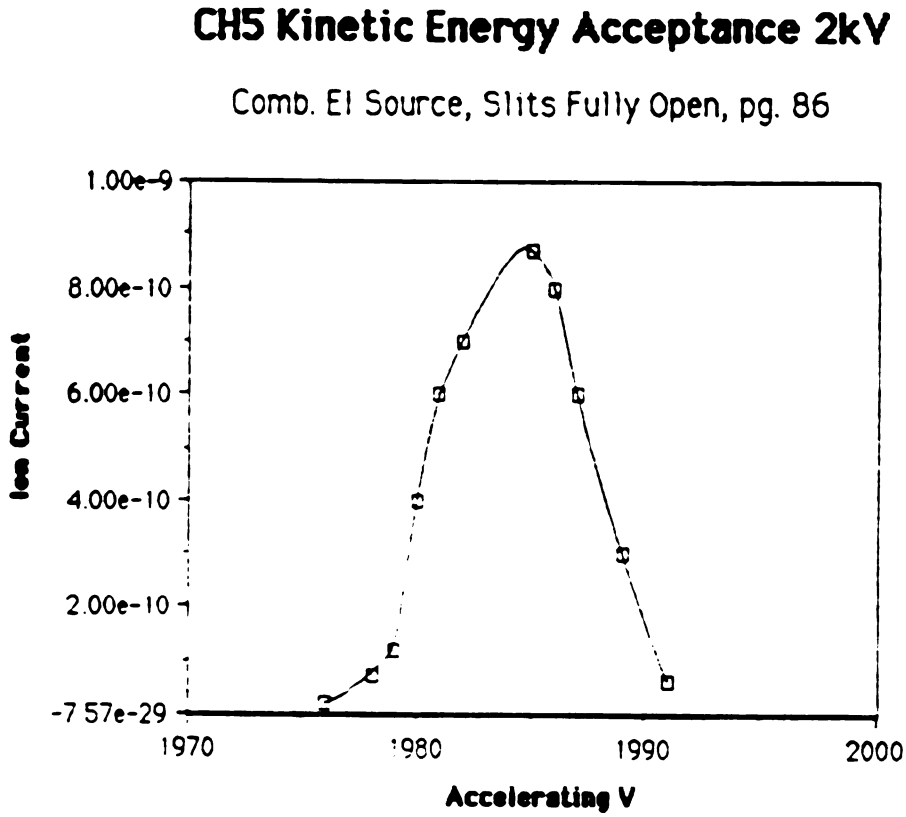

Figure A.2. Ion kinetic energy acceptance at 2000 V acceleration.

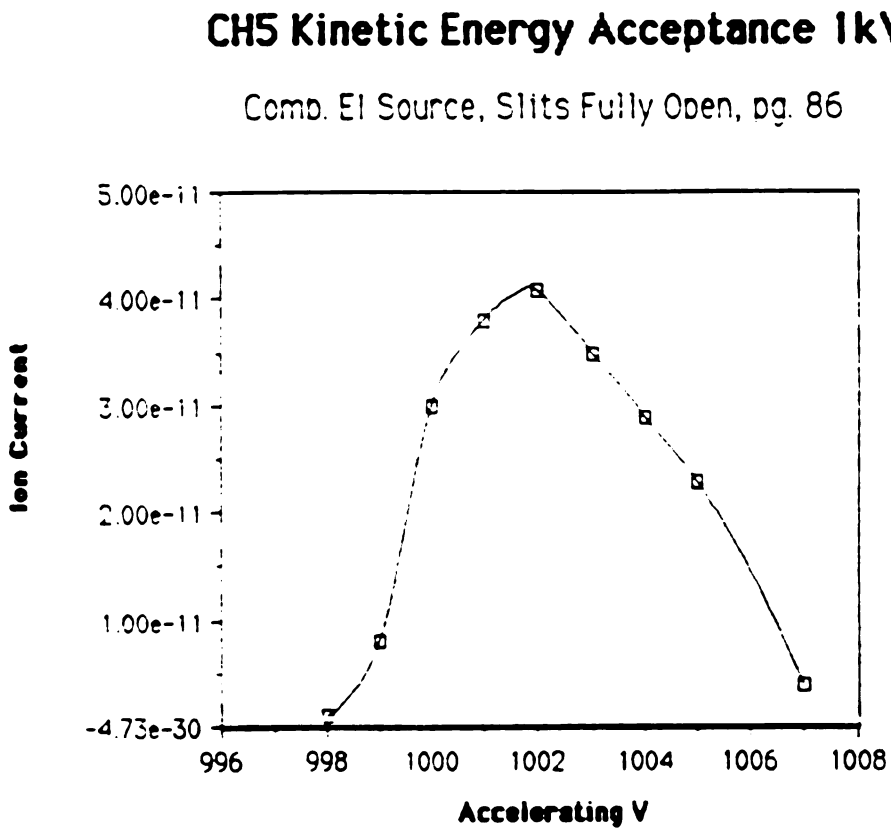

Figure A.3. Ion kinetic energy acceptance at 1000 V acceleration.

Appendix B

Magnetic Hall Probe Calibration

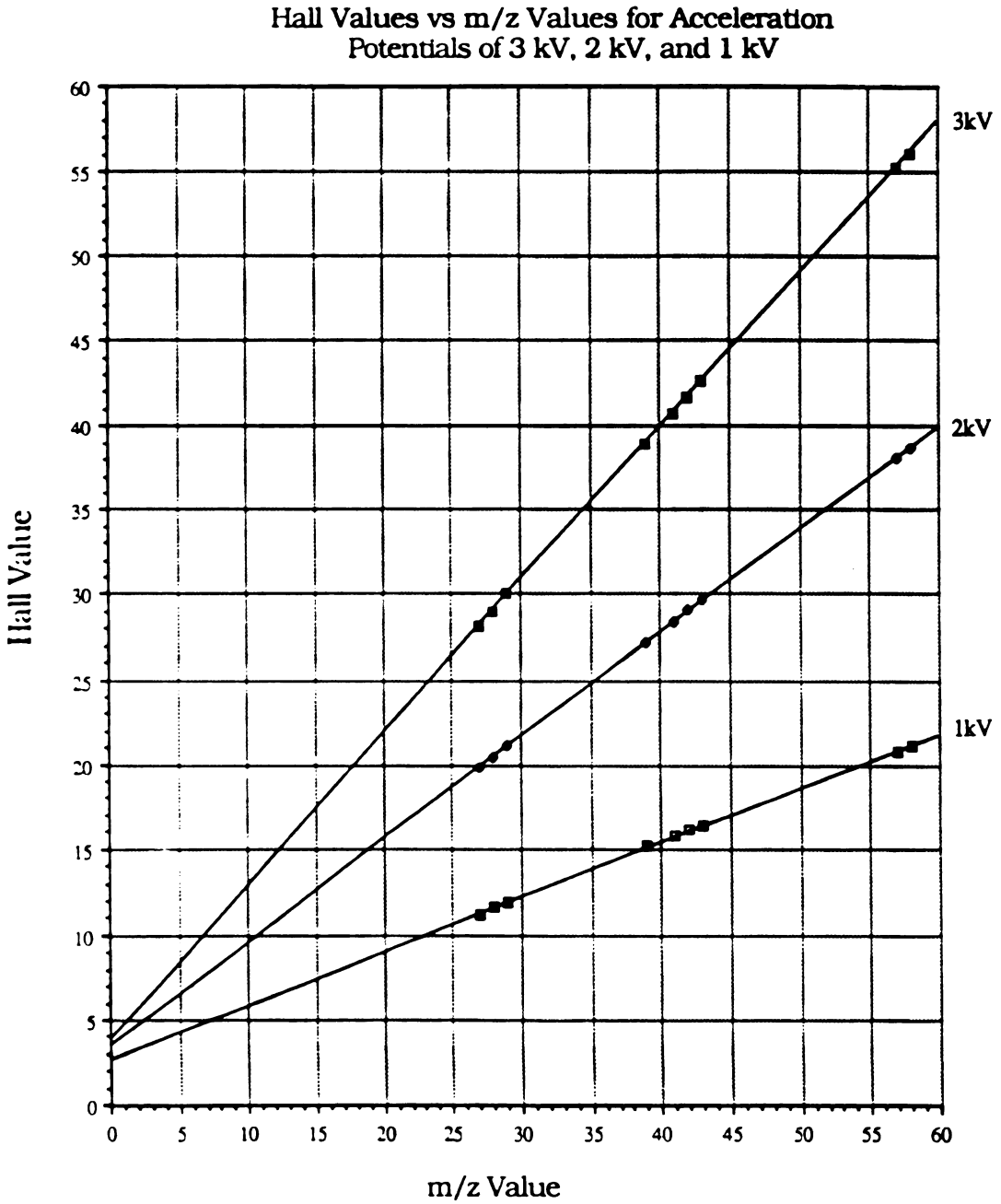

Figure B.1. Hall values vs. m/z values for 3,2, and 1 kV acceleration.

Appendix C

Mass Discrimination in a RF-Only Quadrupole

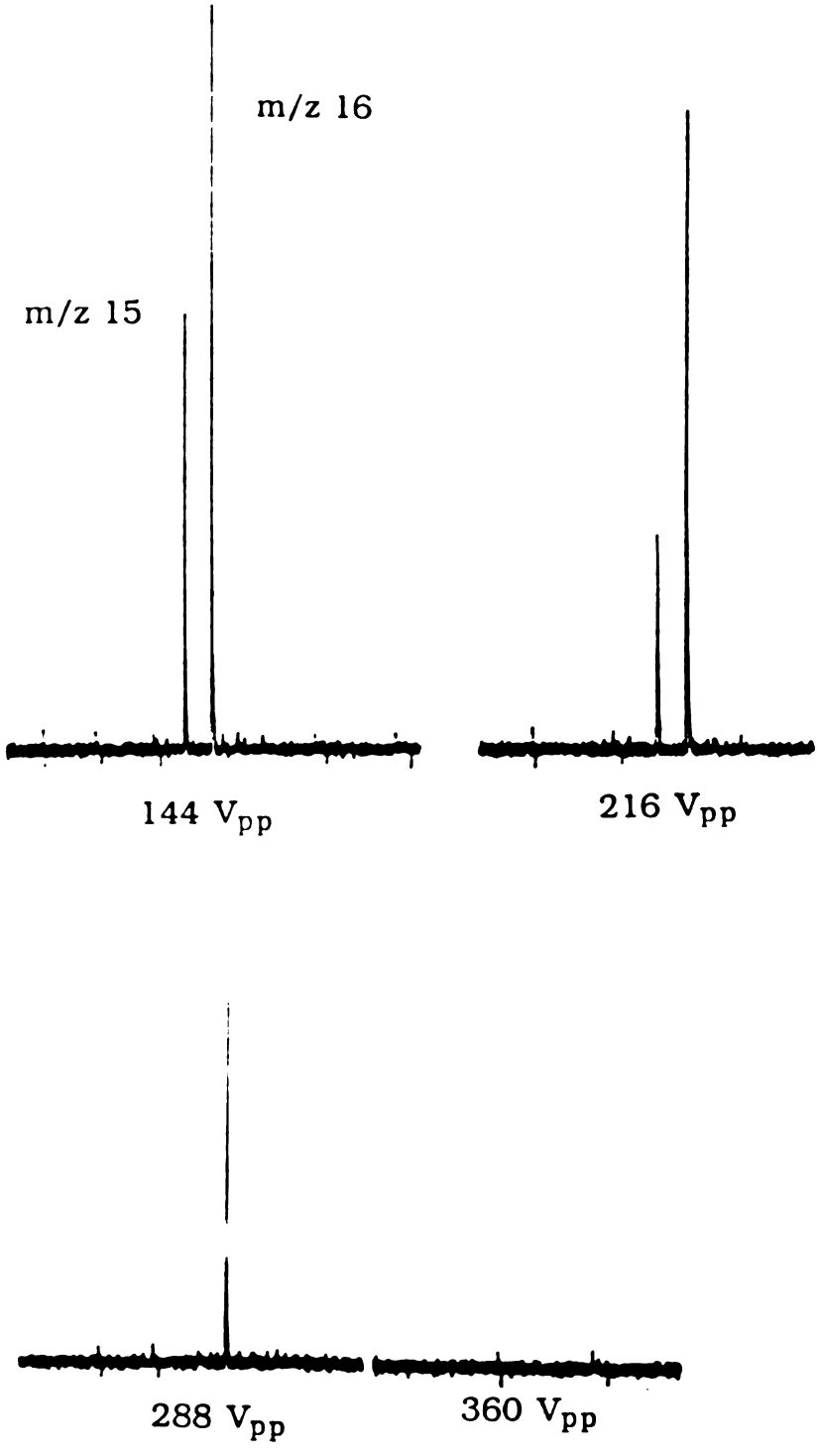

Figure C.1. Effect of RF amplitude on transmission in Extrel Quad.

Appendix D

Retarding Field Energy Analyzers

Parallel grid retarding field energy analyzers were used to evaluate ion energy spreads as described in Chapter 3. Most of the data in this appendix were generated using argon gas in the Intensitron EI source or in the combination EI/FD/FI source operated in the EI mode. Although various grid configurations were employed, the general configuration may be found in Chapter 3.

Figures D.1 and D.2 show the stopping potential curves obtained using a three-grid analyzer with both sectors (BE) in operation and the object/image slits fully open, and ions generated in the combination source. The stopping potential curves for 1000, 2000, and 3000 V acceleration is shown. The analyzer was constructed from moderate transmission (<80%) grids which were spaced 3.5 mm and 7 mm apart, respectively. Detection was accomplished using a 4800 series Channeltron biased at -2900 volts. Figure D.3 shows the stopping potential obtained using with the source potential at 3000 V and the object/image slits at 8.4.

Figure D.4 shows the stopping potential obtained with a three-grid analyzer placed at the entrance to the electric sector approximately 30 mm following the intermediate ß slit. The grids were spaced 3.3 and 6.3 mm apart, respectively. In this experiment the image (source) slit was fully open and the combination source was used. Figure D.5 shows the stopping potential after the magnetic sector for the Intensitron source with the image slit wide open. Figure D.6 shows the curve with the source slit at 9.0.

A CEMA detector was used in place of the Channeltron in the retarding potential analyzer immediately following the magnetic sector. The CEMA input was biased at -1500 V and was located 7 mm behind the stopping grid. The retarding field distance was 3.5 mm. Figure D.7 shows the stopping potential obtained with this device, when the Intensitron source was used with the slit wide open.

A mask was installed on the last element in the source acceleration lens to restrain the z-dimension (length) of the ion beam profile. With the source (image) slit at 9.0, the beam profile dimension presented to the magnet was approximately 1.5 mm by 0.1 mm. The stopping potential obtained with the CEMA analyzer is shown in Figure D.8. The grid spacings were changed to produce a stopping field 1 mm long with the CEMA detector. The stopping potential obtained using the masked source with the slit fully open is shown in Figure D.9.

The retarding potential analyzer was configured with the retarding field 7 mm long and a distance of 7 mm to the input face of the CEMA. The analyzer was placed at the end of the deceleration lens following the B and E sectors. The stopping potential obtained using this configuration is shown in Figure D.10.

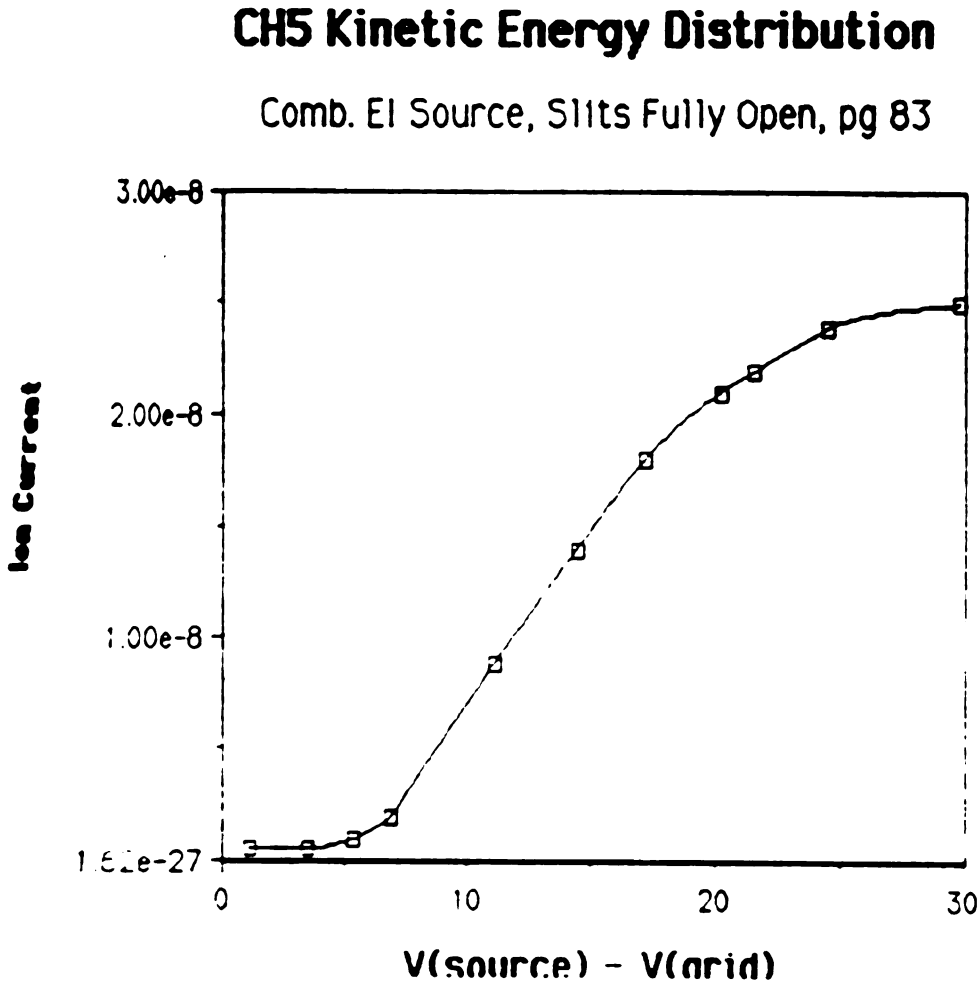

Figure D.1. Retarding potential curve for 3 keV ions.

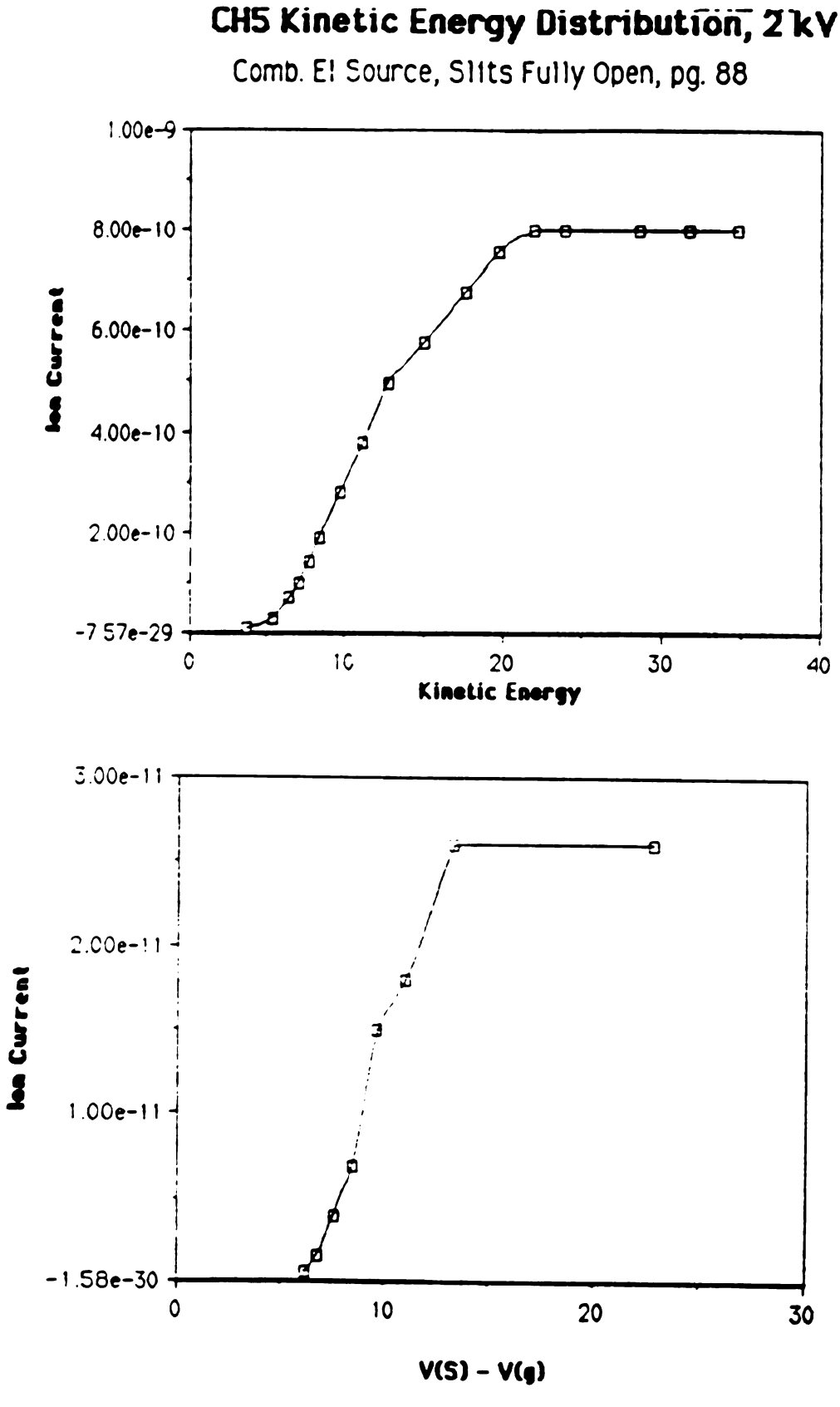

Figure D.2. Retarding potential curve for 2 keV and 1 keV ions.

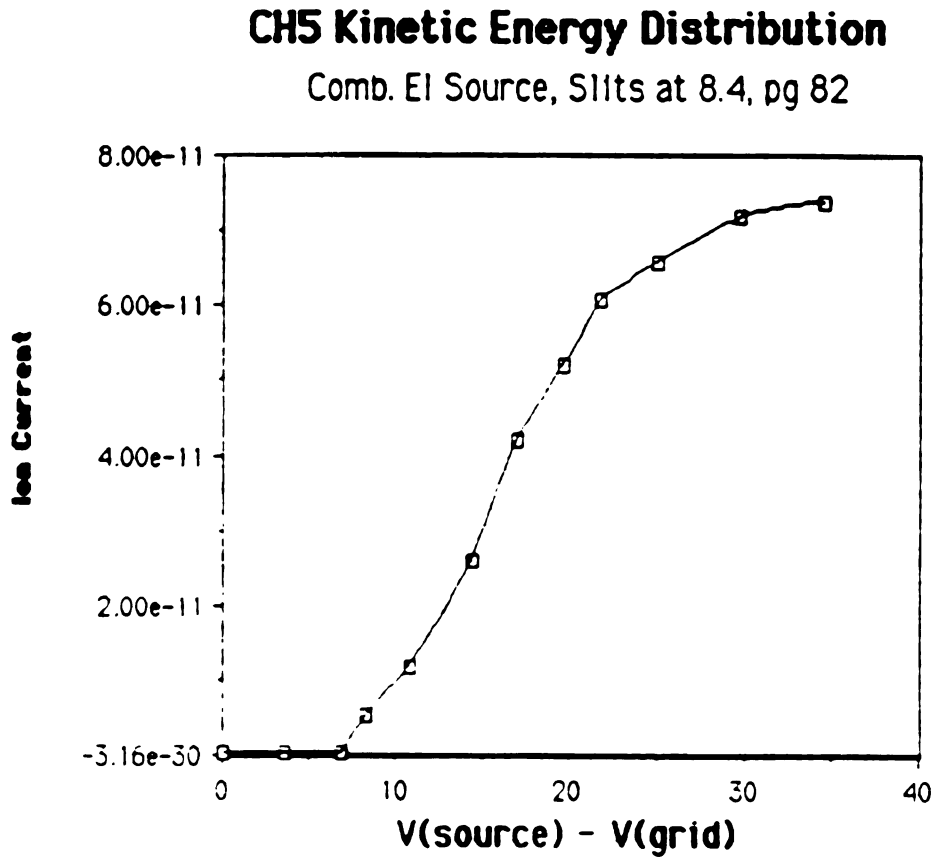

Figure D.3. Retarding potential curve for 3 keV ions, slits at 8.4.

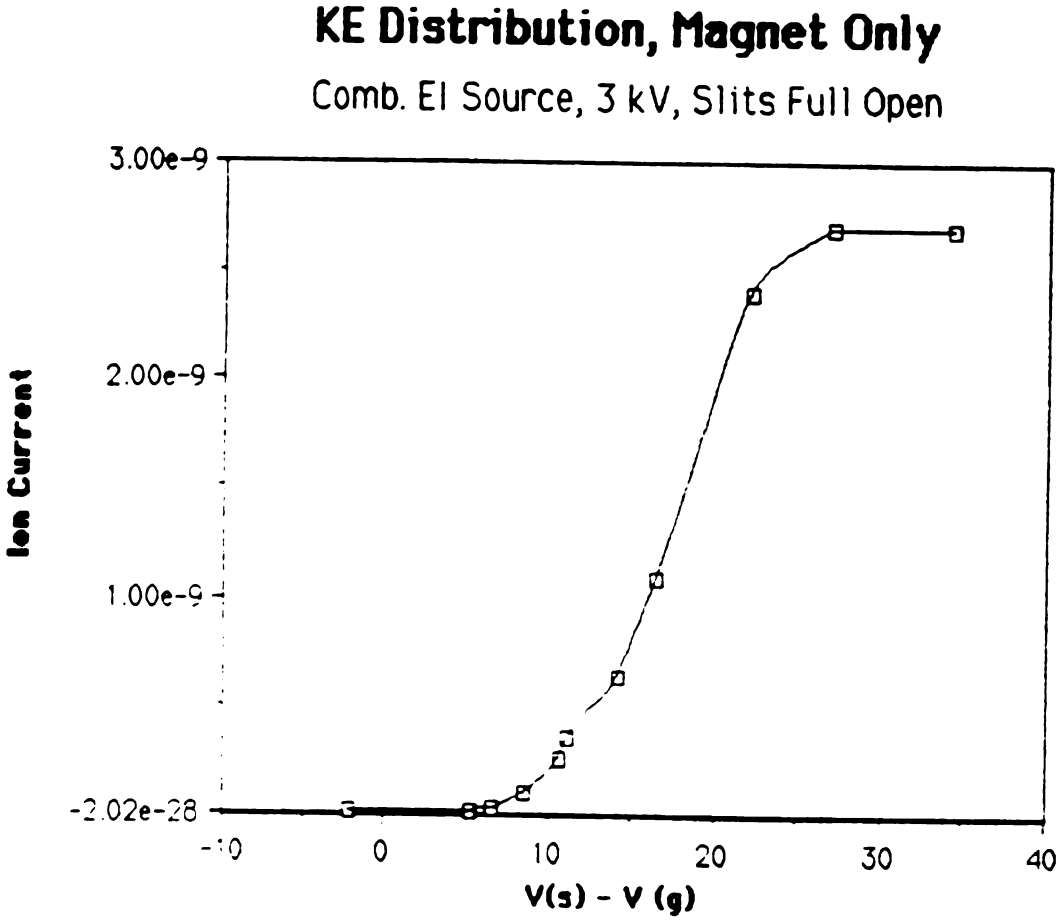

Figure D.4. Retarding potential curve for 3 keV ions, magnet only.

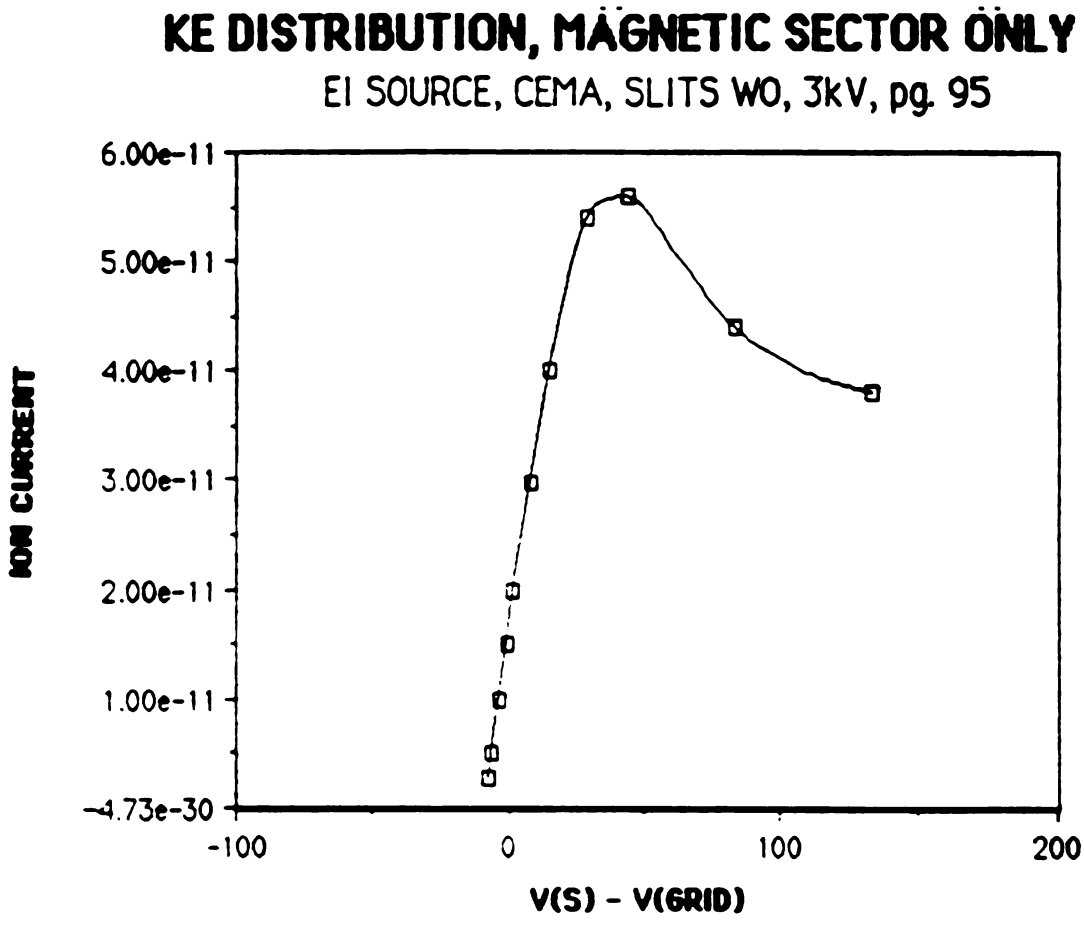

Figure D.5. Retarding potential curve for 3 keV ions, CEMA detector.

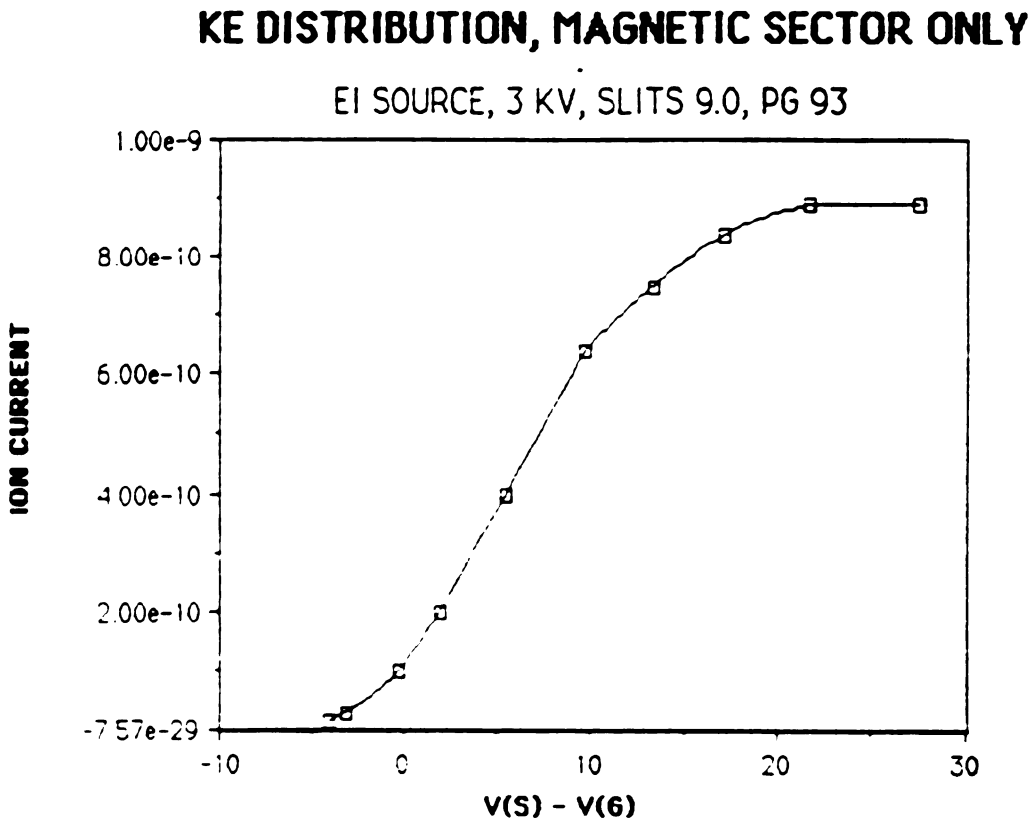

Figure D.6. Retarding potential curve for 3keV ions, slits at 9.0.

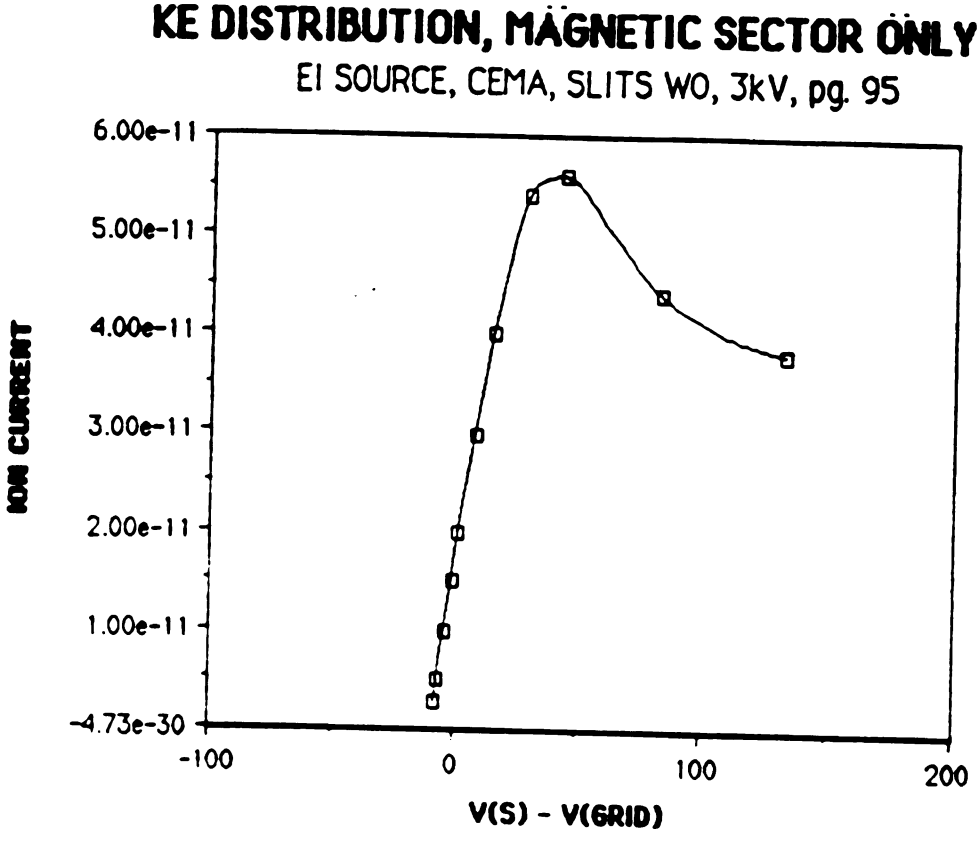

Figure D.7. Retarding potential curve for 3keV ions, CEMA detector, magnet only.

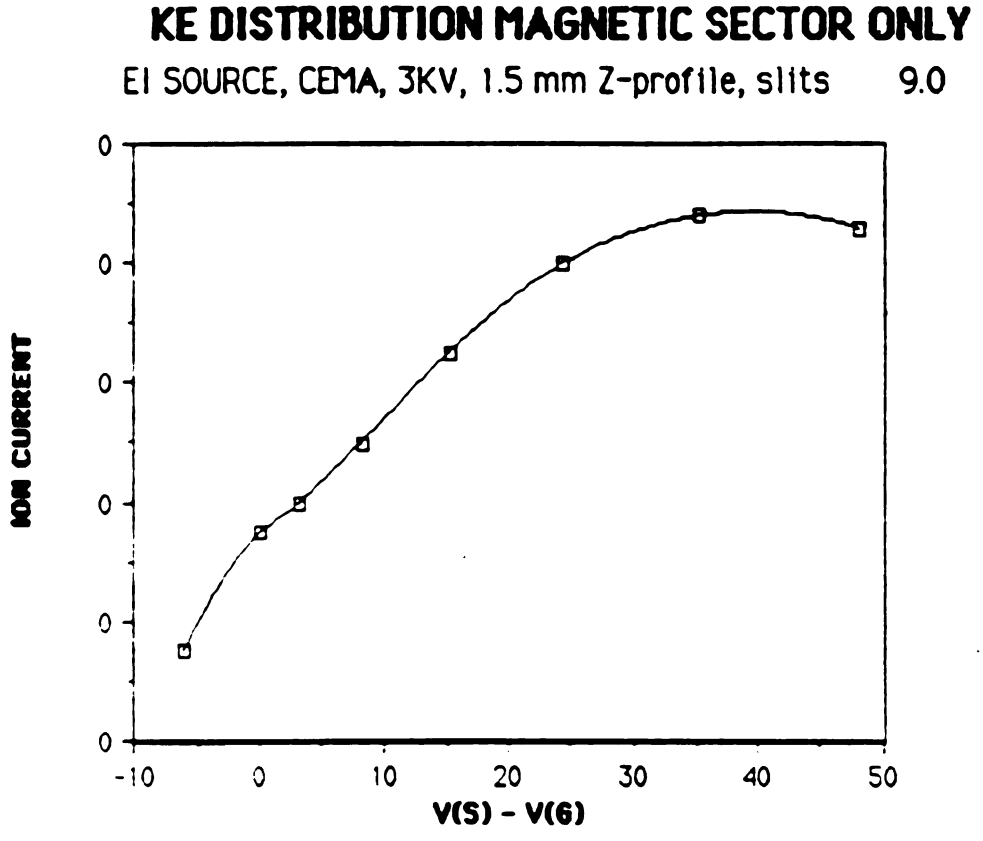

Figure D.8. Retarding potential curve for 3keV ions, slits at 9.0, magnet only, CEMA detector, 1.5 mm source z-mask.

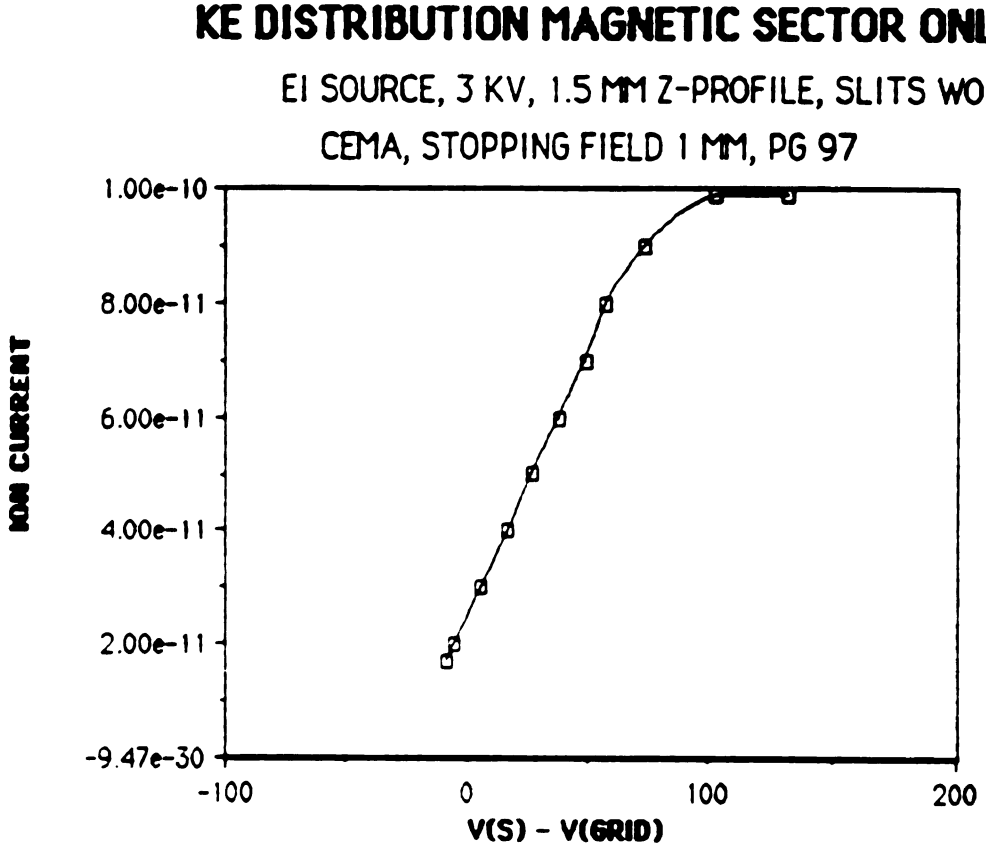

Figure D.9. Retarding potential curve for 3keV ions, slits at open, magnet only, CEMA detector, 1.5 mm source z-mask, 1 mm field.

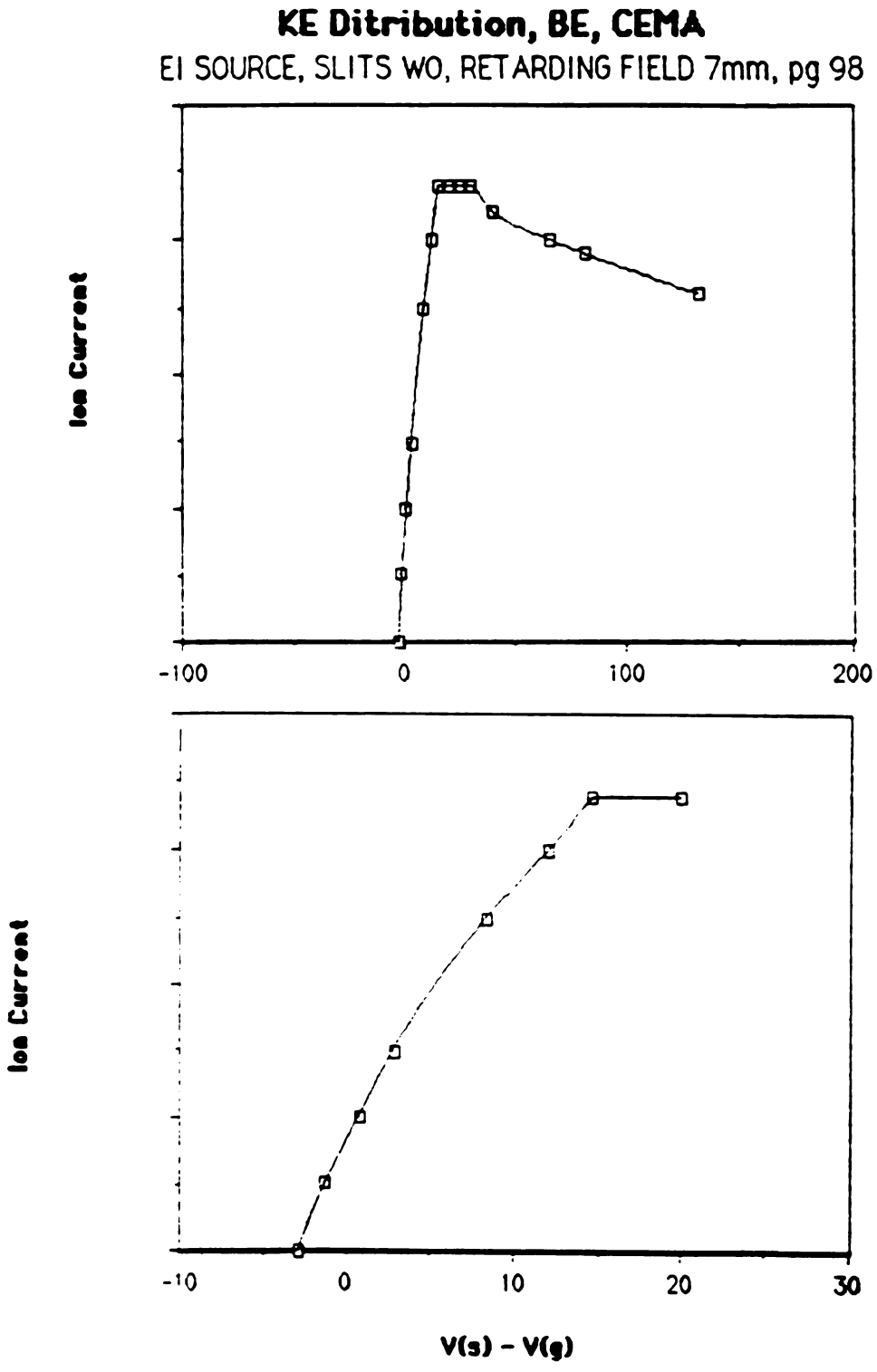

Figure D.10. Retarding potential curve for 3keV ions, slits open, magnet only, CEMA detector, 1.5 mm source z-mask, 7 mm field.

Appendix E

Mn_2^+ Collision Induced Dissociation

The operational parameters used in the CID study are listed in Table E.1. The ionization energy (IE) of nitrogen was used to calibrate the electron energy in the Intensitron source under field conditions identical to those used for the production of Mn_2^+. The m/z 28 ion current is plotted as a function of nominal electron energy in Figure E.1. The nominal electron energy is calculated from the energy setting of the emission control unit of the CH5. The extrapolated onset for ion production is approximately 14.2 eV. The accepted literature value for the nitrogen IE is 15.57 eV. Therefore, a 1.37 ev correction must be applied to the nominal electron energy. Interesting low energy features in the m/z 28 ion current as a function of nominal electron energy are found in Figure E.2.

Table E.1. Ion beam instrument parameters for Mn_2^+ CID experiment.

Experiment	(Mn2)+ CID			
Source Type	Intensitron		RF V(rms-amp)	5
P(source)	2.5 E-5 torr		SWR	1.05
I(e-)	21.2 uA		TUNER (T,I,A)	B, 10, G
Repeller	0		RF Power (HM-9)	0.95 W
Extractor	0		Transfer 1	717 volts
Shield	0		Transfer 2	974
Source Z1 (L,R)	001, 036		Transfer 3	1023
S Lens (L,R)	007, 031		Transfer 4	906
Source R	9.2		Transfer 5	983
Source Z2 (L,R)	094, 099		Transfer 6	---
E symmetry	425		Transfer 7	0
TIC	0.85 range 0.3		Transfer 8	0
Vaccel (Ua/Ub)	846 (1010 V)		Transfer 9	807
Hall	37.1		Quad DC Bias	924
Z1	-0.484		P(collision cell)	0.10 mtorr
Z2	-0.993		P(Chamber A)	base
R	7.03		P(Chamber B)	7.2 E-6 torr
Einzel	733		P(Chamber C)	base
Injection	704		Daly CD	27.04 kV
RF Freq.	2.4815 M Hz		Daly PMT	1000

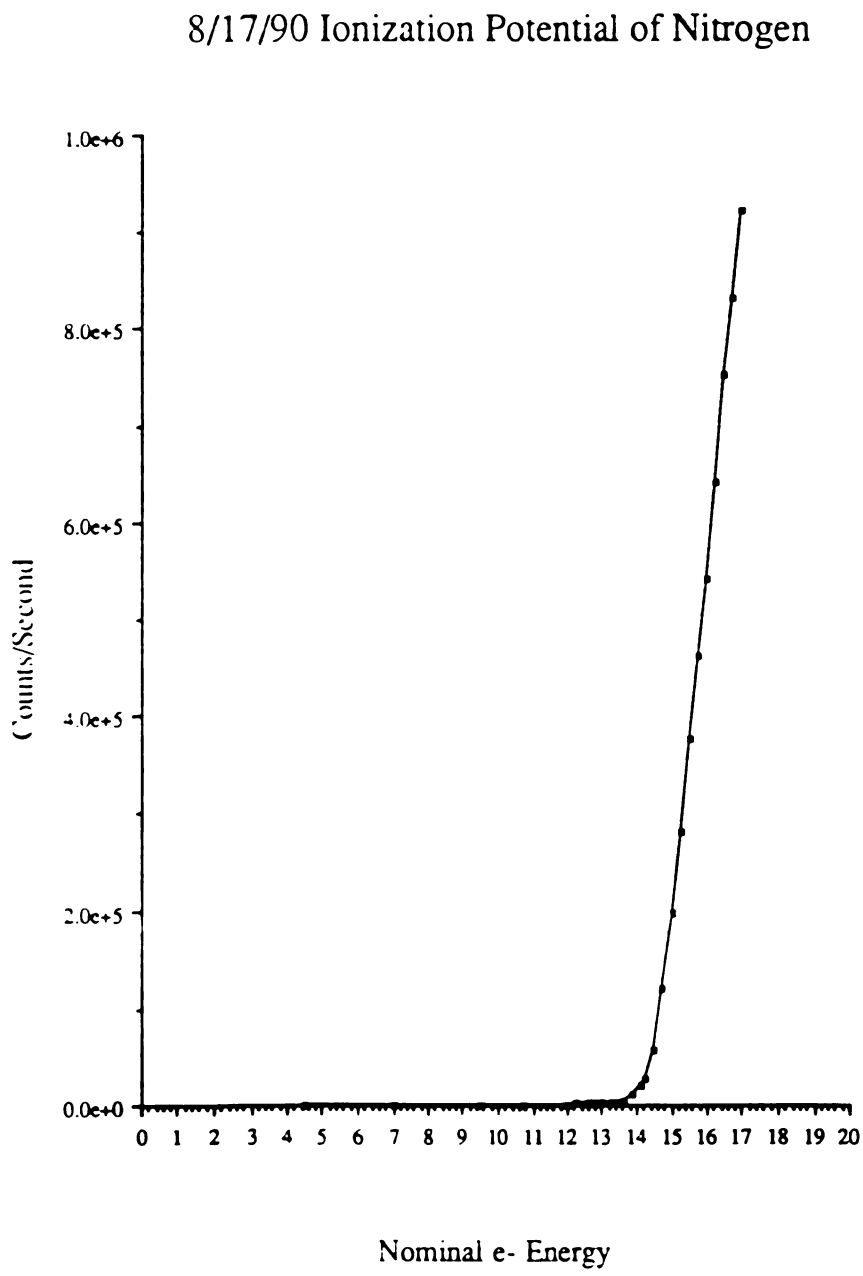

Figure E.1. Ion current for m/z 28 vs. nominal electron energy.

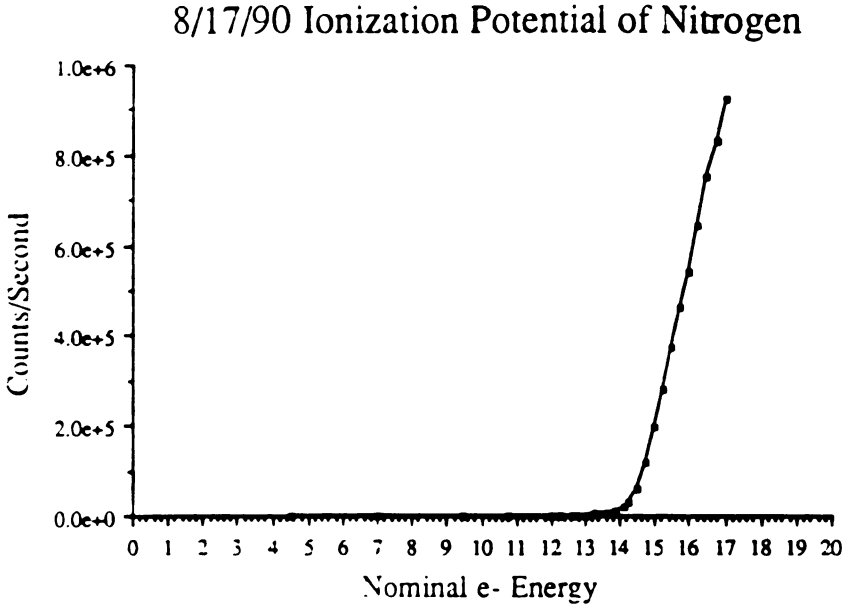

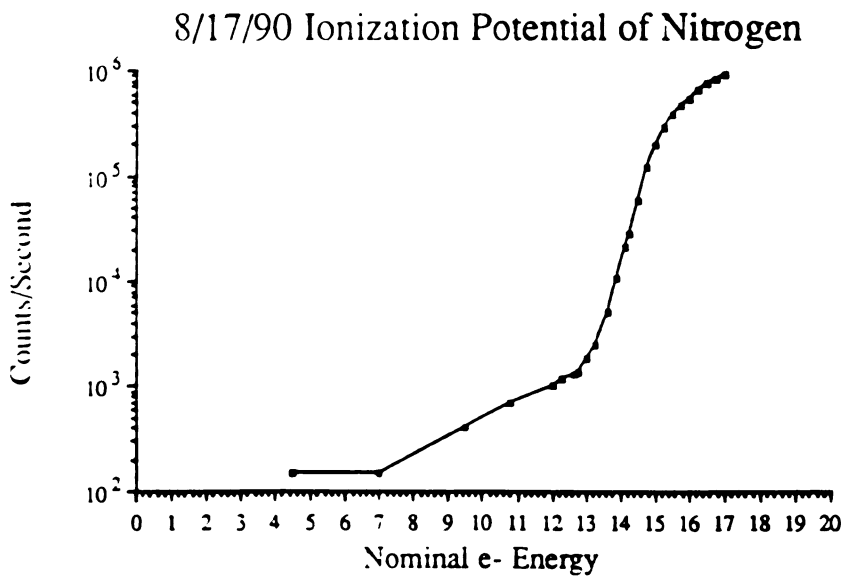

Figure E.2. Plots of m/z 28 ion current vs. nominal electron energy.

Appendix F

Octopole Characterization

Ion stopping curves were generateed by ramping the octopole DC bias through the ion source accelerating potential. Many operational parameters, such as rf amplitude, were varied to characterize the octopole. Ar^+ at a nominal energy of 1000 eV was used as a probe ion for these studies. Figure F.1. shows the effect of the rf amplitude. Figures F.2 and F.3 show the effect of tune bias. The tune bias is the octopole DC potential at which the deceleration optics were optimized for maximum transmission prior to the octopole DC ramp. Figure F.4, Figures F.5-F.7 show the effect of the deceleration lens injection element DC bias. The stopping potential reproducibility is shown in Figure F.8.

The effect of the source extraction element potential is shown in Figure F.9. Curves for runs 20 and 27 were obtained with an extraction element setting of 0.0, whereas the intermediate run 24 was performed with an extraction element setting of 2.0.

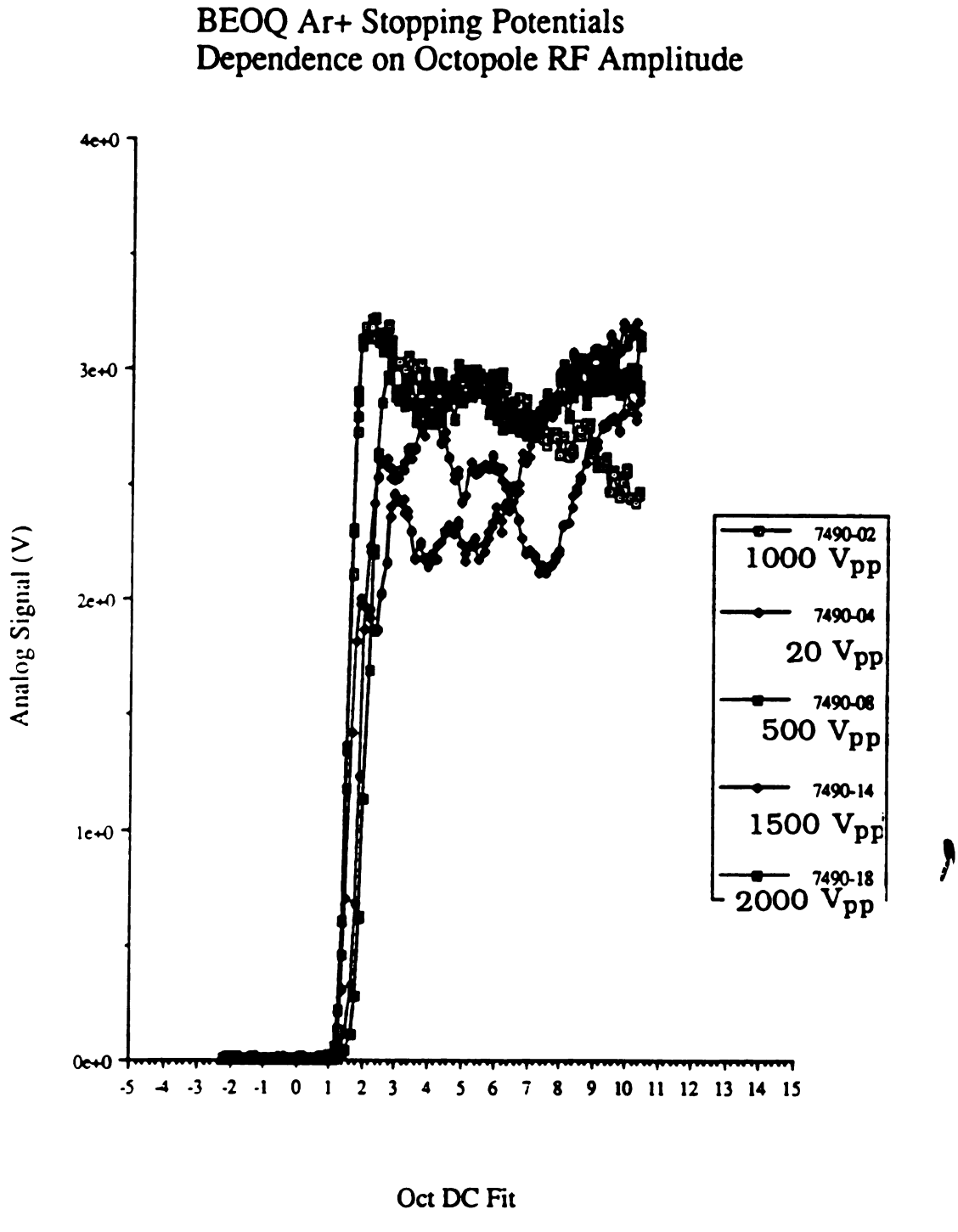

Figure F.1. Effect of octopole rf amplitude on stopping potential.

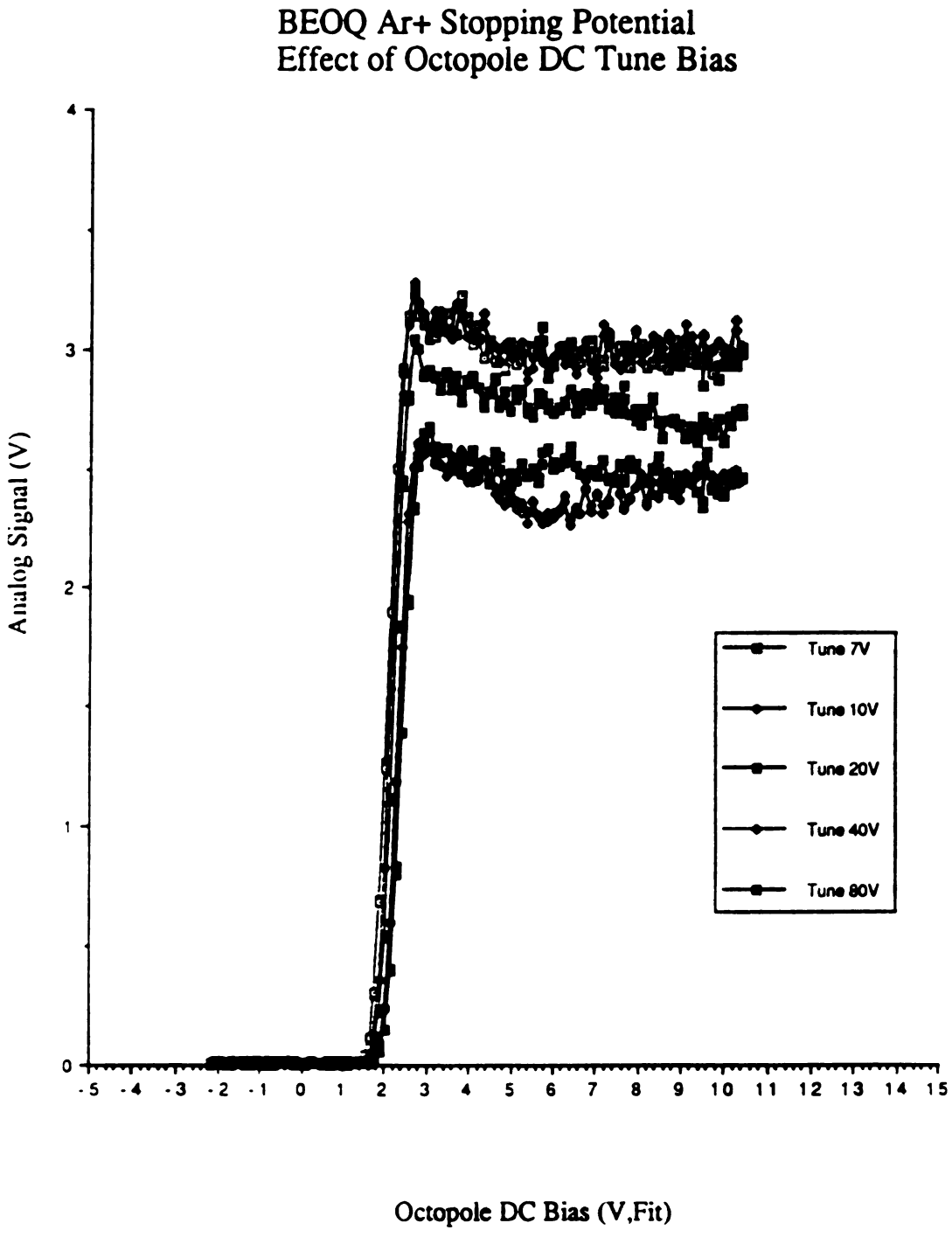

Figure F.2. Effect of octopole DC tune bias on stopping potential.

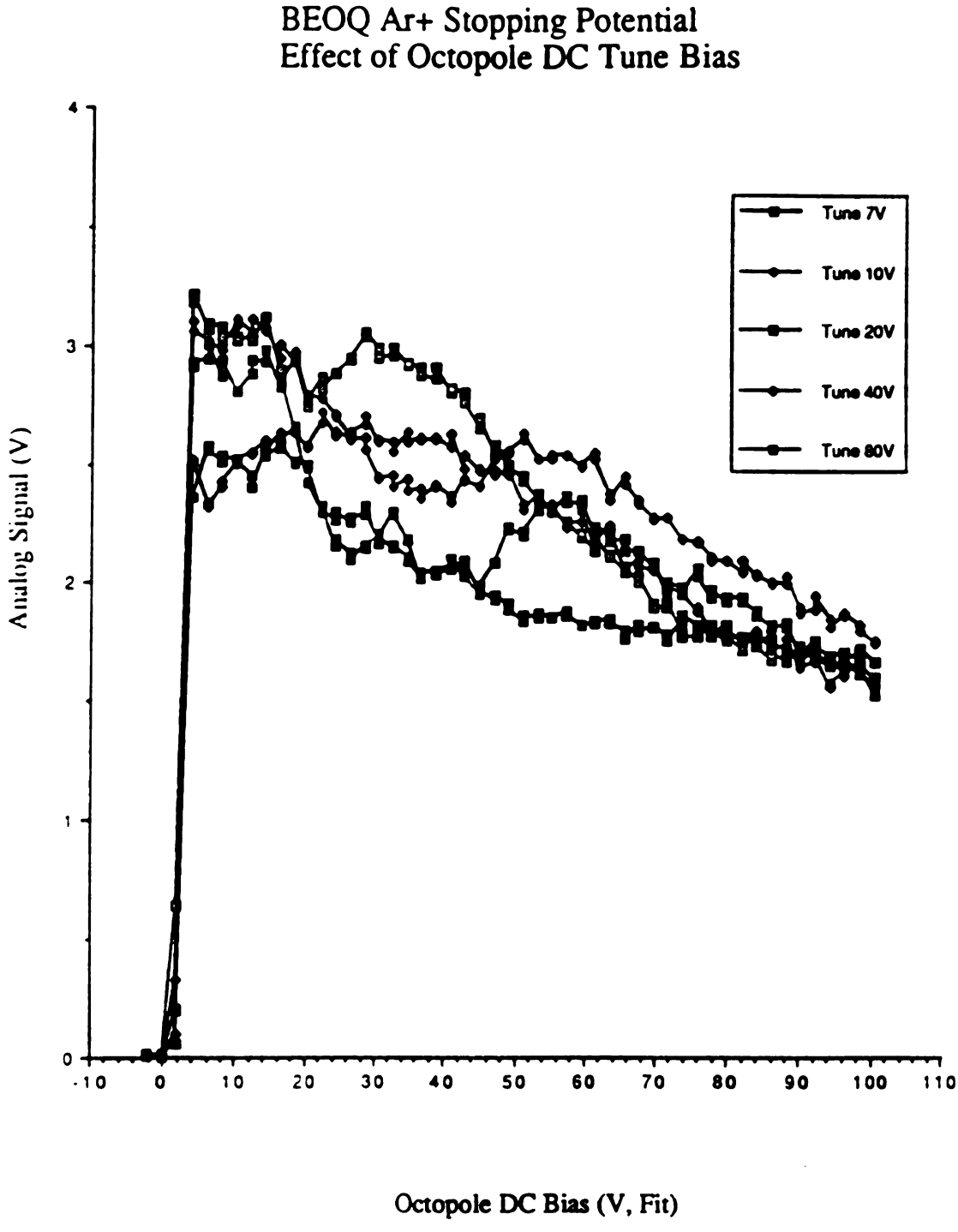

Figure F.3. Effect of DC tune bias on high energy transmission.

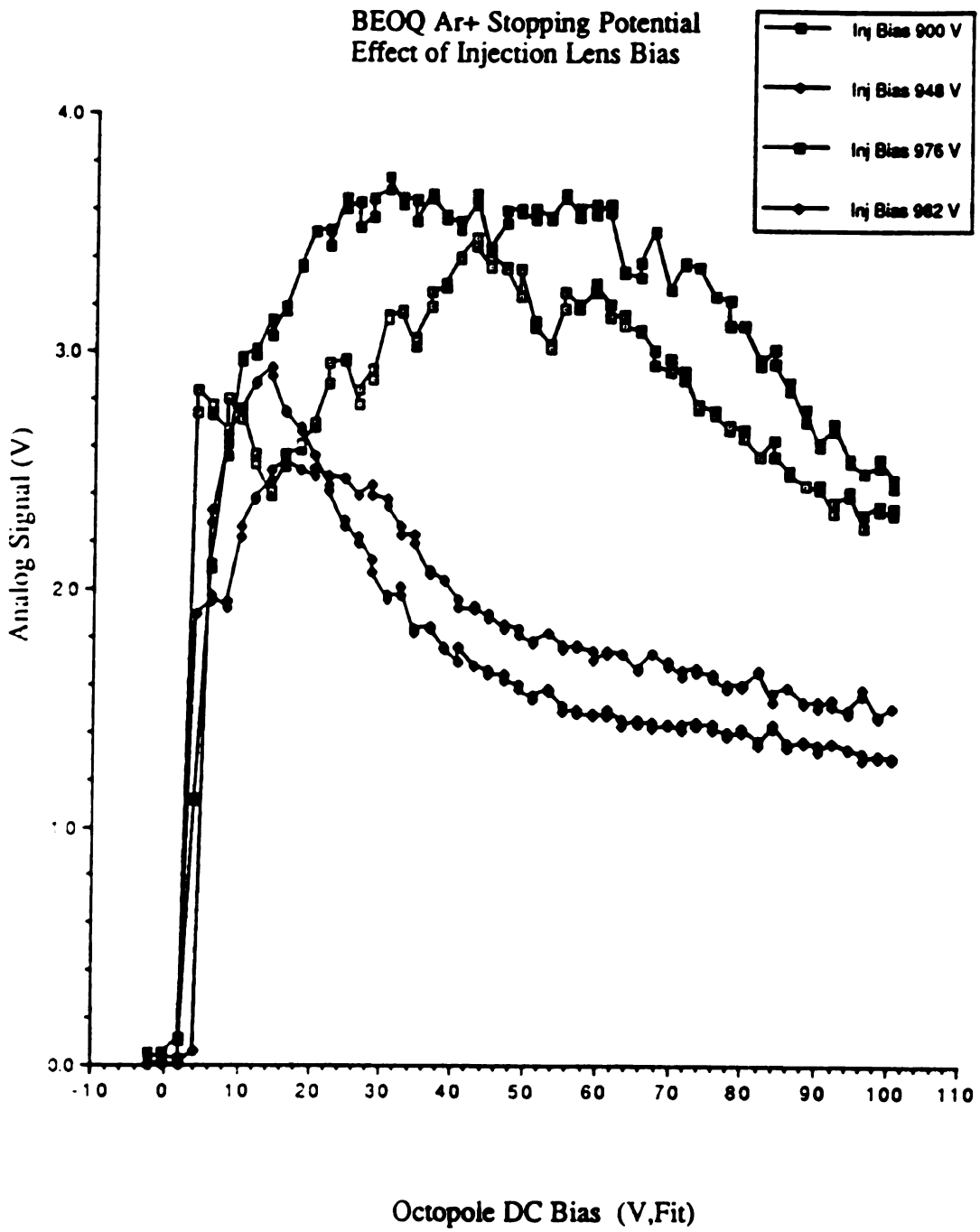

Figure F.4. Effect of ion injection energy on stopping potential.

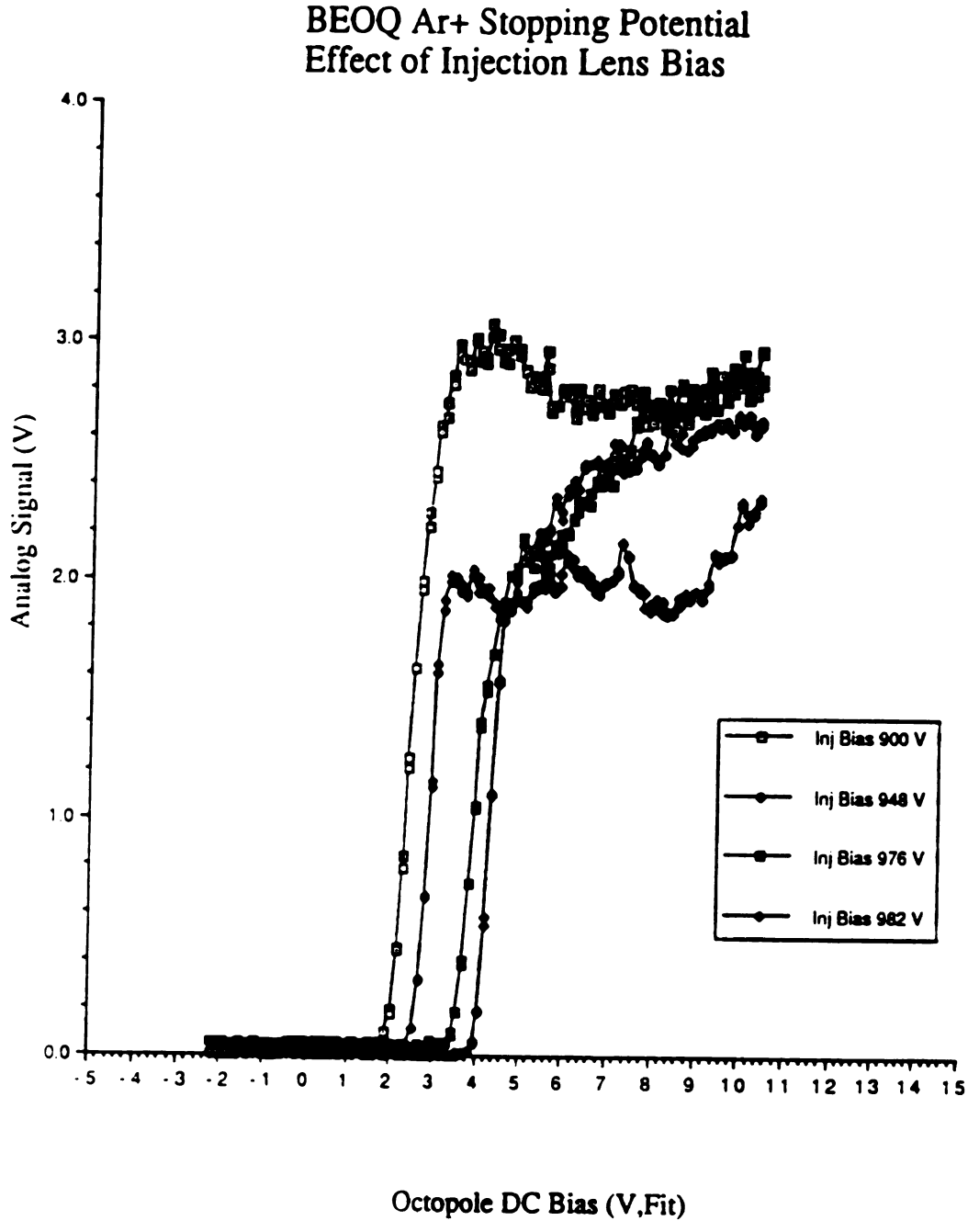

Figure F.5. Effect of ion injection energy high energy transmission.

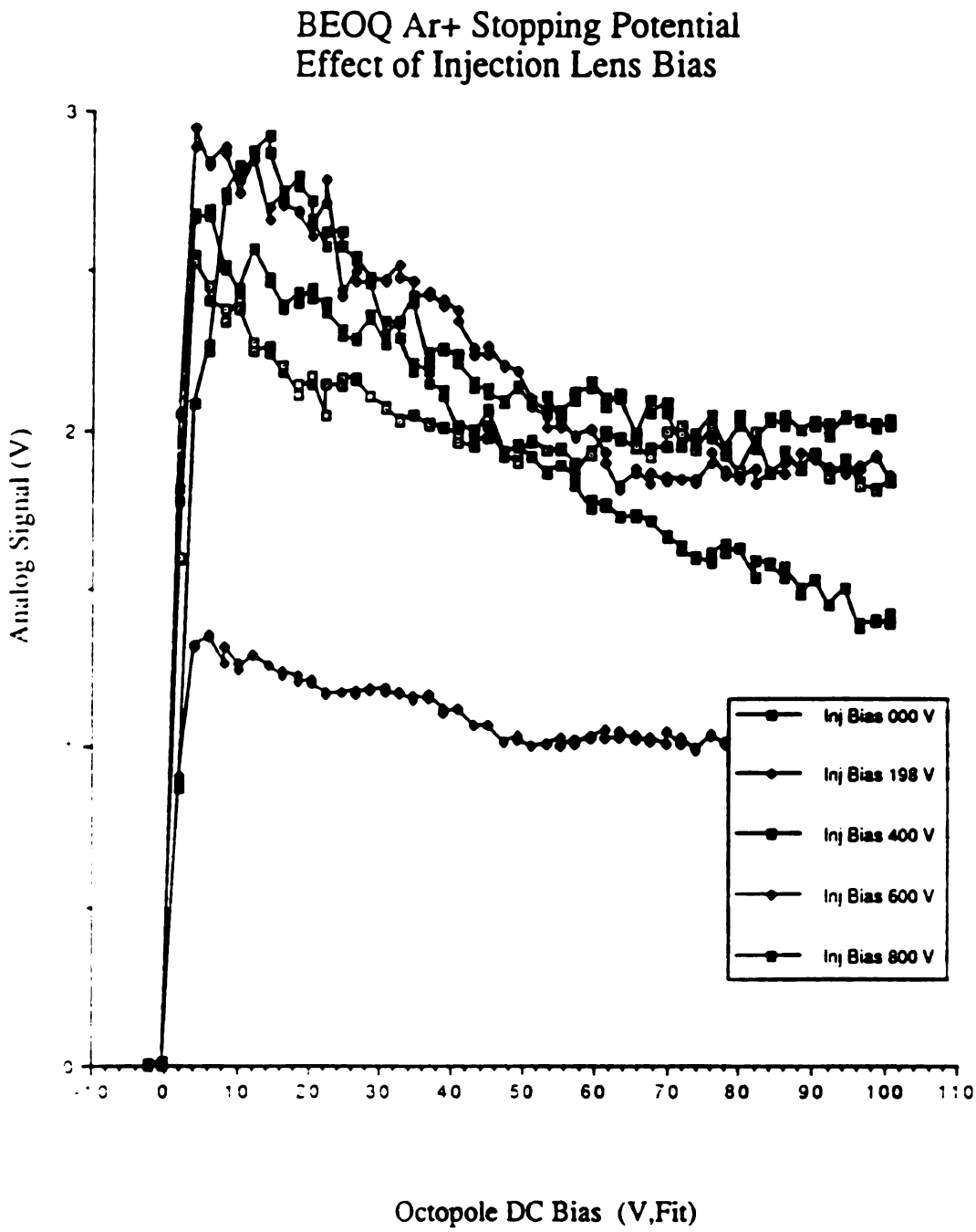

Figure F.6. Effect of ion injection energy on stopping potential.

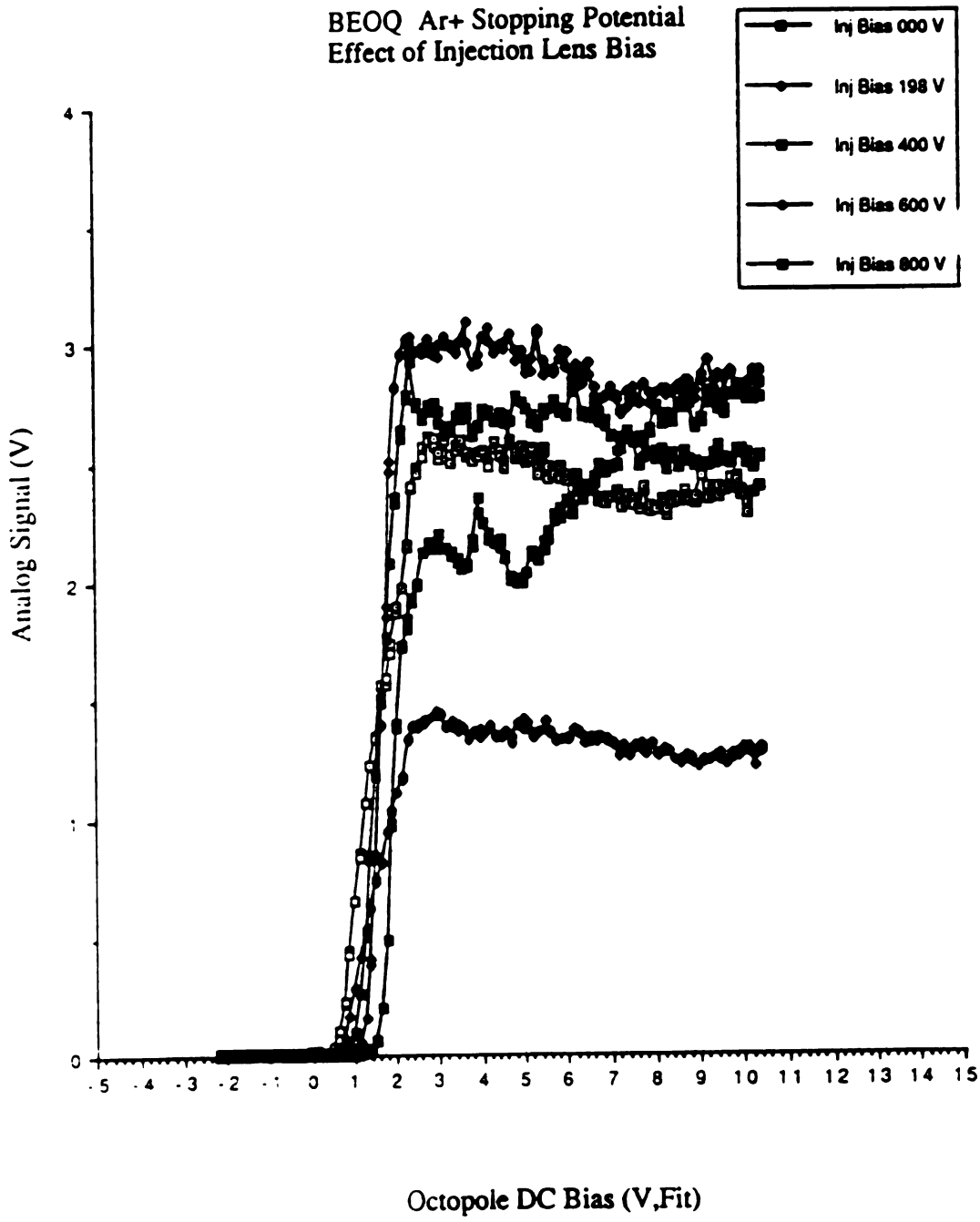

Figure F.7. Effect of ion injection energy high energy transmission.

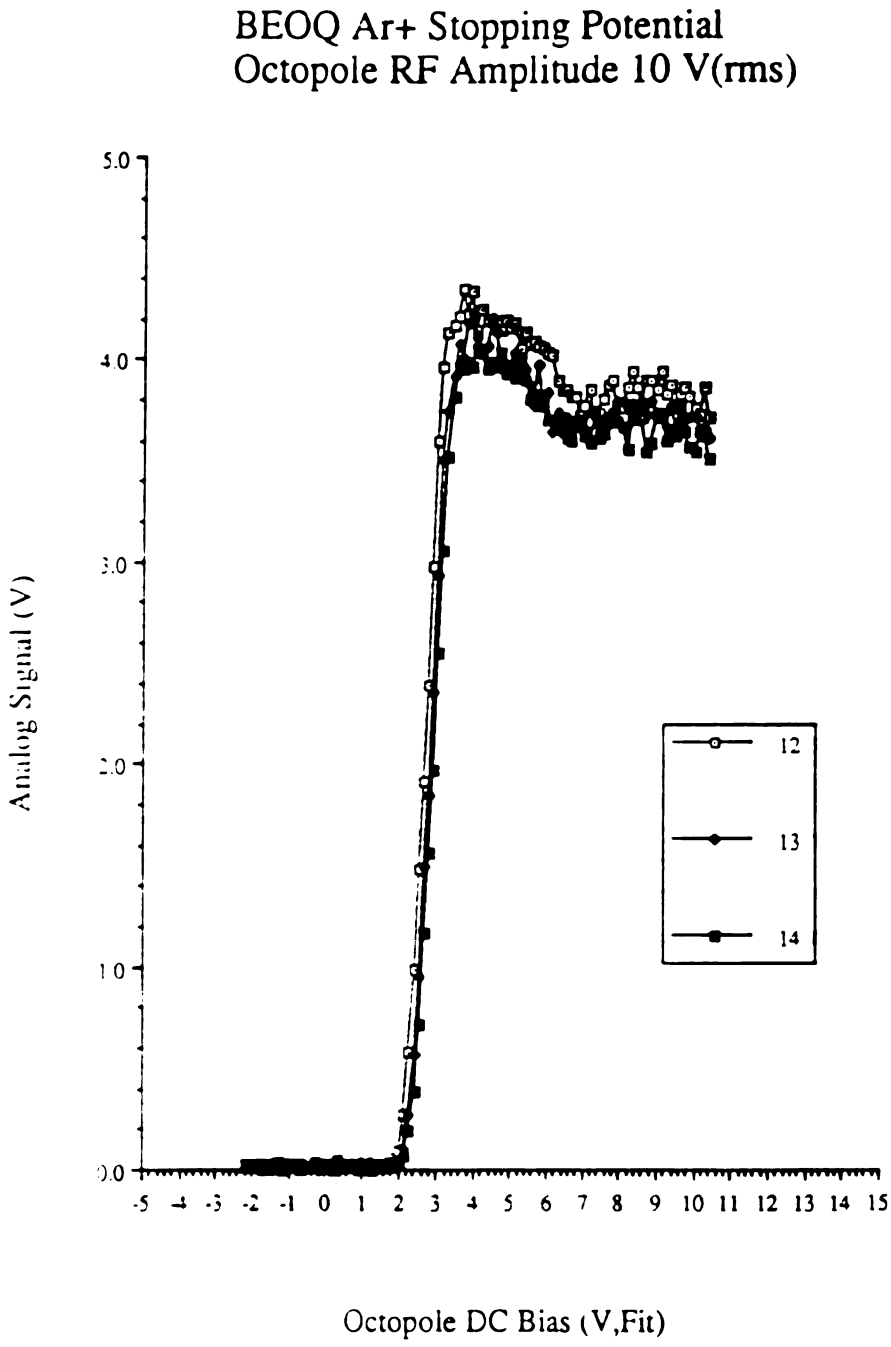

Figure F.8. Stopping potential reproducibility.

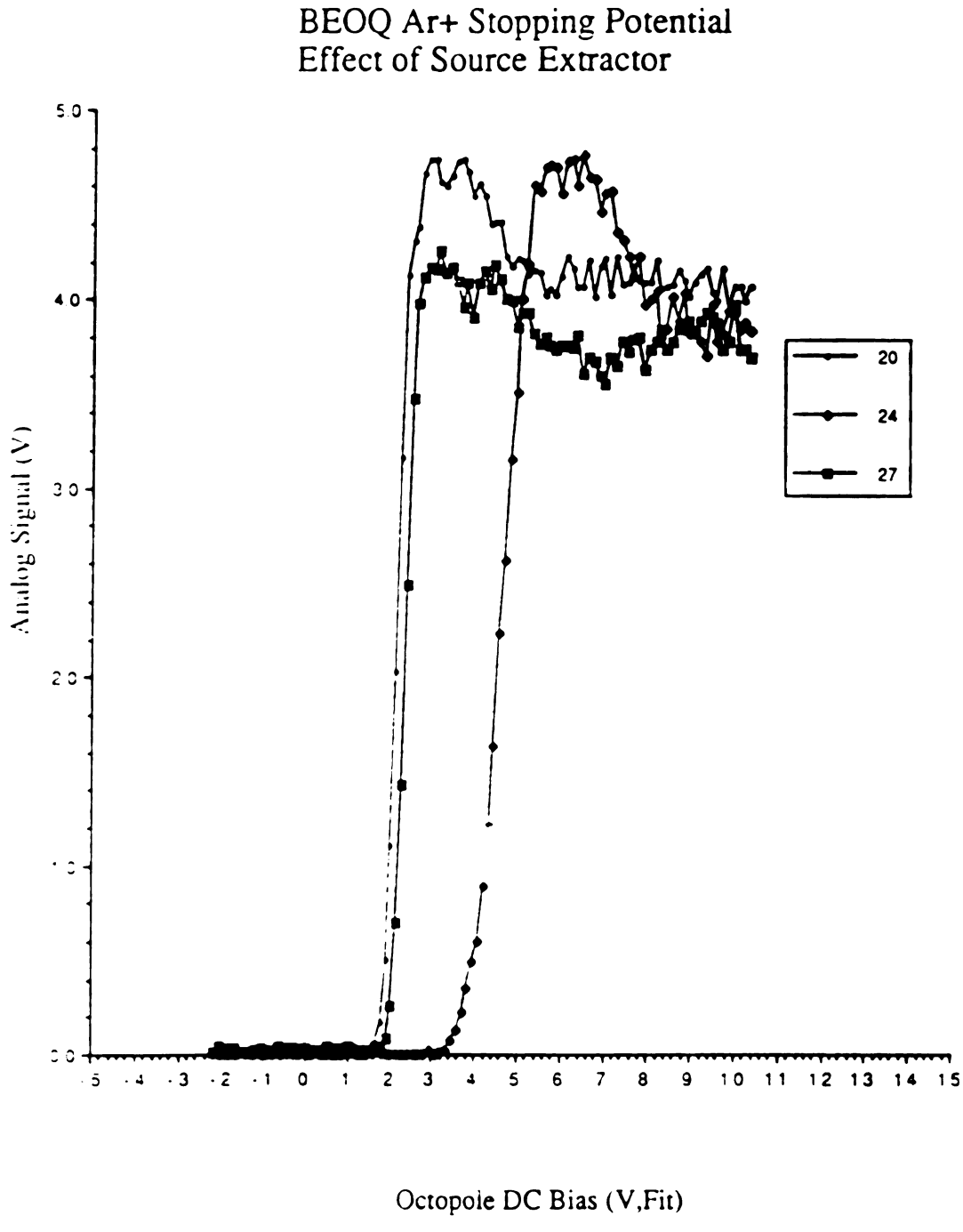

Figure F.9. Effect of ion source extraction field on stopping potential.

Appendix G

Interference With Mn_2^+ CID

As discussed in Chapter 4, low energy features were observed in the Mn_2^+ CID reaction when contaminated argon was used as a collision gas. This feature was eliminated when either high purity (99.999%) argon or getter-scrubbed argon was used. The low energy reactions may be attributed to processes related to water.

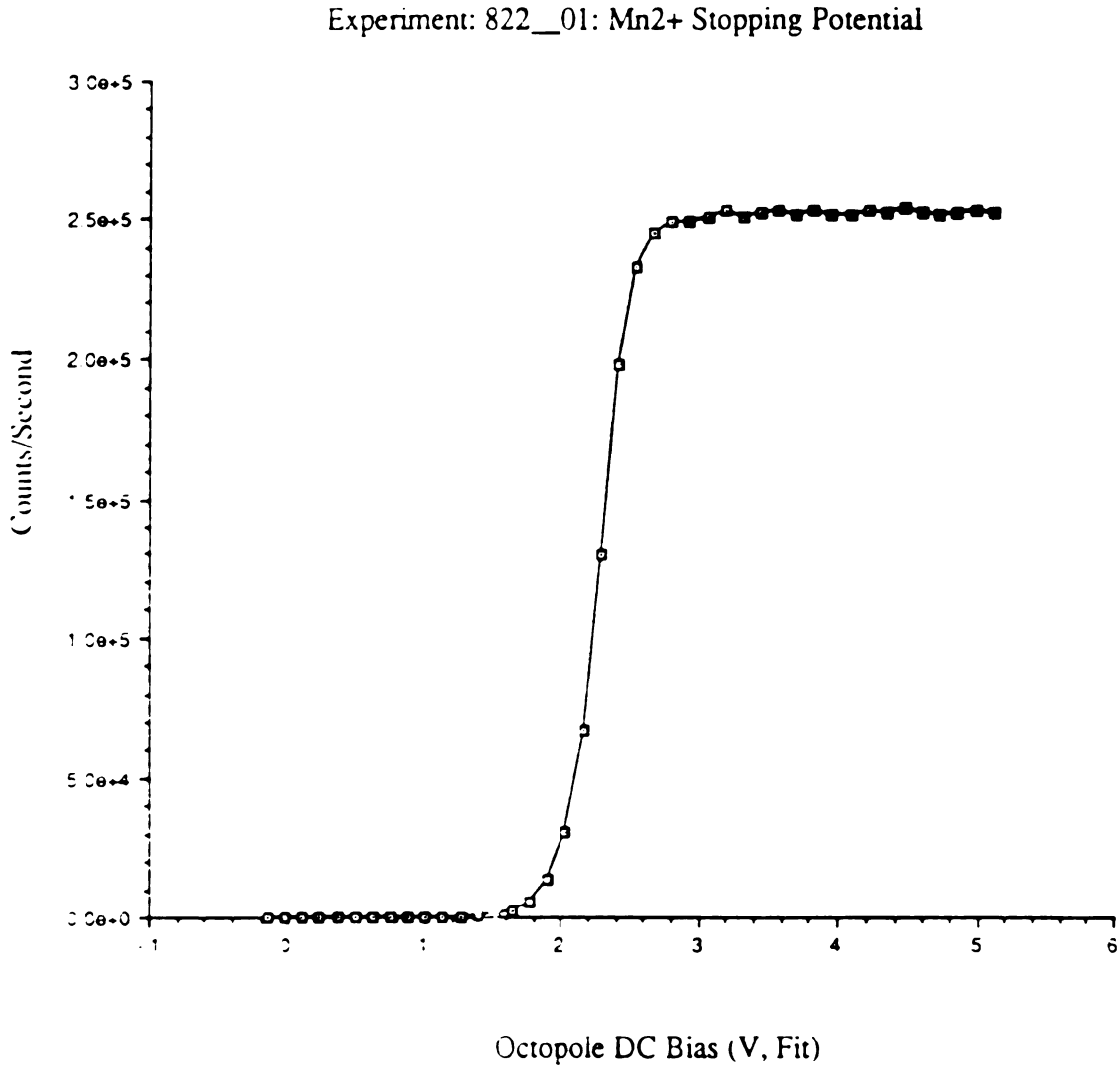

Figure G.1. Mn_2^+ stopping potential.

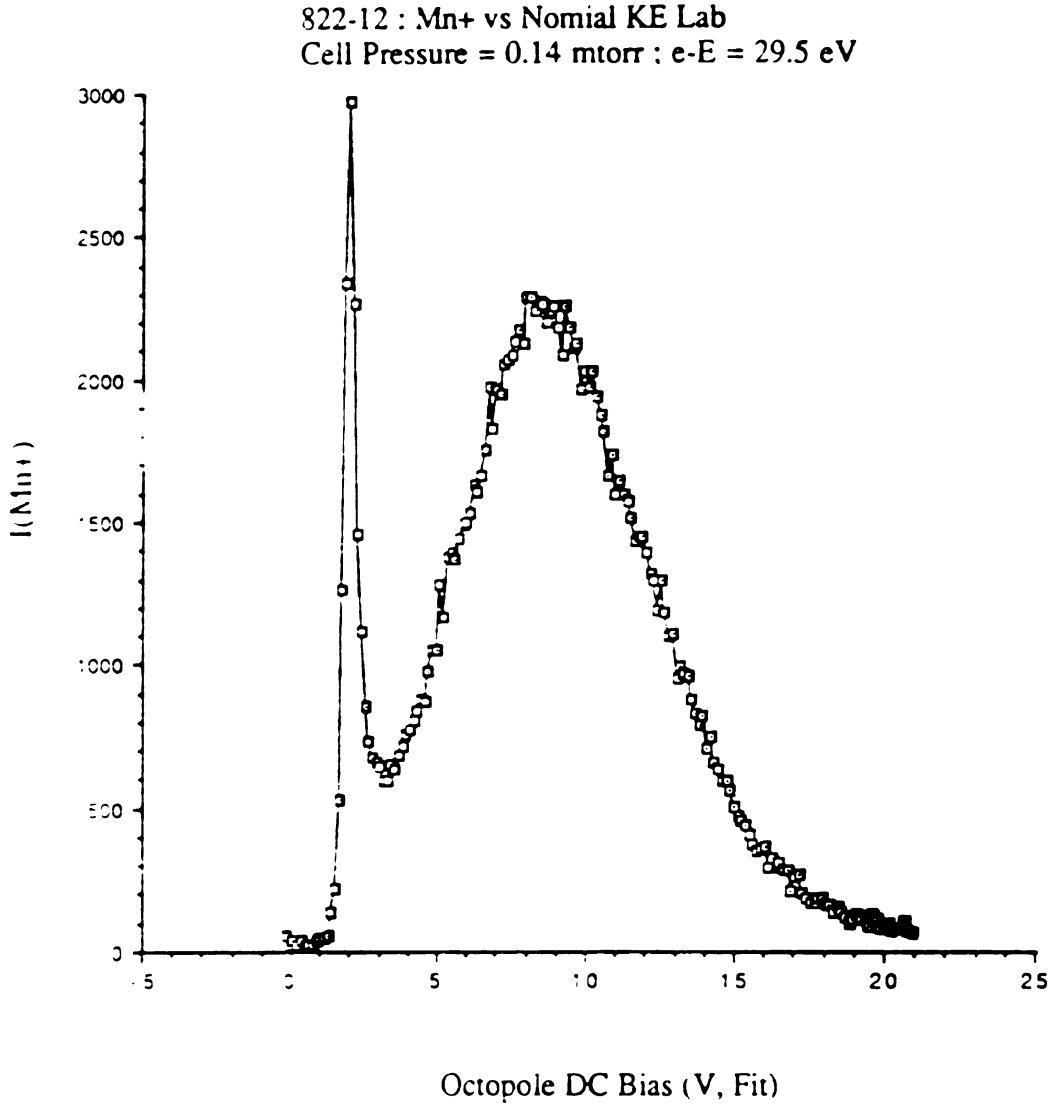

Figure G.2. Ion current for m/z 55 vs. lab collision energy.

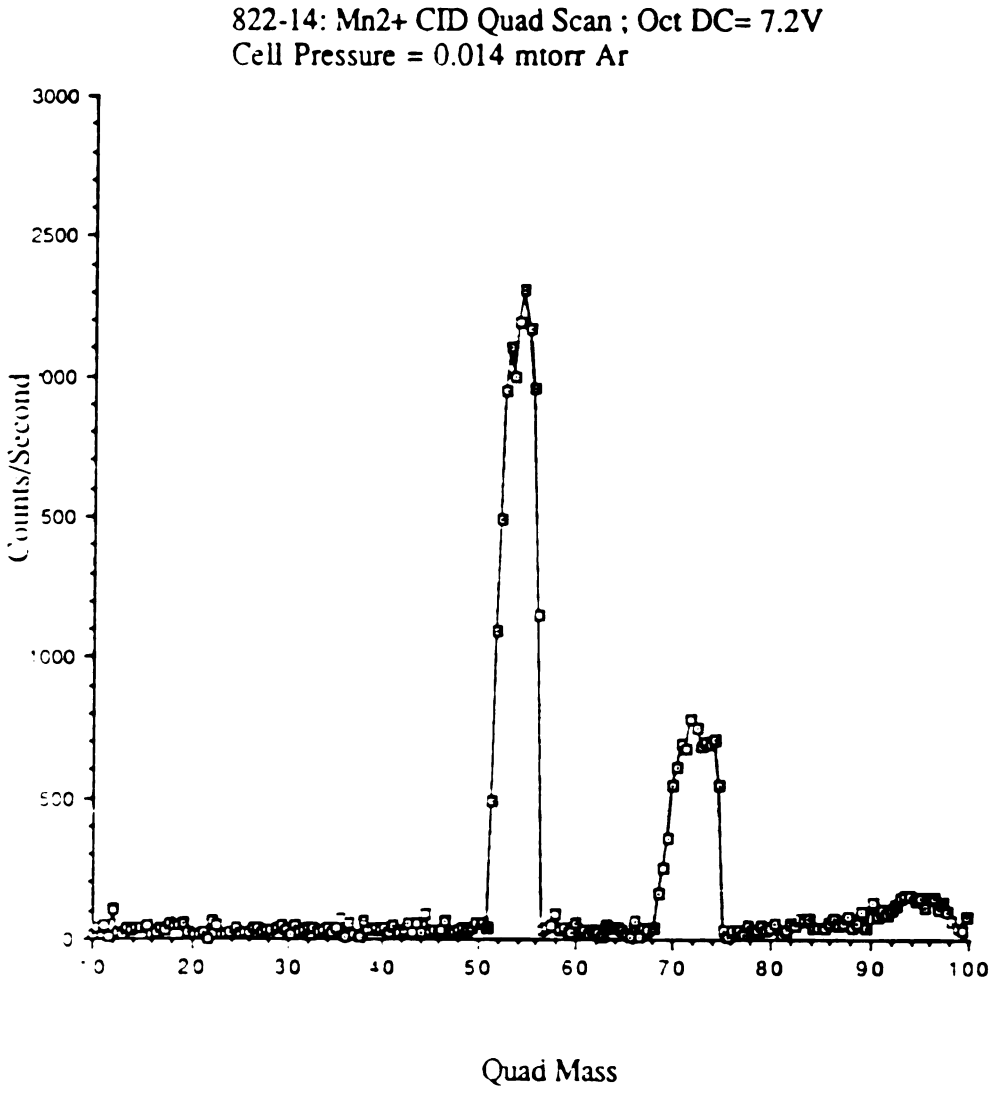

Figure G.3. Quad scan at a nominal collision energy of 2.2 eV.

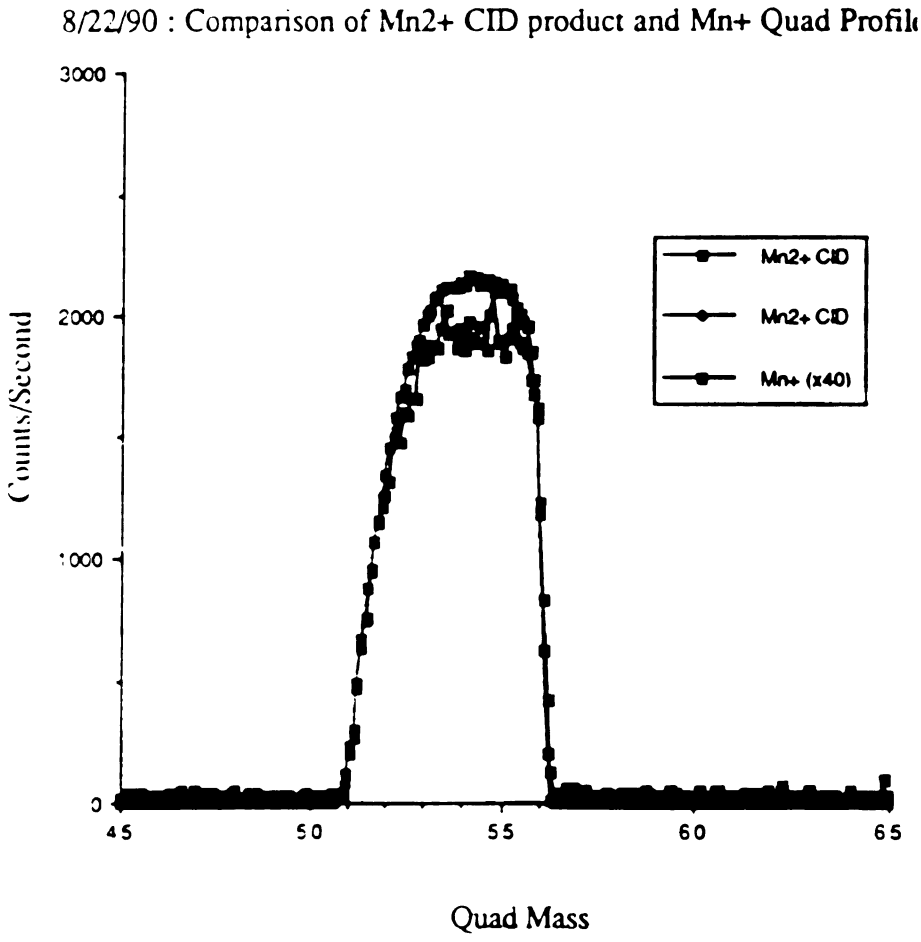

Figure G.4. Comparison of quad profiles for m/z 55 and CID product.

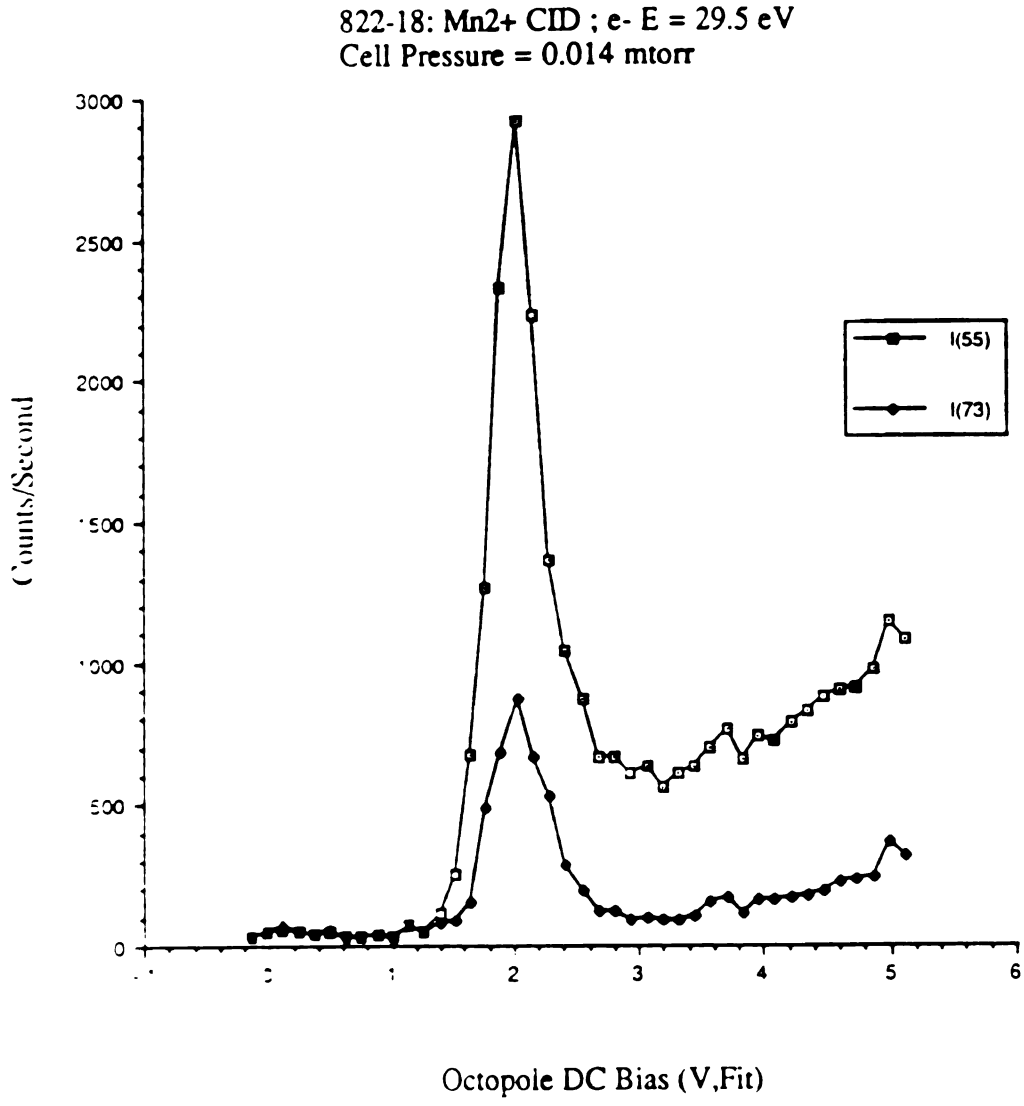

Figure G.5. Ion current for m/z 55 and m/z 73 vs. lab collision energy.

Appendix H

Instrument Parameters for the Ar^+ / D_2 Reaction

The operational parameters for the ion beam instrument used in the argon/deuterium experiments is shown in Table H.1.

Table H.1. Ion beam instrument parameters for Ar^+/D_2 reaction.

Experiment	Ar+/D2 Reaction		
Source Type	Intensitron	RF V(rms-amp)	5
P(source)	7.0 E-6 torr	SWR	1.05
I(e-)	21.0 uA	TUNER (T,I,A)	B, 10, G
Repeller	0	RF Power (HM-9)	0.90 W
Extractor	0	Transfer 1	732 volts
Shield	0	Transfer 2	944
Source Z1 (L,R)	009, 036	Transfer 3	1046
S Lens (L,R)	007, 031	Transfer 4	894
Source R	9.2	Transfer 5	989
Source Z2 (L,R)	081, 099	Transfer 6	---
E symmetry	425	Transfer 7	0
TIC	3.20 range 0.1	Transfer 8	0
Vaccel (Ua/Ub)	845.5 (1009 V)	Transfer 9	706
Hall	11.8	Quad DC Bias	984
Z1	1.142	P(collision cell)	0.10 mtorr
Z2	-9.35	P(Chamber A)	base
R	7.02	P(Chamber B)	base 6.4 E-7 torr
Einzel	614	P(Chamber C)	base
Injection	748	Daly CD	20 kV
RF Freq.	2.4815 M Hz	Daly PMT	1000